

A Framework for Modeling the Mechanical Behavior of Tempered Martensitic Steels at High Temperatures

DISSERTATION

zur Erlangung des akademischen Grades

Doktoringenieur

(Dr.-Ing.)

von M.Sc. Johanna Eisenträger
geboren am 28.09.1990 in Berlin

genehmigt durch die Fakultät für Maschinenbau
der Otto-von-Guericke-Universität Magdeburg

Gutachter:

1. Prof. Dr.-Ing. habil. Dr. h.c. mult. Holm Altenbach
2. Prof. em. Dr.-Ing. Dr.-Ing. E. h. Otto T. Bruhns

Promotionskolloquium am 08.05.2018

Kurzfassung

Wärmebehandelte martensitische Stähle werden für Bauteile in Kraftwerken unter Temperaturen von bis zu 903 K eingesetzt. Diese hohen Temperaturen begünstigen das Kriechen der Bauteile unter konstanten mechanischen Lasten. Zusätzlich unterliegen die Bauteile zyklischen Belastungen bedingt durch häufiges Hoch- und Herunterfahren der Kraftwerke zum Ausgleich von Versorgungslücken im Stromnetz. Martensitische Stähle zeichnen sich durch gute mechanische und thermische Eigenschaften aus, sodass sie sich für den Einsatz unter diesen anspruchsvollen Bedingungen eignen. Nachteilig wirkt sich hingegen aus, dass diese Legierungen sowohl unter konstanten als auch zyklischen Lasten entfestigen.

Zur Abbildung des mechanischen Verhaltens von martensitischen Stählen wird in der vorliegenden Arbeit ein Phasenverbundmodell beispielhaft anhand des martensitischen Stahls X20CrMoV12-1 vorgestellt. Dabei wird der Werkstoff als Mischung zweier Phasen dargestellt, wobei angenommen wird, dass der gleiche Verzerrungszustand in beiden Phasen vorliegt. Während die sogenannte „weiche“ Phase das Innere der Subkörner sowie Bereiche mit einer niedrigen Versetzungsdichte beschreibt, bezieht sich die „harte“ Phase auf die Korngrenzen und Regionen mit einer hohen Versetzungsdichte. Die Modellierung der Entfestigung beruht auf der Annahme, dass der Volumenanteil der harten Phase im Laufe der Deformation abnimmt. In seiner ursprünglichen Form orientiert sich das Phasenverbundmodell an mikrostrukturellen Vorgängen. Damit das Modell aber anhand von makroskopischen Versuchen kalibriert werden kann, werden eine Rückspannung basierend auf dem ARMSTRONG-FREDERICK-Modell und eine dimensionslose Entfestigungsvariable eingeführt, sodass man letztendlich ein gekoppeltes System dreier Entwicklungsgleichungen für die inelastische Verzerrung, die Rückspannung und die Entfestigungsvariable erhält. Wird dieses System für vorgeschriebene Belastungen gelöst, kann die geschwindigkeitsabhängige inelastische Verformung des Materials unter Berücksichtigung von Ver- und Entfestigungsvorgängen beschrieben werden.

Um Daten für die Kalibrierung des einachsigen Modells zu erhalten, werden zahlreiche Warmzug- und Kriechversuche durchgeführt. Die Warmzugversuche werden bei vorgeschriebener Dehnrates und unter konstanter Temperatur durchgeführt, wobei Temperaturen und Dehnrates in den Bereichen 673 K–923 K und $5 \times 10^{-5} \text{ s}^{-1}$ – $1 \times 10^{-3} \text{ s}^{-1}$ berücksichtigt werden. Zusätzlich werden einige Kriechversuche bei einer Temperatur von 873 K durchgeführt. Nach der Bestimmung der Parameter für das elastische Materialverhalten wird das inelastische Materialverhalten kalibriert. Anschließend wird das Verhalten der Ver- und Entfestigungsanteile identifiziert. Die Verifikation des kalibrierten Modells anhand zusätzlicher Kriechversuche zeigt, dass sich das Modell zur Simulation des Werkstoffverhaltens innerhalb eines großen Temperatur- (673 K–923 K) und Spannungsbereichs (100 MPa–700 MPa) eignet, wofür insgesamt nur 14 temperatur-unabhängige Parameter benötigt werden.

Des Weiteren wird das Phasenverbundmodell auf mehrachsige Spannungs- und Verzerrungszustände erweitert, was in Analogie zum einachsigen Modell ein gekoppeltes System dreier Entwicklungsgleichungen bezüglich des Tensors der inelastischen Verzerrungen, des Rückspannungstensors und der skalaren Entfestigungsvariable zur Folge hat. Die thermodynamische Konsistenz des Modells wird anhand der CLAUSIUS-PLANCK-Ungleichung nachgewiesen. Um die Simulation komplexer Bauteile zu ermöglichen, wird das mehrachsige Modell in das Finite-Elemente-Programm ABAQUS implementiert. Zur Integration der Entwicklungsgleichungen wird dabei auf das implizite EULER-Verfahren zurückgegriffen. Die numerische Umsetzung des Modells wird anhand zahlreicher Beispiele unter Berücksichtigung ein- und mehrachsiger Spannungszustände überprüft.

Den Abschluss dieser Arbeit bildet die Simulation der Auswirkungen eines Kaltstarts gefolgt von einem Warmstart auf einen Rotor in einem Kraftwerk. Dazu wird eine entkoppelte thermisch-mechanische Berechnung durchgeführt. Im Zuge der thermischen Analyse wird basierend auf den Dampftemperaturen sowie den Wärmeübergangskoeffizienten das Temperaturfeld im Rotor ermittelt. Dieses dient als Grundlage für die nachfolgende strukturmechanische Berechnung, in der die Spannungs- und Verzerrungszustände im Rotor mittels des entwickelten Phasenverbundmodells bestimmt werden. Diese Ergebnisse können zukünftig zur Berechnung der Schädigung verwendet werden, sodass die Lebensdauer der in Kraftwerken eingesetzten Bauteile präzise vorhergesagt werden kann.

Abstract

Tempered martensitic steels are commonly used for power plant components at elevated temperatures up to 903 K. In addition to the creep deformation induced by mechanical loads at the high temperatures, the components are subjected to cyclic loads because of the frequent start and stop operations of power plants. Due to their mechanical and thermal properties, tempered martensitic steels are ideal candidates to withstand these conditions. Nevertheless, it is well known that tempered martensitic steels suffer from softening effects under constant and cyclic loads.

The thesis at hand presents a framework for modeling the mechanical behavior of this type of steels at high temperatures. Here, the applicability of the proposed methods is demonstrated using the alloy X20CrMoV12-1, which is a typical representative of tempered martensitic steels. A phase mixture model is used to simulate the mechanical behavior of these alloys at elevated temperatures. The phase mixture model describes the alloy under consideration by means of an iso-strain approach including a hard and a soft phase. The hard phase is related to the subgrain boundaries and areas with a high dislocation density, while the soft phase represents the interior of the subgrains and regions with a low dislocation density. Softening effects are taken into account based on the assumption that the volume fraction of the hard phase decreases during deformation. In order to make the calibration of the model based on macroscopic material tests possible, a backstress of ARMSTRONG-FREDERICK-type and a dimensionless softening variable are introduced. This procedure results in a coupled system of three evolution equations with respect to the inelastic strain, the backstress, and the softening variable. Based on these evolution equations, the phase mixture model provides a unified description of the rate-dependent inelastic deformation including hardening and softening effects.

As a basis for the calibration of the model, the results of numerous high temperature tensile and creep tests are presented. During the high temperature tensile tests, a constant temperature and strain rate are prescribed in the intervals $673\text{ K} \leq T \leq 923\text{ K}$ and $5.0 \times 10^{-5}\text{ s}^{-1} \leq \dot{\epsilon} \leq 1.0 \times 10^{-3}\text{ s}^{-1}$, respectively. In addition, several creep tests are conducted at a constant temperature of 873 K under different load levels. The test results serve as basis for the calibration of the one-dimensional phase mixture model. In the first step of the complex calibration procedure, the elastic parameters are determined, which is succeeded by the calibration of the inelastic behavior, the hardening regime, and the softening range. The subsequent verification of the calibrated model using the results of additional creep tests taken from literature reveals that the model provides accurate approximations of the experimental data for wide ranges of both temperature and stress, i.e. $673\text{ K} \leq T \leq 923\text{ K}$ and $100\text{ MPa} \leq \sigma \leq 700\text{ MPa}$, respectively. The calibrated phase mixture model requires only 14 temperature-independent parameters for simulations with respect to the indicated validity ranges.

Furthermore, the phase mixture model is extended to multiaxial stress and deformation states, which results again in a coupled system of three evolution equations with respect to the inelastic strain tensor, the backstress tensor, and the scalar softening variable. In addition, the thermodynamic consistency of the model is demonstrated based on the CLAUSIUS-PLANCK inequality. The three-dimensional phase mixture model is implemented into the finite element code ABAQUS, while the backward EULER method is used for the implicit time integration of the evolution equations. The implementation of the model into the finite element method is verified by various examples, covering both uniaxial and multiaxial stress and deformation states.

As a final step of the proposed framework, the mechanical behavior of an idealized steam turbine rotor is simulated. Therefore, a decoupled thermo-mechanical finite element analysis is employed to simulate a cold start and a subsequent hot start of a power plant. Within the preceding heat transfer analysis, the instationary steam temperature and the heat transfer coefficients are prescribed, and the resulting temperature distribution in the rotor is computed. Based on the obtained temperature fields, the stress and strain tensors are determined in a subsequent structural analysis. For future applications, these results could lay the foundation for the estimation of creep and fatigue damage, thus allowing for a precise prediction of the lifetime of power plant components in use.

Contents

Notation	vii
1 Introduction	1
1.1 Tempered Martensitic Steels	2
1.1.1 Applications	2
1.1.2 Microstructure	3
1.1.3 Mechanical Behavior	4
1.2 Modeling Approaches	7
1.3 Outline	9
2 Theoretical Background	11
2.1 Continuum Mechanics	11
2.1.1 Kinematics	11
2.1.2 Kinetics	15
2.1.3 Mechanical Balance Laws	17
2.1.3.1 Mass	17
2.1.3.2 Linear Momentum	17
2.1.3.3 Angular Momentum	17
2.1.4 Constitutive Equations	18
2.1.4.1 Elasticity	18
2.1.4.2 Inelasticity	19
2.1.5 Initial Boundary Value Problem	22
2.1.6 Rule of Mixtures	24
2.2 Finite Element Method	25
2.2.1 Principle of Virtual Work	25
2.2.2 Spatial Discretization	27
2.2.3 System of Differential-Algebraic Equations	30
2.3 Mathematical Optimization	33
3 Experiments	37
3.1 High Temperature Tensile Tests	37
3.1.1 Experimental Set-Up	37
3.1.2 Results	38
3.1.2.1 Processing of Experimental Data	38
3.1.2.2 Test Series 1	40
3.1.2.3 Test Series 2	41
3.1.3 Discussion	44
3.1.3.1 Test Series 1	44
3.1.3.2 Test Series 2	46
3.2 Creep Tests	47
3.2.1 Experimental Set-Up	47
3.2.2 Results	48

3.2.3	Discussion	49
4	One-Dimensional Phase Mixture Model	51
4.1	Governing Equations	51
4.2	Calibration	57
4.2.1	Elasticity	57
4.2.2	Initial and Steady State	58
4.2.3	Inelasticity	59
4.2.4	Hardening	67
4.2.5	Softening	70
4.2.6	Summary	73
4.3	Verification	77
5	Three-Dimensional Phase Mixture Model	81
5.1	Governing Equations	81
5.2	Thermodynamic Consistency	87
5.3	Finite Element Analyses	90
5.3.1	Backward EULER Method	90
5.3.2	Derivatives for the Linearization	92
5.3.2.1	Derivatives of the Stress Response Functions	92
5.3.2.2	Derivatives of the VON MISES Variables	93
5.3.2.3	Derivatives of the Strain Increments	93
5.3.2.4	Derivatives of the Residual Variables	95
5.3.3	Numerical Implementation	98
5.3.3.1	Stress Update Algorithm	98
5.3.3.2	Inversion of the JACOBIAN Matrix	101
5.3.3.3	Consistent Tangent Operator	102
5.3.4	Verification of the UMAT	102
6	Analysis of a Steam Turbine Rotor	111
6.1	Heat Transfer Analysis	111
6.2	Structural Analysis	113
7	Summary and Outlook	119
	Bibliography	125
	Appendix	A-1
A1	Results of Profilometry	A-1
A2	Stress Response Functions for Inelastic Strain Rates	A-3

Notation

Preliminaries

- Small capitals are used for names, e.g. CAUCHY.
- Applying index notation, Latin indices take the values 1, 2, and 3, if not otherwise stated. Note that the EINSTEIN summation convention is applied.

- For direct tensor notation, the following conventions are valid:

a, A	scalar, tensor of zeroth rank	(italic)
\mathbf{a}	vector, tensor of first rank	(minuscule, italic, bold)
\mathbf{A}	dyad, tensor of second rank	(capital, italic, bold)
\mathcal{A}	tetrad, tensor of fourth rank	(capital, italic, bold, calligraphic)

- We make use of the following products applying the direct tensor notation with respect to orthonormal bases:

- the dyadic product between the vectors $\mathbf{a} = a_i \mathbf{e}_i$ and $\mathbf{b} = b_j \mathbf{e}_j$:

$$\mathbf{a} \otimes \mathbf{b} = a_i b_j \mathbf{e}_i \otimes \mathbf{e}_j,$$

- the dyadic product between the tensors of second rank $\mathbf{A} = A_{kl} \mathbf{e}_k \otimes \mathbf{e}_l$ and $\mathbf{B} = B_{mn} \mathbf{e}_m \otimes \mathbf{e}_n$:

$$\mathbf{A} \otimes \mathbf{B} = A_{kl} B_{mn} \mathbf{e}_k \otimes \mathbf{e}_l \otimes \mathbf{e}_m \otimes \mathbf{e}_n,$$

- the scalar product between the vectors $\mathbf{a} = a_i \mathbf{e}_i$ and $\mathbf{b} = b_j \mathbf{e}_j$:

$$\mathbf{a} \cdot \mathbf{b} = a_i b_i,$$

- the scalar products between the tensor of second rank $\mathbf{A} = A_{kl} \mathbf{e}_k \otimes \mathbf{e}_l$ and the vector $\mathbf{a} = a_i \mathbf{e}_i$:

$$\mathbf{a} \cdot \mathbf{A} = A_{kl} a_l \mathbf{e}_k,$$

$$\mathbf{A} \cdot \mathbf{a} = A_{kl} a_k \mathbf{e}_l,$$

- the double scalar product between the tensors of second rank $\mathbf{A} = A_{kl} \mathbf{e}_k \otimes \mathbf{e}_l$ and $\mathbf{B} = B_{mn} \mathbf{e}_m \otimes \mathbf{e}_n$:

$$\mathbf{A} : \mathbf{B} = A_{kl} B_{lk},$$

- the double scalar products between the tensor of second rank $\mathbf{A} = A_{kl} \mathbf{e}_k \otimes \mathbf{e}_l$ and the tensor of fourth rank $\mathcal{C} = C_{opqr} \mathbf{e}_o \otimes \mathbf{e}_p \otimes \mathbf{e}_q \otimes \mathbf{e}_r$:

$$\mathcal{C} : \mathbf{A} = C_{opqr} A_{rq} \mathbf{e}_o \otimes \mathbf{e}_p,$$

$$\mathbf{A} : \mathcal{C} = A_{po} C_{opqr} \mathbf{e}_q \otimes \mathbf{e}_r,$$

- the vector product between the vectors $\mathbf{a} = a_i \mathbf{e}_i$ and $\mathbf{b} = b_j \mathbf{e}_j$:

$$\mathbf{a} \times \mathbf{b} = a_i b_j \epsilon_{ijk} \mathbf{e}_k,$$

where ϵ_{ijk} is the LEVI-CIVITA symbol with respect to three dimensions.

- For matrix notation, the following conventions are deployed:

\mathbf{a}	vector	(minuscule, upright, bold, sans-serif)
\mathbf{A}	matrix	(capital, upright, bold, sans-serif)

Latin Symbols

A	area	f_η	constitutive function for the volume fraction of the hard phase
\mathbf{A}	JACOBIAN matrix	f_σ	stress response function for the inelastic strain rates
\mathbf{A}_1	auxiliary matrix	f_σ^I	stress response function for the inelastic strain rates w.r.t. low stresses
\mathbf{A}_2	auxiliary matrix	f_σ^{II}	stress response function for the inelastic strain rates w.r.t. high stresses
a_β	material parameter	f_T	temperature response function for the inelastic strain rates
a_Γ	material parameter	g	objective function
b	body force	G	shear modulus
\mathbf{b}	vector of body forces (tensor)	g_μ	approximate objective function
\mathbf{B}	vector of body forces (matrix)	h	inequality constraint function
\mathfrak{B}	strain-displacement matrix	\mathbf{h}	vector of inequality constraint functions
\mathfrak{B}	material body	H	logarithmic HENCKY strain
$\partial\mathfrak{B}$	surface of material body	\mathbf{H}	quadratic matrix
b_β	material parameter	\mathbf{H}	logarithmic HENCKY strain tensor
b_Γ	material parameter	\mathbf{I}	unit tensor of second rank
C	right CAUCHY-GREEN strain	\mathcal{I}	unit tensor of fourth rank
\mathcal{C}	right CAUCHY-GREEN strain tensor	J	invariant of a tensor
\mathcal{C}	elastic stiffness tensor	\mathbf{J}	JACOBIAN matrix
\mathbf{C}	elastic stiffness matrix	k	equality constraint function
$\tilde{\mathcal{C}}$	tangent operator	\mathbf{k}	vector of equality constraint functions
$\tilde{\mathbf{C}}$	tangent operator matrix	K	bulk modulus
c_1	auxiliary variable	\mathbf{K}	stiffness matrix
c_2	auxiliary variable	L	(gauge) length
c_3	auxiliary variable	\mathcal{L}	auxiliary LAGRANGE function
c_4	auxiliary variable	L_c	reduced specimen length
c_5	auxiliary variable	L_t	specimen length
c_Γ	material parameter	m	mass
C_1	material parameter	\mathbf{n}	normal vector
C_2	material parameter	N	normal force
C_3	material parameter	\mathbf{N}	matrix of shape functions
C_4	material parameter	\mathbb{N}	set of natural numbers
C_Γ	material parameter	N^i	shape function w.r.t. i th node
d	diameter	NC	number of cycles
D	domain	NE	number of elements
d_1	thread diameter	NN	number of nodes
\mathbf{e}	basis vector	NP	number of integration points in ξ_1 direction
E	YOUNG's modulus	NQ	number of integration points in ξ_2 direction
E^G	GREEN strain		
\mathbf{E}^G	GREEN strain tensor		
f	frequency		
\mathbf{f}	surface force vector		
\mathbf{f}	vector of forces		
F	deformation gradient (1D)		
\mathbf{F}	deformation gradient (3D)		
f_E	temperature response function for YOUNG's modulus		
f_H	constitutive function for the inelastic strain rates		

NR	number of integration points in ξ_3 direction	t	time
p	pressure	\mathbf{t}	stress vector w.r.t. the force vector and the area element in the current configuration
\mathbf{p}	vector of linear momentum		
\mathbf{p}	vector of unknowns	t_I	stress vector w.r.t. the force vector in the current configuration and the area element in the reference configuration
P	PIOLA-KIRCHHOFF stress		
\mathbf{P}	1st PIOLA-KIRCHHOFF stress tensor		
q	scalar internal variable	t_{II}	stress vector w.r.t. the force vector and the area element in the reference configuration
\mathbf{q}	vector of angular momentum		
Q	activation energy		
\mathbf{Q}	tensorial internal variable	T	temperature
\mathbf{Q}	auxiliary matrix	\mathbf{T}	auxiliary matrix
r	radius	T_L	liquidus temperature
\mathbf{r}	residual vector	u	displacement
R	universal gas constant	\mathbf{u}	displacement vector (tensor)
\mathbb{R}	set of real numbers	\mathbf{u}	displacement vector (matrix)
\mathbf{R}	rotation tensor	\mathbf{U}	right stretch tensor
$R_{p0.2}$	offset yield strength	\mathbf{U}	auxiliary matrix
\mathbb{R}^q	real vector space of dimension q	\mathbf{v}	velocity vector
\mathbf{R}_β	residual tensor w.r.t. the backstress	\mathbf{v}	vector of parameters
\mathbf{R}_σ	residual tensor w.r.t. the stress	V	volume
\mathbf{r}_σ	residual vector w.r.t. the stress	\mathbf{V}	auxiliary matrix
\mathbf{r}_β	residual vector w.r.t. the backstress	∂V	boundary of a body
r_Γ	residuum w.r.t. the softening variable	∂V_t	boundary with traction BCs
$r_{\sigma zz}$	residuum w.r.t. the longitudinal stress	∂V_u	boundary with displacement BCs
		w	weight factor
r_a	outer radius	W	work
r_i	inner radius	\mathbf{W}	auxiliary matrix
s	slack variable	x	coordinate
\mathbf{s}	vector of slack variables	\mathbf{x}	position vector (tensor)
\mathbf{S}	2nd PIOLA-KIRCHHOFF stress tensor	\mathbf{x}	position vector (matrix)

Greek Symbols

α^{th}	coefficient of thermal expansion	λ^{th}	thermal conductivity
β	backstress	$\boldsymbol{\lambda}^h$	vector of LAGRANGE multipliers w.r.t. the inequality constraints
$\boldsymbol{\beta}$	backstress tensor	$\boldsymbol{\lambda}^k$	vector of LAGRANGE multipliers w.r.t. the equality constraints
$\boldsymbol{\beta}$	backstress vector	μ	barrier parameter
γ	isotropic hardening variable	ν	POISSON'S ratio
Γ	softening variable	ξ	natural coordinate
ε	engineering strain	$\boldsymbol{\xi}$	vector of natural coordinates
$\boldsymbol{\varepsilon}$	engineering strain tensor	$\xi_{1p},$	coordinates of integration point
$\boldsymbol{\varepsilon}$	engineering strain vector	$\xi_{2q},$	(p, q, r)
ε_V	volumetric strain	ξ_{3r}	
ζ	softening modulus	Ξ	set of vectors
η	volume fraction		
κ^{th}	heat transfer coefficient		

Notation

Π	functional	$\tilde{\sigma}$	effective stress vector
ρ	mass density	σ_m	mean stress
σ	CAUCHY stress	Υ	HELMHOLTZ free energy
$\tilde{\sigma}$	effective stress	Φ	motion (1D)
$\boldsymbol{\sigma}$	CAUCHY stress tensor	Φ	motion (3D)
$\tilde{\boldsymbol{\sigma}}$	effective stress tensor	Ψ	potential
$\boldsymbol{\sigma}$	CAUCHY stress vector	Ω	domain of a body

Indices and Accents

\square^{calc}	calculated value	\square_k	index for phase: $k \in \{s, h\}$
\square^{dyn}	dynamic	\square_{max}	maximum
\square^{el}	elastic	\square_{min}	minimum
\square^{exp}	experimental value	\square_n	w.r.t. the n th time step
\square^i	w.r.t. the i th iteration step	\square_n	nodal quantity
\square^{in}	inelastic	\square_{ref}	reference value
\square^{int}	internal	\square_s	soft phase
\square^T	transposed value	\square_{st}	steady state
\square^{-1}	inverse value	\square_{vM}	VON MISES variable
\square^*	solution at minimum	\square_*	saturation value
\square_a	w.r.t. the "Test a"	\square_0	reference configuration
\square_{act}	active part	$\check{\square}$	prescribed variable
\square_b	w.r.t. the "Test b"	$\bar{\square}$	normalized variable
\square_e	elemental quantity	\square'	deviator
\square_{end}	w.r.t. the last time step	$\hat{\square}$	amplitude
\square_h	hard phase	$\dot{\square}$	1st derivative w.r.t. the time
\square_{init}	initial state	$\ddot{\square}$	2nd derivative w.r.t. the time

Operators

$\mathbf{A}\square$	assembly operator	$\sinh(\square)$	hyperbolic sine function
$\cosh(\square)$	hyperbolic cosine function	$\text{tr}(\square)$	trace
$d\square$	infinitesimal value	$\Delta\square$	incremental value
$\mathbf{d}_u\square$	GÂTEAUX derivative w.r.t. \mathbf{u}	$\delta\square$	variation
$\det(\square)$	determinant	$\nabla\square$	nabla operator
$\exp(\square)$	exponential function	$ \square $	EUCLIDEAN norm
$\lim\square$	limit	$\square \cdot \square$	scalar product
$\ln(\square)$	natural logarithm	$\square : \square$	double scalar product
$\min(\square)$	minimisation	$\square \times \square$	vector product
$\text{sgn}(\square)$	sign function		

Abbreviations

BC	boundary condition	LVDT	linear variable differential transformer
CTO	consistent tangent operator	ODE	ordinary differential equation
DAE	differential-algebraic equation	SEM	scanning electron microscope
EBSD	electron backscatter diffraction	TEM	transmission electron microscopy
FEM	finite element method	TMF	thermo-mechanical fatigue
HT	high temperature	UMAT	User Material
IC	initial condition		

1 Introduction

The worldwide energy demand continues to increase as the global population grows and the developing world economies expand [1, 2]. In the year 2010, the global energy generating capacity accounted for 5061 GW [3]. Thereby, conventional sources of energy, such as liquid fuels, natural gas, coal, and nuclear technology, contributed the major part, i.e. $\approx 74\%$. The remaining percentage of $\approx 26\%$ is attributed to wind, geothermal, and solar energy, as well as other renewable sources [3]. In addition, estimations of the global energy generating capacity for the year 2040 are provided in [3]. An increased total capacity of 8254 GW is estimated, corresponding to a relative increase in global energy generating capacity of $\approx 63\%$ in comparison to the year 2010. Furthermore, BREEZE forecasts that the conventional sources of energy will provide $\approx 65\%$ of the total capacity, whereas renewable sources of energy will contribute the remaining part of $\approx 35\%$ [3]. Two conclusions can be drawn based on these numbers: Renewable sources of energy gain importance with an increasing contribution to the global energy generation. However, this increase is relatively slow such that the major part of the global energy generation will still be contributed by conventional sources of energy over the next years.

Most conventional sources of energy, such as liquid fuels, natural gas, and coal, are subjected to an increasing resource scarcity since these nonrenewable resources take millions of years to form and reserves are depleted much faster than new resources can be produced [1]. As one example, global natural gas supplies are estimated to suffice for another 63.5 years according to [3]. On top of this, specific regions are under much greater pressure, e.g. the reserves in North America are predicted to last only another 12.5 years at the current rates of consumption. Due to the resource scarcity, efficient power generation is of utmost importance. In addition, environmental aspects should be taken into account. If energy is produced in an efficient way, the emission of air pollutants is reduced, and less nuclear waste must be depolluted [4]. Finally, the production costs of electricity are lowered.

A major part of the global electricity demand is produced in modern power plants with steam turbines. In order to increase the efficiency of these turbines, elevated temperatures are favorable [3, 5], and consequently power plant components have to withstand high temperature loads. On top of this, the contribution of renewable sources of energy to the global energy supply leads to an additional demand on conventional power plants. Many renewable sources including wind and solar energy are intermittent and often unpredictable due to ambient conditions, in contrast to the steady and predictable output of a conventional power plant [3]. In case of a reduced production of energy by renewable sources, conventional power plants have to close this gap. Therefore, power plants are frequently started and shut down, what results in cyclic loads on the power plant components [6–10].

For these reasons, the investigation of the mechanical behavior of the deployed materials for power plant components is still of utmost importance. Tempered martensitic steels with high chromium content are excellent candidates for these high temperature applications. The thesis at hand aims to establish a framework for the numerical analysis of the mechanical behavior of such alloys at elevated temperatures. As a typical representative of this class of materials, the alloy X20CrMoV12-1 is investigated in the thesis at hand.

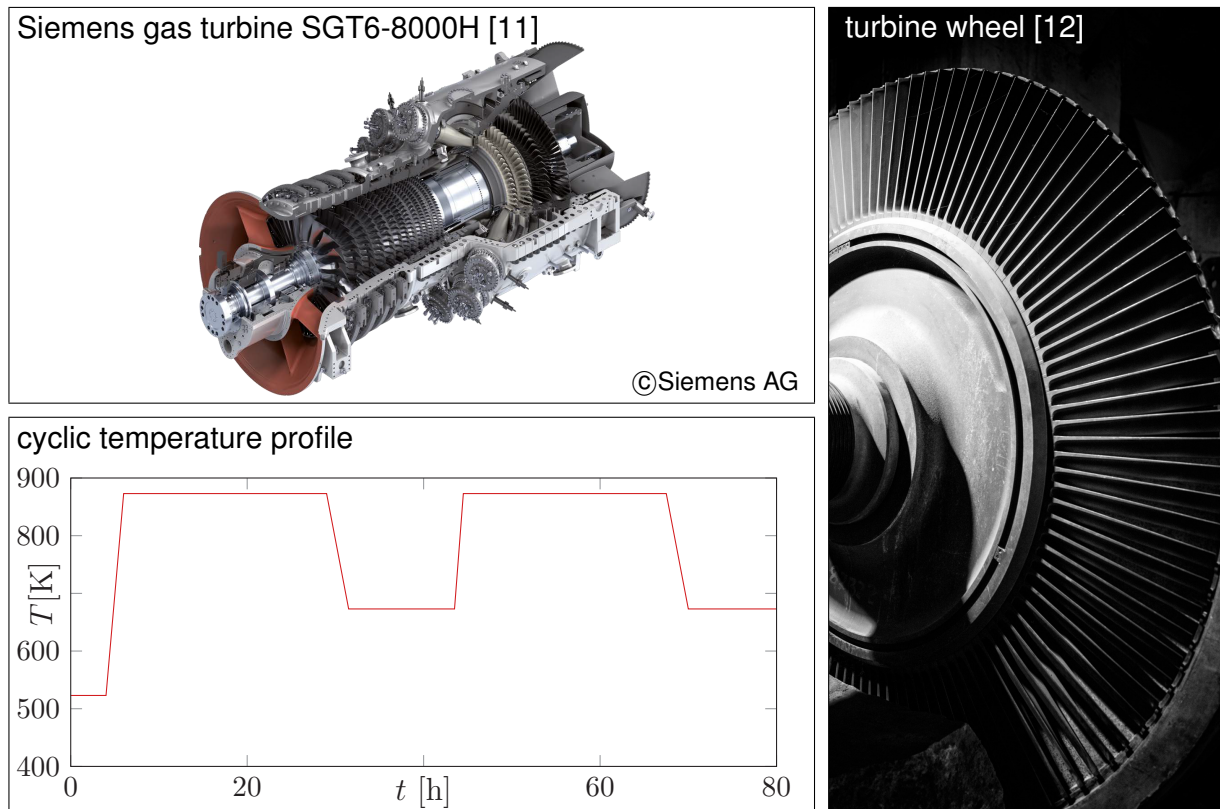


Figure 1.1: Power plant components and a typical temperature profile with day-night cycles.

1.1 Tempered Martensitic Steels

1.1.1 Applications

Tempered martensitic steels with high chromium content (9%–12%) are well-established for applications in fossil-fuel and nuclear power plants at elevated temperatures. Often turbines, tubes, housings, and also other components are made of these materials [13–17], a typical example is given in Fig. 1.1. Starting in the 1950s, the alloy X20CrMoV12-1 (steel number 1.4922 [18]) has widely been used for forged components of turbine shafts for high-pressure applications. Further applications are tubes and pressure vessels subjected to high temperatures [19].

The in-service conditions in power plants lead to challenging demands on the utilized materials. In order to increase the efficiency of power plants, the steam temperature should be as high as possible. Currently, temperatures around 873 K are common in both fossil-fuel and modern nuclear power plants, with a tendency to exploit even higher temperatures in future applications (around 903 K and more) [3, 5, 8, 20]. Furthermore, cyclic loads are induced due to frequent start-ups and shut-downs of power plants. In recent years, renewable energy sources such as the solar and wind energies are gaining constantly more popularity. However, the energy production of renewables is strongly dependent on the day-night cycle and weather conditions. If wind generators and solar power plants do not produce enough energy due to ambient conditions (e.g. not enough wind, many clouds or during night), conventional power plants have to close this gap [21]. These start and stop operations induce cyclic loads with long holding times (typically several hours up to 1 month) [6–10], as depicted schematically in Fig. 1.1.

In order to estimate the impact of thermal loads on a specific material, the applied temper-

atures should always be provided with respect to the liquidus temperature of the material under consideration. It is surprising that in the wide body of literature no information about the liquidus temperature T_L of the alloy X20CrMoV12-1 is available. Therefore, it is estimated based on the thermodynamic approach presented in [22], where empirical expressions for the liquidus temperature of an alloy are derived based on its chemical composition and verified successfully by means of experimental results. The typical chemical composition of the alloy X20CrMoV12-1 is taken from [23] (p. 38, Fig. 3.1) and given at this point for the sake of completeness:

Carbon (C):	0.17–0.23%
Chromium (Cr):	10.00–12.50%
Molybdenum (Mo):	0.80–1.20%
Vanadium (V):	0.25–0.35%
Manganese (Mn):	$\leq 1.00\%$
Niobium (Ni):	0.30–0.80%

In the remainder of this thesis, the liquidus temperature is estimated considering an average composition of 0.20% C, 11.25% Cr, 1.00% Mo, 0.30% V, 0.50% Mn, and 0.50% Ni. Accordingly, a liquidus temperature of $T_L \approx 1764$ K is computed. Thus, an applied temperature of $T = 873$ K corresponds to a relative temperature of $T/T_L \approx 0.49$. The temperature related to the liquidus temperature is also referred to as “homologous temperature” [24], and it is commonly used to classify creep loads. According to [24], one can distinguish three different creep ranges: low temperature creep corresponding to a homologous temperature of $T/T_L \approx 0.1$, high temperature creep ($T/T_L \approx 0.5$), and creep at very high temperatures, i.e. $T/T_L \approx 0.9$. As can be seen, power plant components are subjected to intermediate creep loads. However, one should bear in mind that the frequent temperature changes induce cyclic loads, thus increasing the actual load on power plant components.

In addition to the thermal loads, the rotating turbine parts have to withstand mechanical loads, i.e. the steam pressure p and centrifugal forces due to the rotational frequency f . Usually, steam pressures of $p = 20$ MPa–30 MPa are applied [25, 26], and a frequency of $f = 50$ Hz is used for power generation.

1.1.2 Microstructure

This thesis intends to analyze the macromechanical behavior of tempered martensitic steels. Nevertheless, the properties of a material on the macroscale are strongly dependent on microstructural processes, which is why they are described in the following. Here, a special emphasis is obviously put on martensitic steels with high chromium content. The presentation of the content of this section is based on standard monographs from the field of material sciences, where also further information can be found [27, 28].

On the microscale, metallic materials show a regular structure, the so-called lattice. Under the microscope, one can distinguish individual grains, i.e. areas with similar lattice orientation, and their boundaries. Grain boundaries are designated as two-dimensional lattice defects, separating adjacent grains. Depending on the magnitude of the disorientation of adjacent grains, one differentiates between high-angle and low-angle grain boundaries. Usually, the boundary between adjacent grains with a disorientation angle lower than $\approx 15^\circ$ is termed “low-angle grain boundary”, while boundaries between adjacent grains with a higher disorientation angle are referred to as “high-angle grain boundaries” [29]. Inside a grain, the lattice orientation might vary slightly, such that one can distinguish subgrains separated by low-angle grain boundaries from other subgrains [13].

High chromium martensitic steels are composed of several phases, e.g. ferrite, martensite, austenite, and precipitates. These steels are usually heat-treated in order to improve their mechanical properties. The heat treatment comprises two steps: austenitization and annealing. Before the heat treatment, ferrite represents the primary phase. Steels with a chromium content of 12% are usually heated up to 1323 K, such that austenite forms, and precipitates dissolve. During the cool-down, austenite transforms into hard martensite. Afterwards, annealing is started, and the specimen is heated up to 1003 K–1033 K in order to reduce internal stresses and increase the ductility of the material [13].

If the carbon content of an alloy is smaller than 0.2%, martensite forms a lath structure and represents the primary phase. Such alloys are not capable of forming an austenitic phase. Between and also inside the martensite laths, dislocations, i.e. one-dimensional lattice defects, concentrate, such that subgrain boundaries are formed. In martensitic steels, the formation of subgrain boundaries starts due to an initial heat treatment. In contrast, high-angle grain boundaries separate lath packs of different orientations. Furthermore, there are carbides, which segregate primarily during annealing on the boundaries of martensite laths [13]. Carbides and other microstructural elements of high chromium martensitic steels are shown in the micrographs compiled in Fig. 1.2.

1.1.3 Mechanical Behavior

Considering the high thermo-mechanical loads mentioned in Sect. 1.1.1, the choice of material is crucial in order to achieve long lifetimes of components. For this reason, Table 1.1 provides an overview with respect to the mechanical and thermal properties of different steels according to [30]. Values for the offset yield strength $R_{p0.2}$ (at room temperature), the averaged coefficient of thermal expansion α^{th} (for $293 \text{ K} \leq T \leq 873 \text{ K}$), and the thermal conductivity λ^{th} (at room temperature) are given. One should consider these values as exemplary since a limited number of representative alloys per group has been taken into account in [30]. Nevertheless, it becomes obvious that high chromium martensitic steels have a relatively high tensile strength as well as a low coefficient of thermal expansion and an increased thermal conductivity. This is confirmed in [6, 15, 17, 31–34], where the good corrosion resistance and creep strength of high chromium martensitic steels are underlined, too.

These properties distinguish tempered martensitic steels from other classes of steels and make them ideal candidates for operations under high temperatures. However, it is well known that 9%–12% chromium martensitic steels suffer from softening under creep and

Table 1.1: Mechanical and thermal properties of steel alloys, after [30].

material	$R_{p0.2}$ [MPa]	α^{th} [$\mu\text{m} (\text{m K})^{-1}$]	λ^{th} [$\text{W} (\text{m K})^{-1}$]
high temperature construction steels	225 ... 290	14.0 ... 14.5	35 ... 55
high chromium martensitic steels	450 ... 490	12.3	24
high temperature austenitic steels	160 ... 190	18.5	16
nickel-based alloys	600	15.2	13

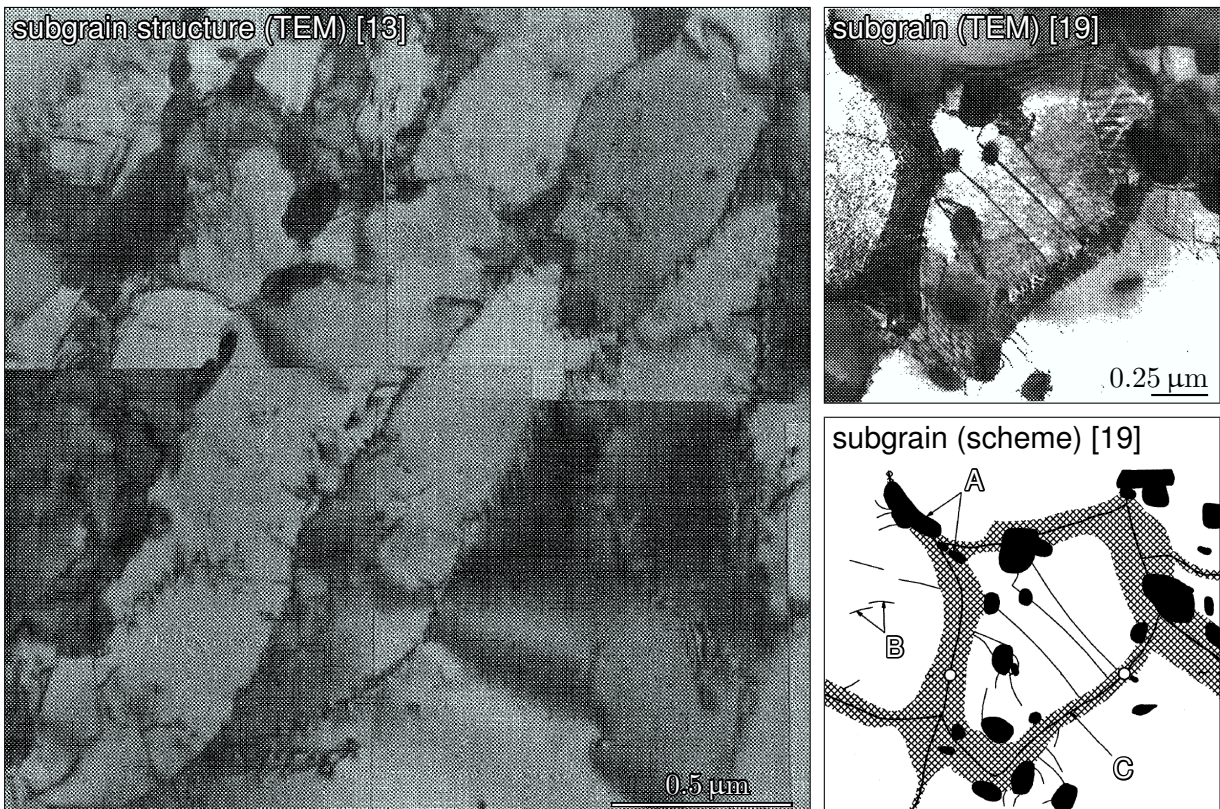


Figure 1.2: Microstructure of martensitic steels (A carbides, B dislocations, C boundary).

fatigue loads [7–10, 13, 14, 35–38]. With respect to creep, the term “softening” refers to an increase of the strain rate with increasing time and deformation [39]. This behavior becomes obvious in the bottom left diagram of Fig. 1.3, presenting the results of creep tests at 873 K under constant compressive stress levels σ (definitions of stress and strain measures are given in Chapt. 2). The absolute inelastic HENCKY strain rate $|\dot{H}^{in}|$ is depicted depending on the absolute inelastic HENCKY strain $|H^{in}|$. All five curves exhibit the primary and tertiary creep stage, cf. [40, 41]. In the primary stage, hardening processes are dominant, and the strain rate decreases until the minimum strain rate is reached. A secondary creep stage with constant strain rate cannot be observed, which is a typical feature of high chromium martensitic steels [42]. During the tertiary creep stage, the strain rate increases since softening processes take place on the microstructural level. Among others, STRAUB has shown that softening is due to the coarsening of subgrains and carbides [13]. The coarsening of precipitates, such as carbides, under creep conditions is confirmed in [35–37].

The behavior of 9%–12% chromium martensitic steels under fatigue loads has also been examined in detail during the last years. In [10], the alloy X20CrMoV12-1 and two other martensitic steels are examined with respect to fatigue. As one example, the top diagrams of Fig. 1.3 present the input and the results of strain-controlled fatigue tests at 873 K. The total strain is prescribed as a triangular function of the time with a frequency of $f = 5$ Hz, cf. the top left diagram in Fig. 1.3. In the top right diagram, the stress amplitude $\hat{\sigma}$ is depicted depending on the number of cycles NC for different prescribed amplitudes of total strain $\hat{\epsilon}$. Particularly for large strain amplitudes, the stress amplitude decreases during the fatigue test. Reference [10] confirms this cyclic softening effect for all three considered alloys. In [43], results from cyclic tests demonstrate that also the examined 9% chromium martensitic steel exhibits this cyclic softening effect. Additionally, FOURNIER and co-workers have examined the cyclic behavior of other martensitic steels [7–9, 14, 38]. In [7, 8], the softening

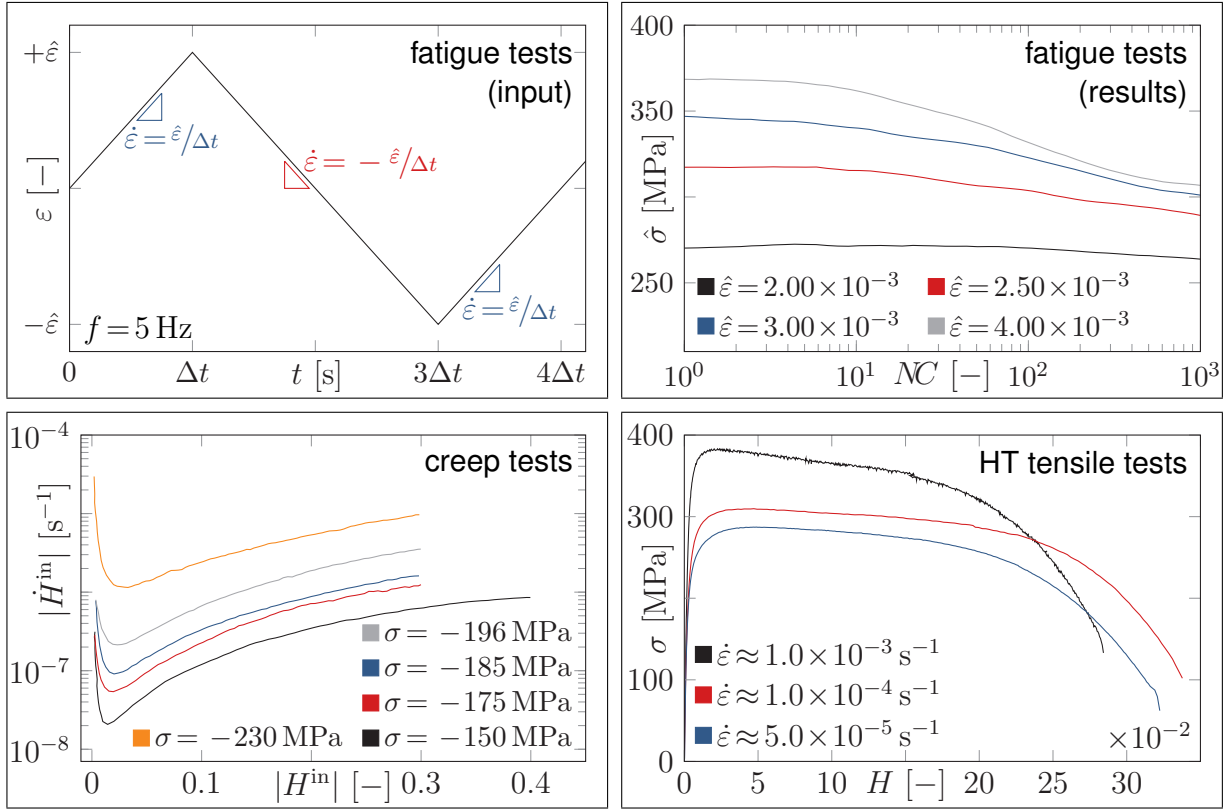


Figure 1.3: Material tests on X20CrMoV12-1 at 873 K. Engineering strain ε vs time t for one cycle during fatigue tests with prescribed strain amplitudes $\hat{\varepsilon}$ (top left), CAUCHY stress amplitude $\hat{\sigma}$ vs number of cycles NC as result of fatigue tests [10] (top right), absolute inelastic HENCKY strain rate $|\dot{H}^{in}|$ vs absolute inelastic HENCKY strain $|H^{in}|$ for creep tests under constant compressive stress σ [13] (bottom left), stress σ vs HENCKY strain H for HT tensile tests at constant strain rates $\dot{\varepsilon}$ (bottom right).

processes on the microstructure are observed via transmission electron microscopy (TEM) and electron backscatter diffraction (EBSD). It is found that the softening behavior is due to the disappearance of most of the microstructural subgrain boundaries and the decrease of the dislocation density. Furthermore, the microstructural coarsening is heterogeneous for low applied strains since only a few very large subgrains have been detected. However, the coarsening becomes homogeneous with increasing applied strain. In contrast, no significant precipitate coarsening is qualitatively noticed on TEM observations, cf. [38]. This is attributed to the relatively short duration of the fatigue or creep-fatigue tests such that precipitate coarsening is only observable during creep tests, which usually take more time.

In [31, 44], it has recently been demonstrated that softening occurs also during high temperature (HT) tensile tests. Here, stress-strain curves confirm the existence of a softening stage during deformation at low strain rates ($\dot{\varepsilon} \leq 2.5 \times 10^{-4} \text{ s}^{-1}$). This stage is characterized by constantly decreasing load and CAUCHY stress. A similar behavior can be observed at the bottom right diagram of Fig. 1.3, which summarizes the results of the strain-controlled HT tensile tests at 873 K, cf. also Fig. 3.4 on p. 42. Three different strain rates $\dot{\varepsilon}$ are prescribed, and the corresponding stress-strain curves are presented with respect to the CAUCHY stress σ and the HENCKY strain H . After the instant elastic response of the material, hardening processes prevail, and the slope of the curves decreases up to the maximum stress value. This hardening stage is succeeded by the softening stage over a relatively wide

strain range, i.e. the stress decreases constantly with increasing deformation. Microstructural observations in [31] reveal that the softening mechanisms are based on the annihilation of subgrain boundaries and mobile dislocations. Because of the relatively short test duration (compared to creep tests), nucleation, growth, and coarsening of precipitates are not taken into account. Furthermore, HT tensile tests are also presented in [32, 33]. Both publications confirm a long and stable softening stage for tensile tests at high temperatures and low strain rates.

1.2 Modeling Approaches

Several models have been proposed during the last years in order to simulate the mechanical behavior of tempered martensitic steels with high chromium content at elevated temperatures. Generally speaking, one can distinguish macromechanical and micromechanical models. Macromechanical models provide a macroscopic description and are usually calibrated by means of mechanical tests, e.g. HT tensile, creep, or fatigue tests. Two different classes of macromechanical approaches are established in literature: unified and nonunified models. CHABOCHE introduced the notion of unified models [45], which take only one time-dependent inelastic strain into account, while nonunified models use separate variables for instantaneous plastic strains and time-dependent inelastic deformation. Two typical examples of nonunified models for tempered martensitic steels are the models presented in the treaties of WANG *et al.* [46] and VELAY *et al.* [47]. In [47], a nonunified elasto-viscoplastic model based on several internal variables is introduced to model the cyclic behavior of the tempered martensitic steel 55NiCrMoV7. The cyclic softening is reproduced through an isotropic component. Another approach for cyclic viscoplasticity is presented in [46] in order to model the thermo-mechanical behavior of a high chromium steel. The total rate-dependent inelastic strain is decomposed into the creep strain and the viscoplastic strain. In addition, isotropic and kinematic hardening as well as a damage variable are taken into account. Kinematic hardening is considered based on the CHABOCHE model [48] with three backstresses. Note that one of the first approaches to model nonlinear kinematic hardening goes back to the backstress concept introduced by ARMSTRONG and FREDERICK [49]. CHABOCHE showed that the superposition of several ARMSTRONG-FREDERICK-type backstresses results in a better description of the cyclic behavior [48].

Another contribution to the class of nonunified approaches is the two-layer viscoplasticity model. It is applied by FARRAGHER *et al.* [50, 51] to predict the thermo-mechanical cyclic behavior of a P91 pipe. The two-layer viscoplasticity model comprises an elasto-plastic network in parallel with an elastic-viscous network. Farragher *et al.* develop a temperature-dependent version of this model along with a combined nonlinear kinematic and isotropic hardening cyclic plasticity model for the time-independent behavior and Norton's power law to capture secondary creep. This results in 10 temperature-dependent parameters, which are determined based on macroscopic material tests.

Note that nonunified models suffer from three main drawbacks [45]. Firstly, the notion of "instantaneous" strains is not precisely defined. Secondly, the implementation of different flow rules for instantaneous plastic strains and time-dependent inelastic strains leads to numerical difficulties. Thirdly, interactions between instantaneous plasticity and time-dependent creep are not taken into account. As a remedy, unified models are often applied to model rate-dependent inelasticity in combination with nonlinear kinematic hardening of CHABOCHE type, e.g. [52–58]. KOO and KWON use a CHABOCHE viscoplasticity model with kinematic hardening and isotropic softening for a 9Cr-1Mo steel [52]. Three backstresses are employed

1 Introduction

to model the kinematic hardening, and the material parameters are identified based on uniaxial macroscopic material tests in combination with computer simulations. The model results in 12 temperature-dependent parameters for a relatively narrow temperature range of 773 K–873 K. Here, one should bear in mind that additional parameters are required to determine the temperature dependence of the individual parameters such that the actual number of required material parameters is at least twice as much. Furthermore, WANG *et al.* present a unified viscoplastic constitutive model to simulate the behavior of the forged steel X12CrMoWVNbN10-1-1 under complex thermo-mechanical service-type loadings [53]. A modified ARMSTRONG-FREDERICK ansatz for kinematic hardening is taken into account, and an isotropic damage variable is incorporated in the model to describe the fatigue and creep damage. In [54, 55, 59], the viscoplastic behavior of P91 and P92 steels under fatigue loads is simulated considering isotropic hardening and softening as well as kinematic hardening with the CHABOCHE model. Altogether, 10 temperature-dependent material parameters are required, and the model is restricted to the temperature range 673 K–873 K. The same temperature range is taken into account in [56, 58]. In [56], HT fatigue of P91 steel is simulated considering isotropic and kinematic hardening as well, such that 12 temperature-dependent parameters are required. Similarly, a unified CHABOCHE model with isotropic and kinematic hardening is used in [58] for the fatigue and creep behavior of a rotor steel, resulting in 11 temperature-dependent parameters. In [57], the fatigue and creep behavior of 9%–12% chromium steels at a constant temperature of 898 K is simulated with a unified viscoplastic CHABOCHE-type model. As before, nonlinear isotropic and kinematic hardening are considered, resulting here in 27 material parameters. As can be seen, the CHABOCHE model is widely applied despite the large number of material parameters, that are typically required. This is a consequence of the introduction of several backstresses in order to model the nonlinear kinematic hardening effects. Furthermore, if several backstresses are implemented, it is difficult to provide physical interpretations for all quantities.

In contrast to the macromechanical approaches, micromechanical models are based on parameters which can be directly and explicitly related to microstructural parameters, like dislocation densities or grain sizes [47]. One example of a micromechanical model is presented in [60]. Here, the authors present a micromechanical model with dislocation densities as internal variables for the description of the cyclic behavior. GIROUX makes use of a dislocation-mechanics approach, which incorporates dislocation densities and the subgrain width as key variables to predict the macroscopic softening behavior as well as the microstructural evolution during cycling for the P92 steel [44]. The material parameters are determined based on microscopic observations, macroscopic material tests, and data from literature. Additionally, SAUZAY and co-workers introduce a micromechanical model for the mechanism of cyclic softening in a martensitic steel with 9% chromium based on a dislocation-mechanics model for the annihilation of subgrain boundaries [61, 62]. FOURNIER *et al.* use this approach to model the behavior of martensitic steels with a chromium content of 9%–12% at 823 K [14]. A self-consistent homogenization scheme is incorporated for the transition from the microscale to the macroscale. However, this model results in more than 20 material parameters, which are determined in a complex calibration procedure. Another example of a micromechanical approach is the complex cyclic viscoplasticity model developed by BARRETT *et al.* The model accounts for several microstructural strengthening and softening mechanisms by using the dislocation density as a key variable [63, 64], and it is calibrated by means of macroscopic tests as well as results from microscopic observations with respect to a high chromium steel.

In addition, phase mixture models are established in material science, e.g. [13, 19, 65]. Originally, these models are also closely related to the microscale, i.e. the hardening

and softening behavior is simulated based on an iso-strain composite with soft and hard constituents [13, 19]. One assumes that the alloy is made of soft subgrains surrounded by hard boundaries [66], while the volume fraction of the hard constituent is closely related to the microstructure (e.g. mean subgrain size) and assumed to decrease towards a saturation value to model softening due to the coarsening of subgrains [42]. These micromechanical models are usually calibrated based on microstructural observations [13, 19, 65].

However, observations with microscopes, e.g. TEM or scanning electron microscope (SEM), often require a lot of effort, financial resources, and time. On the contrary, macroscopic material tests like HT tensile tests are less time-consuming and relatively easy to conduct. For these reasons, a micromechanical phase mixture model is transformed into a macroscopic mixture model in [42, 67]. To simplify the identification of parameters, a backstress of ARMSTRONG-FREDERICK-type and a softening variable are introduced as internal variables. In [42], the model is calibrated based on creep tests for a relatively narrow range of stresses and temperatures ($150 \text{ MPa} \leq \sigma \leq 200 \text{ MPa}$, $773 \text{ K} \leq T \leq 873 \text{ K}$). To verify the calibrated model, a creep test with stress changes and HT tensile tests are simulated. This reveals the good performance of the model, particularly concerning the description of the softening behavior, even though a minimum number of response functions and material parameters is used. The calibrated model requires 11 material parameters of which only 2 are temperature-dependent.

Altogether, the phase mixture model offers two main advantages compared to other approaches. Firstly, the number of material parameters is relatively small because only one backstress and a softening variable are introduced as internal variables. Secondly, the model is calibrated based only on simple macroscopic tests, i.e. time-consuming microscopic observations are not required for the identification of the parameters. For these reasons, this thesis makes use of a modified phase mixture model for the unified description of the mechanical behavior of tempered martensitic steels.

1.3 Outline

This thesis aims to develop a framework for modeling the mechanical behavior of tempered martensitic steels at elevated temperatures. Exemplarily, the specific alloy X20CrMoV12-1 was chosen to demonstrate the applicability of the proposed method. The framework comprises the execution of experiments, the set-up of a model, the calibration of the model, the implementation into the finite element method (FEM), and the simulation of the mechanical behavior of power plant components under practical boundary conditions (BCs).

The thesis at hand is divided into seven chapters including the current introductory chapter. Chapter 2 begins by laying the theoretical foundations for the conducted research. The governing equations of continuum mechanics (kinematics, kinetics, balance laws, and constitutive equations) are introduced with special emphasis on constitutive models for rate-dependent inelasticity. Based on these equations from continuum mechanics, the principle of virtual work is derived for the subsequent numerical solution via the FEM. Furthermore, the spatial discretization into finite elements is described, and the implementation of nonlinear constitutive models is discussed.

The third chapter deals with the experiments conducted on specimens made of the alloy X20CrMoV12-1. In a first test series, HT tensile tests are conducted, in which the temperatures and strain rates are varied systematically within the ranges $T = \{673 \text{ K}, 723 \text{ K}, \dots, 923 \text{ K}\}$ and $\dot{\epsilon} = \{5.0 \times 10^{-5} \text{ s}^{-1}, 1.0 \times 10^{-4} \text{ s}^{-1}, 1.0 \times 10^{-3} \text{ s}^{-1}\}$. In the second test series, the same HT tensile test is performed several times, while the test is terminated at different strain

1 Introduction

levels in order to examine the onset of necking. Finally, three creep tests at 873 K have been conducted.

Chapter 4 presents the one-dimensional phase mixture model, which is applicable to rate-dependent inelasticity. Two internal variables are introduced: a softening variable to describe the nonlinear softening and an ARMSTRONG-FREDERICK-type backstress for nonlinear kinematic hardening. The model is purely mechanical since the temperature is considered a state variable, influencing the material parameters only. In the remainder of this chapter, the complex calibration procedure is described based on the experimental data from the preceding chapter and literature. The calibrated model is verified with additional creep tests under constant and variable stress.

In Chapt. 5, the phase mixture model is introduced with respect to three-dimensional stress and strain states. For isothermal processes, the thermodynamic consistency of the model is demonstrated, i.e. it is shown that the model fulfills the CLAUSIUS-DUHEM inequality. In addition, the chapter focuses on the numerical implementation of the three-dimensional model into the finite element code ABAQUS via the subroutine User Material (UMAT). The implicit stress update algorithm is based on the backward EULER method in conjunction with the NEWTON-RAPHSON method. Furthermore, the numerical implementation is verified by comparison with the results obtained using MATLAB's RUNGE-KUTTA solver `ode45` for the HT tensile tests. As additional benchmarks, creep and shear tests as well as cyclic strain-controlled tests are simulated. Finally, a pressurized cylinder is simulated deploying an axisymmetric model, and a service-like uniaxial thermo-mechanical fatigue (TMF) test is analyzed.

Chapter 6 focuses on the numerical analysis of a power plant component in order to demonstrate the capability of the model. The mechanical behavior of a steam turbine rotor with an inlet groove is simulated during a cold start and a subsequent hot start. In a first step, a transient thermal analysis is conducted in order to compute the inhomogeneous temperature field. The subsequent structural analysis provides the stress and strain fields, which are discussed in detail.

The final chapter draws upon the entire thesis and briefly summarizes the main results. Furthermore, it includes a discussion of the implication of the findings to future research in this area and identifies areas for further research.

2 Theoretical Background

2.1 Continuum Mechanics

In the present section, the fundamental principles of continuum mechanics are briefly introduced. This serves as the foundation for the concepts presented in the following chapters. Since a comprehensive discussion of continuum mechanics is out of the scope of the thesis at hand, only the most important aspects, which are relevant for the derivation of the proposed models, are provided. This introduction to continuum mechanics is primarily based on [68–70], where further information and details can be found.

2.1.1 Kinematics

The overall aim of continuum mechanics is the description of the spatial and temporal movement of deformable bodies through a three-dimensional space, the EUCLIDEAN space, where EUCLIDEAN geometry can be performed, e.g. describing points and straight lines or measuring distances and angles [68–70]. A material body \mathfrak{B} is defined as a continuous set of material points, while the boundary points define its surface $\partial\mathfrak{B}$. For the spatial description of the movement of bodies, we use a Cartesian coordinate system $\{x_i e_i\}$. Furthermore, it is common to distinguish between the current and the reference configuration. The reference configuration refers to the specific initial time $t = t_0$, while the current configuration is a description with respect to the actual time $t > t_0$. Based on these two configurations, we can introduce the motion Φ [69, 70]:

$$\mathbf{x} = \Phi(\mathbf{x}_0, t) \quad \text{with } \mathbf{x}_0 = \Phi(\mathbf{x}_0, t_0). \quad (2.1)$$

The vector \mathbf{x} defines the position of a material point, and the index \square_0 describes quantities with respect to the reference configuration. In addition, one defines the displacement vector \mathbf{u} :

$$\mathbf{u} = \mathbf{x} - \mathbf{x}_0. \quad (2.2)$$

Figure 2.1 depicts the material body in both configurations. Considering the description of motions in continuum mechanics, one distinguishes the material or LAGRANGIAN description from the spatial or EULERIAN description [69, 70]. In a LAGRANGIAN framework, all variables refer to the reference configuration, whereas the EULERIAN description makes use of the current configuration. In Eq. (2.1), the LAGRANGIAN description of the motion is given. Based on the inverse Φ^{-1} , we can derive the EULERIAN description of the motion [70]:

$$\mathbf{x}_0 = \Phi^{-1}(\mathbf{x}, t). \quad (2.3)$$

The EULERIAN description is mainly applied in fluid mechanics, whereas in solid mechanics, the LAGRANGIAN description is preferred. For this reason, we focus on the latter in this work. As an alternative, the motion can be interpreted as a time-dependent change of

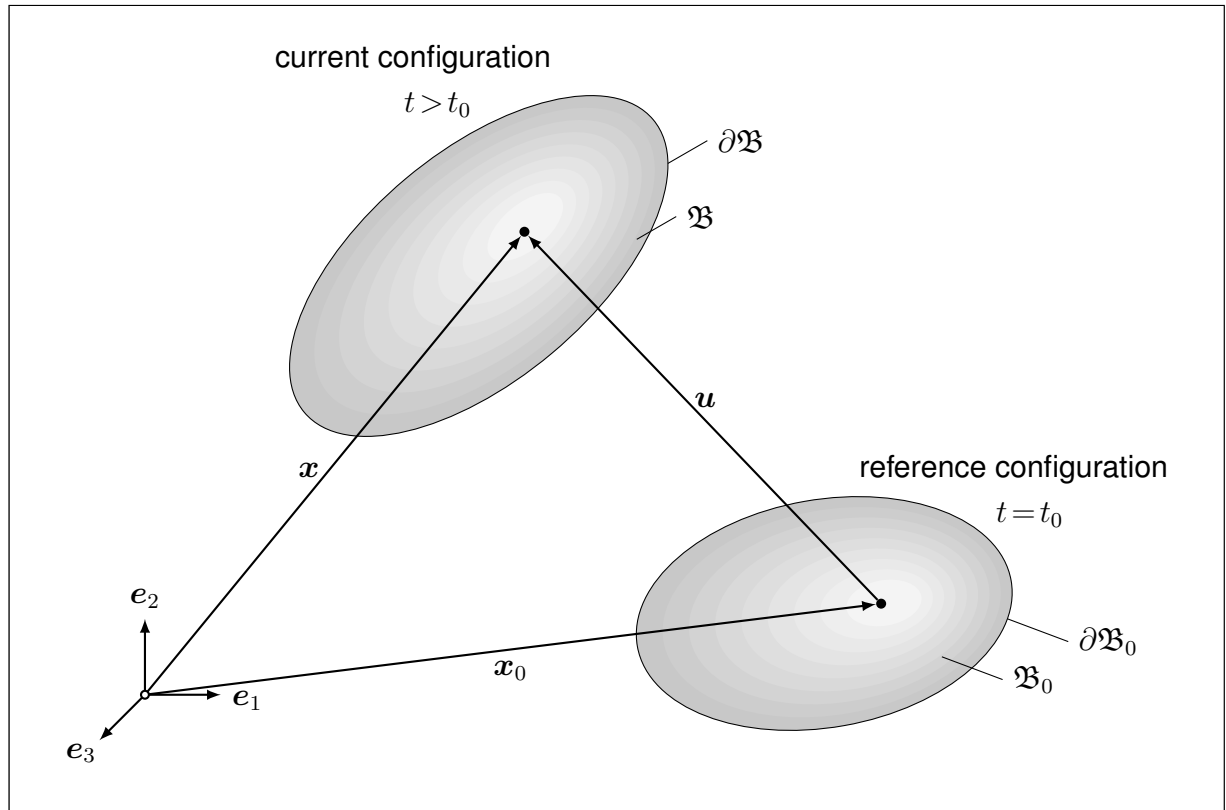


Figure 2.1: The material body in both configurations.

coordinates [69]. For this purpose, we introduce the material coordinate system $\{x_0, e_{0,i}\}$ with respect to the reference configuration and the spatial coordinate system $\{x_i, e_i\}$ with respect to the current configuration.

In order to describe the deformation of a body, the transformation of infinitesimal line elements from the reference to the current configuration is examined. The deformation gradient \mathbf{F} maps an infinitesimal line element dx_0 from the reference configuration into the current configuration [69]:

$$dx = \mathbf{F} \cdot dx_0. \quad (2.4)$$

\mathbf{F} is a two-point tensor since the right side of Eq. (2.4) refers to the reference configuration, while its left side belongs to the current configuration. The tensor \mathbf{F} is invertible and has a positive determinant $\det(\mathbf{F}) > 0$ [69, 70]. If one introduces the material nabla operator ∇_0 and takes Eq. (2.2) into account, \mathbf{F} can also be defined as follows [69, 70]:

$$\mathbf{F} = (\nabla_0 x)^T = (\nabla_0 u)^T + \mathbf{I} \quad \text{with } \nabla_0 = e_{0,i} \frac{\partial}{\partial x_{0,i}}. \quad (2.5)$$

The variable \mathbf{I} represents the unit tensor of second rank. The polar decomposition of the deformation gradient is given as:

$$\mathbf{F} = \mathbf{R} \cdot \mathbf{U} \quad (2.6)$$

with the material right stretch tensor \mathbf{U} , which is symmetric and positive definite, and the proper orthogonal rotation tensor \mathbf{R} . In order to describe deformations, the tensors \mathbf{F} and \mathbf{U} could be used. However, both tensors are not invariant with respect to rigid body

motions [68–70]. On top of that, \mathbf{F} is not symmetric, which complicates the mathematical operations. For these reasons, the right CAUCHY-GREEN tensor \mathbf{C} is introduced:

$$\mathbf{C} = \mathbf{U}^2 = \mathbf{F}^T \cdot \mathbf{F} = (\nabla \mathbf{u})^T \cdot \nabla \mathbf{u} + \nabla \mathbf{u} + (\nabla \mathbf{u})^T + \mathbf{I}. \quad (2.7)$$

The material tensor \mathbf{C} is invariant with respect to rigid body motions such that this tensor serves as basis for the definition of different strain tensors. Frequently, the GREEN strain tensor \mathbf{E}^G is used:

$$\mathbf{E}^G = \frac{1}{2} (\mathbf{C} - \mathbf{I}) = \frac{1}{2} [(\nabla \mathbf{u})^T \cdot \nabla \mathbf{u} + \nabla \mathbf{u} + (\nabla \mathbf{u})^T]. \quad (2.8)$$

The term $(\nabla \mathbf{u})^T \cdot \nabla \mathbf{u}$ in Eq. (2.8) is nonlinear such that the GREEN strain tensor is nonlinear with respect to the displacement gradient (geometrical nonlinearity). If we restrict the derivation to small deformations, the GREEN strain tensor reduces to the linear strain tensor $\boldsymbol{\varepsilon}$, which is also referred to as engineering strain tensor [69, 70]:

$$\boldsymbol{\varepsilon} = \frac{1}{2} [\nabla \mathbf{u} + (\nabla \mathbf{u})^T]. \quad (2.9)$$

As an alternative, the material logarithmic strain tensor \mathbf{H} (also called “HENCKY strain tensor”) can be used:

$$\mathbf{H} = \ln \mathbf{U} = \frac{1}{2} \ln \mathbf{C}. \quad (2.10)$$

Since one-dimensional material tests are deployed to calibrate the phase mixture model, introduced in Chapt. 4 based on one-dimensional considerations and extended to three-dimensional applications in Chapt. 5, the following discussions are limited to the one-dimensional setting. Figure 2.2 shows a rod in the reference and in the current configuration. Its left end is clamped, whereas a longitudinal tensile force N is applied to the right end. The coordinate x_0 and the length L_0 indicate the reference configuration, while the coordinate x and the length L describe the current configuration. In analogy to Eq. (2.1), we introduce the motion Φ of the rod:

$$x = \Phi(x_0, t) \quad \text{with } x_0 = \Phi(x_0, t_0). \quad (2.11)$$

The one-dimensional displacement u is defined as follows (compare to Eq. (2.2)):

$$u = x - x_0. \quad (2.12)$$

Furthermore, we can compute the deformation gradient F in one dimension (compare to Eq. (2.5)):

$$F = \frac{\partial x}{\partial x_0} = \frac{\partial u}{\partial x_0} + 1. \quad (2.13)$$

In addition, one introduces the one-dimensional CAUCHY-GREEN strain C (compare to Eq. (2.7)):

$$C = F^2 = \left(\frac{\partial u}{\partial x_0} + 1 \right)^2. \quad (2.14)$$

2 Theoretical Background

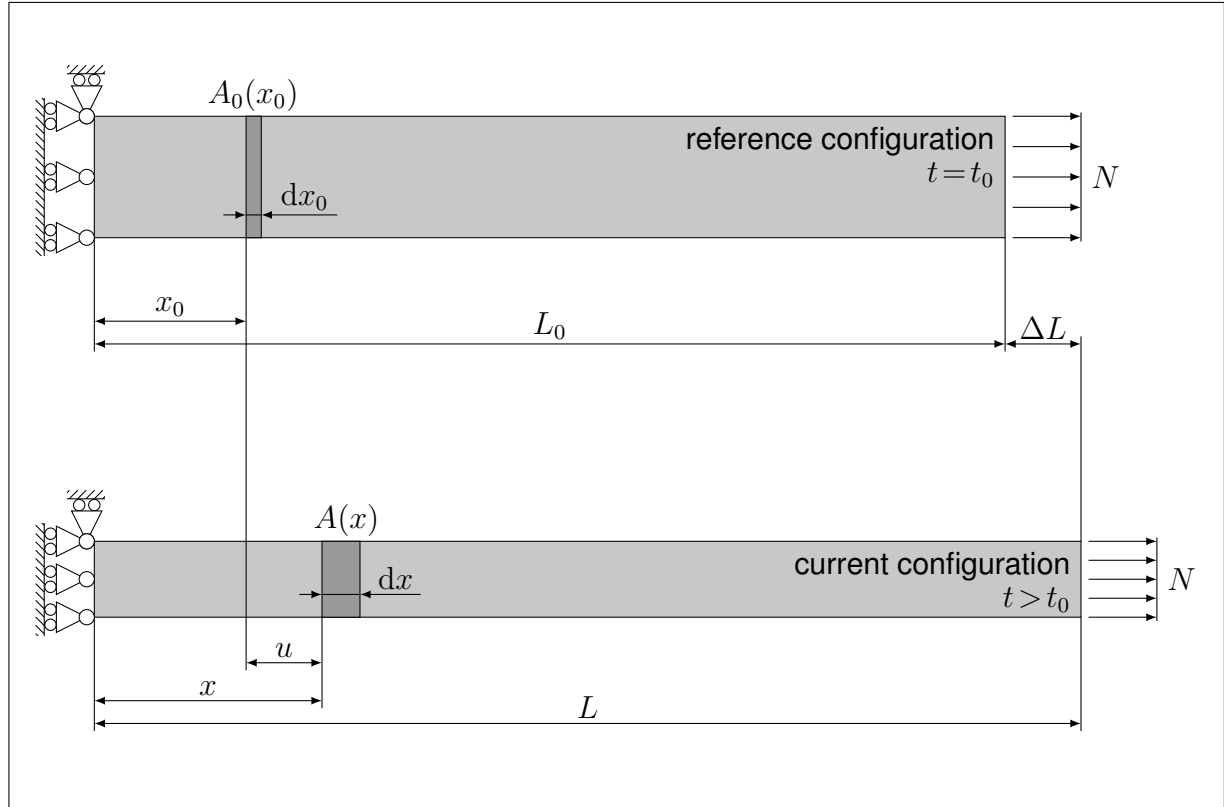


Figure 2.2: A rod in the current and the reference configuration, based on [71].

The GREEN strain E^G , the engineering strain ε , and the HENCKY strain H are calculated as follows (compare to Eqs. (2.8)–(2.10)):

$$E^G = \frac{1}{2} \left(\frac{\partial u}{\partial x_0} \right)^2 + \frac{\partial u}{\partial x_0}, \quad (2.15)$$

$$\varepsilon = \frac{\partial u}{\partial x_0}, \quad (2.16)$$

$$H = \ln \left(\frac{\partial u}{\partial x_0} + 1 \right). \quad (2.17)$$

If the rod is homogeneous, i.e. the material properties and the geometry of the rod do not depend on x_0 , the equations above can be simplified:

$$E^G = \frac{1}{2} \left(\frac{\Delta L}{L_0} \right)^2 + \frac{\Delta L}{L_0}, \quad (2.18)$$

$$\varepsilon = \frac{\Delta L}{L_0}, \quad (2.19)$$

$$H = \ln \left(\frac{\Delta L}{L_0} + 1 \right), \quad (2.20)$$

where $\Delta L = L - L_0$ stands for the increase in length, cf. Fig. 2.2. In the remainder of the thesis at hand, the operator $\Delta \square$ denotes incremental quantities. The definitions of the one-dimensional strain measures given above are used during the processing of the experimental data, cf. Chapt. 3. Furthermore, the one-dimensional phase mixture model is discussed in Chapt. 4.

2.1.2 Kinetics

In mechanical derivations, the cut principle is widely used [69]. The material body is separated from its environment, while the ambient influences are represented by forces and moments. We assume that both quantities can be divided into surface/contact parts (acting on the boundary) and body parts (acting on the volume). In the following, we focus on the surface forces. If we consider the surface force vector $\Delta \mathbf{f}$ with respect to an area element ΔA , we obtain the stress vector \mathbf{t} [68]:

$$\mathbf{t} = \lim_{\Delta A \rightarrow 0} \frac{\Delta \mathbf{f}}{\Delta A}. \quad (2.21)$$

In the following, we assume that the load $\Delta \mathbf{f}$ fulfills certain smoothness requirements. Moreover, CAUCHY has found that the stress vector \mathbf{t} depends linearly on the normal vector \mathbf{n} of the area element ΔA [68–70]:

$$\mathbf{t} = \mathbf{n} \cdot \boldsymbol{\sigma}, \quad (2.22)$$

where $\boldsymbol{\sigma}$ denotes the CAUCHY stress tensor. For nonpolar media, the CAUCHY stress tensor is symmetric due to BOLTZMANN's axiom [69]. In order to determine $\boldsymbol{\sigma}$ from experimental data, the current force and area need to be known. However, it requires often much less effort to measure the area in the reference configuration. For this reason, we introduce the stress vector \mathbf{t}_I with respect to the area element in the reference configuration ΔA_0 [68]:

$$\mathbf{t}_I = \lim_{\Delta A_0 \rightarrow 0} \frac{\Delta \mathbf{f}}{\Delta A_0}. \quad (2.23)$$

The corresponding stress tensor is the first PIOLA-KIRCHHOFF stress tensor \mathbf{P} , which relates the stress vector \mathbf{t}_I and the normal vector \mathbf{n}_0 of the area element in the reference configuration:

$$\mathbf{t}_I = \mathbf{n}_0 \cdot \mathbf{P}. \quad (2.24)$$

This stress tensor is often referred to as “nominal” or “engineering stress” tensor. Like the deformation gradient, it is a two-point tensor, and it can be computed based on the CAUCHY stress tensor and the deformation gradient [68]:

$$\mathbf{P} = \det(\mathbf{F}) \mathbf{F}^{-1} \cdot \boldsymbol{\sigma}. \quad (2.25)$$

Since the deformation gradient is not symmetric, the first PIOLA-KIRCHHOFF stress tensor inherits this property. As a remedy, one introduces a pseudo surface force vector $\Delta \mathbf{f}_0$ with respect to the reference configuration:

$$\Delta \mathbf{f}_0 = \mathbf{F}^{-1} \cdot \Delta \mathbf{f}. \quad (2.26)$$

If we relate this pseudo surface force vector to the area element in the reference configuration, we obtain another stress vector \mathbf{t}_{II} :

$$\mathbf{t}_{II} = \lim_{\Delta A_0 \rightarrow 0} \frac{\Delta \mathbf{f}_0}{\Delta A_0}. \quad (2.27)$$

2 Theoretical Background

Here, the second PIOLA-KIRCHHOFF stress tensor S relates the stress vector t_{II} and the normal vector n_0 [68, 69]:

$$t_{II} = n_0 \cdot S. \quad (2.28)$$

Based on the CAUCHY stress tensor and the deformation gradient, one can calculate the symmetric tensor S as follows:

$$S = \det(\mathbf{F}) \mathbf{F}^{-1} \cdot \boldsymbol{\sigma} \cdot \mathbf{F}^{-T}. \quad (2.29)$$

Similar to the previous section about three-dimensional and one-dimensional deformation states, we introduce one-dimensional stress measures in the following. These measures are used during the processing of the experimental data, cf. Chapt. 3, and for the one-dimensional phase mixture model in Chapt. 4. For the sake of brevity, the following sections concerning the mechanical balance laws and the constitutive modeling are only provided in a three-dimensional formulation. Further information concerning continuum mechanics in one dimension can be found in [71, 72].

The CAUCHY stress σ relates the infinitesimal tensile force dN and the cross-section element dA in the current configuration (compare to Eq. (2.22)):

$$dN = \sigma dA. \quad (2.30)$$

For a homogeneous rod,

$$N = \sigma A \quad (2.31)$$

holds. The PIOLA-KIRCHHOFF stress P relates the current tensile force dN to the initial cross-section dA_0 (compare to Eq. (2.24)):

$$dN = P dA_0. \quad (2.32)$$

Considering a homogeneous rod, Eq. (2.32) can be simplified even further. Here, the PIOLA-KIRCHHOFF stress relates the force N and the cross-section A_0 in the reference configuration:

$$N = P A_0. \quad (2.33)$$

In the following, Eq. (2.25) is evaluated for a homogeneous rod. If we assume incompressible material behavior, the determinant of the deformation gradient equals 1 since this determinant is equal to the current volume dV related to the reference volume dV_0 , i.e. $\det(\mathbf{F}) = dV/dV_0 = 1$. If we substitute this result into Eq. (2.25) and use the definition provided in Eq. (2.13), the PIOLA-KIRCHHOFF stress in a homogeneous rod can be written as:

$$P = \frac{L_0}{L} \sigma. \quad (2.34)$$

Vice versa, it holds for the CAUCHY stress:

$$\sigma = \frac{L}{L_0} P = \left(1 + \frac{\Delta L}{L_0}\right) P. \quad (2.35)$$

2.1.3 Mechanical Balance Laws

After the kinematic and kinetic quantities have been introduced in the previous sections, they are used to formulate the balance laws with respect to mass, linear momentum, and angular momentum. These considerations are restricted to the local form of the balance laws, i.e. balance laws with respect to an infinitesimal material volume element.

2.1.3.1 Mass

The mass dm of an infinitesimal volume element dV in the current configuration is determined based on the mass density ρ :

$$dm = \rho dV. \quad (2.36)$$

We assume mass conservation, i.e. mass is not removed or added to a body, such that the following relation holds [68, 71]:

$$dm = \rho dV = \rho_0 dV_0. \quad (2.37)$$

2.1.3.2 Linear Momentum

The vector of linear momentum \mathbf{p} is defined for an infinitesimal part of a body as [68, 71]:

$$d\mathbf{p} = \mathbf{v} dm = \mathbf{v} \rho dV, \quad (2.38)$$

where \mathbf{v} denotes the velocity vector. EULER's first law of motion [69] states that the rate of change of the linear momentum equals the resultant force:

$$d\dot{\mathbf{p}} = \mathbf{t} dA + \rho \mathbf{b} dV. \quad (2.39)$$

The dot represents the first derivative with respect to time, i.e. $\dot{\square} = \partial \square / \partial t$, and the vector \mathbf{b} comprises all body forces, e.g. gravity or magnetic forces. As before, we assume that all forces can be described either as surface or body forces. Introducing the CAUCHY stress tensor, cf. Eq. (2.22), into Eq. (2.39) and applying the GAUSS-OSTROGRADSKY theorem to transform the surface integral into a volume integral results in CAUCHY's first law of motion [68, 73]:

$$\nabla \cdot \boldsymbol{\sigma} + \rho \mathbf{b} = \rho \dot{\mathbf{v}}. \quad (2.40)$$

2.1.3.3 Angular Momentum

The vector of angular momentum \mathbf{q} is defined for an infinitesimal part of a body in analogy to the vector of linear momentum \mathbf{p} as [68, 71]:

$$d\mathbf{q} = \mathbf{x} \times \mathbf{v} dm = \mathbf{x} \times \mathbf{v} \rho dV. \quad (2.41)$$

In the following, we exploit EULER's second law of motion [69], which states that the rate of change of the angular momentum equals the resultant moment:

$$d\dot{\mathbf{q}} = \mathbf{x} \times \mathbf{t} dA + \rho \mathbf{x} \times \mathbf{b} dV. \quad (2.42)$$

2 Theoretical Background

After some transformations and consideration of Eq. (2.40), Eq. (2.42) proves the symmetry of the CAUCHY stress tensor for nonpolar media [68, 69, 71]:

$$\boldsymbol{\sigma} = \boldsymbol{\sigma}^T. \quad (2.43)$$

2.1.4 Constitutive Equations

The equations presented in the preceding sections do not account for the specific material properties of a body. Thus, additional equations are required. The so-called constitutive equations bridge this gap and describe the relation between stresses and strains (or the corresponding time derivatives) within the framework of a mechanical model. The following considerations are restricted to isotropic materials, i.e. the material properties do not depend on specific directions.

2.1.4.1 Elasticity

Elasticity models simulate rate-independent material behavior without hysteresis. In this case, it is assumed that the current state of stress depends on the current state of deformation only [69, 74]:

$$\boldsymbol{\sigma} = \mathcal{F}(\boldsymbol{\epsilon}^{\text{el}}). \quad (2.44)$$

The superscript \square^{el} denotes elastic variables. Equation (2.44) illustrates that the stress response is independent from the deformation path and time. For linear isotropic elasticity, HOOKE'S law is applied [73]:

$$\boldsymbol{\sigma} = K \text{tr}(\boldsymbol{\epsilon}^{\text{el}}) \mathbf{I} + 2G \boldsymbol{\epsilon}^{\text{el}}, \quad (2.45)$$

where only two parameters, i.e. the bulk modulus K and the shear modulus G , determine the elastic behavior completely. For isotropic materials, these parameters are related to the YOUNG'S modulus E and the POISSON'S ratio ν by:

$$G = \frac{E}{2(1+\nu)}, \quad K = \frac{E}{3(1-2\nu)}. \quad (2.46)$$

Let us introduce the decomposition of the stress tensor into its spheric and deviatoric part:

$$\boldsymbol{\sigma} = \sigma_m \mathbf{I} + \boldsymbol{\sigma}' \quad \text{with} \quad \sigma_m = \frac{1}{3} \text{tr}(\boldsymbol{\sigma}), \quad \text{tr}(\boldsymbol{\sigma}') = 0. \quad (2.47)$$

The variable σ_m represents the mean stress, and the prime \square' denotes traceless tensors, i.e. the deviatoric parts. Introducing this decomposition into Eq. (2.45) yields:

$$\boldsymbol{\epsilon}^{\text{el}} = \frac{\sigma_m}{3K} \mathbf{I} + \frac{\boldsymbol{\sigma}'}{2G}. \quad (2.48)$$

If one considers Eq. (2.47) and applies the trace operator to both sides of Eq. (2.45), one obtains a constitutive relation only between the spheric parts of the stress and strain tensors [71]:

$$\sigma_m = K \varepsilon_V \quad (2.49)$$

with the volumetric strain $\varepsilon_V = \text{tr}(\boldsymbol{\varepsilon}^{\text{el}})$. Taking only the deviatoric parts of Eq. (2.48) into account yields:

$$\boldsymbol{\sigma}' = 2G\boldsymbol{\varepsilon}^{\text{el}'}. \quad (2.50)$$

2.1.4.2 Inelasticity

In this section, rate-dependent material behavior including hysteresis effects is described. This is one building block required to model the mechanical behavior of tempered martensitic steels, which is at the heart of this thesis. In contrast to elastic deformations, inelastic deformations are irreversible because energy dissipates during deformation. Furthermore, the load history influences the current deformation [68], and the stress and deformation states are time-dependent due to viscous effects.

As already pointed out in Sect. 1.2, we can distinguish between unified and nonunified models for the description of rate-dependent inelasticity. Nonunified models use separate variables for instantaneous plastic strains and the time-dependent inelastic deformation. The definition of plastic strains requires the demarcation of an elastic domain by means of a yield surface [75]. Stress states outside the yield surface lead to the evolution of the plastic deformation [74]. In the thesis at hand, the term “plastic strains” is only used for instantaneous inelastic strains, which are caused by a deformation state exceeding the yield surface. In contrast, the term “inelastic strains” denotes all irreversible deformation processes, without the necessity to define a yield surface. Due to the properties of tempered martensitic steels and the aforementioned drawbacks of the nonunified models, cf. Chapt. 1, a uniform constitutive model is applied in this thesis, taking only one time-dependent inelastic strain tensor $\boldsymbol{\varepsilon}^{\text{in}}$ into account. For this reason, the definition of a yield surface is not required. Additional examples of unified models without a yield surface are presented in [76–78]. The absence of the yield surface can also be motivated from a physical point of view because inelastic deformations of tempered martensitic steels are based on thermally activated processes. That is to say, they already occur at stresses far below a potential yield stress [71].

For the description of rate-dependent inelasticity, we use the concept of internal variables, cf. [79], for example. Hereby, it is assumed that the stress tensor $\boldsymbol{\sigma}$ depends on the strain tensor $\boldsymbol{\varepsilon}$ as well as on tensorial internal variables $\mathbf{Q}_i \forall i \in \{1, 2, \dots, m\}$ and scalar internal variables $q_j \forall j \in \{1, 2, \dots, n\}$ [74]:

$$\boldsymbol{\sigma} = \mathcal{F}(\boldsymbol{\varepsilon}, \mathbf{Q}_i, q_j). \quad (2.51)$$

The internal variables represent a material state that depends on the process history. To determine the current values of the internal variables, a system of ordinary differential equations (ODEs) needs to be solved [74]:

$$\dot{\mathbf{Q}}_i(t) = \mathcal{G}_i(\boldsymbol{\varepsilon}(t), T(t), \mathbf{Q}_i(t), q_j(t)) \quad \forall i \in \{1, 2, \dots, m\}, \quad (2.52)$$

$$\dot{q}_j(t) = \mathcal{H}_j(\boldsymbol{\varepsilon}(t), T(t), \mathbf{Q}_i(t), q_j(t)) \quad \forall j \in \{1, 2, \dots, n\}. \quad (2.53)$$

These ODEs are also referred to as “evolution equations”. Additionally, the influence of the temperature has been taken into account in Eqs. (2.52) and (2.53). In order to formulate a constitutive model with respect to elasticity in conjunction with inelasticity, the additive decomposition of the strain tensor $\boldsymbol{\varepsilon}$ into its elastic and inelastic parts is introduced:

$$\boldsymbol{\varepsilon} = \boldsymbol{\varepsilon}^{\text{el}} + \boldsymbol{\varepsilon}^{\text{in}}. \quad (2.54)$$

2 Theoretical Background

Furthermore, one must formulate an evolution equation with respect to the inelastic strain tensor:

$$\dot{\boldsymbol{\epsilon}}^{\text{in}}(t) = \mathcal{E}(\boldsymbol{\epsilon}(t), T(t), \mathbf{Q}_i(t), q_j(t)). \quad (2.55)$$

In the remainder of this section, we provide the set of equations, being required to formulate a constitutive model based on elastic material behavior in conjunction with rate-dependent inelasticity:

- the additive decomposition of the strain tensor $\boldsymbol{\epsilon}$ into its elastic and inelastic parts, cf. Eq. (2.54):

$$\boldsymbol{\epsilon} = \boldsymbol{\epsilon}^{\text{el}} + \boldsymbol{\epsilon}^{\text{in}},$$

- HOOKE's law for linear isotropic elasticity, cf. Eq. (2.45):

$$\boldsymbol{\sigma} = K \text{tr}(\boldsymbol{\epsilon}^{\text{el}}) \mathbf{I} + 2G \boldsymbol{\epsilon}^{\text{el}},$$

- an evolution equation with respect to the inelastic strain tensor, cf. Eq. (2.55):

$$\dot{\boldsymbol{\epsilon}}^{\text{in}}(t) = \mathcal{E}(\boldsymbol{\epsilon}(t), T(t), \mathbf{Q}_i(t), q_j(t)),$$

- evolution equations for the internal variables, cf. Eqs. (2.52) and (2.53):

$$\begin{aligned} \dot{\mathbf{Q}}_i(t) &= \mathcal{G}_i(\boldsymbol{\epsilon}(t), T(t), \mathbf{Q}_i(t), q_j(t)) & \forall i \in \{1, 2, \dots, m\}, \\ \dot{q}_j(t) &= \mathcal{H}_j(\boldsymbol{\epsilon}(t), T(t), \mathbf{Q}_i(t), q_j(t)) & \forall j \in \{1, 2, \dots, n\}. \end{aligned}$$

In a next step, we focus on the evolution equation for the inelastic strain, cf. Eq. (2.55). One can reformulate this equation by introducing the potential Ψ [80]:

$$\dot{\boldsymbol{\epsilon}}^{\text{in}} = \frac{\partial \Psi(\boldsymbol{\sigma})}{\partial \boldsymbol{\sigma}}. \quad (2.56)$$

One should keep in mind that the stress is still a function of the strain and the internal variables, cf. Eq. (2.51), although these arguments have not been written explicitly for the sake of brevity. In the case of isotropic inelasticity, the potential is an isotropic function such that it depends only on three invariants $J_1(\boldsymbol{\sigma})$, $J_2(\boldsymbol{\sigma})$, and $J_3(\boldsymbol{\sigma})$ of the stress tensor [69, 71]:

$$\Psi(\boldsymbol{\sigma}) = \Psi(J_1(\boldsymbol{\sigma}), J_2(\boldsymbol{\sigma}), J_3(\boldsymbol{\sigma})). \quad (2.57)$$

The thesis at hand makes use of the following three invariants of the stress tensor:

$$J_1(\boldsymbol{\sigma}) = \text{tr}(\boldsymbol{\sigma}), \quad (2.58)$$

$$J_2(\boldsymbol{\sigma}) = \frac{1}{2} \{ [\text{tr}(\boldsymbol{\sigma})]^2 - \text{tr}(\boldsymbol{\sigma}^2) \}, \quad (2.59)$$

$$J_3(\boldsymbol{\sigma}) = \det(\boldsymbol{\sigma}). \quad (2.60)$$

In the framework of the classical theory of inelasticity, it is assumed that the inelastic deformation does not produce a significant change in volume, i.e. $\text{tr}(\dot{\boldsymbol{\epsilon}}^{\text{in}}) = 0 \Rightarrow (\dot{\boldsymbol{\epsilon}}^{\text{in}})' = \dot{\boldsymbol{\epsilon}}^{\text{in}}$. In this case, one can show that the potential Ψ does not depend on the first invariant of the stress tensor anymore [71]. Furthermore, it is sufficient to rewrite Eq. (2.56) in terms of the

deviatoric part of the stress tensor only:

$$\dot{\boldsymbol{\epsilon}}^{\text{in}} = \frac{\partial \Psi(J_2(\boldsymbol{\sigma}'), J_3(\boldsymbol{\sigma}'))}{\partial \boldsymbol{\sigma}'}. \quad (2.61)$$

Equation (2.61) accounts for the dependence of the potential Ψ on the third invariant $J_3(\boldsymbol{\sigma}')$ of the stress deviator. This allows for the description of several nonclassical or second-order effects of the material behavior [71]. For the sake of simplicity, the dependence on the third invariant is often neglected, which results in a VON MISES-type potential. Here, the potential is only a function of the second invariant $J_2(\boldsymbol{\sigma}')$ of the stress deviator:

$$\dot{\boldsymbol{\epsilon}}^{\text{in}} = \frac{\partial \Psi(J_2(\boldsymbol{\sigma}'))}{\partial \boldsymbol{\sigma}'}. \quad (2.62)$$

Evaluating the derivatives in Eq. (2.62) yields a modified evolution equation for the inelastic strains [71, 81]:

$$\dot{\boldsymbol{\epsilon}}^{\text{in}} = \frac{3}{2} \dot{\epsilon}_{\text{vM}}^{\text{in}} \frac{\boldsymbol{\sigma}'}{\sigma_{\text{vM}}} \quad (2.63)$$

with the VON MISES stress σ_{vM} and the inelastic VON MISES strain rate $\dot{\epsilon}_{\text{vM}}^{\text{in}}$:

$$\sigma_{\text{vM}} = \sqrt{\frac{3}{2} \boldsymbol{\sigma}' : \boldsymbol{\sigma}'}, \quad (2.64)$$

$$\dot{\epsilon}_{\text{vM}}^{\text{in}} = \sqrt{\frac{2}{3} \dot{\boldsymbol{\epsilon}}^{\text{in}} : \dot{\boldsymbol{\epsilon}}^{\text{in}}}. \quad (2.65)$$

One should keep in mind that the stress deviator $\boldsymbol{\sigma}'$ and the VON MISES stress σ_{vM} are functions of the strain and the internal variables, cf. Eq. (2.51). In addition, a function is required to account for the dependence of the inelastic VON MISES strain rate on the stress and temperature. Frequently, a separation ansatz is used for the inelastic VON MISES strain rate, and therefore it is approximated as a product of two functions with respect to the stress and temperature states, respectively [71]:

$$\dot{\epsilon}_{\text{vM}}^{\text{in}} = f_{\sigma}(\sigma_{\text{vM}}) f_T(T). \quad (2.66)$$

During the last years, several stress and temperature response functions have been introduced in literature. The interested reader is referred to the comprehensive review articles by CHABOCHE [82], PENNY and MARRIOTT [83], ODQVIST and HULT [81], and ILSCHNER [84]. Selected response functions are discussed in Sect. 4.2.3.

The internal variables mentioned before are often used to model isotropic and/or kinematic hardening. In the case of isotropic hardening, scalar variables are used as internal variables. As one example, let us introduce the hardening variable γ , i.e. $q_1 \equiv \gamma$, $n \equiv 1$. In contrast, kinematic hardening is modeled by means of tensorial variables. To this end, the stress deviator $\boldsymbol{\sigma}'$ is additively decomposed into an active part $\boldsymbol{\sigma}_{\text{act}}$ and the backstress tensor $\boldsymbol{\beta}$ [71]:

$$\boldsymbol{\sigma}' = \boldsymbol{\sigma}_{\text{act}} + \boldsymbol{\beta} \Rightarrow \boldsymbol{\sigma}_{\text{act}} = \boldsymbol{\sigma}' - \boldsymbol{\beta}. \quad (2.67)$$

The backstress tensor is a tensorial internal variable: $Q_1 \equiv \boldsymbol{\beta}$, $m \equiv 1$. Moreover, we assume that the potential Ψ is only depending on the active stress, and therefore the inelastic strain

2 Theoretical Background

rate can be computed by means of the active stresses only, cf. Eq. (2.62) [71]:

$$\dot{\Psi} = \dot{\Psi} \left(J_2 \left(\frac{\boldsymbol{\sigma}_{\text{act}}}{\gamma} \right) \right) = \dot{\Psi} \left(J_2 \left(\frac{\boldsymbol{\sigma}' - \boldsymbol{\beta}}{\gamma} \right) \right). \quad (2.68)$$

In the next step, evolution equations are formulated with respect to the hardening variable γ and the backstress tensor $\boldsymbol{\beta}$, cf. Eqs. (2.52) and (2.53). A very simple ansatz for isotropic hardening is the linear strain hardening [69]:

$$\dot{\gamma} = B_1 \dot{\epsilon}_{\text{vM}}^{\text{in}}. \quad (2.69)$$

In the following, we introduce the material parameters $B_l > 0 \forall l \in \{1, 2, \dots, 7\}$, which have to be determined by fitting the equations to experimental data. The simple linear ansatz in Eq. (2.69) results in an infinite increase of the hardening, which is not realistic. For this reason, more sophisticated approaches should be employed, for example [69, 71]:

$$\dot{\gamma} = B_2 (\gamma_* - \gamma) \dot{\epsilon}_{\text{vM}}^{\text{in}}. \quad (2.70)$$

Considering steady state applications, the hardening variable converges towards a saturation value, which is indicated by γ_* . A very simple evolution equation for the backstress is provided by PRAGER's linear kinematic hardening model [82]:

$$\dot{\boldsymbol{\beta}} = B_3 \dot{\boldsymbol{\epsilon}}^{\text{in}}. \quad (2.71)$$

Similar to Eq. (2.69), the collinearity of the backstress with the inelastic strain is rarely observed in reality. As a remedy, the well-known model of ARMSTRONG and FREDERICK for nonlinear kinematic hardening can be employed [49]:

$$\dot{\boldsymbol{\beta}} = B_4 \dot{\boldsymbol{\epsilon}}^{\text{in}} - B_5 \dot{\epsilon}_{\text{vM}}^{\text{in}} \boldsymbol{\beta}. \quad (2.72)$$

The second term in Eq. (2.72) is a dynamic recovery term and improves the simulation results significantly [82]. CHABOCHE suggested to superpose several backstresses for further improvement of the simulation results [45]:

$$\boldsymbol{\beta} = \sum_{i=1}^r \boldsymbol{\beta}_i \quad (2.73)$$

with a separate evolution equation for each backstress:

$$\dot{\boldsymbol{\beta}}_i = B_{6_i} \dot{\boldsymbol{\epsilon}}^{\text{in}} - B_{7_i} \dot{\epsilon}_{\text{vM}}^{\text{in}} \boldsymbol{\beta}_i. \quad (2.74)$$

2.1.5 Initial Boundary Value Problem

This section summarizes the governing equations, which form the basis for the numerical solution via the FEM. Within the mechanical initial boundary value problem, the dependence of the material parameters on the temperature is taken into account. The mechanical initial boundary value problem is described by the following set of equations, comprising the balance laws and the constitutive equations:

- the conservation of mass, cf. Eq. (2.37):

$$dm = \rho dV = \rho_0 dV_0,$$

- the balance of linear momentum, cf. Eq. (2.40):

$$\nabla \cdot \boldsymbol{\sigma} + \rho \mathbf{b} = \rho \dot{\mathbf{v}},$$

- the balance of angular momentum, cf. Eq. (2.43):

$$\boldsymbol{\sigma} = \boldsymbol{\sigma}^T,$$

- the kinematic equations, cf. Eq. (2.9):

$$\boldsymbol{\epsilon} = \frac{1}{2} \left[\nabla \mathbf{u} + (\nabla \mathbf{u})^T \right],$$

- the additive split of strains, cf. Eq. (2.54):

$$\boldsymbol{\epsilon} = \boldsymbol{\epsilon}^{\text{el}} + \boldsymbol{\epsilon}^{\text{in}},$$

- HOOKE's law for linear isotropic elasticity, cf. Eq. (2.45):

$$\boldsymbol{\sigma} = K \text{tr}(\boldsymbol{\epsilon}^{\text{el}}) \mathbf{I} + 2G \boldsymbol{\epsilon}^{\text{el}},$$

- an evolution equation with respect to the inelastic strain tensor, cf. Eq. (2.55):

$$\dot{\boldsymbol{\epsilon}}^{\text{in}}(t) = \mathcal{E}(\boldsymbol{\epsilon}(t), T(t), \mathbf{Q}_i(t), q_j(t)),$$

- evolution equations for the internal variables, cf. Eqs. (2.52) and (2.53):

$$\begin{aligned} \dot{\mathbf{Q}}_i(t) &= \mathcal{G}_i(\boldsymbol{\epsilon}(t), T(t), \mathbf{Q}_i(t), q_j(t)) & \forall i \in \{1, 2, \dots, m\}, \\ \dot{q}_j(t) &= \mathcal{H}_j(\boldsymbol{\epsilon}(t), T(t), \mathbf{Q}_i(t), q_j(t)) & \forall j \in \{1, 2, \dots, n\}. \end{aligned}$$

In order to formulate the entire initial boundary value problem, additional boundary and initial conditions (ICs) must be defined. Primarily, two types of BCs are used in continuum mechanics: displacement BCs (DIRICHLET type) and traction BCs (NEUMANN type). Displacement BCs are defined in the following way [68, 69]:

$$\mathbf{u}(\mathbf{x}_0, t) = \check{\mathbf{u}}(\mathbf{x}_0, t) \quad \forall \mathbf{x}_0 \in \partial V_u \quad \wedge \quad t \in [t_{\text{init}}, t_{\text{end}}]. \quad (2.75)$$

The accent $\check{\square}$ marks prescribed variables, while the subscripts \square_{init} and \square_{end} indicate variables with respect to the first and the last time step, respectively. Equation (2.75) is valid for the material points belonging to the boundary ∂V_u . With respect to the boundary material points, which do not belong to the boundary ∂V_u , traction BCs are prescribed [68, 69]:

$$\mathbf{t}(\mathbf{x}_0, t) = \check{\mathbf{t}}(\mathbf{x}_0, t) = \mathbf{n} \cdot \boldsymbol{\sigma}(\mathbf{x}_0, t) \quad \forall \mathbf{x}_0 \in \partial V_t \quad \wedge \quad t \in [t_{\text{init}}, t_{\text{end}}]. \quad (2.76)$$

For the entire set of points at the boundary, either displacement or traction boundary conditions need to be defined ($\partial V = \partial V_t \cup \partial V_u$). Initial conditions are usually formulated with

2 Theoretical Background

respect to the displacements or velocities [68, 69]:

$$\mathbf{u}(\mathbf{x}_0, t_{\text{init}}) = \check{\mathbf{u}}(\mathbf{x}_0) \quad \forall \mathbf{x}_0 \in V, \quad (2.77)$$

$$\mathbf{v}(\mathbf{x}_0, t_{\text{init}}) = \check{\mathbf{v}}(\mathbf{x}_0) \quad \forall \mathbf{x}_0 \in V. \quad (2.78)$$

The entire set of equations provided in the present section describes the general initial boundary value problem for rate-dependent inelastic deformations of a body considering additional internal variables.

2.1.6 Rule of Mixtures

In Sect. 4.1, the phase mixture model is presented. Thus, this section briefly provides the theoretical background to define the interactions of the constituents in a mixture. Continuum mechanical models of mixtures have been extensively treated in the last decades, cf. [85–91]. In this work, we consider a mixture, which is comprised of two different nonreacting solid constituents. Usually, a continuum mechanical framework is set up for every constituent individually, i.e. the kinematic equations, balance laws, and constitutive equations are formulated with respect to each constituent. In a following step, the constituents are assembled to a mixture by defining their interactions.

Primarily, two principal approaches are used to define the relation between two constituents: the iso-strain concept and the iso-stress approach. VOIGT was the first to present an iso-strain model in [92]. Computing the effective properties of a binary solid mixture, he assumed a homogeneous strain field:

$$\boldsymbol{\varepsilon}_a = \boldsymbol{\varepsilon}_b = \boldsymbol{\varepsilon}. \quad (2.79)$$

The indices a and b refer to the two different constituents. In contrast, REUSS suggested a homogeneous stress field, i.e. the iso-stress concept [93]:

$$\boldsymbol{\sigma}_a = \boldsymbol{\sigma}_b = \boldsymbol{\sigma}. \quad (2.80)$$

Equations (2.79) and (2.80) are only simple approximations of reality and both have their drawbacks. The iso-strain concept is statically inadmissible since the tractions at the phase boundaries are not in equilibrium anymore, whereas the iso-stress model is kinematically inadmissible because the phases are not perfectly bounded [94]. However, HILL has proven that both models provide an upper and lower bound for the observed material behavior [95], i.e. the iso-strain concept overestimates the material stiffness, while the iso-stress approach underestimates this property.

In the current work, a phase mixture model is applied to describe the mechanical behavior of a binary mixture. Hardening and softening mechanisms are taken into account based on the stress redistribution between the two constituents [13, 42]. For this reason, the iso-strain concept is applied such that the mixture strain is defined by Eq. (2.79). In the next step, the overall stress $\boldsymbol{\sigma}$ needs to be defined. In many publications, the stress is computed based on the volume fractions η of the constituents, e.g. [96–101]:

$$\boldsymbol{\sigma} = \eta_a \boldsymbol{\sigma}_a + \eta_b \boldsymbol{\sigma}_b \quad \text{with} \quad \eta_a + \eta_b = 1. \quad (2.81)$$

The one-dimensional form of Eq. (2.81) can be derived by applying the iso-strain approach to a unidirectional lamina under one-dimensional loading [102]. However, one should bear in mind that the extension to three-dimensional stress states in Eq. (2.81) is only an

approximation to reality. Nevertheless, this simple approach is often successfully applied in mixture models [96–101] such that the current thesis also makes use of it.

2.2 Finite Element Method

This section presents the governing equations for the numerical implementation of a nonlinear material model in the FEM. In a first step, the principle of virtual work (PVW) is derived. Thereafter, the implementation of nonlinear material models into the FEM is presented. Finally, the spatial discretization into finite elements is described, and the entire system of equations is provided as a system of differential-algebraic equations (DAEs).

2.2.1 Principle of Virtual Work

The principle of virtual work serves as the basis for the FEM. The following derivation of the PVW is given in the style of standard monographs from the field of numerical mechanics, e.g. [103, 104]. Point of departure for the derivation of the PVW is the multiplication of the local balance of linear momentum, cf. Eq. (2.40), and the traction BCs (2.76) with an admissible test function, in our case the virtual displacements $\delta \mathbf{u}$. The arbitrarily chosen test function has to fulfill the kinematic equations, cf. Eq. (2.9), and the essential BCs in Eq. (2.75):

$$\delta \boldsymbol{\varepsilon} = \frac{1}{2} \left[\nabla \delta \mathbf{u} + (\nabla \delta \mathbf{u})^T \right], \quad (2.82)$$

$$\delta \mathbf{u}(\mathbf{x}_0, t) = \mathbf{0} \quad \forall \mathbf{x}_0 \in \partial V_u \quad \wedge \quad t \in [t_{\text{init}}, t_{\text{end}}]. \quad (2.83)$$

The resulting equations are integrated over the volume V and the boundary ∂V of the domain. These two terms are then summed:

$$\int_V \delta \mathbf{u} \cdot (\rho \ddot{\mathbf{u}} - \rho \mathbf{b} - \nabla \cdot \boldsymbol{\sigma}) dV + \int_{\partial V} \delta \mathbf{u} \cdot (\mathbf{n} \cdot \boldsymbol{\sigma} - \check{\mathbf{t}}) d\partial V = 0. \quad (2.84)$$

Here, the two dots denote the second derivative with respect to time, i.e. $\ddot{\square} = \partial^2 \square / \partial t^2$. In the following, we employ the product rule of differentiation for the nabla operator and exploit the symmetry of the CAUCHY stress tensor:

$$\delta \mathbf{u} \cdot (\nabla \cdot \boldsymbol{\sigma}) = \nabla \cdot (\delta \mathbf{u} \cdot \boldsymbol{\sigma}) - \delta \boldsymbol{\varepsilon} : \boldsymbol{\sigma}. \quad (2.85)$$

The expression given in Eq. (2.85) is inserted into Eq. (2.84). Furthermore, the integral over the boundary is restricted to the boundary ∂V_t since Eq. (2.83) holds for all points on the boundary ∂V_u :

$$\int_V \delta \mathbf{u} \cdot \ddot{\mathbf{u}} \rho dV + \int_V \delta \boldsymbol{\varepsilon} : \boldsymbol{\sigma} dV = \int_V \delta \mathbf{u} \cdot \mathbf{b} \rho dV + \int_{\partial V_t} \delta \mathbf{u} \cdot \check{\mathbf{t}} d\partial V_t. \quad (2.86)$$

Equation (2.86) represents the PVW. In order to derive a more compact formulation, we introduce the virtual kinetic energy δW^{dyn} , the internal virtual work δW^{int} , and the external

2 Theoretical Background

virtual work δW^{ext} :

$$\delta W^{\text{dyn}} = \int_V \delta \mathbf{u} \cdot \ddot{\mathbf{u}} \rho dV, \quad (2.87)$$

$$\delta W^{\text{int}} = \int_V \delta \boldsymbol{\varepsilon} : \boldsymbol{\sigma} dV, \quad (2.88)$$

$$\delta W^{\text{ext}} = \int_V \delta \mathbf{u} \cdot \mathbf{b} \rho dV + \int_{\partial V_t} \delta \mathbf{u} \cdot \check{\mathbf{t}} d\partial V_t. \quad (2.89)$$

The abbreviations defined above are inserted into Eq. (2.86):

$$\delta W^{\text{dyn}} + \delta W^{\text{int}} = \delta W^{\text{ext}}. \quad (2.90)$$

As can be seen, the PVW states that the sum of the virtual kinetic energy and the virtual work done by the internal forces is equal to the virtual work of the external forces. Up to now, all parts of the initial boundary value problem (see Sect. 2.1.5) except the constitutive equations have been considered. For this reason, the combination of the PVW with the constitutive model is demonstrated in the following. This derivation is based on [105, 106]. In the following, only static problems are considered, i.e. $\delta W^{\text{dyn}} = 0$.

First of all, we reformulate Eq. (2.86) for static problems by introduction of the functional $\Pi(\mathbf{u}, \delta \mathbf{u})$:

$$\Pi(\mathbf{u}, \delta \mathbf{u}) = 0 \quad (2.91)$$

with

$$\Pi(\mathbf{u}, \delta \mathbf{u}) = \int_V \delta \boldsymbol{\varepsilon} : \boldsymbol{\sigma} dV - \int_V \delta \mathbf{u} \cdot \mathbf{b} \rho dV - \int_{\partial V_t} \delta \mathbf{u} \cdot \check{\mathbf{t}} d\partial V_t. \quad (2.92)$$

Since nonlinear constitutive equations are taken into account, the entire initial boundary value problem is nonlinear such that the BCs can only be realized incrementally, i.e. the initial boundary value problem is resolved by the computation of a sequence of equilibrium configurations. We assume that the equilibrium configuration \mathbf{u}_n is already known such that

$$\Pi(\mathbf{u}_n, \delta \mathbf{u}) = \int_V \delta \boldsymbol{\varepsilon} : \boldsymbol{\sigma}_n dV - \int_V \delta \mathbf{u} \cdot \mathbf{b}_n \rho dV - \int_{\partial V_t} \delta \mathbf{u} \cdot \check{\mathbf{t}}_n d\partial V_t = 0 \quad (2.93)$$

holds. To determine the new equilibrium configuration \mathbf{u}_{n+1} , the following problem must be solved with respect to the field \mathbf{u}_{n+1} :

$$\Pi(\mathbf{u}_{n+1}, \delta \mathbf{u}) = 0. \quad (2.94)$$

Within the FEM, the nonlinear equation given in Eq. (2.94) is solved by means of the NEWTON-RAPHSON method [103]. During the iteration, intermediate displacement fields occur. These fields do not fulfill the equilibrium conditions and are denoted by right superscripts, such as \square^i . If the iteration process is finished, the last intermediate displacement field defines the new equilibrium configuration, i.e. $\mathbf{u}_{n+1} = \mathbf{u}^i$. For the iteration, the functional Π is expanded

in a TAYLOR series, which is truncated after the first two terms:

$$\Pi(\mathbf{u}^{i+1}, \delta \mathbf{u}) = \Pi(\mathbf{u}^i, \delta \mathbf{u}) + \mathbf{d}_u \Pi(\mathbf{u}^i, \delta \mathbf{u}) \cdot \Delta \mathbf{u} = 0 \quad (2.95)$$

where $\Delta \mathbf{u} = \mathbf{u}^{i+1} - \mathbf{u}^i$ denotes the displacement increment. The GÂTEAUX derivative of $\Pi(\mathbf{u}^i, \delta \mathbf{u})$ with respect to \mathbf{u} in the direction of $\Delta \mathbf{u}$ is defined as [106]:

$$\mathbf{d}_u \Pi(\mathbf{u}^i, \delta \mathbf{u}) \cdot \Delta \mathbf{u} = \left. \frac{d}{d\lambda} \Pi(\mathbf{u}^i + \lambda \Delta \mathbf{u}, \delta \mathbf{u}) \right|_{\lambda=0}. \quad (2.96)$$

To find the new intermediate displacement \mathbf{u}^{i+1} , the following equation is solved via the NEWTON-RAPHSON method, see also Eq. (2.95):

$$\mathbf{d}_u \Pi(\mathbf{u}^i, \delta \mathbf{u}) \cdot \Delta \mathbf{u} = -\Pi(\mathbf{u}^i, \delta \mathbf{u}). \quad (2.97)$$

By evaluating the GÂTEAUX derivative in Eq. (2.95), we obtain the linearized PVW [105, 106]:

$$\int_V \delta \boldsymbol{\varepsilon} : \tilde{\mathbf{C}}^i : \Delta \boldsymbol{\varepsilon} dV = \int_V \delta \mathbf{u} \cdot \mathbf{b}_{n+1} \rho dV + \int_{\partial V_t} \delta \mathbf{u} \cdot \check{\mathbf{t}}_{n+1} d\partial V_t - \int_V \delta \boldsymbol{\varepsilon} : \boldsymbol{\sigma}^i dV \quad (2.98)$$

with the strain increment $\Delta \boldsymbol{\varepsilon}$ and the tangent operator $\tilde{\mathbf{C}}^i$:

$$\Delta \boldsymbol{\varepsilon} = \frac{1}{2} \left[\nabla \Delta \mathbf{u} + (\nabla \Delta \mathbf{u})^T \right], \quad (2.99)$$

$$\tilde{\mathbf{C}}^i = \left. \frac{d\boldsymbol{\sigma}}{d\boldsymbol{\varepsilon}} \right|_{\mathbf{u}=\mathbf{u}^i}. \quad (2.100)$$

In order to solve Eq. (2.98) for $\Delta \boldsymbol{\varepsilon}$ or $\Delta \mathbf{u}$ respectively, the current state of stress $\boldsymbol{\sigma}^i$ and the tangent operator $\tilde{\mathbf{C}}^i$ need to be computed. This procedure depends on the chosen material model. Details on the stress update algorithm and the computation of the tangent operator with respect to the phase mixture model are provided in Sect. 5.3.3.

2.2.2 Spatial Discretization

The preceding section focuses on the discretization of the PVW with respect to time. In contrast, this section briefly presents the spatial discretization within the FEM, which is finally introduced into the linearized PVW in Eq. (2.98). The content of this section is based on standard textbooks on FEM, e.g. [103, 107–109], where also further information can be found.

Within the FEM, the material body is partitioned into elements, which must not intersect:

$$\Omega = \bigcup_{i=1}^{NE} \Omega_{e_i} \quad \forall \Omega_{e_i} \cap \Omega_{e_j} = \emptyset \text{ if } i \neq j, \quad (2.101)$$

where Ω denotes the computational domain, Ω_e is the elemental domain, and NE stands for the total number of elements. In the following, the subscript \square_e is used to denote quantities on the element level. The PVW must be fulfilled in every domain, cf. Eq. (2.90):

$$\delta W_e^{\text{dyn}} + \delta W_e^{\text{int}} = \delta W_e^{\text{ext}}, \quad (2.102)$$

2 Theoretical Background

and consequently the overall virtual works are computed by summing all elemental contributions:

$$\delta W^\square = \sum_{i=1}^{NE} \delta W_{e_i}^\square \quad \forall \square \in \{\text{dyn}, \text{int}, \text{ext}\}. \quad (2.103)$$

In this work, we mainly consider hexahedral finite elements with linear or quadratic shape functions. The reference elements including their nodal distributions and shape functions are depicted in Fig. 2.3. For the sake of generality, the derivation of finite elements is based on the concept of master elements which are defined in a local reference space. Therefore, the natural coordinates ξ_i are introduced:

$$\boldsymbol{\xi} = [\xi_1 \quad \xi_2 \quad \xi_3]^\text{T} \quad \text{with } -1 \leq \xi_i \leq 1. \quad (2.104)$$

Applying the isoparametric element concept, the geometry and the displacement field of a finite element are interpolated using the same set of shape functions. Thus, the approximation of both quantities is given as:

$$\mathbf{x}_e(\boldsymbol{\xi}) = [x_1(\boldsymbol{\xi}) \quad x_2(\boldsymbol{\xi}) \quad x_3(\boldsymbol{\xi})]^\text{T} = \mathbf{N}(\boldsymbol{\xi}) \mathbf{x}_n, \quad (2.105)$$

$$\mathbf{u}_e(\boldsymbol{\xi}) = [u_1(\boldsymbol{\xi}) \quad u_2(\boldsymbol{\xi}) \quad u_3(\boldsymbol{\xi})]^\text{T} = \mathbf{N}(\boldsymbol{\xi}) \mathbf{u}_n, \quad (2.106)$$

where \mathbf{x}_e denotes the element position vector, and \mathbf{u}_e is the displacement vector. The vectors \mathbf{x}_n and \mathbf{u}_n are comprised of all nodal coordinates and displacements for one element:

$$\mathbf{x}_n = [\mathbf{x}_n^1 \quad \mathbf{x}_n^2 \quad \dots \quad \mathbf{x}_n^{NV}]^\text{T}, \quad \mathbf{x}_n^i = [x_1^i \quad x_2^i \quad x_3^i]^\text{T} \quad \forall i \in \{1, 2, \dots, NV\}, \quad (2.107)$$

$$\mathbf{u}_n = [\mathbf{u}_n^1 \quad \mathbf{u}_n^2 \quad \dots \quad \mathbf{u}_n^{NV}]^\text{T}, \quad \mathbf{u}_n^i = [u_1^i \quad u_2^i \quad u_3^i]^\text{T} \quad \forall i \in \{1, 2, \dots, NV\}, \quad (2.108)$$

where \square^i is the node index, and NV denotes the number of nodes per element. The matrix $\mathbf{N}(\boldsymbol{\xi})$ includes all shape functions:

$$\mathbf{N}(\boldsymbol{\xi}) = [\mathbf{N}^1(\boldsymbol{\xi}) \quad \mathbf{N}^2(\boldsymbol{\xi}) \quad \dots \quad \mathbf{N}^{NV}(\boldsymbol{\xi})], \quad (2.109)$$

where \mathbf{N}^i stands for the matrix of the shape functions with respect to the i th node:

$$\mathbf{N}^i(\boldsymbol{\xi}) = N^i(\boldsymbol{\xi}) \begin{bmatrix} 1 & 0 & 0 \\ 0 & 1 & 0 \\ 0 & 0 & 1 \end{bmatrix} \quad \forall i \in \{1, 2, \dots, NV\}. \quad (2.110)$$

To transform the differential line elements $d\mathbf{x}$ in physical coordinates to the line elements $d\boldsymbol{\xi}$ in natural coordinates, the JACOBIAN matrix $\mathbf{J}(\boldsymbol{\xi})$ and its inverse $\mathbf{J}^{-1}(\boldsymbol{\xi})$ are required. The mappings between the reference domain and the global one and vice versa are given as:

$$\frac{\partial}{\partial \boldsymbol{\xi}} = \mathbf{J}(\boldsymbol{\xi}) \frac{\partial}{\partial \mathbf{x}} \quad \Leftrightarrow \quad \frac{\partial}{\partial \mathbf{x}} = \mathbf{J}^{-1}(\boldsymbol{\xi}) \frac{\partial}{\partial \boldsymbol{\xi}} \quad (2.111)$$

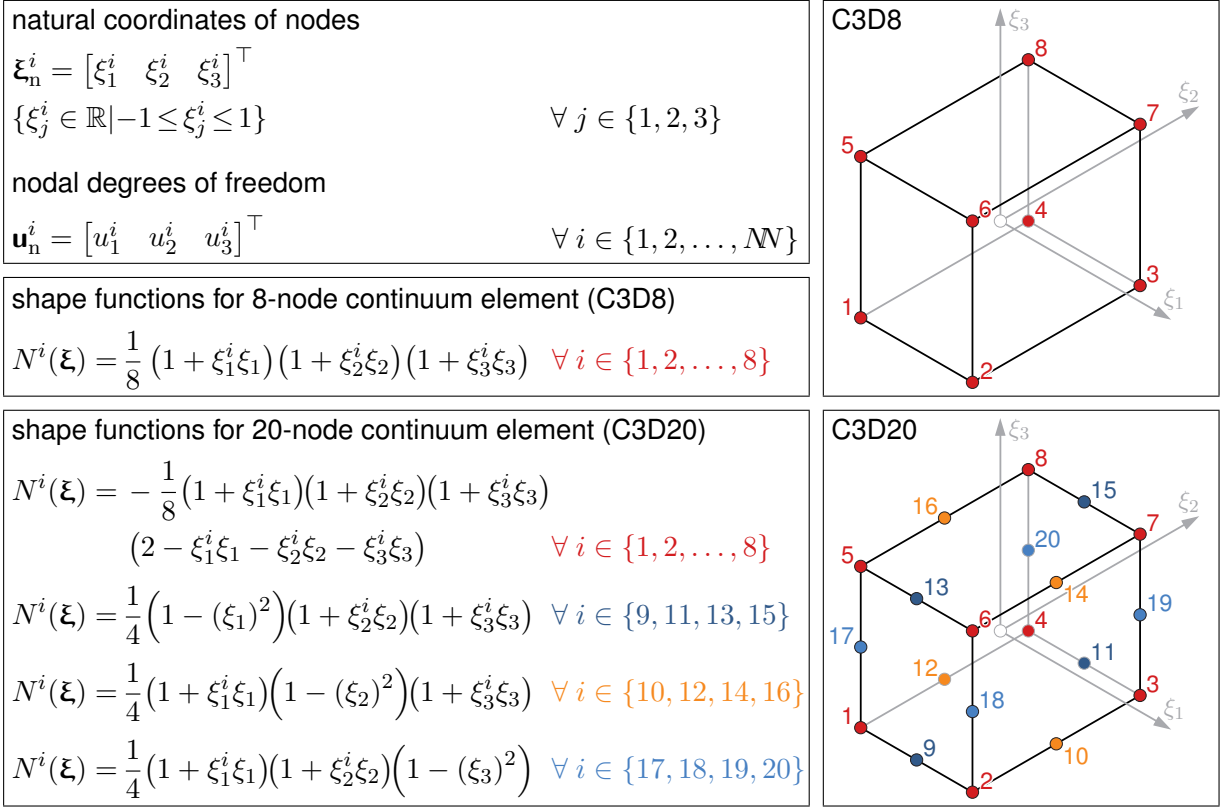


Figure 2.3: Geometry, nodes, and shape functions for 8- and 20-node hexahedral elements.

with

$$\mathbf{J}(\boldsymbol{\xi}) = \begin{bmatrix} \frac{\partial x_1}{\partial \xi_1} & \frac{\partial x_2}{\partial \xi_1} & \frac{\partial x_3}{\partial \xi_1} \\ \frac{\partial x_1}{\partial \xi_2} & \frac{\partial x_2}{\partial \xi_2} & \frac{\partial x_3}{\partial \xi_2} \\ \frac{\partial x_1}{\partial \xi_3} & \frac{\partial x_2}{\partial \xi_3} & \frac{\partial x_3}{\partial \xi_3} \end{bmatrix}, \quad \mathbf{J}^{-1}(\boldsymbol{\xi}) = \begin{bmatrix} \frac{\partial \xi_1}{\partial x_1} & \frac{\partial \xi_2}{\partial x_1} & \frac{\partial \xi_3}{\partial x_1} \\ \frac{\partial \xi_1}{\partial x_2} & \frac{\partial \xi_2}{\partial x_2} & \frac{\partial \xi_3}{\partial x_2} \\ \frac{\partial \xi_1}{\partial x_3} & \frac{\partial \xi_2}{\partial x_3} & \frac{\partial \xi_3}{\partial x_3} \end{bmatrix}, \quad (2.112)$$

$$\frac{\partial}{\partial \boldsymbol{\xi}} = \begin{bmatrix} \frac{\partial}{\partial \xi_1} & \frac{\partial}{\partial \xi_2} & \frac{\partial}{\partial \xi_3} \end{bmatrix}^\top, \quad \frac{\partial}{\partial \mathbf{x}} = \begin{bmatrix} \frac{\partial}{\partial x_1} & \frac{\partial}{\partial x_2} & \frac{\partial}{\partial x_3} \end{bmatrix}^\top. \quad (2.113)$$

Furthermore, the determinant of the JACOBIAN matrix $\det(\mathbf{J}(\boldsymbol{\xi}))$ relates an infinitesimal volume element dV in physical coordinates to the natural coordinates:

$$dV = dx_1 dx_2 dx_3 = \det(\mathbf{J}(\boldsymbol{\xi})) d\xi_1 d\xi_2 d\xi_3. \quad (2.114)$$

In the next step, the spatial discretization is also introduced into the kinematic equations, cf. Eq. (2.9):

$$\boldsymbol{\varepsilon}(\boldsymbol{\xi}) \approx \mathbf{B}(\boldsymbol{\xi}) \mathbf{u}_n. \quad (2.115)$$

The strain vector $\boldsymbol{\varepsilon}(\boldsymbol{\xi})$ in VOIGT notation is defined as:

$$\boldsymbol{\varepsilon}(\boldsymbol{\xi}) = [\varepsilon_{11}(\boldsymbol{\xi}) \ \varepsilon_{22}(\boldsymbol{\xi}) \ \varepsilon_{33}(\boldsymbol{\xi}) \ 2\varepsilon_{12}(\boldsymbol{\xi}) \ 2\varepsilon_{13}(\boldsymbol{\xi}) \ 2\varepsilon_{23}(\boldsymbol{\xi})]^\top. \quad (2.116)$$

2 Theoretical Background

The strain-displacement matrix $\mathbf{B}(\boldsymbol{\xi})$ is compiled analogously to the matrix of shape functions:

$$\mathbf{B}(\boldsymbol{\xi}) = [\mathbf{B}^1(\boldsymbol{\xi}) \quad \mathbf{B}^2(\boldsymbol{\xi}) \quad \dots \quad \mathbf{B}^{NV}(\boldsymbol{\xi})]. \quad (2.117)$$

Enforcing the isoparametric element concept, the nodal strain-displacement matrix for node i can be written as:

$$\mathbf{B}^i(\boldsymbol{\xi}) = \begin{bmatrix} \frac{\partial \xi_j}{\partial x_1} \frac{\partial N^i}{\partial \xi_j}(\boldsymbol{\xi}) & 0 & 0 \\ 0 & \frac{\partial \xi_j}{\partial x_2} \frac{\partial N^i}{\partial \xi_j}(\boldsymbol{\xi}) & 0 \\ 0 & 0 & \frac{\partial \xi_j}{\partial x_3} \frac{\partial N^i}{\partial \xi_j}(\boldsymbol{\xi}) \\ \frac{\partial \xi_j}{\partial x_2} \frac{\partial N^i}{\partial \xi_j}(\boldsymbol{\xi}) & \frac{\partial \xi_j}{\partial x_1} \frac{\partial N^i}{\partial \xi_j}(\boldsymbol{\xi}) & 0 \\ \frac{\partial \xi_j}{\partial x_3} \frac{\partial N^i}{\partial \xi_j}(\boldsymbol{\xi}) & 0 & \frac{\partial \xi_j}{\partial x_1} \frac{\partial N^i}{\partial \xi_j}(\boldsymbol{\xi}) \\ 0 & \frac{\partial \xi_j}{\partial x_3} \frac{\partial N^i}{\partial \xi_j}(\boldsymbol{\xi}) & \frac{\partial \xi_j}{\partial x_2} \frac{\partial N^i}{\partial \xi_j}(\boldsymbol{\xi}) \end{bmatrix}, \quad (2.118)$$

where N^i denotes the shape functions which are also used to approximate the geometry of an element.

2.2.3 System of Differential-Algebraic Equations

This section introduces the spatial discretization into the linearized PVW in Eq. (2.98) and discusses the interpretation of the resulting system of equations as a system of DAEs.

For the sake of simplicity, the following considerations are restricted to the elemental domain, while quantities on the element level are denoted with the subscript \square_e , and indices with respect to the time or iteration steps are omitted. Equation (2.98) is rewritten in matrix notation:

$$\int_{V_e} \delta \mathbf{e}^T \tilde{\mathbf{C}} \Delta \mathbf{e} dV_e = \int_{V_e} \delta \mathbf{u}_e^T \mathbf{b} \rho dV_e + \int_{\partial V_{te}} \delta \mathbf{u}_e^T \mathbf{t} d\partial V_{te} - \int_{V_e} \delta \boldsymbol{\varepsilon}^T \boldsymbol{\sigma} dV_e. \quad (2.119)$$

The tangent operator matrix $\tilde{\mathbf{C}}$, the stress vector $\boldsymbol{\sigma}$, the vector of body forces \mathbf{b} , and the vector of surface forces \mathbf{t} are derived based on the components of the corresponding tensors of first, second, and fourth rank $\tilde{\mathbf{C}} = \tilde{C}_{ijmn} \mathbf{e}_i \otimes \mathbf{e}_j \otimes \mathbf{e}_m \otimes \mathbf{e}_n$, $\boldsymbol{\sigma} = \sigma_{ij} \mathbf{e}_i \otimes \mathbf{e}_j$, $\mathbf{b} = b_i \mathbf{e}_i$, and $\mathbf{t} = \dot{t}_i \mathbf{e}_i$:

$$\tilde{\mathbf{C}} = \begin{bmatrix} \tilde{C}_{1111} & \tilde{C}_{1122} & \tilde{C}_{1133} & \tilde{C}_{1123} & \tilde{C}_{1131} & \tilde{C}_{1112} \\ \tilde{C}_{1122} & \tilde{C}_{2222} & \tilde{C}_{2233} & \tilde{C}_{2223} & \tilde{C}_{2231} & \tilde{C}_{2212} \\ \tilde{C}_{1133} & \tilde{C}_{2233} & \tilde{C}_{3333} & \tilde{C}_{3323} & \tilde{C}_{3331} & \tilde{C}_{3312} \\ \tilde{C}_{1123} & \tilde{C}_{2223} & \tilde{C}_{3323} & \tilde{C}_{2323} & \tilde{C}_{2331} & \tilde{C}_{2312} \\ \tilde{C}_{1131} & \tilde{C}_{2231} & \tilde{C}_{3331} & \tilde{C}_{2331} & \tilde{C}_{3131} & \tilde{C}_{3112} \\ \tilde{C}_{1112} & \tilde{C}_{2212} & \tilde{C}_{3312} & \tilde{C}_{2312} & \tilde{C}_{3112} & \tilde{C}_{1212} \end{bmatrix}, \quad (2.120)$$

$$\boldsymbol{\sigma} = [\sigma_{11} \quad \sigma_{22} \quad \sigma_{33} \quad \sigma_{12} \quad \sigma_{13} \quad \sigma_{23}]^T, \quad (2.121)$$

$$\mathbf{b} = [b_1 \quad b_2 \quad b_3]^T, \quad (2.122)$$

$$\check{\mathbf{t}} = [\check{t}_1 \quad \check{t}_2 \quad \check{t}_3]^T. \quad (2.123)$$

The representations given above are obtained based on the VOIGT notation [68], taking the symmetries of the tensors into account. Finally, the spatial discretization is introduced into the PVW by inserting Eqs. (2.106) and (2.115) into Eq. (2.119):

$$\int_{V_e} \delta \mathbf{u}_n^T \mathbf{B}^T \tilde{\mathbf{C}} \mathbf{B} \Delta \mathbf{u}_n dV_e = \int_{V_e} \delta \mathbf{u}_n^T \mathbf{N}^T \mathbf{b} \rho dV_e + \int_{\partial V_{te}} \delta \mathbf{u}_n^T \mathbf{N}^T \check{\mathbf{t}} d\partial V_{te} - \int_{V_e} \delta \mathbf{u}_n^T \mathbf{B}^T \boldsymbol{\sigma} dV_e. \quad (2.124)$$

For the sake of brevity, the element stiffness matrix \mathbf{K}_e , the vector of external forces $\mathbf{f}_e^{\text{ext}}$, and the vector of internal forces $\mathbf{f}_e^{\text{int}}$ are introduced:

$$\mathbf{K}_e = \int_{V_e} \mathbf{B}^T \tilde{\mathbf{C}} \mathbf{B} dV_e, \quad (2.125)$$

$$\mathbf{f}_e^{\text{ext}} = \int_{V_e} \mathbf{N}^T \mathbf{b} \rho dV_e + \int_{\partial V_{te}} \mathbf{N}^T \check{\mathbf{t}} d\partial V_{te}, \quad (2.126)$$

$$\mathbf{f}_e^{\text{int}} = \int_{V_e} \mathbf{B}^T \boldsymbol{\sigma} dV_e, \quad (2.127)$$

such that Eq. (2.124) can be recast into a compact form:

$$\delta \mathbf{u}_n^T (\mathbf{K}_e \Delta \mathbf{u}_n + \mathbf{f}_e^{\text{int}} - \mathbf{f}_e^{\text{ext}}) = 0. \quad (2.128)$$

Due to the fundamental lemma of calculus of variations, Eq. (2.128) can be rewritten:

$$\mathbf{K}_e \Delta \mathbf{u}_n = \mathbf{f}_e^{\text{ext}} - \mathbf{f}_e^{\text{int}}. \quad (2.129)$$

In order to compute the integrals in Eqs. (2.125)–(2.127), Eq. (2.114) is taken into account, and GAUSS quadrature is applied [103, 107–109]. Thus, a volume integral can be transformed into a triple sum over all integration points:

$$\begin{aligned} \int_{V_e} \square dV_e &= \int_{-1}^{+1} \int_{-1}^{+1} \int_{-1}^{+1} \square \det(\mathbf{J}(\boldsymbol{\xi})) d\xi_1 d\xi_2 d\xi_3 \\ &\approx \sum_{p=1}^{NP} \sum_{q=1}^{NQ} \sum_{r=1}^{NR} w_p w_q w_r \square \det(\mathbf{J}(\xi_{1p}, \xi_{2q}, \xi_{3r})), \end{aligned} \quad (2.130)$$

where NP , NQ , NR denote the numbers of integration points with respect to the ξ_1 , ξ_2 , ξ_3 directions. The variables p , q , and r are the corresponding indices, ξ_{1p} , ξ_{2q} , and ξ_{3r} denote the coordinates of the integration point (p, q, r) , and w_p , w_q , and w_r represent the corresponding weights. The coordinates and weights of each integration point can be found in the literature for the two elements under consideration, i.e. C3D8 and C3D20 [103, 107–109].

Equation (2.129) represents a system of nonlinear algebraic equations with respect to the displacement increments $\Delta \mathbf{u}_n$. However, this equation refers to one element only. In order to formulate equations with respect to the entire structure, we introduce the assembly

2 Theoretical Background

operator \mathbf{A} , which is used to formally represent the assembly process for all elemental quantities to the global system. Thus, one obtains the global stiffness matrix \mathbf{K} , the global vectors of internal and external forces \mathbf{f}^{int} and \mathbf{f}^{ext} as well as the global vector of the displacement increments $\Delta\mathbf{u}$:

$$\mathbf{K} = \mathbf{A} \mathbf{K}_{e_i}, \quad (2.131)$$

$$\mathbf{f}^{\text{int}} = \mathbf{A} \mathbf{f}_{e_i}^{\text{int}}, \quad (2.132)$$

$$\mathbf{f}^{\text{ext}} = \mathbf{A} \mathbf{f}_{e_i}^{\text{ext}}, \quad (2.133)$$

$$\Delta\mathbf{u} = \mathbf{A} \Delta\mathbf{u}_{n_i}. \quad (2.134)$$

Further details concerning the assembly process can be found in the literature [103, 107–109]. With the quantities introduced above, the global system of equations can be formulated based on Eq. (2.129):

$$\mathbf{K}\Delta\mathbf{u} = \mathbf{f}^{\text{ext}} - \mathbf{f}^{\text{int}}. \quad (2.135)$$

Equation (2.135) describes a set of nonlinear algebraic equations, which has been obtained by introducing a spatial discretization into the PVW. It is solved with respect to the incremental nodal displacements $\Delta\mathbf{u}$ by applying the NEWTON-RAPHSON method, cf. Eq. (2.97). According to [110], this iteration takes place on a “global” level. However, the current stress vector σ and the tangent operator $\tilde{\mathbf{C}}$ are required to compute the stiffness matrix \mathbf{K} and the vector of internal forces $\mathbf{f}_e^{\text{int}}$. Due to the use of a nonlinear constitutive model, one must solve a system of first-order ODEs, i.e. Eqs. (2.45) and (2.52)–(2.55), in order to update the stresses and to compute the tangent operator. Usually, implicit RUNGE-KUTTA methods are applied in conjunction with the NEWTON-RAPHSON method to integrate the differential equations numerically, cf. e.g. [105, 106, 111, 112]. For the numerical time integration, variables are evaluated at the quadrature points of the numerical integration in space, cf. Eq. (2.130). For this reason, the numerical solution of the system of ODEs is related to a “local” or “elemental” level [110]. The local solution procedure influences the solution of the global system of equations since, amongst others, the global system is evaluated at the time points provided by the RUNGE-KUTTA methods.

Frequently, the element and global levels are considered independently. In contrast, it is suggested in [110] to interpret the global system of equations (2.135) together with a system of ODEs, i.e. Eqs. (2.45) and (2.52)–(2.55), as a system of DAEs. The solution of this system of DAEs requires the application of the NEWTON-RAPHSON method twice, i.e. on the local and the global level. For this reason, the notion of the “Multilevel-NEWTON algorithm” was established in [110, 113]. In a first step, the local system of equations, i.e. Eqs. (2.45) and (2.52)–(2.55), is solved in order to obtain the internal variables depending on the displacements. Afterwards, the global system of equations (2.135) is solved in order to obtain the increments in nodal displacements.

In the current thesis, a UMAT is used to implement the proposed constitutive model into ABAQUS, and therefore it is sufficient to implement the numerical integration on the local

level only. The solution on the global level is carried out by the numerical solver provided by ABAQUS. Details on the numerical integration of the constitutive model on the local level are given in Sect. 5.3.

2.3 Mathematical Optimization

In order to formulate a mechanical material model, response functions are required to express the dependence of primary variables like the stress or the strain on secondary variables, such as the temperature. These functions include material parameters, which are often found by fitting a curve to experimental data. As a first guess, a manual adaptation could be executed. However, the fitted material parameters should be optimized numerically in a second step in order to minimize the deviations from the experimental data and to improve the overall accuracy of the model. The procedure which is explained in the remainder of this section is also applied for the calibration of the phase mixture model in Sect. 4.2. To this end, it makes sense to briefly introduce the reader to the fundamental principles of mathematical optimization in this section. The implementation is closely related to the works presented in [114, 115]. For more details, the interested reader is referred to the mentioned monographs.

The general problem of mathematical optimization is stated as follows:

$$\min \{g(\mathbf{v}) \mid \mathbf{h}(\mathbf{v}) \leq \mathbf{0}, \mathbf{k}(\mathbf{v}) = \mathbf{0}\} \quad (2.136)$$

with the functions $g: D \mapsto \mathbb{R}$, $\mathbf{h}: D \mapsto \mathbb{R}^m$, $\mathbf{k}: D \mapsto \mathbb{R}^n$, and the domain $D \subseteq \mathbb{R}^q$. The scalar objective function $g(\mathbf{v})$ is minimized with respect to the vector of parameters \mathbf{v} , considering the inequality and equality constraints defined by the vectorial functions $\mathbf{h}(\mathbf{v})$ and $\mathbf{k}(\mathbf{v})$, respectively:

$$\mathbf{h}(\mathbf{v}) = [h_1(\mathbf{v}) \quad h_2(\mathbf{v}) \quad \dots \quad h_m(\mathbf{v})]^T, \quad (2.137)$$

$$\mathbf{k}(\mathbf{v}) = [k_1(\mathbf{v}) \quad k_2(\mathbf{v}) \quad \dots \quad k_n(\mathbf{v})]^T. \quad (2.138)$$

Here, $m \in \mathbb{N}$ denotes the number of inequality constraint functions, and $n \in \mathbb{N}$ represents the number of equality constraint functions. If no additional constraints have to be taken into account, the unconstrained optimization problem is formulated in the following way:

$$\min \{g(\mathbf{v}) \mid \mathbf{v} \in D\}. \quad (2.139)$$

If $g(\mathbf{v})$, $\mathbf{h}(\mathbf{v})$, and $\mathbf{k}(\mathbf{v})$ are linear functions, the whole optimization problem is called linear. However, most engineering applications result in nonlinear optimization problems. The optimization problem is differentiable if also the functions $g(\mathbf{v})$, $\mathbf{h}(\mathbf{v})$, and $\mathbf{k}(\mathbf{v})$ are differentiable. To simplify the formulation of the constrained optimization problem, we introduce the set of vectors \mathbf{v} that satisfy the equality and inequality constraints:

$$\Xi \equiv \{ \mathbf{v} \mid \mathbf{h}(\mathbf{v}) \leq \mathbf{0}, \mathbf{k}(\mathbf{v}) = \mathbf{0} \}. \quad (2.140)$$

Considering the definition provided in Eq. (2.140), Eq. (2.136) can be reformulated in analogy to Eq. (2.139):

$$\min \{g(\mathbf{v}) \mid \mathbf{v} \in \Xi\}. \quad (2.141)$$

2 Theoretical Background

In order to solve the optimization problem, we need to introduce necessary conditions for a vector \mathbf{v}^* to be a minimum of the objective function $g(\mathbf{v})$. In [115, 116], these conditions are called “first-order optimality conditions” since they are concerned with the gradients of the objective and constraint functions. First of all, an auxiliary LAGRANGE function \mathcal{L} is defined:

$$\mathcal{L}(\mathbf{v}, \boldsymbol{\lambda}^h, \boldsymbol{\lambda}^k) = g(\mathbf{v}) + (\boldsymbol{\lambda}^h)^\top \mathbf{h}(\mathbf{v}) + (\boldsymbol{\lambda}^k)^\top \mathbf{k}(\mathbf{v}), \quad (2.142)$$

where $\boldsymbol{\lambda}^h$ and $\boldsymbol{\lambda}^k$ denote the LAGRANGE multiplier vectors with respect to the inequality and the equality constraints, respectively:

$$\boldsymbol{\lambda}^h = [\lambda_1^h \ \lambda_2^h \ \dots \ \lambda_m^h]^\top, \quad (2.143)$$

$$\boldsymbol{\lambda}^k = [\lambda_1^k \ \lambda_2^k \ \dots \ \lambda_n^k]^\top. \quad (2.144)$$

Finally, the KARUSH-KUHN-TUCKER conditions can be formulated [115, 116]. If the vector \mathbf{v}^* is a local solution of Eq. (2.136) and the objective function as well as the constraint functions are continuously differentiable, there are LAGRANGE multiplier vectors $\boldsymbol{\lambda}^{h^*}$ and $\boldsymbol{\lambda}^{k^*}$ such that the following conditions are satisfied:

$$\nabla \mathcal{L}(\mathbf{v}^*, \boldsymbol{\lambda}^{h^*}, \boldsymbol{\lambda}^{k^*}) = \mathbf{0}, \quad (2.145)$$

$$\mathbf{h}(\mathbf{v}^*) \leq \mathbf{0}, \quad (2.146)$$

$$\mathbf{k}(\mathbf{v}^*) = \mathbf{0}, \quad (2.147)$$

$$\lambda_i^{h^*} \geq 0 \quad \forall i \in \{1, 2, \dots, m\}, \quad (2.148)$$

$$\lambda_i^{h^*} h_i(\mathbf{v}^*) = 0 \quad \forall i \in \{1, 2, \dots, m\}, \quad (2.149)$$

$$\lambda_i^{k^*} k_i(\mathbf{v}^*) = 0 \quad \forall i \in \{1, 2, \dots, n\}. \quad (2.150)$$

Basically, the KARUSH-KUHN-TUCKER conditions are analogous to the condition that the gradient must be equal to zero at a minimum, modified to take constraints into account. The conditions serve as basis for the numerical solution of the optimization problem with the computing environment MATLAB. The function `fmincon` from MATLAB's Optimization Toolbox is used, cf. [116], to solve the system of equations. As default option, the interior point algorithm [117] is chosen to solve constrained optimization problems numerically. In the sequel, only basics concerning this algorithm are given. Further mathematical details can be found in [117].

Instead of the actual minimization problem given in Eq. (2.136), the interior point algorithm solves a sequence of approximate minimization problems, which are formulated as follows with respect to the approximate objective function $g_\mu(\mathbf{v}, \mathbf{s})$:

$$\min \left\{ g_\mu(\mathbf{v}, \mathbf{s}) = g(\mathbf{v}) - \mu \sum_{i=1}^m \ln(s_i) \mid \mathbf{h}(\mathbf{v}) + \mathbf{s} = \mathbf{0}, \mathbf{k}(\mathbf{v}) = \mathbf{0} \right\} \quad (2.151)$$

with the slack variables

$$\mathbf{s} = [s_1 \ s_2 \ \dots \ s_m]^\top \quad \forall s_i > 0 \quad (2.152)$$

and the barrier parameter $\mu > 0$. As μ decreases to zero, the minimum of g_μ should approach the minimum of g . Thus, the original inequality minimization problem has become an equality minimization problem such that the solution procedure requires less effort [116]. In order to solve the approximate minimization problem, the algorithm chooses between two steps:

a direct step and a conjugate gradient step. First of all, the algorithm tries to solve the problem with the direct step, i.e. the KARUSH-KUHN-TUCKER conditions are solved via a linear approximation. If this step fails, the algorithm continues with the conjugate gradient step. Here, a quadratic approximation to the approximate problem is minimized in a trust region, subjected to linearized constraints. In general, the algorithm is very stable since it is capable of solving a wide range of problems, even if the problems are ill-conditioned or nonconvex [117].

3 Experiments

In the present chapter, the different experimental investigations conducted on a multitude of specimens made of the alloy X20CrMoV12-1 are described. In addition, the results, which are the basis for the calibration of the phase mixture model in Chapt. 4 are discussed. To this end, the chapter is divided into two parts. The first part focuses on the high temperature (HT) tensile tests, while the second part presents the results of the creep tests. Each of the two parts is composed of three sections. In the first section, the experimental set-up is briefly described. The subsequent section presents the results of the experiments, which are discussed in the third section. The content of this chapter is partly based on [118], where the results of the HT tensile tests have been published. All tests have been conducted by the author at the creep laboratory of Politecnico di Milano (Italy)¹.

3.1 High Temperature Tensile Tests

3.1.1 Experimental Set-Up

In order to analyze the mechanical behavior of the alloy X20CrMoV12-1, several HT tensile tests are conducted at constant temperatures with shouldered round specimens produced by a turning machine. The geometrical data, the exact dimensions, the chemical composition, and information regarding the heat treatment of the investigated specimens are compiled in Fig. 3.1. The tests are conducted on the electromechanical testing frame CERMAC CSR50 with a tubular resistance furnace, cf. the left photo in Fig. 3.2. In order to measure the elongation of the specimens, two linear variable differential transformers (LVDTs) are used in conjunction with an extensometer mounted to the collars of the specimen, as depicted in Figs. 3.1 and 3.2. The arithmetic average of the resulting two displacement signals serves as basis to calculate the strains. Furthermore, three S-type thermocouples, i.e. 90% platinum and 10% rhodium–platinum, have been used to measure the surface temperature of the specimen at three locations: near the beginning, at the middle, and near the end of the gauge length L_0 . The locations of the thermocouples are indicated in Fig. 3.1 as red points. An uncertainty of ≈ 1.63 K due to the thermocouples is taken into account by the temperature control.

In a first test series, temperatures and strain rates are varied systematically. Six different temperature levels $T = \{673 \text{ K}, 723 \text{ K}, \dots, 923 \text{ K}\}$ and three different engineering strain rates $\dot{\epsilon} \approx \{5.0 \times 10^{-5} \text{ s}^{-1}, 1.0 \times 10^{-4} \text{ s}^{-1}, 1.0 \times 10^{-3} \text{ s}^{-1}\}$ are taken into account. One HT tensile test is conducted with respect to each combination of temperature and strain rate. Note that a maximum temperature of 923 K is chosen in order to account for the high temperatures in power plants, cf. Chapt. 1. The minimum temperature is set to 673 K due to the limitations of the testing frame, i.e. the high tensile forces at temperatures < 673 K exceed the capacity of the testing frame. Furthermore, we only consider strain rates $\dot{\epsilon} \geq 5.0 \times 10^{-5} \text{ s}^{-1}$ for a

¹At this point, I'd like to thank Elisabetta Gariboldi from Politecnico di Milano for the fruitful discussions and the access to her laboratory to conduct the experiments. Special thanks go to Oksana Baer for her helpful advice and the supervision in the laboratory.

3 Experiments

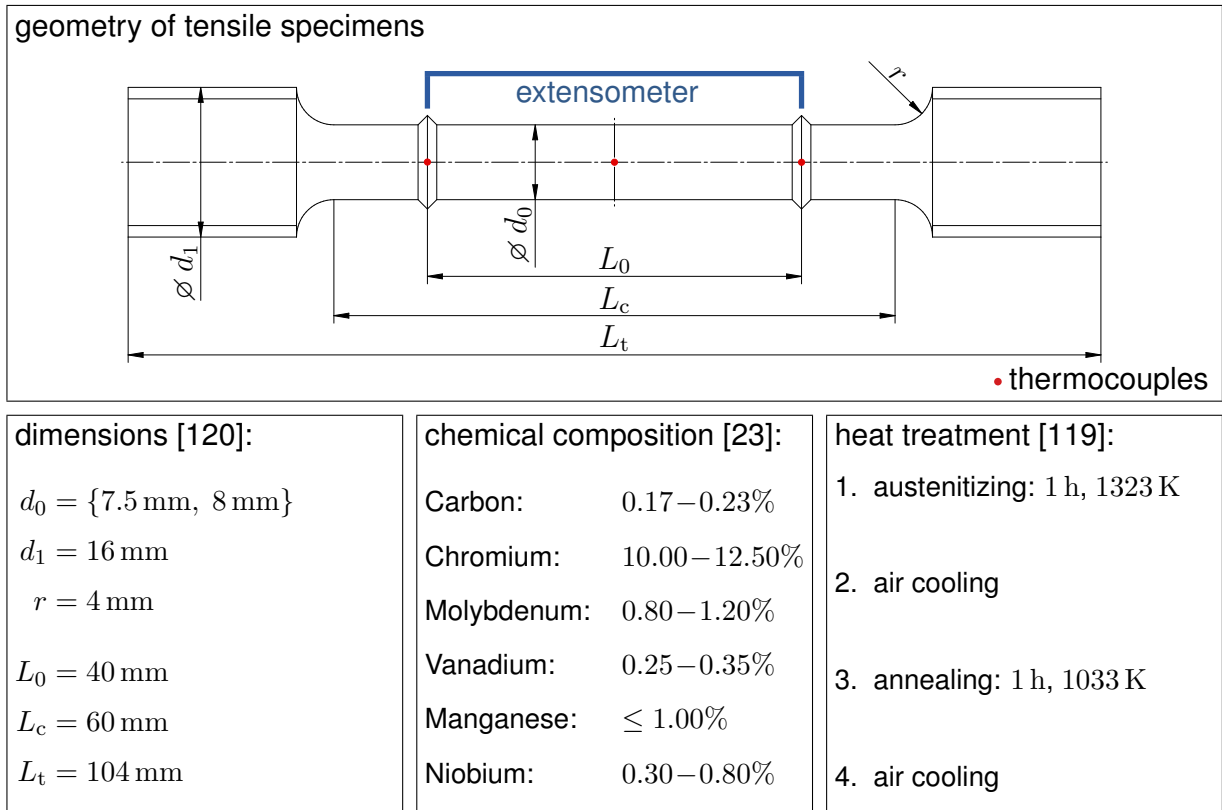


Figure 3.1: Geometry, dimensions, chemical composition, and heat treatment of the specimens.

time-saving and efficient test procedure, such that each test takes less than 3 h. All tests are conducted until the rupture of the specimen. In a second test series, a tensile test is performed several times at a temperature of 923 K under a strain rate of $5.0 \times 10^{-5} \text{ s}^{-1}$, while the test is terminated at different strain levels in order to examine the onset of necking. The term “necking” describes nonuniform changes in the cross-section over the gauge length. For the analysis of the stress-strain curves, it is crucial to distinguish necking as a macroscopic phenomenon from softening due to microstructural changes. For this reason, the shape of the deformed specimens from the second test series is examined with a profilometer. Here, the three-dimensional surface measurement device FORM TALYSURF 120 PC (Taylor Hobson) with a smallest scale division of 32 nm is used to gauge the specimens’ surface.

3.1.2 Results

3.1.2.1 Processing of Experimental Data

The experimental set-up provides an averaged increase in gauge length of the specimen $\Delta L(t_n)$ and the corresponding tensile force $N(t_n)$ for each time step t_n . With the initial gauge length L_0 and the initial diameter d_0 , the engineering stress $P(t_n)$ and the engineering strain $\varepsilon(t_n)$ are computed according to Eqs. (2.33) and (2.19):

$$P(t_n) = \frac{N(t_n)}{A_0} \quad \text{with } A_0 = \frac{\pi d_0^2}{4}, \quad (3.1)$$

$$\varepsilon(t_n) = \frac{\Delta L(t_n)}{L_0}. \quad (3.2)$$

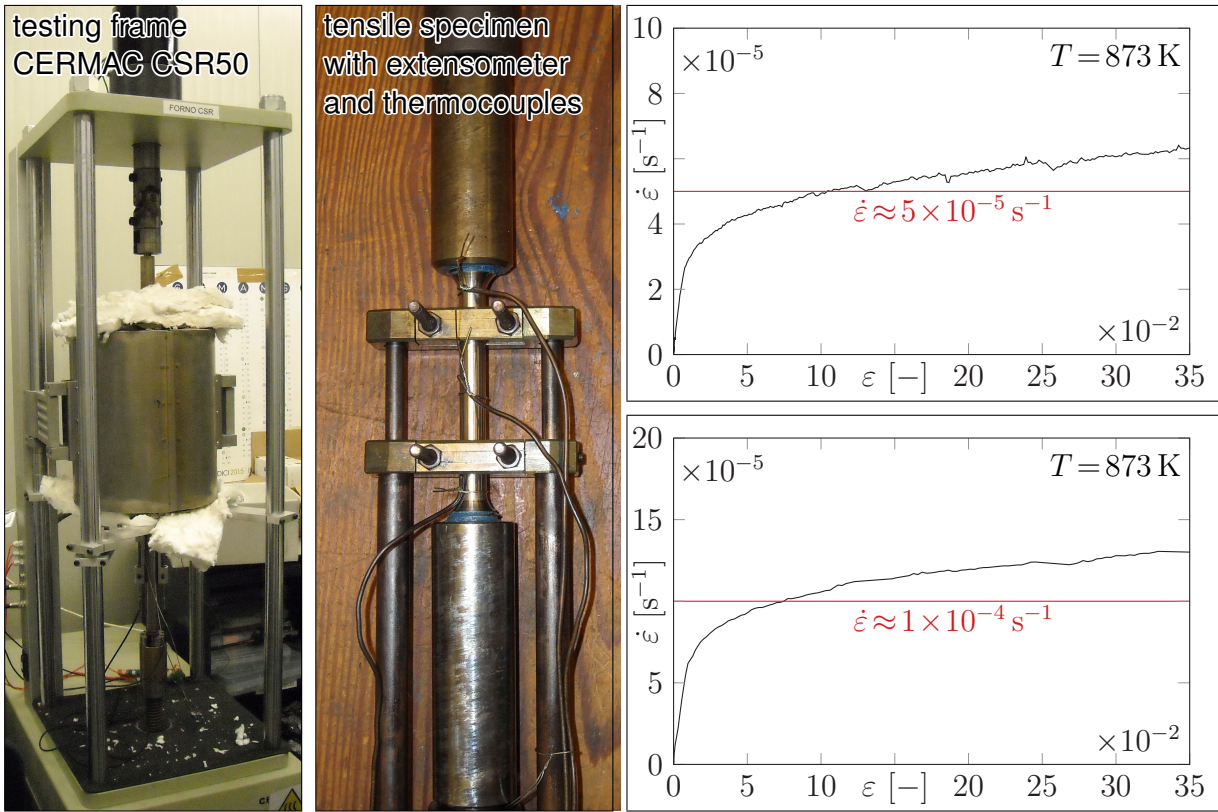


Figure 3.2: Testing frame and prepared specimen with extensometer and thermocouples (left), engineering strain rate $\dot{\varepsilon}$ vs engineering strain ε for two tensile tests at 873 K.

The corresponding engineering strain rate is computed by approximating the temporal derivative by means of a backward difference formula:

$$\dot{\varepsilon}(t_n) = \frac{\varepsilon(t_n) - \varepsilon(t_{n-1})}{t_n - t_{n-1}}. \quad (3.3)$$

During the tests, the strain rate cannot be prescribed directly due to the limitations of the testing frame, and therefore the displacement rate is prescribed. This results in a slight increase of the strain rate with respect to the elongation of the specimens, as shown on the right-hand side of Fig. 3.2. The engineering strain rate $\dot{\varepsilon}$ is depicted vs the engineering strain ε for two tensile tests at 873 K. Here, the slight scatter in data is attributed to the computation of the strain rates as finite differences, cf. Eq. (3.3). The diagrams on the right-hand side of Fig. 3.2 show that the slightly increasing strain rates can be approximated by the constant values $\dot{\varepsilon} \approx 5 \times 10^{-5} \text{ s}^{-1}$ and $\dot{\varepsilon} \approx 1 \times 10^{-4} \text{ s}^{-1}$, respectively.

However, the engineering measures P and ε do not take changes in the geometry of the specimen into account since they correspond to the undeformed specimen in the reference state. For this reason, stress and strain measures related to the current dimensions of the specimen, i.e. the CAUCHY stress σ and the HENCKY strain H , are used in addition to the engineering measures. They can be computed based on Eqs. (2.31) and (2.20):

$$\sigma(t_n) = \frac{N(t_n)}{A(t_n)}, \quad (3.4)$$

$$H(t_n) = \ln\left(1 + \frac{\Delta L(t_n)}{L_0}\right). \quad (3.5)$$

3 Experiments

Due to the limitations of the experimental set-up, one cannot measure the current cross-section A of the specimen directly. For this reason, the stress σ is calculated based on the engineering stress P by Eq. (2.35). One should emphasize that Eq. (2.35) is only valid if the cross-section deforms uniformly over the gauge length such that Eq. (2.35) should not be applied after the onset of necking. Furthermore, the inelastic part of the logarithmic strain H^{in} is of importance. It is determined by subtracting the elastic part:

$$H^{\text{in}}(t_n) = H(t_n) - H^{\text{el}}(t_n) \quad \text{with} \quad H^{\text{el}}(t_n) = \frac{\sigma(t_n)}{E}. \quad (3.6)$$

3.1.2.2 Test Series 1

Within the first test series, HT tensile tests are conducted at different temperatures and strain rates to systematically examine the mechanical behavior of the alloy X20CrMoV12-1 at high temperatures. Six different temperature levels $T = \{673 \text{ K}, 723 \text{ K}, \dots, 923 \text{ K}\}$ and three different engineering strain rates $\dot{\varepsilon} \approx \{5.0 \times 10^{-5} \text{ s}^{-1}, 1.0 \times 10^{-4} \text{ s}^{-1}, 1.0 \times 10^{-3} \text{ s}^{-1}\}$ are taken into account. In the remainder of this chapter, these three strain rates are referred to as “minimum”, “medium”, and “maximum” strain rate.

The first three diagrams depicted in Fig. 3.3 show the engineering stress depending on the engineering strain for the three strain rates. Each diagram corresponds to a constant strain rate, while the results of the tensile tests at different temperatures are depicted. This representation is useful to analyze the influence of the temperature on the tensile behavior. In addition, material parameters, i.e. the YOUNG's modulus E , the strain to rupture ε_{max} , and the maximum tensile stress P_{max} are displayed with respect to the temperature. While the strain to rupture and the maximum stress can be easily read from the individual stress-strain curves, the YOUNG's modulus is determined by a linear regression of the experimental data in the elastic range, i.e. for small strains $\varepsilon \leq 0.2\%$. Due to the scatter of the data and in order to obtain reliable results, the strain interval for the determination of the YOUNG's modulus has to be readjusted for every test individually. Furthermore, the experimental values for the YOUNG's modulus are compared to the results from [10].

Additionally, the dependence of the CAUCHY stress on the inelastic HENCKY strain is analyzed in Fig. 3.4. Each diagram contains the stress-strain curves at constant temperature with respect to all three strain rates. This figure is used to examine the strain rate dependence of the material. With respect to the temperature 873 K, additional data is available in [10].

Figure 3.5 presents data that has been extracted from the stress-strain curves in Fig. 3.4. On the left-hand side, the maximum CAUCHY stress is displayed depending on the temperature at different strain rates, while the softening modulus $\zeta = \left| \frac{\Delta\sigma}{\Delta H^{\text{in}}} \right|$ is shown with respect to the temperature on the right-hand side. The softening modulus refers to the approximately constant slope of the stress-strain curves, as schematically depicted in Fig. 3.4 at the bottom right. After the maximum tensile stress has been reached, i.e. for strains exceeding the strain $H^{\text{in}}(\sigma_{\text{max}})$ corresponding to the maximum stress, most stress-strain curves for higher temperatures, i.e. $T \geq 773 \text{ K}$, exhibit a relatively wide strain range with constantly decreasing stress. In order to quantify the softening behavior, the softening modulus is determined based on a linear approximation of this strain range, and the results are depicted on the right-hand side of Fig. 3.5.

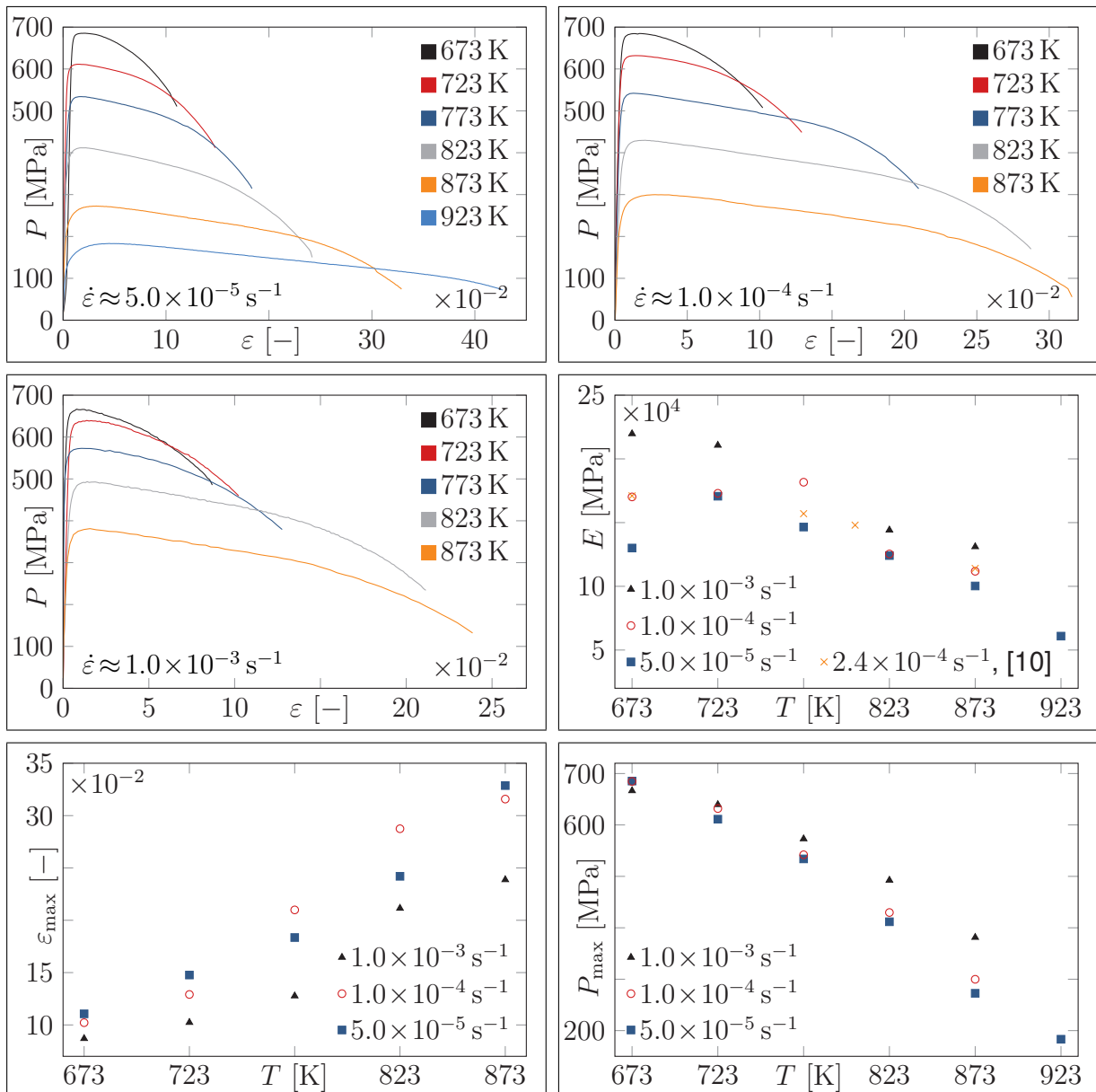


Figure 3.3: Test Series 1. Engineering stress P vs strain ϵ for minimum, medium, and maximum strain rate; YOUNG's modulus E vs temperature T ; strain to rupture ϵ_{\max} vs temperature T ; maximum engineering stress P_{\max} vs temperature T (from top left to bottom right).

3.1.2.3 Test Series 2

In the following, the results of the second test series are presented. To examine the onset of necking, a tensile test at the highest temperature, i.e. 923 K, under the minimum strain rate of $5.0 \times 10^{-5} \text{ s}^{-1}$ is performed several times. As has been discussed in Sect. 3.1.2.2, particularly stress-strain curves with respect to higher temperatures show an extended softening stage, i.e. a strain range with constantly decreasing stress. Furthermore, it is presumed that the softening effect becomes stronger with decreasing strain rate. Thus, in order to observe a long softening stage, the lowest strain rate and the highest temperature are chosen as parameters for the tensile test. The test is terminated at different strain levels, and the results are summarized in Fig. 3.6, which shows the engineering stress depending on the engineering strain. Photographs of the deformed specimens are included in the figure. The

3 Experiments

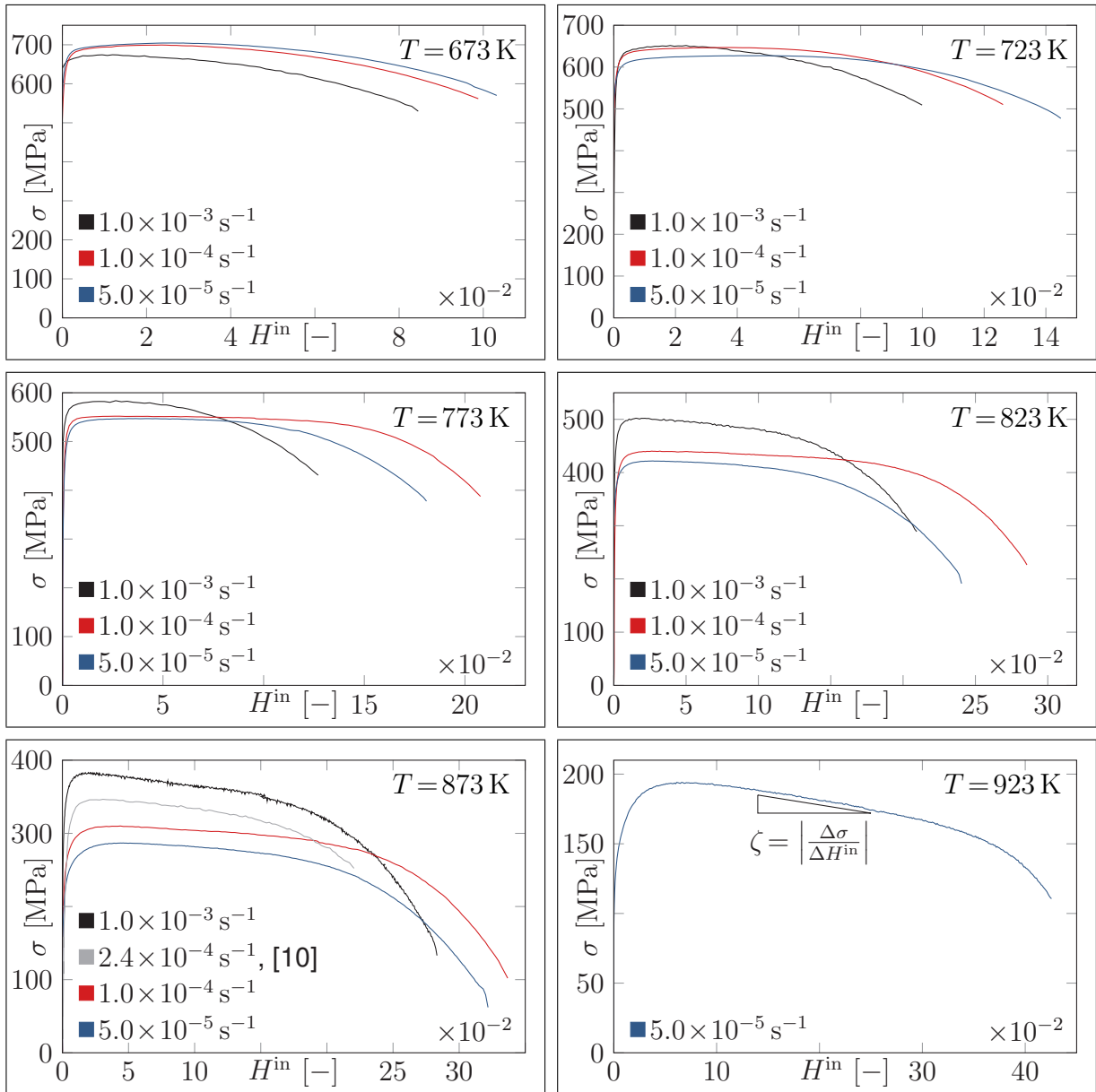


Figure 3.4: Test Series 1. CAUCHY stress σ vs inelastic HENCKY strain H^{in} for different temperatures.

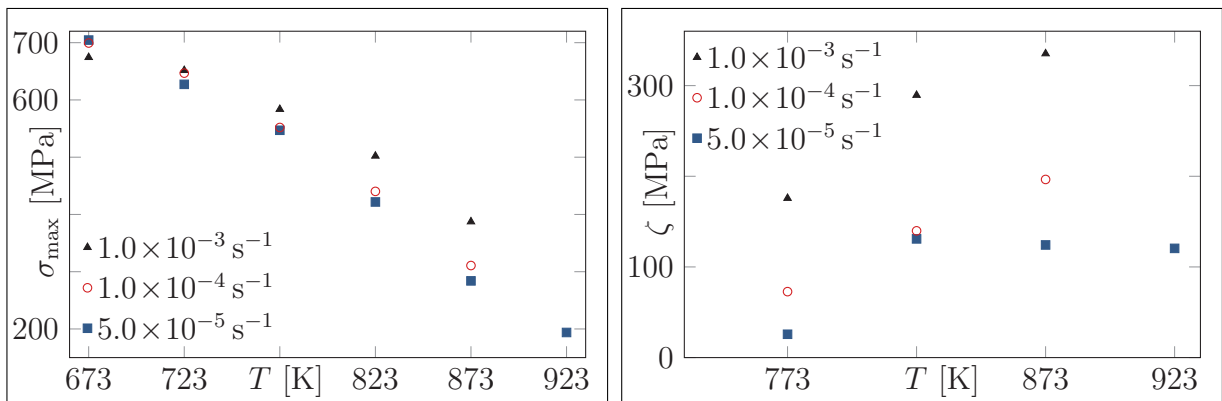


Figure 3.5: Test Series 1. Maximum CAUCHY stress σ (left) and softening modulus ζ (right) vs temperature T .

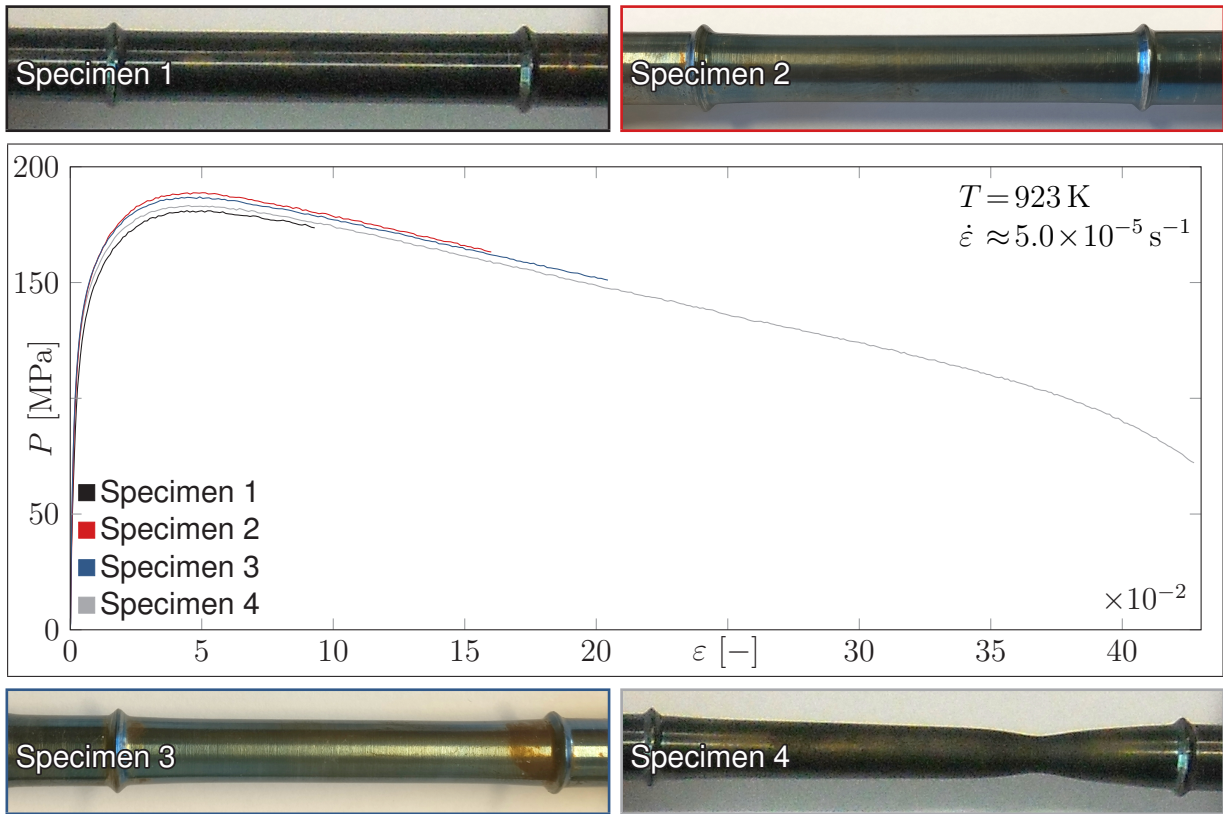


Figure 3.6: Test Series 2. Engineering stress P vs engineering strain ε .

test with Specimen 1 is terminated at an approximate strain level of $\varepsilon \approx 10\%$, while the test with Specimen 2 is continued until the strain level of $\varepsilon \approx 15\%$ is reached. Finally, the test with Specimen 3 is terminated at $\varepsilon \approx 20\%$, and the test with Specimen 4 has been terminated at the largest elongation of $\varepsilon \approx 43\%$. The corresponding photographs clearly show the changes in the cross-section with increasing deformation. Note that all photographs have different scale factors.

Only the photograph of Specimen 4 shows considerable nonuniform change in the cross-section, i.e. necking. For this reason, further investigations are required to determine precisely whether necking has already started during the Tests 1, 2, and 3. In addition to the visual examination of the specimens' shape, the hypothesis of volume conservation during inelastic deformation can be applied to roughly determine the onset of necking, as presented in [31]. If the inelastic deformation is isotropic, such that the circular cross-sections remain circular after the deformation, the deformations are homogeneous, and the elastic strains are negligible, the trace of the HENCKY strain tensor is equal to zero, thus resulting in a linear relation between the longitudinal strain H_{11} and the two transverse strains $H_{22} = H_{33}$:

$$\text{tr}(\mathbf{H}) = 0 \Rightarrow H_{11} + 2H_{22} = 0. \quad (3.7)$$

Table 3.1 summarizes the results of the application of this hypothesis. The first column corresponds to the specimen number, whereas the second column contains the experimental longitudinal strains H_{11}^{exp} at the end of the corresponding test. The third column provides the experimental values of the radial strain H_{22}^{exp} , calculated based on the diameter measurements on homogeneously deformed cross-sections far from the potential necking region. The fourth column contains the radial strains H_{22}^{calc} , computed based on Eq. (3.7) based on the results for H_{11}^{exp} . Finally, a relative deviation $\Delta H_{22} = |H_{22}^{\text{exp}} - H_{22}^{\text{calc}}| / |H_{22}^{\text{exp}}|$ with respect to the

3 Experiments

calculated and the experimental transverse strains is determined.

As a third way to determine the onset of necking, the shape of a specimen in virgin state as well as the shapes of Specimens 2 and 3 are examined with a tactile profilometer. The surface of the specimens is scanned mechanically across the gauge length, omitting the collars as depicted in Fig. 3.1. Figure 3.7 summarizes the results. The abscissa shows a normalized $\bar{x} = x/x_{\max}$ coordinate referring to the longitudinal direction of the specimen. The vertical movement of the scanner is depicted on the ordinate as z coordinate, thus reflecting the *change* in diameter. The two upper diagrams show the results of the surface measurement of a virgin specimen. At the left-hand side, an overview over the whole measured length is given, while the diagram on the right-hand side shows a close-up view of the corresponding adjacent diagram. The four diagrams below refer to the deformed specimens 2 and 3, which have been subjected to strains up to 16% and 20%, respectively. For the sake of brevity, the results of only one profilometry per specimen are presented. Originally, two measurements per specimen have been conducted, i.e. the specimen has been rotated about 180° around its longitudinal axis such that each measurement refers to another circumferential position. Figures A1.1 and A1.2 in the appendix present the results for the two profilometry measurements for the Specimens 2 and 3. It becomes obvious that the measurements at different angles lead to similar results with insignificant deviations such that it suffices to discuss only one measurement per specimen.

3.1.3 Discussion

3.1.3.1 Test Series 1

The results presented in Fig. 3.3 are used to analyze the influence of the temperature on the deformation behavior. The stress-strain curves start with a fast increase in the elastic range. Afterwards, the slope decreases since microstructural hardening processes dominate the material behavior. The curves attain their maxima at relatively low strains, around $\approx 1\%$ – 2% . Behind the maximum, i.e. for higher strains, softening, which is also related to processes on the microstructure, dominates the material behavior. Especially at high temperatures, the softening stage is extended and pronounced. Approaching the strain to rupture, i.e. in the last third of the curves, their slope decreases even faster, which can be attributed to necking. For the interpretation of the stress-strain curves, it is crucial to distinguish the softening stage from the stage, where necking dominates the material behavior. Therefore, the second series of HT tensile tests has been performed, and the onset of necking is examined and discussed in Sect. 3.1.3.2. The obtained stress-strain curves are in good agreement with [31], where HT tensile tests of a 9% chromium steel under similar strain rates and temperatures are presented.

As can be seen in Fig. 3.3, the YOUNG's modulus decreases with the temperature. Many

Table 3.1: Determination of the onset of necking by the hypothesis of constant volume

Test	H_{11}^{exp} [%]	H_{22}^{exp} [%]	H_{22}^{calc} [%]	ΔH_{22} [%]
1	9.50	−4.38	−4.75	8.45
2	16.03	−6.37	−8.02	25.90
3	20.14	−8.05	−10.07	25.09
4	43.58	−8.42	−21.79	158.79

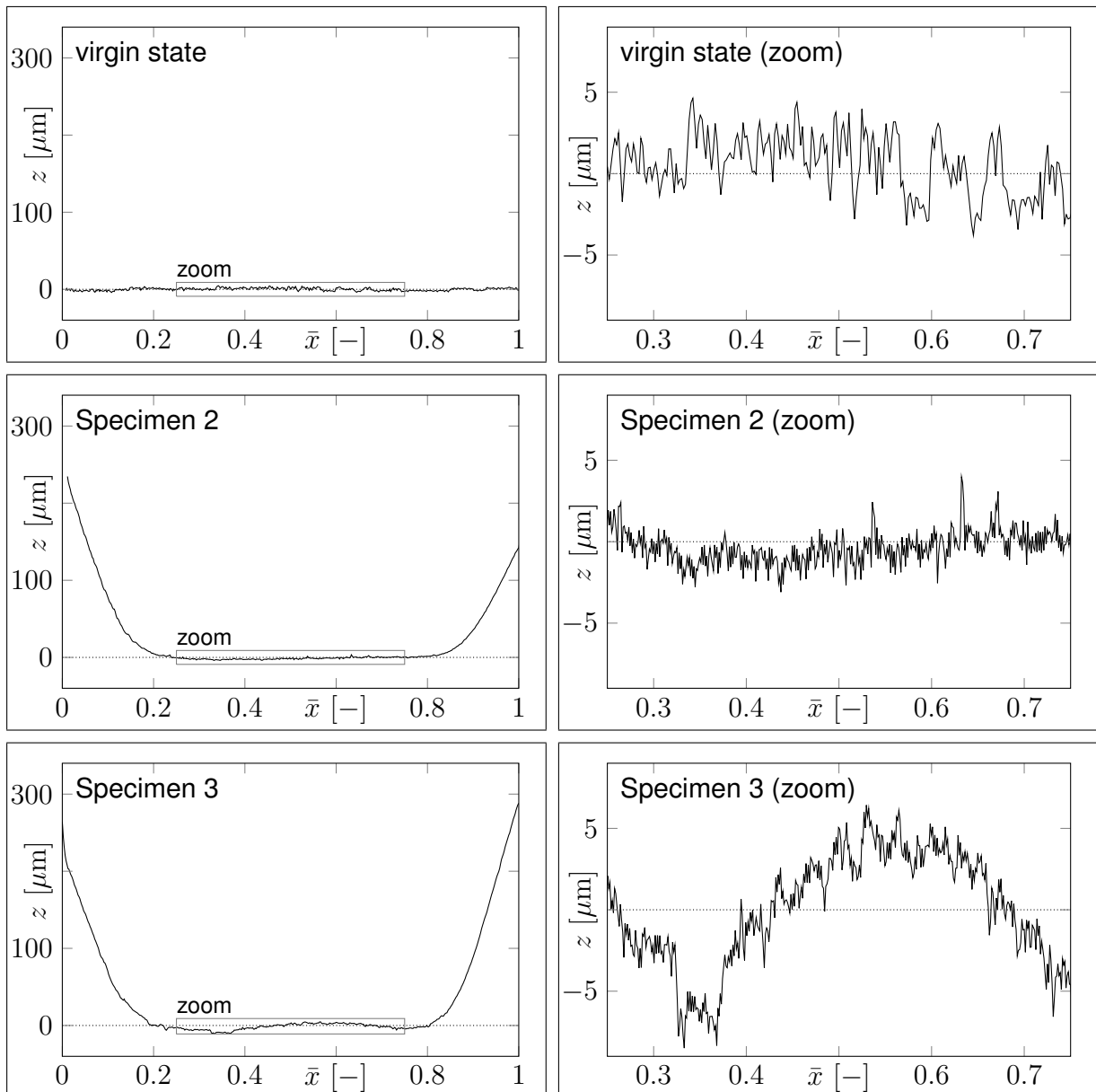


Figure 3.7: Test Series 2. Profilometry of different specimens

mechanical models neglect the influence of the strain rate on the YOUNG's modulus, although our results demonstrate a slight strain rate dependence of this stiffness measure. To be precise, a decrease in the strain rate also results in a decrease in the YOUNG's modulus. At a temperature of 673 K, the strain rate seems to exert a high influence on the YOUNG's modulus. However, this large deviation in the results is most likely due to a higher scatter in the data because of the strain rate control and the very high tensile forces applied by the testing frame at low temperatures. For example during a tensile test under a strain rate of $\dot{\epsilon} = 5.0 \times 10^{-5} \text{ s}^{-1}$ at a low temperature of 673 K, tensile forces three times as high as the tensile forces during a test under the same strain rate at a temperature of 923 K occur. In contrast to the YOUNG's modulus, the strain to rupture ϵ_{\max} , which is a measure used to quantify the ductility of a material, increases with the temperature, whereas the maximum stress P_{\max} shows the same behavior as the YOUNG's modulus: it becomes smaller while the temperature increases. Furthermore, the influence of the strain rate on the strain to rupture and the maximum stress grows with higher temperatures.

3 Experiments

Figure 3.4 provides additional information concerning the strain rate dependence of the tensile behavior. With increasing strain rate, the overall stress level generally increases, which is also true for the maximum stress. One can observe this effect for temperatures $723\text{ K} \leq T \leq 923\text{ K}$, and it is emphasized with increasing temperature. After the stress maxima of each curve has been reached, the slope of the curves remains constant over a wide strain range. For the temperatures $673\text{ K} \leq T \leq 773\text{ K}$, the stress level is nearly constant behind the maximum, while one observes a slight, but constant decrease in the stress for the temperatures $823\text{ K} \leq T \leq 923\text{ K}$.

In the following, the maximum CAUCHY stress and the slight decrease in stress at higher temperatures are investigated in detail based on the results depicted in Fig. 3.5. The left diagram in Fig. 3.5 confirms the previous findings concerning the maximum stress: the higher the temperature, the lower the maximum stress, and the higher the strain rate, the higher the maximum stress. The softening modulus on the right-hand side in Fig. 3.5 shows a similar dependence on the strain rate. For temperatures $T \leq 773\text{ K}$ and small strain rates, the softening modulus approaches zero, thus indicating a constant stress level, such as it is shown in the middle left diagram in Fig. 3.4, for example. The modulus grows with increasing temperatures. Interestingly, the softening modulus seems to reach a saturation level at the higher strain rates. At the lowest strain rate, the modulus is constant for $T \geq 823\text{ K}$.

The softening stage, i.e. the constant decrease in stress, is closely related to the microstructural changes as discussed in Sect. 1.1. Here, one should bear in mind that most microstructural processes require time to evolve. With respect to the presented HT tensile tests, the maximum test duration accounts to roughly 3 h at the lowest strain rate. Due to this relatively short time period compared to creep tests, softening can be predominantly attributed to the coarsening of subgrains and to the decrease of the dislocation density since the coarsening of the precipitates requires more time to develop [38]. The correlation to the microstructural processes could also explain the strain rate dependence of the softening behavior.

Discussing Figs. 3.4 and 3.5, it is important to keep in mind that the stress has been approximated by Eq. (2.35), which is valid only for homogeneous deformations, i.e. *before* the onset of necking. For this reason, it is crucial to determine the strain level related to the onset of necking. This important issue is comprehensively discussed in Sect. 3.1.3.2.

3.1.3.2 Test Series 2

The phase mixture model, which is introduced in the following chapter, describes the elastic and inelastic deformations of tempered martensitic steels including hardening and softening processes. In addition, it is presumed that the main variables, i.e. the stress, strains, hardening and softening variables, reach a steady saturation state after a certain time and deformation. The phenomenon of necking is not taken into account by the model, and therefore it is essential to determine the cut-off strain level, where no deformation due to necking is present. For this purpose, the CONSIDÈRE criterion [121] is widely applied in engineering mechanics. This criterion states that necking starts at the point of the maximum stress in the stress-strain curves [122]. Therefore, the strain corresponding to the maximum stress is referred to as “CONSIDÈRE strain” in the remainder of this thesis. Figure 3.4 reveals that the CONSIDÈRE strain is significantly lower than $\approx 5\%$ for the alloy under consideration, depending on the applied temperature and strain rate. In order to examine the onset of necking in circular bars, NEEDLEMAN has conducted finite element analyses [123], using a rate-dependent plasticity model with isotropic hardening. He could show that the onset of necking takes place at strain levels larger than the CONSIDÈRE strain. An experimental

validation of these findings is provided in [31], presenting the results of a series of HT tensile tests with a P92 steel at a temperature of $T = 823 \text{ K}$ under a strain rate of $\dot{\varepsilon} = 2.5 \times 10^{-4} \text{ s}^{-1}$. The HT tensile tests are terminated at different strain levels in order to determine the onset of the macroscopic necking. Primarily by visual inspection of the shape of the specimen, it is found that the macroscopic necking starts at strain levels $\varepsilon \geq 15\%$ with respect to the alloy under consideration and the test parameters [31].

According to the findings discussed in the previous paragraph, it is deemed necessary to conduct a second series of HT tensile tests. These experimental measurements are employed to assess the onset of macroscopic necking. Figure 3.6 gives an overview of the results of the second measurement campaign. The photographs indicate that macroscopic necking has definitely occurred in the fourth test. From visual inspection alone it can, however, not be clarified whether necking has taken place during the Tests 1–3 such that further investigations are required.

As an alternative approach, the hypothesis of constant volume during inelastic deformation has been presented in Sect. 3.1.2.3. Table 3.1 reveals a relatively good agreement between the experimental and the calculated values of the radial strain H_{22} for Specimen 1. In contrast, there are significantly higher deviations between the experimental and the calculated measures for Specimens 2–4. These results suggest that necking has already started during Test 2, thus also occurring during Tests 3 and 4.

To verify these findings, the results of the profilometry in Fig. 3.7 are analyzed. The diagrams at the top, i.e. the results with respect to the virgin state, show the typical surface structure due to the production process of the specimens. The comparison of the diagrams at the middle and the bottom right reveals that the diameter of the Specimen 2 is almost constant near the middle of the specimen ($0.3 < \bar{x} < 0.7$), whereas the diameter of the Specimen 3 is highly reduced at $\bar{x} \approx 0.35$. Thus, necking has not yet occurred during Test 2, but has already started before the end of Test 3. After all, this leads to the conclusion that necking starts at an approximate strain level of $15\% < \varepsilon < 20\%$, taking the test parameters ($T = 923 \text{ K}$, $\dot{\varepsilon} = 5.0 \times 10^{-5} \text{ s}^{-1}$) into account. As has been shown, this result is in good agreement with the findings in [31]. At this point, one should bear in mind that softening and necking are two fundamentally different processes. Since softening is attributed to changes in the microstructure, it is a time-dependent slow process. In contrast, necking is based on an instability, which leads to abrupt strain localization in the vicinity of imperfections, e.g. material inhomogeneities, surface defects due to the manufacturing, or an inhomogeneous temperature distribution during the tests [124]. Therefore, one should keep in mind that the presented methods provide only a rough estimation of the onset of necking, which can vary strongly due to the properties of the specimens and the test procedure. Nevertheless, it is noticeable that the softening stage starts at strain levels $\varepsilon < 5\%$, which is significantly lower than the strains with respect to the onset of necking, i.e. $\varepsilon > 15\%$.

3.2 Creep Tests

3.2.1 Experimental Set-Up

In addition to the HT tensile tests, three creep tests at a constant temperature of $T = 873 \text{ K}$ are conducted. This temperature is chosen bearing in mind the maximum temperature in power plants, cf. Chapt. 1. Photos of the experimental set-up are provided in Fig. 3.8. A constant tensile force N is applied by attaching physical weights to the test specimens such that the engineering stress P is constant, while the CAUCHY stress σ varies with time due

3 Experiments

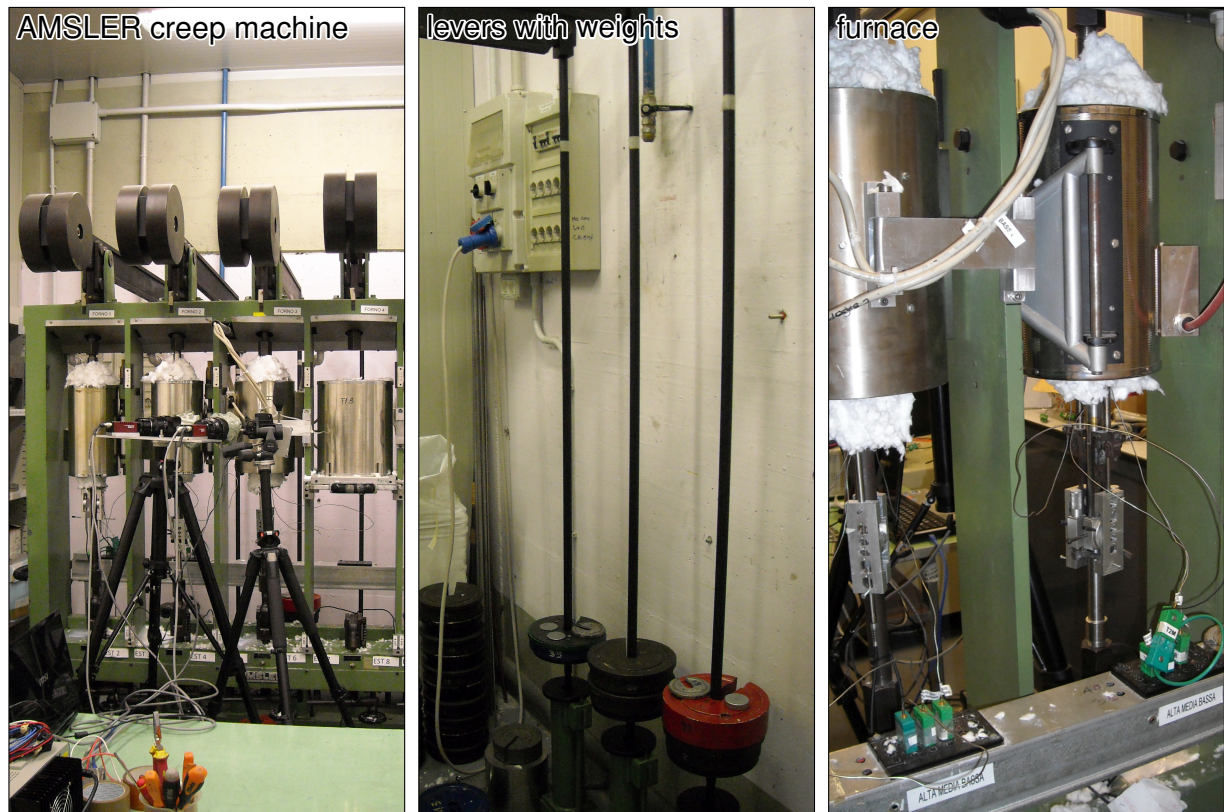


Figure 3.8: Experimental set-up for the creep tests, conducted at the laboratory at Politecnico di Milano, Italy.

to the changes in the cross-section. The tests are conducted on an AMSLER lever-arm creep machine with a nominal lever ratio of 1:25. Similar to the measurement equipment during the HT tensile tests, an extensometer is placed at the collars of the specimens, and the displacement of the collars is recorded by two LVDTs. Once more, three S-type thermocouples are used for monitoring the temperatures along the gauge length.

3.2.2 Results

Figure 3.9 presents the results of the three creep tests. The first creep test is conducted until rupture, while the other two tests are terminated before rupture. At the top left of Fig. 3.9, the prescribed engineering stress P is displayed with respect to a normalized time $\bar{t} = t/t_{\text{end}}$, while t_{end} refers to the duration of every individual creep test. The maximum stress level is set to $P_{\text{max}} \approx 150$ MPa, while the minimum stress level is $P_{\text{min}} \approx 100$ MPa. During the first test, the stress level varies between these two extrema, whereas the creep tests 2 and 3 are conducted at the constant maximum and minimum stress levels, respectively. The conduction of a cyclic creep test, i.e. the first test, is based on [13], where also results of a creep tests under varying loads are presented. While the standard creep tests 2 and 3 are useful to calibrate the model, cf. Sect. 4.2.2, the cyclic creep test 1 is used to verify the calibrated model, cf. Sect. 4.3. In the top right diagram of Fig. 3.9, the inelastic HENCKY strain is depicted with respect to the time. The diagram at the bottom of Fig. 3.9 shows the inelastic HENCKY strain rate on a logarithmic scale depending on the inelastic HENCKY strain.

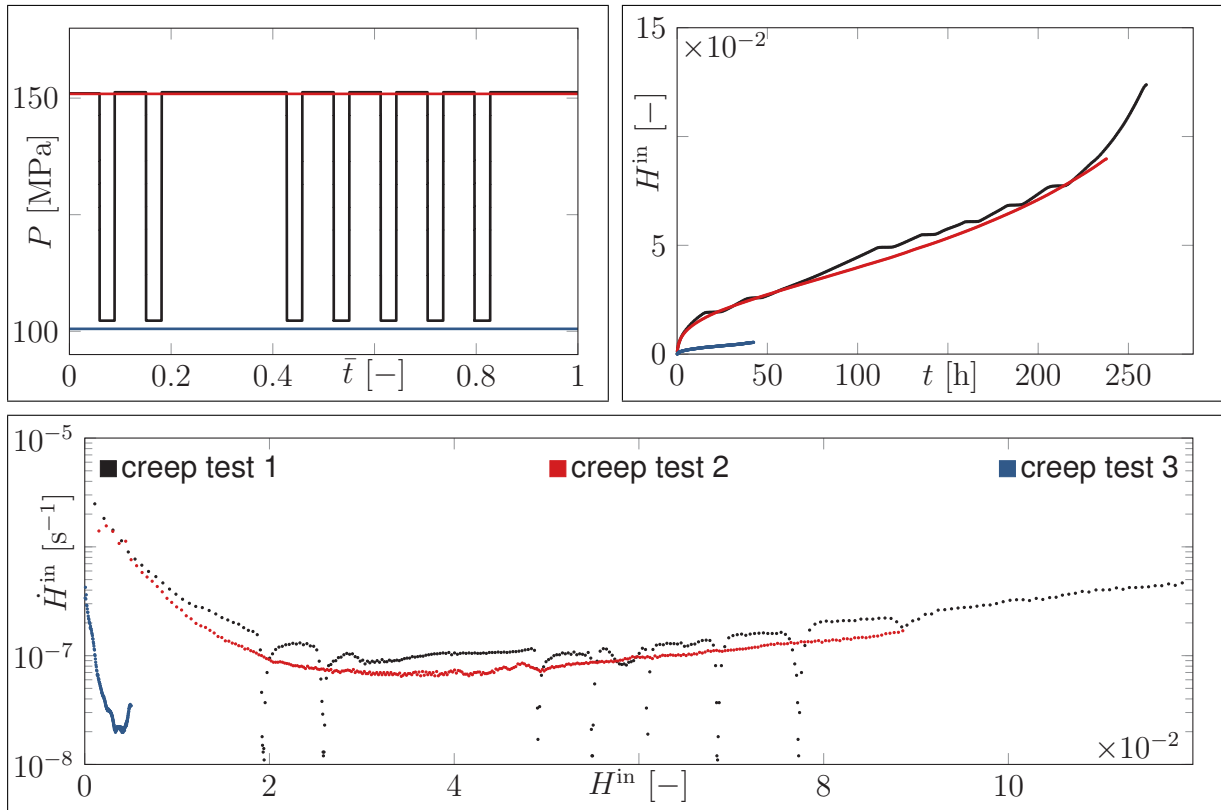


Figure 3.9: Results of the creep tests 1, 2, and 3 at a temperature of $T = 873$ K. Engineering stress P vs normalized time \bar{t} (top left), inelastic HENCKY strain H^{in} vs time t (top right), inelastic HENCKY strain rate \dot{H}^{in} vs inelastic HENCKY strain H^{in} (bottom).

3.2.3 Discussion

We start by discussing the results of the creep tests 2 and 3 since these are standard tests with respect to constant engineering stress levels. The results of both tests show the primary and the tertiary creep stage, as already explained in Chapt. 1. The primary creep stage is characterized by the decreasing strain rate because of the hardening processes on the microstructural level. This behavior can be easily observed in the bottom diagram of Fig. 3.9. After reaching the minimum strain rates, the strain rate increases again in the tertiary creep stage. A secondary creep stage with a constant strain rate is not observed. Due to the higher load during the second creep test compared to the third test, the strain rate is naturally higher throughout the entire test. Here, one should note that the third test has been stopped after only ≈ 42 h due to a problem in the temperature control. Thus, the tertiary creep stage has not developed yet, cf. the top right diagram in Fig. 3.9.

During the first creep test, the engineering stress is prescribed as a piecewise constant function of time, cf. the top left diagram in Fig. 3.9. It is worth noticing that the results of the first creep test are similar to the results of the second creep test, i.e. the test corresponding to the maximum stress level. From the top right diagram, it becomes apparent that the inelastic strain increases primarily during the creep stages at the maximum stress level. During the creep stages at the minimum stress level, the inelastic strain does not change significantly resulting in the horizontal segments in the top right diagram in Fig. 3.9. Furthermore, the inelastic strain rate is more than one order of magnitude lower than the strain rates corresponding to the maximum stress level, as can be seen in the bottom diagram of Fig. 3.9.

4 One-Dimensional Phase Mixture Model

In this chapter, the phase mixture model is introduced considering uniaxial stress and deformation states. It is divided into three sections, whereas Sect. 4.1 presents the governing equations of the one-dimensional phase mixture model. The calibration procedure for the phase mixture model – applied to the alloy X20CrMoV12-1 – is discussed in Sect. 4.2. It is based on the experimental measurements provided in Chapt. 3 and on additional data taken from the body of literature. In a last step, the calibrated model is validated against other experimental results that are also available in the literature.

4.1 Governing Equations

In this section, the governing equations for the one-dimensional phase mixture model are introduced. This material model is the basis for simulating the mechanical behavior of the high temperature steel X20CrMoV12-1. The phase mixture model under consideration assumes that the material constitutes a mixture being composed of two distinct constituents. Here, we assume that the individual constituents exhibit an identical elastic behavior, while their inelastic behavior differs significantly. Note that the identical elastic behavior of the constituents is a significant, but realistic assumption, which substantially simplifies the governing equations [125]. To indicate the difference in the inelastic response of the two phases, one is referred to as “inelastic-soft”, while the other is labelled “inelastic-hard”. However, for the sake of brevity, we only use the terms “soft” and “hard” to distinguish the two phases; usually we will indicate this by employing the index k which can take the values s and h ($\square_k \forall k \in \{s, h\}$). The derivation of the governing equations is based on [16, 42, 71], where further information can be found. As already pointed out in Sect. 1.2, the hard phase is related to the subgrain or grain boundaries, i.e. regions with a high dislocation density and a large number of carbides, while the soft phase represents the subgrain interior, i.e. regions with a low dislocation density and a small number of carbides. The division of the real microstructure into the two phases is depicted in Fig. 4.1.

For our phase mixture model, the equality of the total strain H in both phases is postulated. Hence, this model belongs to the group of the iso-strain concepts [16, 42, 71, 92, 118, 126], which have been introduced in Sect. 2.1.6:

$$H = H_h = H_s. \quad (4.1)$$

For the overall stress σ , a rule of mixture is applied, cf. also Eq. (2.81):

$$\sigma = \eta_s \sigma_s + \eta_h \sigma_h. \quad (4.2)$$

The dimensionless variable η_k is the volume fraction of the specific constituent. Due to the mass conservation constraint, the following relation holds:

$$\eta_s + \eta_h = 1 \quad \forall \quad 0 < \eta_k < 1. \quad (4.3)$$

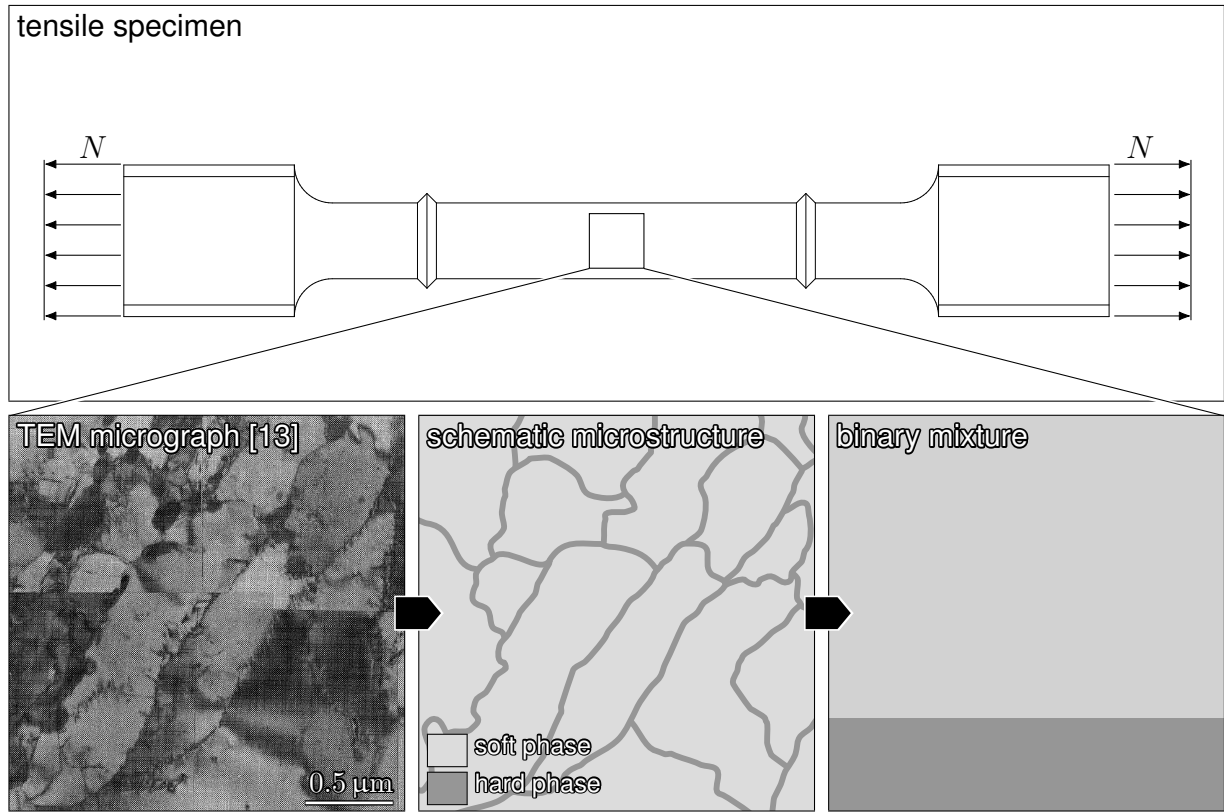


Figure 4.1: Representation of the microstructure by means of the binary phase mixture model.

In analogy to Eq. (2.54), the additive split of the strains into the elastic and the inelastic part is used:

$$H = H_k^{\text{el}} + H_k^{\text{in}}. \quad (4.4)$$

As mentioned before, the elastic behavior is identical for both phases:

$$\sigma_k = E H_k^{\text{el}}. \quad (4.5)$$

The parameter $E = E_k$ denotes the YOUNG's modulus, which is identical for both phases. In order to capture the temperature-dependent behavior of the YOUNG's modulus, a temperature response function $f_E(T)$ is introduced:

$$E = f_E(T). \quad (4.6)$$

In addition, constitutive equations for the inelastic material behavior of both phases need to be developed. Since a unified constitutive model is used, the overall inelastic strains H_k^{in} contain both instantaneous plastic strains and time-dependent creep strains [45]. Evolution equations for the inelastic strain rates are formulated as follows:

$$\dot{H}_k^{\text{in}} = f_{H_k}(\sigma_k, T). \quad (4.7)$$

The phase mixture model based on an iso-strain approach is illustrated by means of a rheological material model in Fig. 4.2 for time-independent volume fractions η_k , i.e. they are constant over time. In the following, the model is extended by taking a time-varying volume

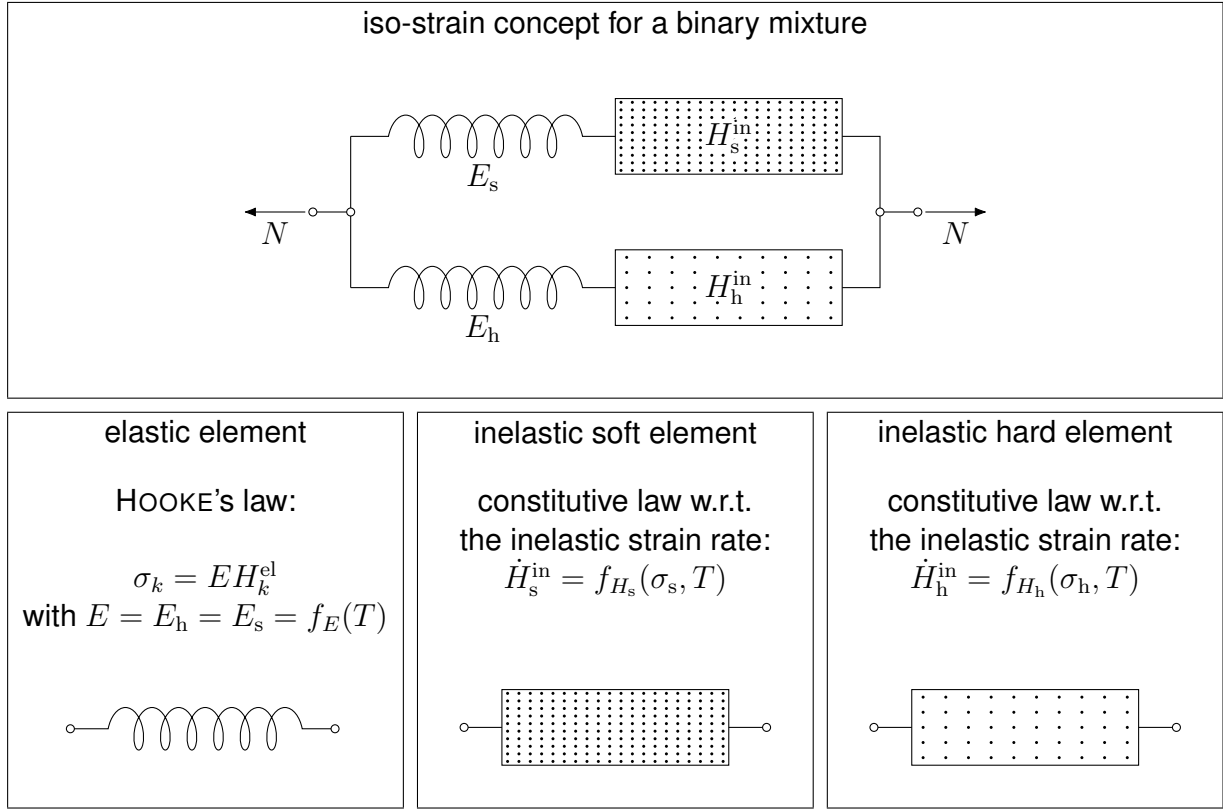


Figure 4.2: Graphical representation of the phase mixture model with constant volume fractions of the phases.

fraction into account, such that an evolution equation for the volume fraction of one phase has to be found:

$$\dot{\eta}_h = f_\eta(\sigma_h, \dot{H}_h^{\text{in}}, T). \quad (4.8)$$

Once Eq. (4.8) has been solved with respect to the volume fraction of the hard phase, the volume fraction of the soft phase is computed by means of Eq. (4.3). In order to reduce the number of equations, Eqs. (4.1) and (4.4) are inserted into Eq. (4.5) such that one obtains:

$$\sigma_k = E (H - H_k^{\text{in}}). \quad (4.9)$$

In a similar procedure, Eqs. (4.9) and (4.3) are inserted into Eq. (4.2):

$$\sigma = E (H - H^{\text{in}}), \quad (4.10)$$

$$H^{\text{in}} \equiv (1 - \eta_h) H_s^{\text{in}} + \eta_h H_h^{\text{in}}, \quad (4.11)$$

where H^{in} denotes the inelastic strain of the mixture. Equations (4.3)–(4.11) and additional BCs and ICs determine the phase mixture model, which is physically motivated by the microstructural processes taking place at the subgrain level. The presented model can be used to simulate the material response under uniaxial loads. However, the model in the present form is closely related to the microstructure, and the material parameters are usually identified with data concerning the microstructural evolution, cf. for example [13, 19]. Nevertheless, in the thesis at hand, the results of *macroscopic* tests – presented in Chapt. 3 – should be used, and therefore Eqs. (4.3)–(4.11) have to be transformed in order to obtain

4 One-Dimensional Phase Mixture Model

a model based on internal variables. In this way, the response functions and the material parameters can be identified based on the data from macroscopic tests only, cf. [42].

As a first step, the evolution equations in Eq. (4.7) are specified. In [42, 71], the following expressions for the inelastic strain rates \dot{H}_k^{in} are suggested:

$$\dot{H}_s^{\text{in}} = \text{sgn}(\sigma_s) f_\sigma(|\sigma_s|) f_T(T), \quad (4.12)$$

$$\dot{H}_h^{\text{in}} = \frac{\sigma_h - \sigma}{|\sigma_{h^*} - \sigma|} |\dot{H}^{\text{in}}|. \quad (4.13)$$

Here, $f_\sigma(|\sigma_s|)$ and $f_T(T)$ denote the stress and temperature response functions, while σ_{h^*} is the saturation stress. Note that the phase mixture model does not include necking effects or damage such that it predicts a stationary state for the macroscopic variables. All variables with respect to the saturation state are marked with the index \square_* . After a spontaneous loading in the elastic range, the stresses are equal ($\sigma = \sigma_h = \sigma_s$) since the elastic properties are identical. Due to this behavior, the initial inelastic strain rate \dot{H}_h^{in} is zero in the elastic range. If the load is increased beyond the elastic range, the stress in the hard phase approaches the saturation stress $\sigma_h \rightarrow \sigma_{h^*}$, and the inelastic strain rate in the hard phase is approximately equal to the absolute value of the inelastic strain rate of the mixture $\dot{H}_h^{\text{in}} \approx |\dot{H}^{\text{in}}|$. Then, the stresses in both phases approach the corresponding saturation values [42].

For the transformation of the phase mixture model and an efficient way to identify the material parameters, the new internal variables β and Γ are introduced:

$$\beta = \frac{\eta_{h_0}}{1 - \eta_{h_0}} (\sigma_h - \sigma) \quad \forall \quad 0 < \eta_{h_0} < 1, \quad 0 \leq \beta \leq \beta_*, \quad (4.14)$$

$$\Gamma = \frac{\eta_h}{1 - \eta_h} \frac{1 - \eta_{h_0}}{\eta_{h_0}} \quad \forall \quad \Gamma_* \leq \Gamma \leq 1 \quad (4.15)$$

with their corresponding saturation values:

$$\beta_* = \frac{\eta_{h_0}}{1 - \eta_{h_0}} |\sigma_{h^*} - \sigma|, \quad (4.16)$$

$$\Gamma_* = \frac{\eta_{h^*}}{1 - \eta_{h^*}} \frac{1 - \eta_{h_0}}{\eta_{h_0}} \quad \forall \quad 0 < \eta_{h^*} < 1. \quad (4.17)$$

In [42], it is shown that the variable β can be interpreted as a backstress similar to the backstress introduced by ARMSTRONG and FREDERICK [49]. The internal variable Γ is related to the volume fraction η_h of the hard phase, which is assumed to decrease during the deformation in order to describe the softening processes. For this reason, Γ is referred to as “softening variable”. The variable η_{h_0} represents the volume fraction of the hard phase in the initial state, i.e. $\eta_{h_0} = \eta_h(t=0)$ and is determined by fitting the model to the experimental data. Keeping in mind the definition of η_{h_0} , $\Gamma(t=0) = 1$ holds in the initial state. With increasing deformation, the volume fraction of the hard phase decreases until the saturation value η_{h^*} is reached, i.e. $\eta_h(t \rightarrow \infty) \rightarrow \eta_{h^*}$.

To implement the backstress and the softening variable into the governing equations of the phase mixture model, the definitions (4.14)–(4.17) and the Eqs. (4.2), (4.12), and (4.13) are used to evaluate the stresses and the inelastic strain rates of both phases depending on the introduced internal variables:

$$\sigma_h = \sigma + \frac{1 - \eta_{h_0}}{\eta_{h_0}} \beta, \quad (4.18)$$

$$\sigma_s = \sigma - \Gamma\beta, \quad (4.19)$$

$$\dot{H}_h^{\text{in}} = \frac{\beta}{\beta_\star} |\dot{H}^{\text{in}}|, \quad (4.20)$$

$$\dot{H}_s^{\text{in}} = \text{sgn}(\sigma - \Gamma\beta) f_\sigma(|\sigma - \Gamma\beta|) f_T(T). \quad (4.21)$$

Afterwards, Eq. (4.10) is differentiated once with respect to time and transformed such that one obtains:

$$\dot{H}^{\text{in}} = \dot{H} - \frac{\partial}{\partial t} \left(\frac{\sigma}{E} \right). \quad (4.22)$$

In addition, Eq. (4.9), which refers to the individual phases, is processed analogously:

$$\dot{H} = \frac{\partial}{\partial t} \left(\frac{\sigma_k}{E} \right) + \dot{H}_k^{\text{in}}. \quad (4.23)$$

Equation (4.23) is first evaluated for the soft phase and inserted into Eq. (4.22). Furthermore, the stress σ_s and the inelastic strain rate \dot{H}_s^{in} are replaced by Eqs. (4.19) and (4.21), respectively. After simple transformations, this results in the following evolution equation with respect to the inelastic strain H^{in} , compare to Eq. (2.55):

$$\dot{H}^{\text{in}} = \text{sgn}(\sigma - \Gamma\beta) f_\sigma(|\sigma - \Gamma\beta|) f_T(T) - \frac{\partial}{\partial t} \left(\frac{\Gamma\beta}{E} \right). \quad (4.24)$$

The last term in Eq. (4.24) influences the inelastic strain rate only at the very beginning of the inelastic deformation [42], and consequently it is omitted to simplify the resulting system of equations:

$$\dot{H}^{\text{in}} = \text{sgn}(\sigma - \Gamma\beta) f_\sigma(|\sigma - \Gamma\beta|) f_T(T). \quad (4.25)$$

In a next step, the procedure is repeated for the hard phase: Equation (4.23) is evaluated for the hard phase and inserted into Eq. (4.22). The stress σ_h and the inelastic strain rate \dot{H}_h^{in} are replaced by Eqs. (4.18) and (4.20). As a result, one obtains an evolution equation for the backstress β :

$$\dot{\beta} = \frac{1}{E} \frac{dE}{dT} \dot{T} \beta + E \frac{\eta_{h_0}}{1 - \eta_{h_0}} \left(\dot{H}^{\text{in}} - \frac{\beta}{\beta_\star} |\dot{H}^{\text{in}}| \right). \quad (4.26)$$

Now, only an evolution equation for the softening variable Γ is still required. As pointed out before, Γ is closely connected to the volume fraction of the hard phase η_h , and therefore the evolution equation for Γ is used to replace Eq. (4.8). In agreement with [42], the following evolution equation is used:

$$\dot{\Gamma} = C_\Gamma (\Gamma_\star - \Gamma) |\dot{H}^{\text{in}}|, \quad (4.27)$$

where C_Γ is a material parameter. Note that the evolution equation (4.27) is only applicable to proportional loading. In the case of nonproportional loading, refined approaches must be applied, e.g. [127]. As can be seen, one obtains a system of three evolution equations with respect to the inelastic strain, the backstress, and the softening variable, cf. Eqs. (4.25)–(4.27).

In order to explain the meaning of the parameters and the functions in the model, the governing equations are evaluated for a creep test. Therefore, we assume that the temperature and

4 One-Dimensional Phase Mixture Model

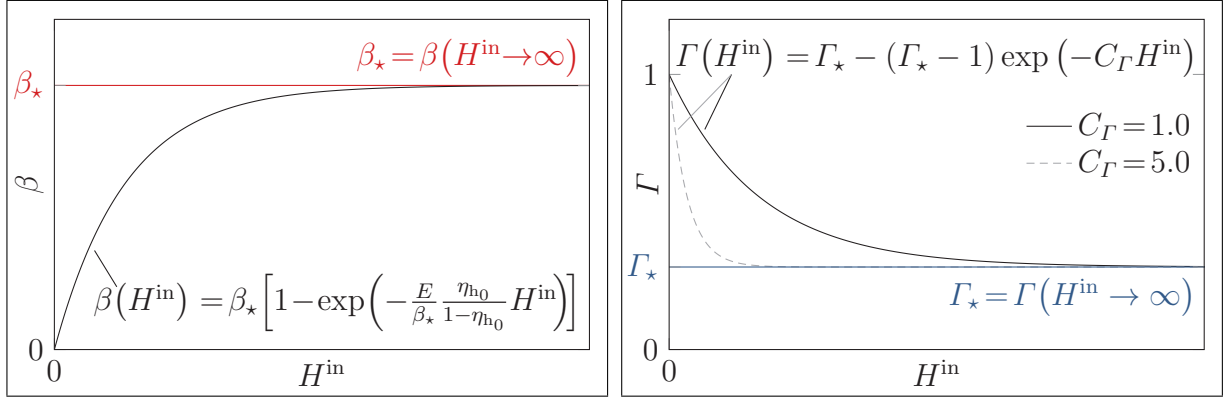


Figure 4.3: Backstress β (left) and softening variable Γ (right) vs inelastic strain H^{in} in a creep test at stationary stress and temperature.

the stress are stationary, i.e. $\dot{T} = 0$ and $\dot{\sigma} = 0$. Furthermore, only tensile stresses $\sigma > 0$ are taken into account. With these assumptions, Eqs. (4.25)–(4.27) can be simplified as follows:

$$\dot{H}^{\text{in}} = f_\sigma(\sigma - \Gamma\beta) f_T(T), \quad (4.28)$$

$$\dot{\beta} = E \frac{\eta_{\text{h0}}}{1 - \eta_{\text{h0}}} \left(1 - \frac{\beta}{\beta_*} \right) \dot{H}^{\text{in}}, \quad (4.29)$$

$$\dot{\Gamma} = C_\Gamma (\Gamma_* - \Gamma) \dot{H}^{\text{in}}. \quad (4.30)$$

In the case of stationary stress and temperature values, both the YOUNG'S modulus and the saturation values β_* and Γ_* do not change with time either. For these reasons, Eqs. (4.29) and (4.30) can be solved analytically using the method of separation of variables. Taking the following ICs $\beta(H^{\text{in}} = 0) = 0$ and $\Gamma(H^{\text{in}} = 0) = 1$ into account, we arrive at:

$$\beta(H^{\text{in}}) = \beta_* \left[1 - \exp\left(-\frac{E}{\beta_*} \frac{\eta_{\text{h0}}}{1 - \eta_{\text{h0}}} H^{\text{in}}\right) \right], \quad (4.31)$$

$$\Gamma(H^{\text{in}}) = \Gamma_* - (\Gamma_* - 1) \exp(-C_\Gamma H^{\text{in}}). \quad (4.32)$$

Finally, Eqs. (4.31) and (4.32) are inserted into Eq. (4.28):

$$\dot{H}^{\text{in}} = f_\sigma[\sigma - \Gamma(H^{\text{in}})\beta(H^{\text{in}})] f_T(T) = f(H^{\text{in}}, \sigma, T). \quad (4.33)$$

Equation (4.33) can be solved analytically or numerically depending on the chosen functions f_σ and f_T such that one obtains the inelastic strain as a function of time. For the simulation of a creep test under prescribed stationary stress $\sigma > 0$ and temperature T , Fig. 4.3 depicts the backstress and the softening variable with respect to the inelastic strain, based on Eqs. (4.31) and (4.32). The diagram on the left-hand side demonstrates that the backstress β increases towards its saturation value β_* with increasing strain. In contrast, the softening variable Γ decreases towards its saturation value Γ_* with increasing strain, as can be seen on the diagram on the right-hand side. Here, two curves are shown with respect to two exemplary values of the parameter $C_\Gamma \in \{1.0, 5.0\}$. This parameter controls the decrease of Γ , i.e. the intensity of the softening effect: for higher values of C_Γ , the saturation state is reached at lower inelastic strains H^{in} . For infinite strains, i.e. $H^{\text{in}} \rightarrow \infty$, the mixture is in a saturation state, thus $\beta = \beta_*$, $\Gamma = \Gamma_*$, and $\dot{H}^{\text{in}} = f_\sigma(\sigma - \Gamma_*\beta_*) f_T(T)$.

4.2 Calibration

In the previous section, the phase mixture model has been introduced. This section focuses on the calibration of the model by means of the experimental results (cf. Chapt. 3) and additional data published in the literature. Note that the remainder of this section is based on [128]. The response functions $f_E(T)$, $f_\sigma(|\sigma|)$, $f_T(T)$ as well as the parameters β_* , η_{h_0} , Γ_* , C_T are determined based on the following set of macroscopic material tests:

- HT tensile tests under constant engineering strain rates $\dot{\varepsilon} \approx \{5 \times 10^{-5} \text{ s}^{-1}, 1 \times 10^{-4} \text{ s}^{-1}, 1 \times 10^{-3} \text{ s}^{-1}\}$ at the temperature levels $T = \{673 \text{ K}, 723 \text{ K}, \dots, 923 \text{ K}\}$, cf. Sect. 3.1,
- creep tests at constant PIOLA-KIRCHHOFF stress $P = \{100 \text{ MPa}, 150 \text{ MPa}\}$ at a temperature of $T = 873 \text{ K}$, cf. Sect. 3.2,
- creep tests at a temperature of 873 K and constant CAUCHY stress levels $\sigma = \{150 \text{ MPa}, 175 \text{ MPa}, 185 \text{ MPa}, 196 \text{ MPa}\}$ from [13],
- data from creep tests, i.e. the minimum creep rates and the corresponding stress levels, at the temperature levels $T = \{773 \text{ K}, 823 \text{ K}, 873 \text{ K}\}$ from [13].

The measurement campaign has been executed using a large number of specimens made of the alloy X20CrMoV12-1. In order to enlarge the database for the calibration, additional results of creep tests with the same alloy from [13] are taken into account.

4.2.1 Elasticity

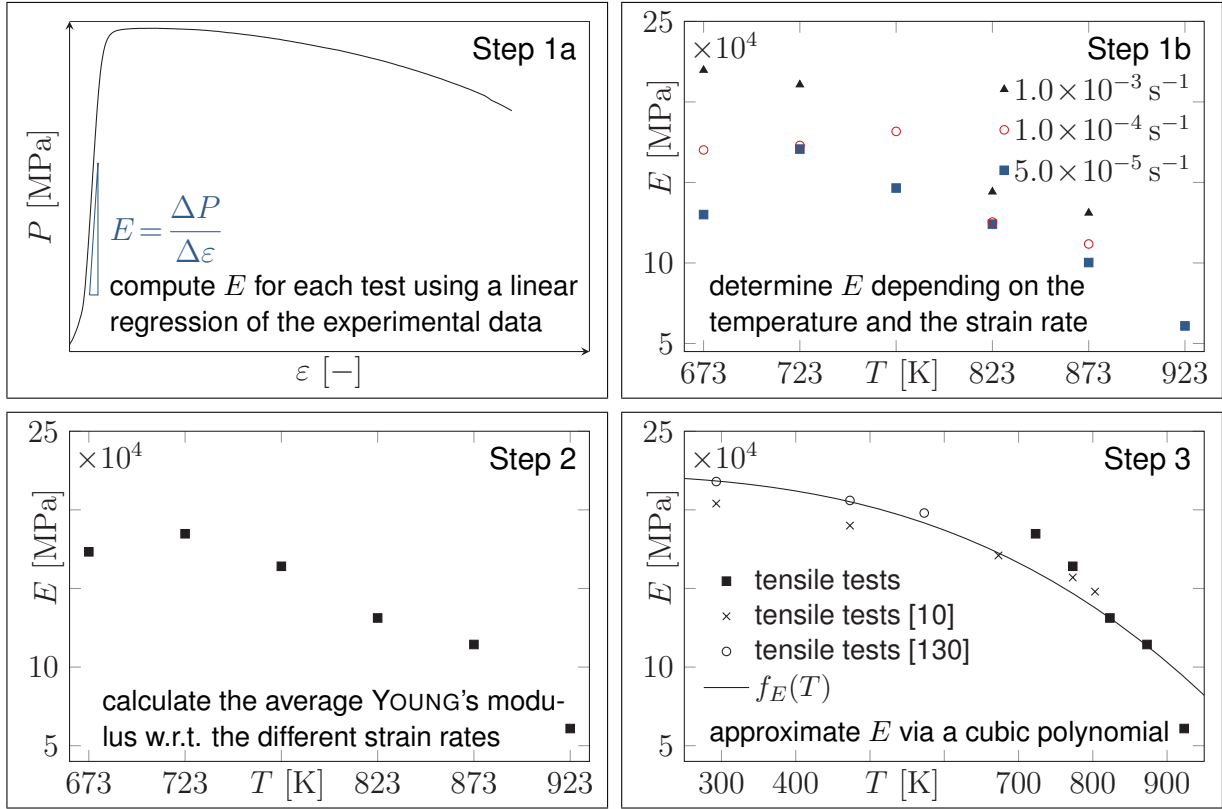
The experimental results for the YOUNG's modulus have already been presented in Fig. 3.3. Figure 4.4 explains the processing of the experimental data in order to find the temperature response function $f_E(T)$ for the YOUNG's modulus, cf. Eq. (4.6). In the first step, cf. the top left diagram in Fig. 4.4, the YOUNG's modulus is determined by a linear regression of the experimental data in the elastic range, i.e. for small strains $\varepsilon \leq 0.2\%$. Due to the scatter of the data and in order to obtain reliable results, the strain interval for the determination of the YOUNG's modulus must be readjusted manually for every test. As a result of this first step, one obtains the YOUNG's modulus depending on the temperature and the strain rate, cf. the top right diagram in Fig. 4.4. The strain rate dependence of the YOUNG's modulus has already been discussed in Sect. 3.1.3.1. Nevertheless in the phase mixture model, it is assumed that the YOUNG's modulus does not depend on the strain rate. For this reason, the YOUNG's modulus is averaged with respect to the strain rate for each specific temperature in Step 2, cf. the bottom left diagram in Fig. 4.4. Note that the decrease of the YOUNG's modulus at the temperature 673 K in comparison to the value at 723 K is considered as nonphysical. This effect is attributed to the very high tensile forces at 673 K, which approach the maximum force of the testing frame, resulting in a high experimental scatter at this temperature, see also the discussion in Sect. 3.1.3.1. For this reason, the value for the YOUNG's modulus at 673 K is not taken into account during the approximation in the next step.

In the last step (bottom right diagram of Fig. 4.4), the temperature dependence of the YOUNG's modulus is approximated by a cubic polynomial. This ansatz was successfully applied for cast irons in [129]:

$$f_E(T) = C_1 + C_2 T^3 \quad (4.34)$$

with the fitting parameters:

$$C_1 = 2.23 \times 10^5 \text{ MPa}, \quad C_2 = -1.64 \times 10^{-4} \text{ MPa K}^{-3}. \quad (4.35)$$


 Figure 4.4: Calibration of the temperature response function for the YOUNG's modulus E .

In order to extend the database to lower temperatures, additional experimental values for the YOUNG's modulus are taken into account [10, 130], cf. the bottom right diagram of Fig. 4.4.

4.2.2 Initial and Steady State

In the following sections, the calibration procedure with respect to the inelastic material behavior and hardening as well as softening is described. This calibration is based on the discrimination between an initial and a steady state, which are introduced in this section. A similar identification procedure by means of an initial and a steady state can be found in [131]. In the following, the subscripts \square_{init} and \square_{st} denote variables with respect to the initial and the steady state, respectively. Figure 4.5 illustrates the identification of the stresses and strain rates in both states for a HT tensile test and a creep test. For the tensile tests, the initial stress σ_{init} is defined as the stress at the beginning of the inelastic deformation, i.e. $\sigma_{\text{init}} = \sigma(H^{\text{in}} = 0)$. In analogy, the initial strain rate $\dot{H}_{\text{init}}^{\text{in}}$ is the strain rate at the beginning of the inelastic deformation, thus $\dot{H}_{\text{init}}^{\text{in}} = \dot{H}^{\text{in}}(H^{\text{in}} = 0)$. The steady state in the HT tensile tests refers to the maximum stress σ_{max} , i.e. $\sigma_{\text{st}} = \sigma_{\text{max}}$. This is due to the fact that the stress is approximately equal to the maximum stress level over a wide strain range in many measured stress-strain curves, cf. Fig. 3.4. The steady inelastic strain rate is the inelastic strain rate with respect to the lowest inelastic strain corresponding to the maximum stress level: $\dot{H}_{\text{st}}^{\text{in}} = \dot{H}^{\text{in}}(H^{\text{in}} = H_{\text{st}}^{\text{in}})$, cf. the top diagram in Fig. 4.5.

During the creep tests, cf. Sect. 3.2, the PIOLA-KIRCHHOFF stress P is prescribed as a constant value. At the beginning of the deformation, the differences between the PIOLA-KIRCHHOFF stress and the CAUCHY stress are negligible such that the initial stress equals the PIOLA-KIRCHHOFF stress, i.e. $\sigma_{\text{init}} = P$. Due to the testing conditions, the initial inelastic strain rate $\dot{H}_{\text{init}}^{\text{in}} = \dot{H}^{\text{in}}(H^{\text{in}} = 0)$ cannot be read from the creep curve directly, cf. the bottom diagram

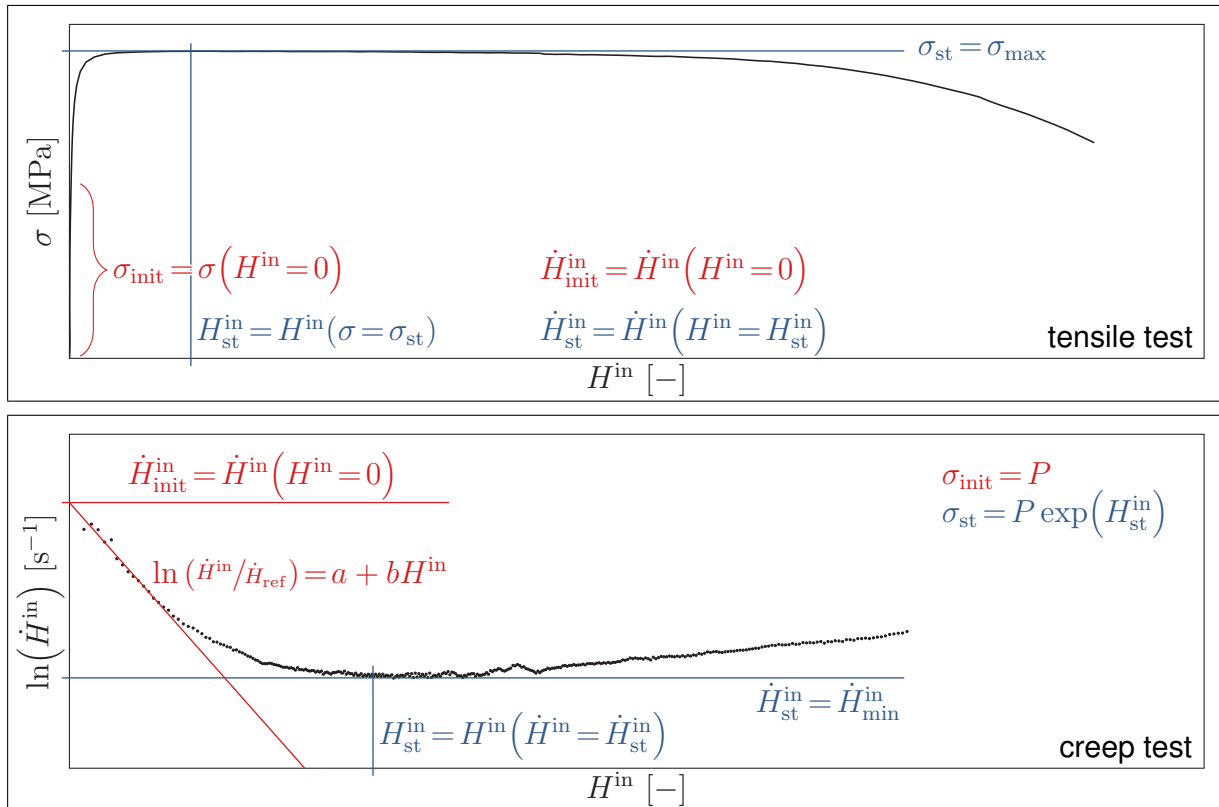


Figure 4.5: Extraction of initial and steady stresses and strain rates from experimental data.

in Fig. 4.5. Instead, in the beginning of the deformation, the creep curve is approximated with the tangent $\ln(\dot{H}^{\text{in}}/\dot{H}_{\text{ref}}) = a + bH^{\text{in}}$. Here, the index \square_{ref} denotes reference values. The initial inelastic strain rate is determined as the intersection of the tangent and the ordinate. The steady inelastic strain rate $\dot{H}_{\text{st}}^{\text{in}}$ equals the minimum strain rate $\dot{H}_{\text{min}}^{\text{in}}$, whereas the steady stress $\sigma_{\text{st}} = P \exp(H_{\text{st}}^{\text{in}})$ is approximated based on the PIOLA-KIRCHHOFF stress by inserting Eq. (2.20) into Eq. (2.35), thus taking the changes in the cross-section into account.

In order to determine the strain rates and the stresses in the initial and the steady state, the procedure described in this section is applied to all material tests used for the calibration, cf. the list at the beginning of Sect. 4.2. These data sets form the basis for the subsequent calibration of the inelastic material behavior.

4.2.3 Inelasticity

The main goal of this section is to find adequate stress and temperature response functions $f_{\sigma}(|\sigma|)$ and $f_T(T)$ for the inelastic strain rate \dot{H}^{in} , cf. Eq. (4.25). In the initial state, the influence of the hardening and softening processes is negligible because these microstructural processes require some time to develop. Therefore, Eq. (4.25) is simplified in the initial state considering $\Gamma = 1$ and $\beta = 0$:

$$\dot{H}_{\text{init}}^{\text{in}} = f_{\sigma_{\text{init}}}(\sigma) f_T(T). \quad (4.36)$$

Since only tensile tests are used for the calibration of the model, $|\sigma| = \sigma$ holds. In a first step, the temperature response function $f_T(T)$ is determined. In the current thesis, we make use of the well-known ARRHENIUS function, which is often applied to model creep deformations

4 One-Dimensional Phase Mixture Model

in martensitic steels [71, 83, 84, 132]:

$$f_T(T) = \exp\left(-\frac{Q}{RT}\right), \quad (4.37)$$

where $R \approx 8.31696 \text{ J (mol K)}^{-1}$ is the universal gas constant [133]. The variable Q is usually referred to as “activation energy” [84] and it is determined by fitting the experimental data with Eq. (4.37). For this purpose, two tensile tests (in the following referred to as “Tests a and b”) are chosen such that the stresses in the initial state are approximately equal ($\sigma_{\text{init}_a} \approx \sigma_{\text{init}_b}$), whereas the temperatures differ ($T_a \neq T_b$). Now, Eq. (4.36) is evaluated for both tests:

$$\dot{H}_{\text{init}_a}^{\text{in}} = f_\sigma(\sigma_{\text{init}_a}) f_T(T_a), \quad (4.38)$$

$$\dot{H}_{\text{init}_b}^{\text{in}} = f_\sigma(\sigma_{\text{init}_b}) f_T(T_b). \quad (4.39)$$

Afterwards, Eq. (4.38) is divided by Eq. (4.39) – keep in mind that $f_\sigma(\sigma_{\text{init}_a}) \approx f_\sigma(\sigma_{\text{init}_b})$ – and the temperature response function is substituted by Eq. (4.37) only. Using this approach, a reference value for Q is obtained:

$$Q_{\text{ref}} = R \frac{T_a - T_b}{T_a T_b} \ln\left(\frac{\dot{H}_{\text{init}_a}^{\text{in}}}{\dot{H}_{\text{init}_b}^{\text{in}}}\right) \approx 350.3 \times 10^3 \text{ J mol}^{-1}. \quad (4.40)$$

Equation (4.40) provides a starting point for the determination of Q . In a next step, the normalized inelastic strain rates are defined with respect to the initial and the steady state:

$$\bar{\dot{H}}_i^{\text{in}}(\sigma_i) = \frac{\dot{H}_i^{\text{in}}(\sigma_i, T)}{f_T(T)} = f_{\sigma_i}(\sigma_i) \quad \forall i \in \{\text{st, init}\}. \quad (4.41)$$

We make use of a bar $\bar{\square}$ to denote the normalized values. Note that in the remainder of this chapter the index \square_i represents variables with respect to the initial or the steady state. Although hardening and softening processes take place in the steady state such that Eq. (4.36) is not valid anymore, the steady inelastic strain rates are also normalized using Eq. (4.41), thus providing an initial value for the calibration. Due to this normalization, the temperature dependence of the strain rates is eliminated such that the normalized inelastic strain rates only depend on the stress levels. Based on the starting value for Q given in Eq. (4.40), Q is varied manually in such a way that the dependence of the normalized inelastic strain rates on the stress becomes obvious. This procedure is explained by means of Fig. 4.6, which shows the normalized inelastic strain rates in the steady state with respect to the stress on a double logarithmic scale. The stress values are extracted from the experimental data with the procedure described in Sect. 4.2.2. In contrast, the normalized strain rates are obtained based on the inelastic strain rates extracted from the experimental data, which are divided by the temperature response function, cf. Eq. (4.41). Note that the large dimensions of the values on the ordinate are due to this normalization. The diagram on the left-hand side in Fig. 4.6 shows the normalized strain rates based on the normalization with the reference activation energy Q_{ref} , cf. Eq. (4.40). This normalization results in a large scatter of the normalized strain rates with respect to constant stress values. Since this scatter does not capture a realistic material behavior, the parameter Q is varied in order to reduce the scatter of the strain rates. The result of this variation is depicted in the diagram on the right-hand side of Fig. 4.6, in which the normalization of the strain rates is based on a parameter of $Q \approx 540.6 \times 10^3 \text{ J mol}^{-1}$. Compared to the left diagram, the scatter is significantly reduced, and

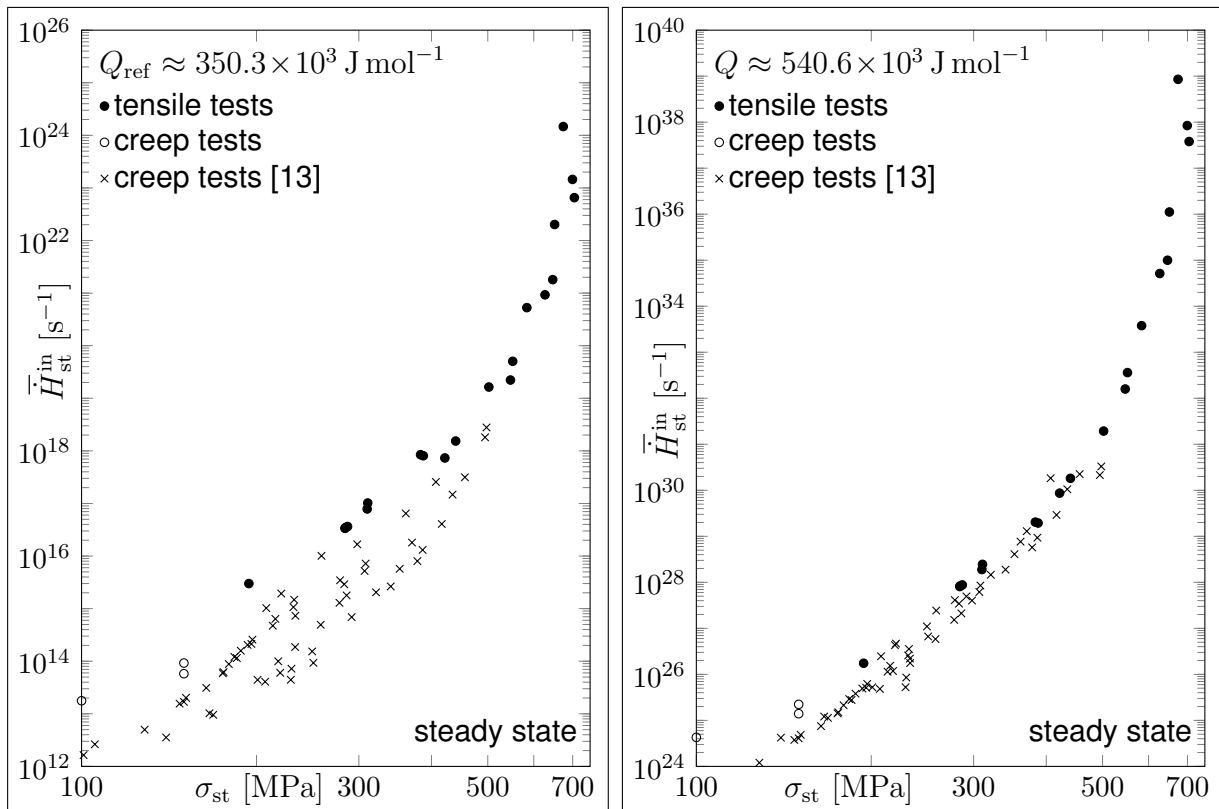


Figure 4.6: Inelastic normalized strain rate vs stress in initial and steady state. Normalization with respect to the reference value Q_{ref} (left) and with respect to an optimized value Q (right).

consequently the following calibration is based on the normalized strain rates with respect to this value for the parameter Q . For the sake of completeness, Fig. 4.7 depicts the normalized inelastic strain rates depending on the stresses with respect to the initial and the steady state as well.

In a next step, the stress response functions $f_{\sigma_i}(\sigma_i)$ are identified based on the dependence of the normalized inelastic strain rates on the stresses, cf. Fig. 4.7. For the stress response functions, many suggestions have been made [82, 84]. Most often, a power law function is used:

$$f_{\sigma}(\sigma) = a \left(\frac{\sigma}{b} \right)^m. \quad (4.42)$$

The parameter m is the power law exponent, which usually takes values between 3 and 7 [84]. However, many materials exhibit the so-called “power law breakdown”. This phenomenon describes the change of the exponent m with the stress [82], i.e. m rises as the stress increases [134–136]. In order to examine this phenomenon in detail, the diagram on the left-hand side of Fig. 4.8 depicts the normalized inelastic strain rate depending on the stress in the steady state. A power law function – cf. Eq. (4.42) – is used to approximate the experimental data in the low stress range, i.e. $\sigma_{\text{st}} < 500$ MPa. The diagram on the left-hand side clearly shows that one power law function is not able to fit the experimental data for high stresses $\sigma_{\text{st}} > 500$ MPa, which indicates that the alloy under consideration exhibits the power law breakdown. In contrast, the diagram on the right-hand side shows the results of the approximation with a piecewise power law. It becomes obvious that a piecewise function is able to account for the increase in the exponent m . Nevertheless, the transition from the

4 One-Dimensional Phase Mixture Model

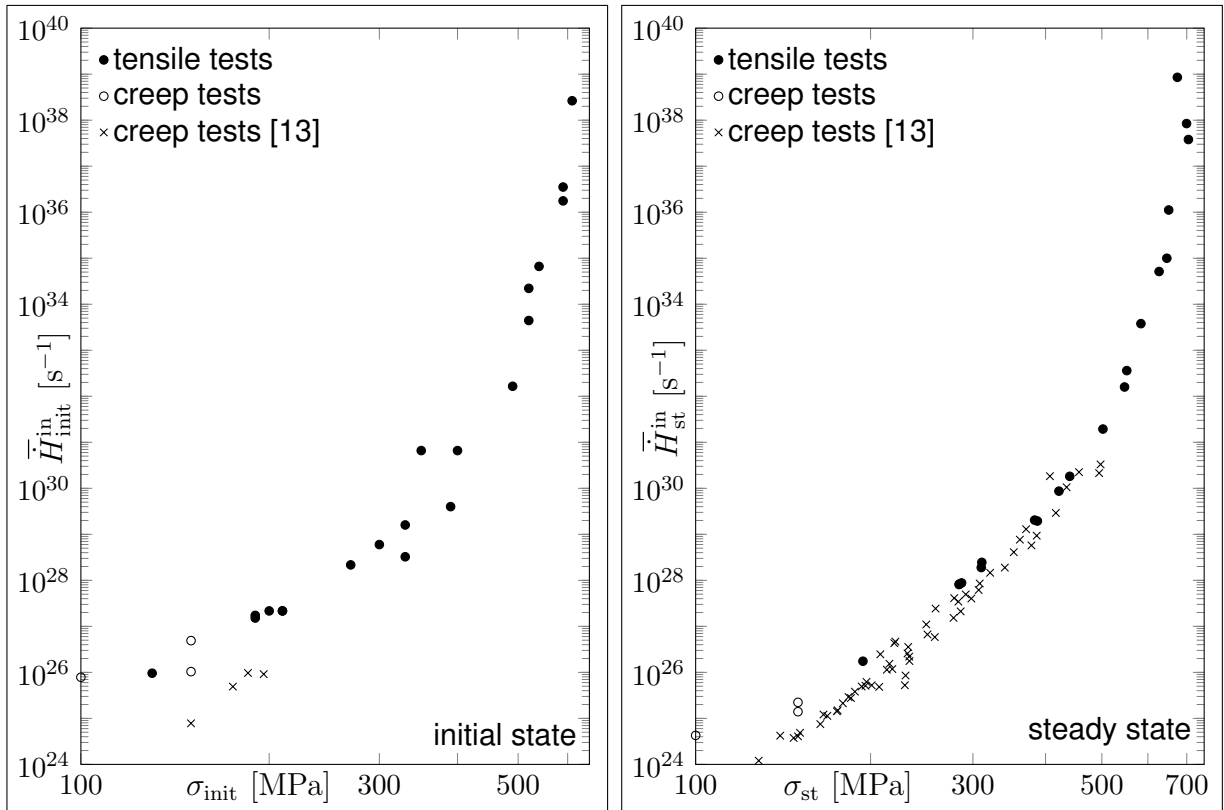


Figure 4.7: Inelastic normalized strain rate vs stress in the initial (left) and the steady state (right).

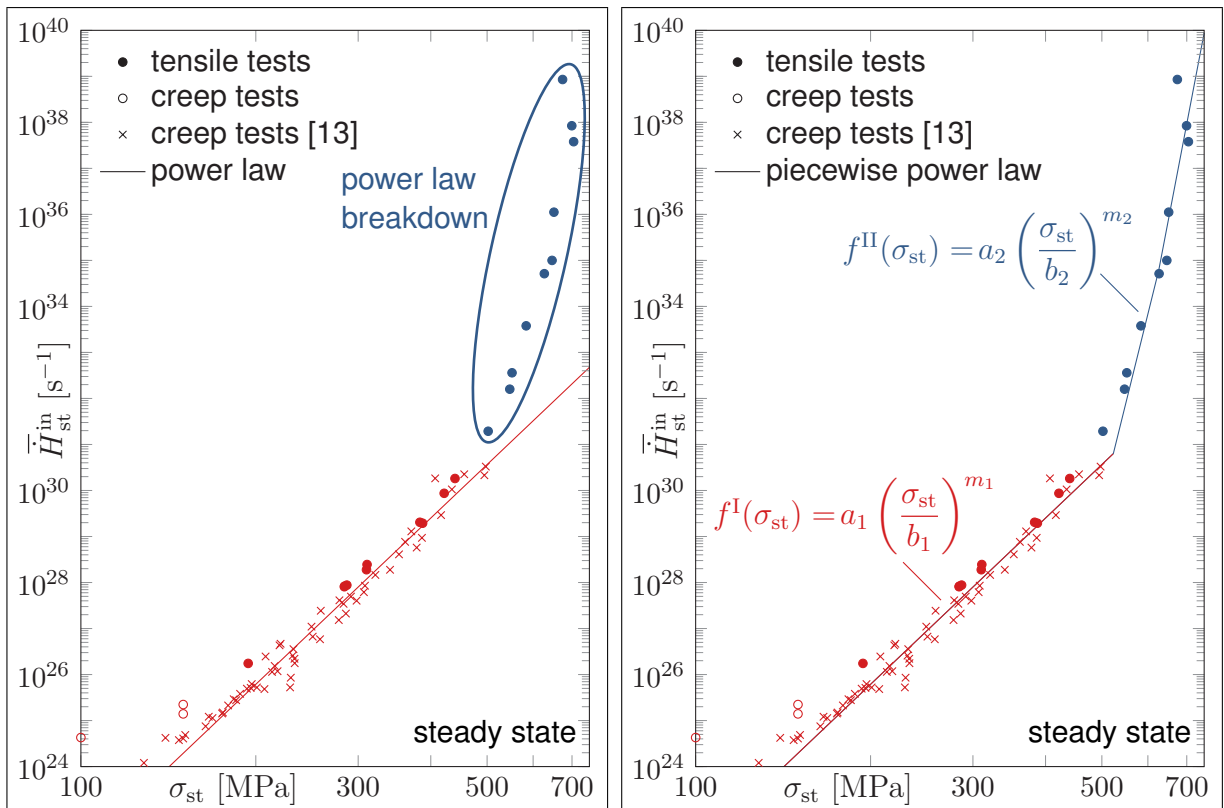


Figure 4.8: Inelastic normalized strain rate vs stress in the steady state. Power law breakdown (left) and approximations via power law functions (right).

function $f^I(\sigma_{st})$ used for low stresses to the second function $f^{II}(\sigma_{st})$ in the high stress regime is not smooth, i.e. the derivatives of the two stress response functions are not continuous. As a remedy to this phenomenon, the following stress response functions are suggested:

$$f_{\sigma_{i_j}}(\sigma) = \sqrt{\left[f_{i_j}^I(\sigma)\right]^2 + \left[f_{i_j}^{II}(\sigma)\right]^2} \quad \forall j \in \{1, 2, \dots, 9\}, i \in \{\text{st, init}\}, \quad (4.43)$$

where the index j is introduced since 9 different functions are examined in the thesis at hand. The function $f_{i_j}^I(\sigma)$ is valid for low stresses $\sigma < 500$ MPa, while the function $f_{i_j}^{II}(\sigma)$ describes the inelastic normalized strain rates with respect to higher stresses $\sigma \geq 500$ MPa. Adding the squares of both functions and computing the square root results in a smooth transition from the first function $f_{i_j}^I(\sigma)$ to the second function $f_{i_j}^{II}(\sigma)$. The current thesis takes 9 different stress response functions f_σ according to Eq. (4.43) into account, which are based on these 4 basis functions, cf. Table 4.1:

$$f_1(\sigma) = a_1 \left(\frac{\sigma}{b_1}\right)^m, \quad (4.44)$$

$$f_2(\sigma) = a_2 \exp\left(\frac{\sigma}{b_2}\right), \quad (4.45)$$

$$f_3(\sigma) = a_3 \sinh\left(\frac{\sigma}{b_3}\right), \quad (4.46)$$

$$f_4(\sigma) = a_4 \left[\sinh\left(\frac{\sigma}{b_4}\right)\right]^n. \quad (4.47)$$

The parameters a_l , b_l , m , and $n \forall l \in \{1, 2, \dots, 4\}$ are determined by approximating the experimental data. As already mentioned, power law functions, as the one given in Eq. (4.44), are employed for a wide variety of materials. However for higher stress levels, exponential functions provide a more accurate approximation of the experimental data [83, 137]. Therefore, Eq. (4.45) is taken into account when constructing a suitable stress response function. The main disadvantage of this ansatz is that a nonzero strain rate is computed even if no loads are applied, i.e. $\sigma = 0$. For this reason, the exponential function should not be used in the low stress regime. Instead, the hyperbolic function in Eq. (4.46) is recommended for small stresses in [83, 84]. Nevertheless, according to this function, the strain rate approaches zero in a linear function for small loads $\sigma \rightarrow 0$. This behavior contradicts the experimental findings [84], such that a combination of the power law function and the hyperbolic function is proposed as an alternative in [134], cf. Eq. (4.47). This function reduces to a power law function for small stresses and approaches the exponential form with increasing stress. Each function type has its specific advantages and drawbacks, and therefore a systematic investigation of all basis functions and chosen combinations thereof is needed. The functions $f_{\sigma_{i_j}} \forall j \in \{1, 2, 3, 4\}$ compiled in Table 4.1 deploy only one function type from Eqs. (4.44)–(4.47) with only one set of parameters in order to describe the whole stress interval. In addition, the functions $f_{\sigma_{i_j}} \forall j \in \{5, 6, 7, 8\}$ use the same functions with a different set of parameters for the low stress interval ($f_{i_j}^I$) and for the high stress interval ($f_{i_j}^{II}$). Furthermore, the following function is taken into account:

$$f_{\sigma_{i_9}}(\sigma) = a_i \sinh\left(\frac{\sigma}{b_i}\right) \left[1 + \left(\frac{\sigma}{c_i}\right)^{m_i}\right]. \quad (4.48)$$

This function approaches the hyperbolic sine function $f_{\sigma_{i_9}}(\sigma) \approx a_i \sinh(\sigma/b_i)$ for small stresses

Table 4.1: Stress response functions for the inelastic strain rate and material parameters.

j	$f_{i_j}^I(\sigma)$	$f_{i_j}^{II}(\sigma)$	initial ($i \equiv \text{init}$)	steady ($i \equiv \text{st}$)
1	$a_i \left(\frac{\sigma}{b_i}\right)^{m_i}$	0	$a_i = 4.75 \times 10^{16} \text{ s}^{-1}$ $b_i = 40.1 \text{ MPa}$ $m_i = 15.3$	$a_i = 6.59 \times 10^8 \text{ s}^{-1}$ $b_i = 12.5 \text{ MPa}$ $m_i = 14.3$
2	$a_i \exp\left(\frac{\sigma}{b_i}\right)$	0	$a_i = 1.89 \times 10^{22} \text{ s}^{-1}$ $b_i = 18.9 \text{ MPa}$	$a_i = 2.97 \times 10^{21} \text{ s}^{-1}$ $b_i = 20.5 \text{ MPa}$
3	$a_i \sinh\left(\frac{\sigma}{b_i}\right)$	0	$a_i = 3.79 \times 10^{22} \text{ s}^{-1}$ $b_i = 18.9 \text{ MPa}$	$a_i = 5.94 \times 10^{21} \text{ s}^{-1}$ $b_i = 20.5 \text{ MPa}$
4	$a_i \left[\sinh\left(\frac{\sigma}{b_i}\right)\right]^{m_i}$	0	$a_i = 5.09 \times 10^{21} \text{ s}^{-1}$ $b_i = 17.3 \text{ MPa}$ $m_i = 1.0$	$a_i = 6.76 \times 10^{24} \text{ s}^{-1}$ $b_i = 179.1 \text{ MPa}$ $m_i = 7.9$
5	$a_i \left(\frac{\sigma}{b_i}\right)^{m_i}$	$c_i \left(\frac{\sigma}{d_i}\right)^{n_i}$	$a_i = 2.35 \times 10^{12} \text{ s}^{-1}$ $b_i = 6.3 \text{ MPa}$ $c_i = 1.00 \times 10^{20} \text{ s}^{-1}$ $d_i = 450.6 \text{ MPa}$ $m_i = 9.9$ $n_i = 139.9$	$a_i = 1.00 \times 10^{20} \text{ s}^{-1}$ $b_i = 58.2 \text{ MPa}$ $c_i = 1.00 \times 10^{20} \text{ s}^{-1}$ $d_i = 383.2 \text{ MPa}$ $m_i = 11.4$ $n_i = 69.4$
6	$a_i \exp\left(\frac{\sigma}{b_i}\right)$	$c_i \exp\left(\frac{\sigma}{d_i}\right)$	$a_i = 2.36 \times 10^{23} \text{ s}^{-1}$ $b_i = 24.3 \text{ MPa}$ $c_i = 1.00 \times 10^0 \text{ s}^{-1}$ $d_i = 7.0 \text{ MPa}$	$a_i = 8.45 \times 10^{21} \text{ s}^{-1}$ $b_i = 22.4 \text{ MPa}$ $c_i = 5.56 \times 10^6 \text{ s}^{-1}$ $d_i = 9.7 \text{ MPa}$
7	$a_i \sinh\left(\frac{\sigma}{b_i}\right)$	$c_i \sinh\left(\frac{\sigma}{d_i}\right)$	$a_i = 4.71 \times 10^{23} \text{ s}^{-1}$ $b_i = 24.3 \text{ MPa}$ $c_i = 1.65 \times 10^{-7} \text{ s}^{-1}$ $d_i = 5.9 \text{ MPa}$	$a_i = 3.52 \times 10^{22} \text{ s}^{-1}$ $b_i = 23.7 \text{ MPa}$ $c_i = 8.97 \times 10^8 \text{ s}^{-1}$ $d_i = 10.3 \text{ MPa}$
8	$a_i \left[\sinh\left(\frac{\sigma}{b_i}\right)\right]^{m_i}$	$c_i \left[\sinh\left(\frac{\sigma}{d_i}\right)\right]^{n_i}$	$a_i = 1.36 \times 10^{23} \text{ s}^{-1}$ $b_i = 21.2 \text{ MPa}$ $c_i = 3.75 \times 10^2 \text{ s}^{-1}$ $d_i = 329.9 \text{ MPa}$ $m_i = 1.0$ $n_i = 73.0$	$a_i = 1.27 \times 10^{23} \text{ s}^{-1}$ $b_i = 85.0 \text{ MPa}$ $c_i = 3.92 \times 10^{23} \text{ s}^{-1}$ $d_i = 458.1 \text{ MPa}$ $m_i = 3.8$ $n_i = 42.7$
9	$a_i \sinh\left(\frac{\sigma}{b_i}\right) \left[1 + \left(\frac{\sigma}{c_i}\right)^{m_i}\right]$	0	$a_i = 1.54 \times 10^{24} \text{ s}^{-1}$ $b_i = 25.8 \text{ MPa}$ $c_i = 483.6 \text{ MPa}$ $m_i = 35.7$	$a_i = 1.30 \times 10^{22} \text{ s}^{-1}$ $b_i = 22.4 \text{ MPa}$ $c_i = 593.1 \text{ MPa}$ $m_i = 38.0$

$\sigma < c_i$. Obviously, one could construct several other combinations of the four functions in Eqs. (4.44)–(4.47) by means of Eq. (4.43). Nevertheless, for the sake of brevity, the considerations in the thesis at hand are restricted to the 9 functions in Table 4.1. In a first attempt, all functions in Table 4.1 are fitted manually to the experimental data. This procedure provides the initial solution for the succeeding optimization of the parameters with MATLAB's function `fmincon`. The basic optimization procedure is discussed in Sect. 2.3, and the objective function for this problem is derived from Eq. (4.41) and is given as follows:

$$g_{ij}(\mathbf{v}_{ij}) = \sum_{n=1}^{NP} \left\{ \ln \left[f_{\sigma_{ij}}(\sigma_{in}, \mathbf{v}_{ij}) \right] - \ln \left(\bar{H}_{in}^{\text{in}} \right) \right\}^2 \quad \forall j \in \{1, 2, \dots, 9\}, i \in \{\text{st}, \text{init}\}, \quad (4.49)$$

where NP is the number of the experimental data points and n the corresponding index for the data points. The vector of parameters \mathbf{v} is strongly dependent on the chosen stress response function $f_{\sigma_{ij}}$ and contains all fitting parameters. For example, the vector of parameters for the function $f_{\sigma_{\text{init}8}}$ has 6 entries, cf. also Table 4.1:

$$\mathbf{v}_{\text{init}8} = [a_{\text{init}} \quad b_{\text{init}} \quad c_{\text{init}} \quad d_{\text{init}} \quad m_{\text{init}} \quad n_{\text{init}}]^T. \quad (4.50)$$

Furthermore, the inequality and equality constraint vectors \mathbf{h}_{ij} and \mathbf{k}_{ij} must be defined, cf. Sect. 2.3. All parameters should be positive, cf. Eq. (4.51), while no equality constraints are defined, cf. Eq. (4.52). Thus, it holds:

$$\mathbf{h}_{ij}(\mathbf{v}_{ij}) = -\mathbf{v}_{ij}, \quad (4.51)$$

$$\mathbf{k}_{ij}(\mathbf{v}_{ij}) = \mathbf{0}. \quad (4.52)$$

Equations (4.49), (4.51), and (4.52) define the entire input for the optimization using MATLAB. Table 4.1 summarizes the stress response functions and the parameters found during the optimization procedure, and Fig. 4.9 depicts the normalized inelastic strain rates depending on the stresses with respect to the initial (left-hand side) and the steady state (right-hand side). The figure contains the results of all stress response functions under consideration. Furthermore, Figs. 4.10 and A2.1–A2.8 present the results of the optimization with respect to the normalized inelastic strain rates and the individual stress response functions, while the Figs. 4.11 and A2.9–A2.16 show the results for the inelastic strain rates depending on the stress for each stress response function. Here, one should keep in mind that the inelastic strain rates are easily obtained based on the normalized strain rates, which are multiplied with the temperature response function $f_T(T)$, cf. Eqs. (4.37) and (4.41). For the sake of a better readability, the majority of the figures is shifted to Appendix A2.

Figures 4.9, A2.1–A2.4, and A2.9–A2.12 demonstrate that the use of only one function, i.e. the function $f_{ij}^1(\sigma)$, based on Eqs. (4.44)–(4.47) is not sufficient to resolve the power law breakdown. Note that the decreasing slope of the power law function $f_{\sigma_{i_1}}(\sigma)$, cf. Figs. 4.9 and A2.1, is due to the fact that experimental results with respect to a very wide stress range (i.e. $100 \text{ MPa} \leq \sigma \leq 700 \text{ MPa}$) are taken into account. In case if only low stresses $\sigma < 500 \text{ MPa}$ are used for the identification of the parameters, a power law function is able to approximate the experimental data with high accuracy, cf. Fig. 4.8. The exponential function $f_{\sigma_{i_2}}(\sigma)$, the hyperbolic sine function $f_{\sigma_{i_3}}(\sigma)$, and the function $f_{\sigma_{i_4}}(\sigma)$ based on Eq. (4.47) result in straight lines in the logarithmic diagrams, cf. Figs. 4.9 and A2.2–A2.4, such that the power law breakdown is not accounted for.

The function $f_{\sigma_{i_5}}(\sigma)$ captures the power law breakdown, but yields nonphysical results for stresses $\sigma < 550 \text{ MPa}$, cf. Fig. A2.5. Additionally, several kinks are visible in the approximation

4 One-Dimensional Phase Mixture Model

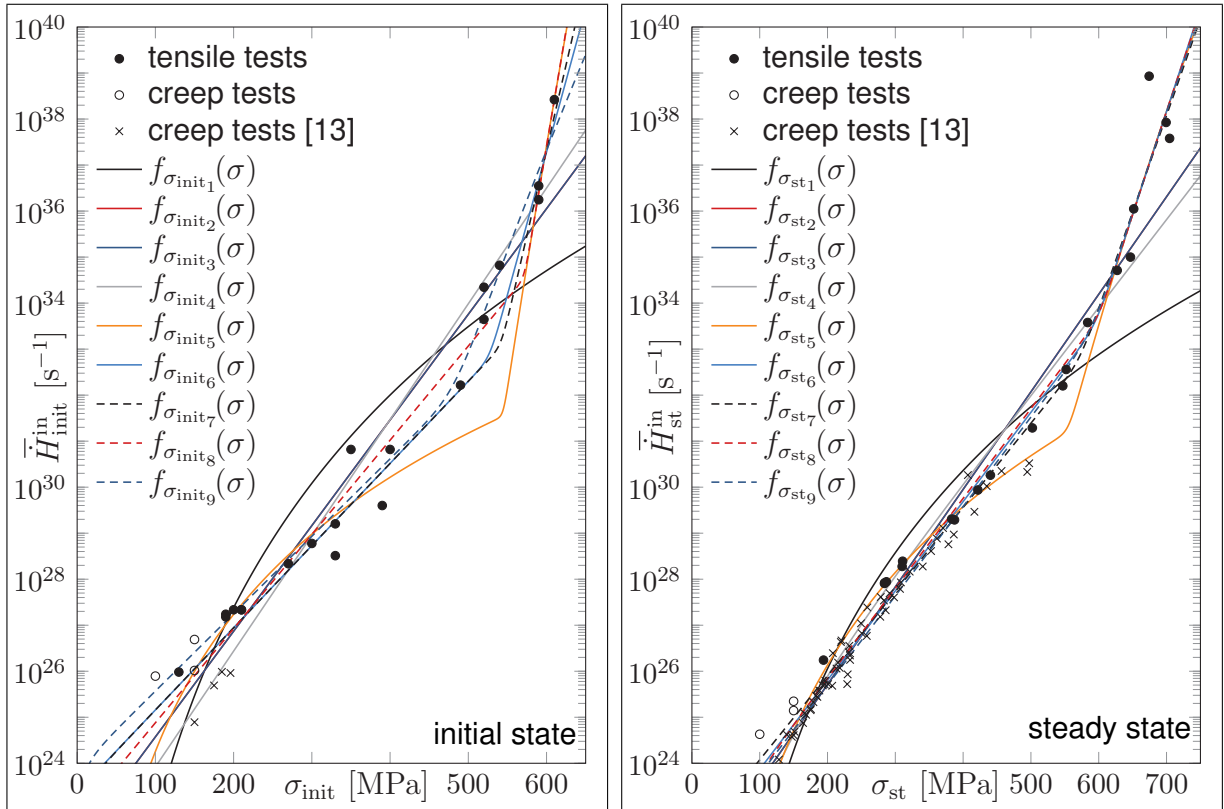


Figure 4.9: Approximation of the normalized inelastic strain rates with the response functions $f_{\sigma_{i_j}}(\sigma)$.

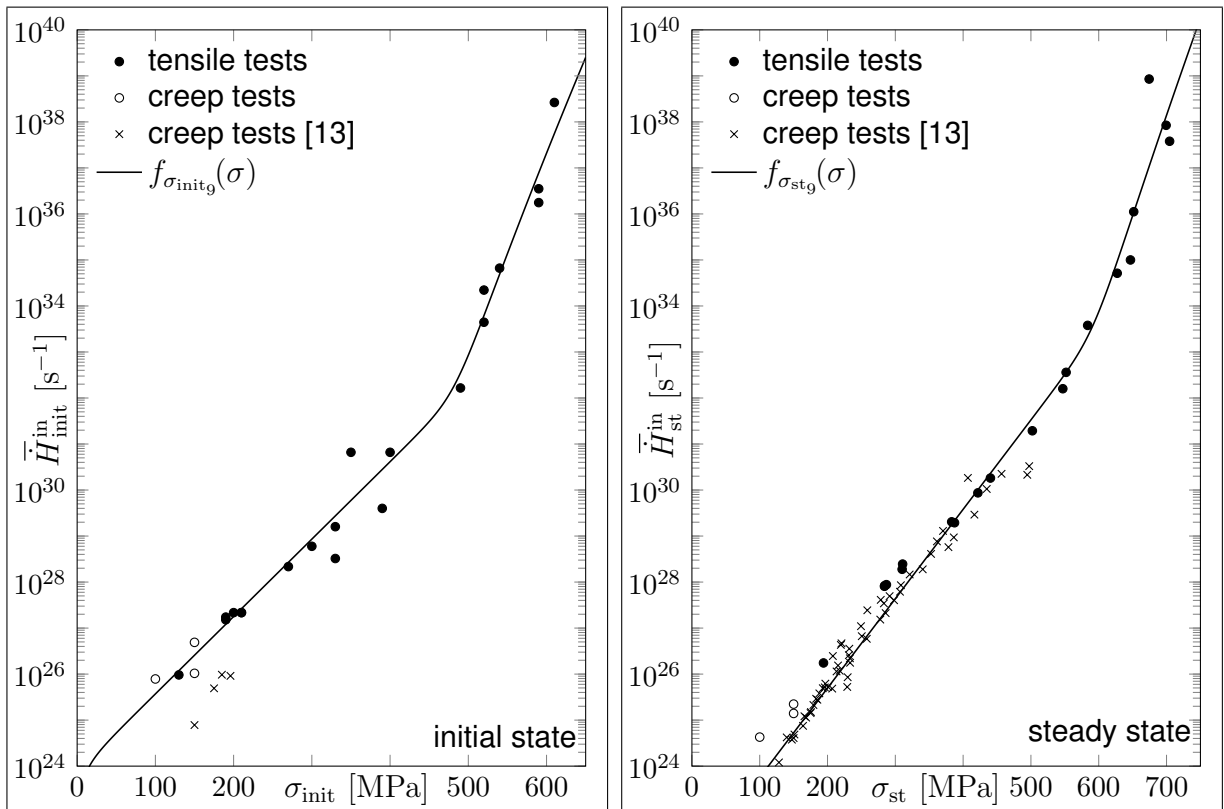


Figure 4.10: Approximation of the normalized inelastic strain rates with the response functions $f_{\sigma_{i_9}}(\sigma)$.

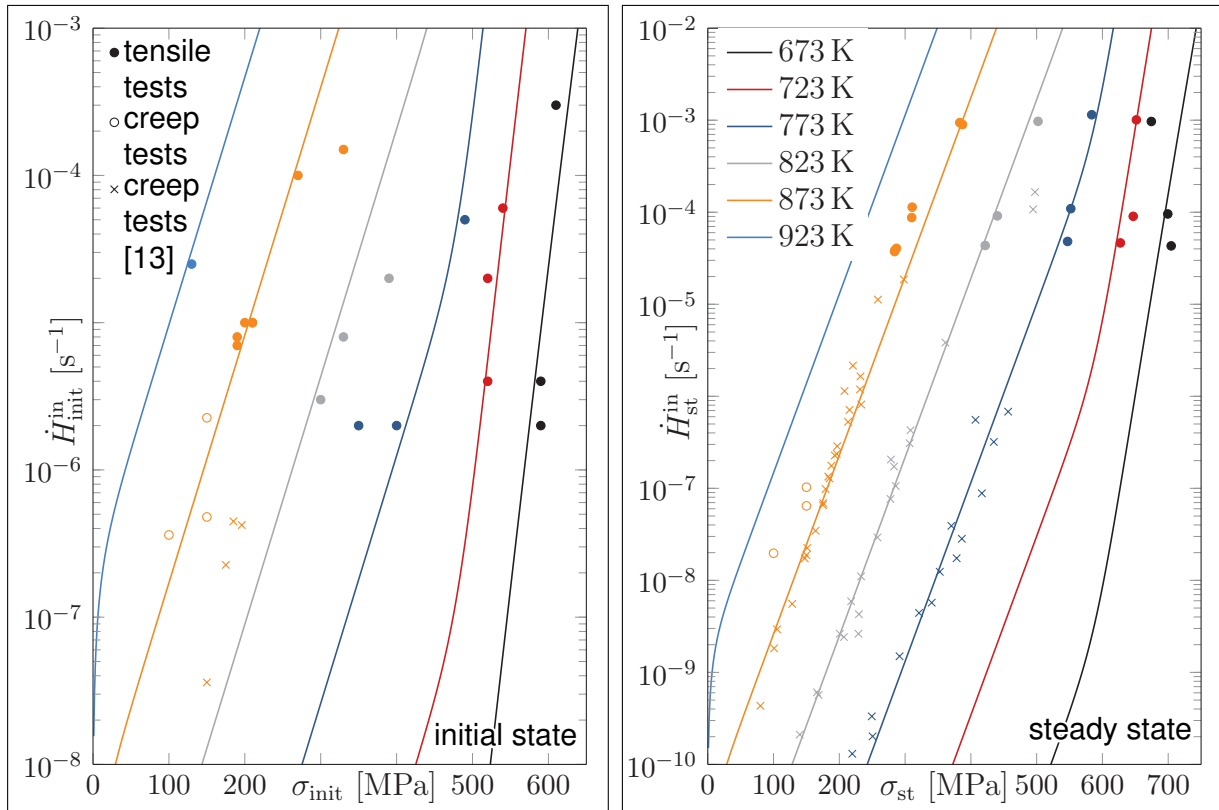


Figure 4.11: Approximation of the inelastic strain rates with the response functions $f_{\sigma_{i_9}}(\sigma)$.

of the inelastic strain rates for lower temperatures $T \leq 773$ K, cf. Fig. A2.13. In contrast, the functions $f_{\sigma_{i_j}}(\sigma) \forall j \in \{6, 7, 8, 9\}$ provide accurate approximations of the normalized strain rates in the initial and the steady state. Significant differences in the quality of the approximation cannot be observed, cf. Figs. 4.9–4.11, A2.6–A2.8, and A2.14–A2.16. Since the sixth function results in nonzero strain rates if no loads are applied, i.e. $f_{\sigma_{i_6}}(\sigma=0) \neq 0$, this function is not considered in the following. In contrast to the functions $f_{\sigma_{i_7}}(\sigma)$ and $f_{\sigma_{i_8}}(\sigma)$, which require two separate functions, one for the low and another for the high stress regime, cf. Eq. (4.43), the function $f_{\sigma_{i_9}}(\sigma)$ is based on one function to describe the entire stress range. Thus, due to its simplicity and the accuracy of the approximation, only this function type is taken into account for the calibration procedure. For the sake of brevity, the index i_9 is omitted in the remainder of the thesis at hand:

$$f_{\sigma_i}(\sigma) \equiv f_{\sigma_{i_9}} = a_i \sinh\left(\frac{\sigma}{b_i}\right) \left[1 + \left(\frac{\sigma}{c_i}\right)^{m_i}\right] \quad \forall i \in \{\text{st, init}\}. \quad (4.53)$$

4.2.4 Hardening

This section focuses on the calibration of the model with respect to the hardening behavior, which is ruled by the backstress β . As a starting point, we consider a state, where the softening processes do not take place and the stress does not change with respect to time:

$$\Gamma = 1, \quad (4.54)$$

$$\dot{\sigma} = 0. \quad (4.55)$$

4 One-Dimensional Phase Mixture Model

Due to these restrictions, only tensile tests with a constant stress level over a relatively wide strain range are taken into account for the calibration in the remainder of this section, i.e. the tensile tests at the lower strain rates $\dot{\epsilon} = \{5 \times 10^{-5} \text{ s}^{-1}, 1 \times 10^{-4} \text{ s}^{-1}\}$ and at the temperatures $T = \{723 \text{ K}, 773 \text{ K}, 823 \text{ K}\}$, cf. Fig. 3.4. The identification of the material parameters starts with the saturation backstress β_* , cf. Eq. (4.26). To this end, Eqs. (4.25) and (4.26) are simplified by inserting Eqs. (4.54) and (4.55). Additionally, it is assumed that the temperature does not vary with time, i.e. $\dot{T} = 0$ (stationary temperature):

$$\dot{H}^{\text{in}} = \text{sgn}(\sigma - \beta) f_{\sigma_{\text{init}}}(|\sigma - \beta|) f_T(T), \quad (4.56)$$

$$\dot{\beta} = E \frac{\eta_{\text{h}_0}}{1 - \eta_{\text{h}_0}} \left(\dot{H}^{\text{in}} - \frac{\beta}{\beta_*} |\dot{H}^{\text{in}}| \right). \quad (4.57)$$

Only tensile tests are used for the calibration, such that $\sigma > 0$ holds. Furthermore, we introduce the physically motivated constraint that the absolute value of the backstress is always smaller than the absolute stress value, i.e. $|\beta| < |\sigma|$. With these considerations, Eqs. (4.56) and (4.57) are further modified:

$$\dot{H}^{\text{in}} = f_{\sigma_{\text{init}}}(\sigma - \beta) f_T(T), \quad (4.58)$$

$$\dot{\beta} = E \frac{\eta_{\text{h}_0}}{1 - \eta_{\text{h}_0}} \left(1 - \frac{\beta}{\beta_*} \right) \dot{H}^{\text{in}}. \quad (4.59)$$

Because of the restrictions given in Eqs. (4.54) and (4.55), the backstress does not change with respect to time, i.e. $\dot{\beta} = 0$, such that Eq. (4.59) results in:

$$\beta = \beta_*. \quad (4.60)$$

In the absence of the softening effects, cf. Eq. (4.54), the normalized inelastic strain rate in the steady state can be determined either with the response function with respect to the initial state or with the corresponding function for the steady state:

$$\bar{H}_{\text{st}}^{\text{in}} = f_{\sigma_{\text{init}}}(\sigma - \beta) = f_{\sigma_{\text{st}}}(\sigma). \quad (4.61)$$

Transforming Eq. (4.61) under consideration of Eq. (4.60) yields an expression for the saturation backstress:

$$\beta_*(\sigma) = \sigma - f_{\sigma_{\text{init}}}^{-1}[f_{\sigma_{\text{st}}}(\sigma)]. \quad (4.62)$$

Due to the complexity of the stress response function in the initial state, cf. Eq. (4.53), its inverse $f_{\sigma_{\text{init}}}^{-1}$ is determined numerically. Equation (4.62) can be used to compute the saturation backstress. However, it must be ensured that the model accurately captures the physical behavior; that is to say, the following condition needs to be fulfilled:

$$\frac{\partial \beta_*}{\partial \sigma} \geq 0. \quad (4.63)$$

In the next step, Eq. (4.61) is differentiated with respect to the steady state stress, and additionally Eq. (4.60) is taken into account. The resulting expressions are thereafter inserted into Eq. (4.63) yielding:

$$\frac{\partial f_{\sigma_{\text{st}}}(\sigma)}{\partial \sigma} \leq \frac{\partial f_{\sigma_{\text{init}}}(\sigma - \beta_*)}{\partial (\sigma - \beta_*)}. \quad (4.64)$$

Thus, if an ansatz function for $\beta_*(\sigma)$ has already been found, Eq. (4.63) can be used to check its validity. Equation (4.64) is useful to check whether the found stress response functions $f_{\sigma_{\text{init}}}(\sigma)$ and $f_{\sigma_{\text{st}}}(\sigma)$ are able to provide physical results for $\beta_*(\sigma)$ – even before the saturation backstress is determined based on Eq. (4.62).

In the following, the saturation backstress is computed using Eq. (4.62) based on the calibrated stress response functions $f_{\sigma_{\text{st}}}(\sigma)$ and $f_{\sigma_{\text{init}}}(\sigma)$, cf. Eq. (4.53). In the top diagram of Fig 4.12, the obtained function $\beta_*(\sigma)$ is evaluated over a wide stress range. It becomes obvious that the function according to Eq. (4.62) is not monotonically increasing as required by Eq. (4.63). For this reason, it is checked whether Eq. (4.64) holds. Therefore, the bottom diagram of Fig. 4.12 depicts the derivatives of the stress response functions in the initial and the steady state depending on the stress. As the previous considerations suggest, Eq. (4.64) is not fulfilled over the *entire* stress range. Here, one should bear in mind that the fulfillment of Eq. (4.64) is highly sensitive with respect to the parameters in the stress response functions. A slight change in the calibration of the stress response functions can lead to strongly varying functions $\beta_*(\sigma)$, according to Eq. (4.62). Nevertheless, Eq. (4.62) still provides an initial guess, and the saturation backstress is approximated by means of a modified logistic function, cf. [138]:

$$\beta_*(\sigma) = \frac{2a_\beta}{1 + \exp(-b_\beta |\sigma|)} - a_\beta, \quad (4.65)$$

where $a_\beta = 80$ MPa is the maximum value, and the parameter $b_\beta = 2.7 \times 10^{-2}$ MPa⁻¹ controls the steepness of the curve. As can be seen in Fig. 4.12, the approximation function is nearly linear for low stresses $\sigma < 50$ MPa and approaches the saturation level $\beta_* = a_\beta$ for high stresses $\sigma > 200$ MPa. Note that the saturation backstress does not depend on the temperature since the same ARRHENIUS functions are used in the steady and the initial state, cf. Eq. (4.41).

In the next step, the reference value η_{h_0} for the volume fraction of the hard phase is determined. For the identification, the experimental data of the tensile tests including the elastic range and the hardening regime are taken into account. Aforementioned simplifications still hold such that the differential equations (4.58) and (4.59) are solved numerically with MATLAB's solver `ode45`, which is based on an explicit RUNGE-KUTTA method [116]. If the stress σ is prescribed as input, Eqs. (4.58) and (4.59) can be solved directly with respect to the strain and the backstress. However, since the total strain rate \dot{H} is prescribed during the tensile tests, the following differential equation with respect to the stress is solved additionally:

$$\dot{\sigma} = E \left(\dot{H} - \dot{H}^{\text{in}} \right). \quad (4.66)$$

Equation (4.66) represents the time derivative of Eq. (4.10), assuming stationary temperatures. The experimental results for the strain rate $\dot{H}(t_n)$ with respect to the time step t_n provide the input for the solution. In order to identify the material parameter η_{h_0} , it is varied systematically within the interval $0 < \eta_{h_0} < 1$. Afterwards, the system of the differential equations (4.58), (4.59), and (4.66) is solved numerically with respect to each tensile test. For each simulation of a tensile test corresponding to a constant parameter η_{h_0} , the error measure $\Delta\sigma$ with respect to the stresses is calculated:

$$\Delta\sigma = \sum_{n=1}^{NP} \left[\sigma^{\text{calc}}(t_n) - \sigma^{\text{exp}}(t_n) \right]^2. \quad (4.67)$$

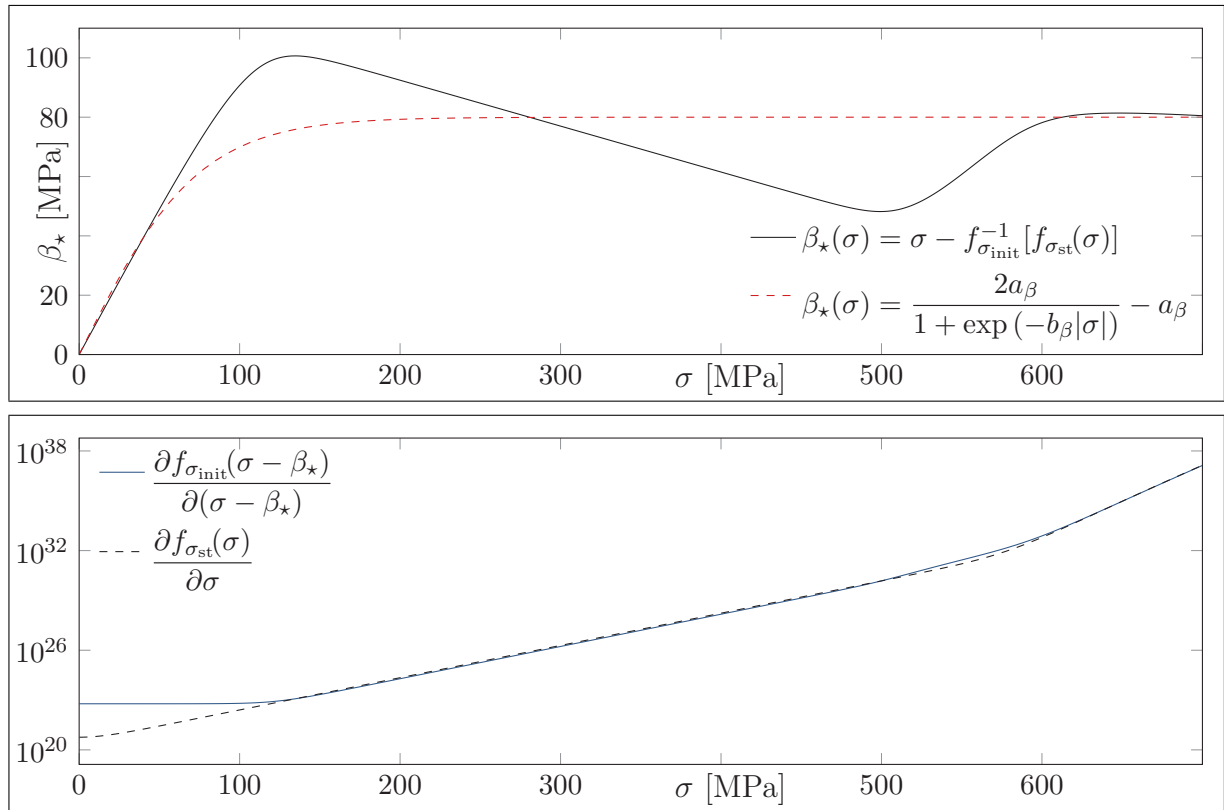


Figure 4.12: Saturation backstress β_* vs stress σ in the steady state (top) and derivatives of the stress response functions vs stress (bottom).

The stress σ^{calc} results from the numerical solution of Eqs. (4.58), (4.59), and (4.66), and σ^{exp} denotes the experimental stress values. During the systematic variation of η_{h_0} , the minimum error measure is found and the corresponding parameter η_{h_0} is determined for each tensile test. In order to obtain one parameter η_{h_0} , which is valid for all tensile tests, the computed values are averaged (arithmetic mean value). As a result of this procedure, the following value is obtained:

$$\eta_{h_0} \approx 0.17. \quad (4.68)$$

In order to assess the quality of the calibration procedure for the hardening behavior, Fig. 4.13 depicts the stress depending on the strain for all HT tensile tests. Only the elastic range and the hardening regime are examined such that the figure is restricted to low strains $H \leq 3\%$. Figure 4.13 reveals that the phase mixture model is capable of capturing the linear increase of the stress in the elastic range and the leveling of the curve in the hardening range until the maximum stress value is reached. Note that this figure represents only an intermediate result since softening processes are not accounted for yet. The calibration of the softening behavior is discussed in detail in the following section.

4.2.5 Softening

Up to now, the parameters C_Γ and Γ_* from Eq. (4.27) are still unknown. Both are related to the variable Γ , which describes the softening behavior, i.e. the range of the stress-strain curves with a constantly decreasing stress level, cf. Fig. 3.6 for example. Since the stress is varying with time, simplifications such as in Eqs. (4.54) and (4.55) are not possible. Taking

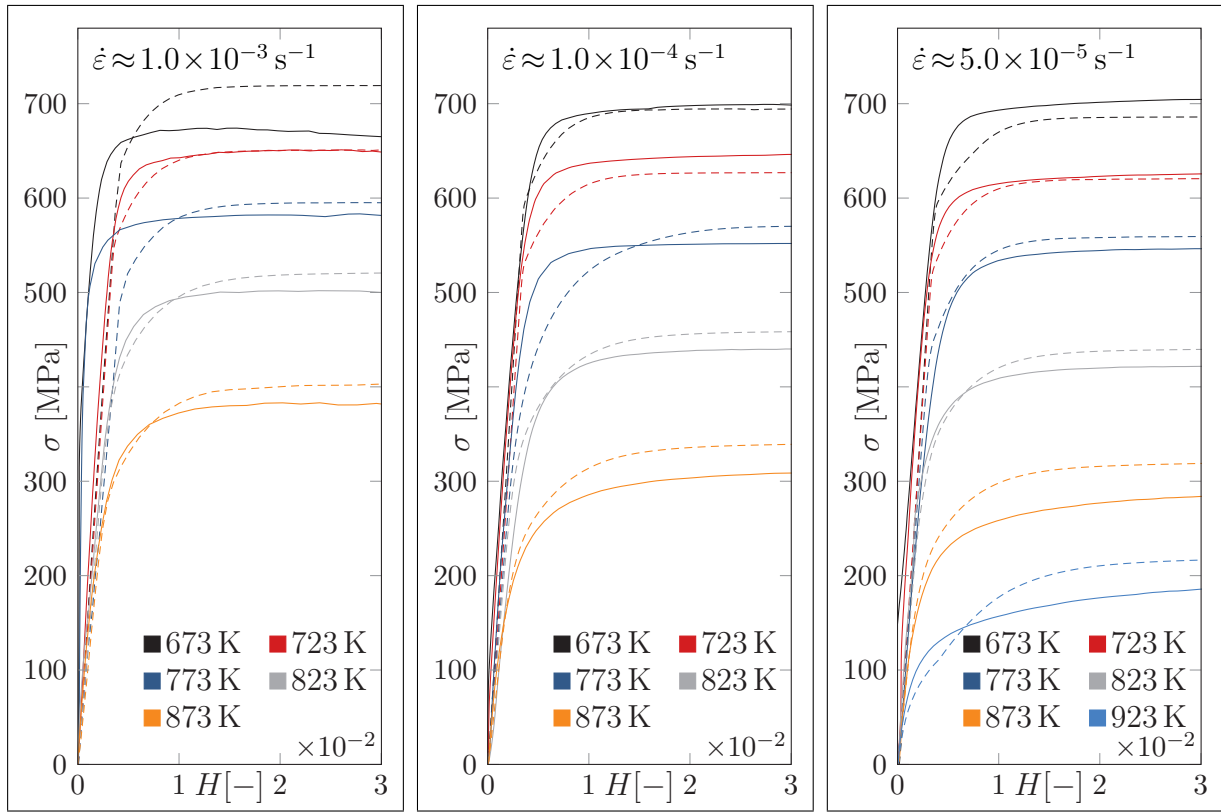


Figure 4.13: Stress σ vs strain H in the elastic range and the hardening regime. Experimental results (solid lines) compared to the phase mixture model (dashed lines).

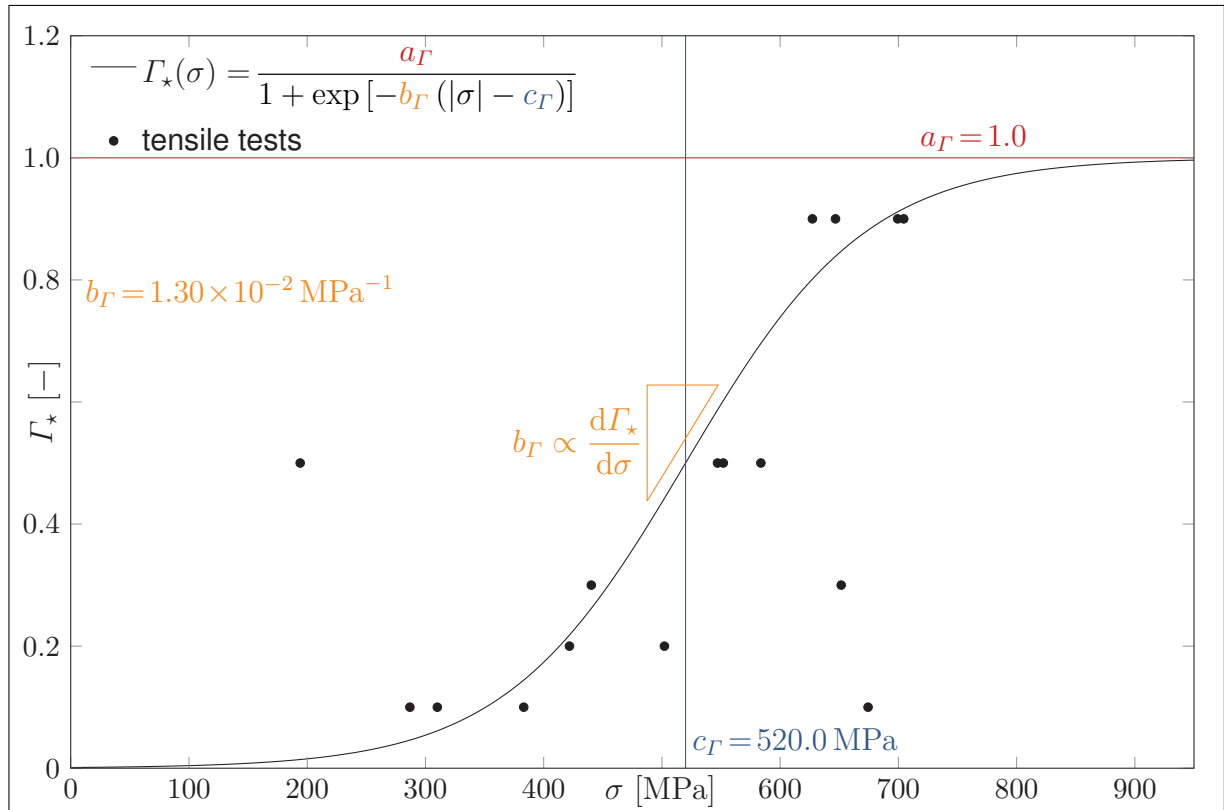
the hardening *and* the softening behavior into account, the following differential equation must be solved in conjunction with Eqs. (4.59) and (4.66):

$$\dot{\Gamma} = C_{\Gamma} (\Gamma_{\star} - \Gamma) \dot{H}^{\text{in}}. \quad (4.69)$$

The inelastic strain rates are determined based on Eq. (4.28):

$$\dot{H}^{\text{in}} = f_{\sigma_{\text{init}}}(\sigma - \Gamma\beta) f_T(T). \quad (4.70)$$

Equations (4.59), (4.66), (4.69), and (4.70) are restricted to stationary temperatures as well as positive strain rates and stresses because only tensile tests are taken into account in the remainder of this section. Since the softening stage is relatively easy to detect in the stress-strain curves of the HT tensile tests and necking takes place at high strains after the onset of softening, cf. the discussions in Chapt. 3, only the HT tensile tests presented in Sect. 3.1 are used for the calibration of the softening behavior. The overall strain rate $\dot{H}(t_n)$ defined with respect to the time step t_n from the experimental data serves as input for the system of the differential equations (4.59), (4.66), (4.69), and (4.70), which is solved numerically with MATLAB's solver `ode45`. In order to determine the parameters C_{Γ} and Γ_{\star} , we proceed in analogy to the calibration of η_{h_0} , described in Sect. 4.2.4. For the first guess, we assume that C_{Γ} and Γ_{\star} are constant with respect to the stress. The calibration procedure reveals that a constant value of $C_{\Gamma} = 5.0$ approximates the experimental data with the highest accuracy. In contrast, the saturation softening variable Γ_{\star} is strongly dependent on the stress level, as observed in Fig. 4.14. This figure depicts the saturation softening variable depending on a steady state stress value, which is extracted as a representative value for each HT tensile test. Although the scatter of the data is high, one can observe


 Figure 4.14: Saturation softening variable Γ_* vs the stress σ .

an increase of the saturation softening variable Γ_* with an increasing stress level. Note that a value of $\Gamma_* = 1$ indicates that the volume fractions of the hard phase in the initial and the saturation state are equal, i.e. $\eta_{h0} = \eta_{h*}$, cf. Eq. (4.17). Since the volume fraction of the hard phase does not change, softening does not occur such that the stress remains constant at the maximum value with increasing deformation. HT tensile tests with a high stress maximum ($\sigma_{\max} > 400$ MPa) exhibit this behavior, cf. Fig. 3.4. As already discussed in Chapt. 3, softening is based on microstructural processes, which are thermally activated and require time to develop. Therefore, particularly HT tensile tests at high temperatures and low strain rates (i.e. tests with a low maximum stress) exhibit softening, whereas HT tensile tests at lower temperatures and high strain rates with a high maximum stress do not show significant softening. During HT tensile tests with lower maximum stress levels ($\sigma_{\max} < 400$ MPa), the stress decreases constantly after the maximum stress is reached such that these tests show an extended softening stage. This refers to a saturation softening variable of $\Gamma_* \rightarrow 0$ or a volume fraction of the hard phase in the saturation state of $\eta_{h*} \rightarrow 0$. In order to account for this behavior, the dependence of the saturation softening variable on the stress is described by the logistic function [138]:

$$\Gamma_*(\sigma) = \frac{a_\Gamma}{1 + \exp[-b_\Gamma(|\sigma| - c_\Gamma)]} \quad (4.71)$$

with the material parameters:

$$a_\Gamma = 1.0, \quad (4.72)$$

$$b_\Gamma = 1.30 \times 10^{-2} \text{ MPa}^{-1}, \quad (4.73)$$

$$c_\Gamma = 520.0 \text{ MPa}. \quad (4.74)$$

As shown in Fig. 4.14, the parameter a_Γ is equal to the maximum value of the logistic function. The parameter b_Γ is proportional to the slope of the sigmoid curve at its midpoint, which is defined by means of the parameter c_Γ .

4.2.6 Summary

In the current chapter, the phase mixture model was calibrated using HT tensile tests and creep tests, such that all unknown parameters and functions are determined. The calibrated model can be used to simulate both strain rate and stress controlled processes at varying temperatures. In its current form, the model is restricted to one-dimensional stress and strain states, accounting for both compression and tension. If a process is controlled by the stress σ , the following system of differential equations needs to be solved with respect to the inelastic strain H^{in} , the backstress β , and the softening variable Γ , cf. Eqs. (4.25)–(4.27):

$$\dot{H}^{\text{in}} = \text{sgn}(\sigma - \Gamma\beta) f_{\sigma_{\text{init}}}(|\sigma - \Gamma\beta|) f_T(T), \quad (4.75)$$

$$\dot{\beta} = \frac{1}{E(T)} \frac{dE(T)}{dT} \dot{T}\beta + E(T) \frac{\eta_{h_0}}{1 - \eta_{h_0}} \left(\dot{H}^{\text{in}} - \frac{\beta}{\beta_*(\sigma)} |\dot{H}^{\text{in}}| \right), \quad (4.76)$$

$$\dot{\Gamma} = C_\Gamma [\Gamma_*(\sigma) - \Gamma] |\dot{H}^{\text{in}}|. \quad (4.77)$$

These three equations constitute a system of ODEs, which is able to capture all physical phenomena of interest. In addition, the following ICs are valid with respect to a virgin material:

$$H^{\text{in}}(t=0) = 0, \quad \beta(t=0) = 0, \quad \Gamma(t=0) = 1. \quad (4.78)$$

For a process controlled by the strain rate \dot{H} , an evolution equation for the stress σ is formulated by differentiating Eq. (4.10) once with respect to time:

$$\dot{\sigma} = E(T) (\dot{H} - \dot{H}^{\text{in}}) + \frac{1}{E(T)} \frac{dE(T)}{dT} \dot{T}\sigma, \quad (4.79)$$

Equation (4.79) must be solved in conjunction with Eqs. (4.76) and (4.77) in order to obtain the stress, the backstress, and the softening variable, while the inelastic strain rate can be computed by means of Eq. (4.75). Furthermore, the following ICs hold for a virgin material subjected to a process controlled by the strain rate:

$$\sigma(t=0) = 0, \quad \beta(t=0) = 0, \quad \Gamma(t=0) = 1. \quad (4.80)$$

During the calibration procedure, the following functions were determined:

- the temperature response function for the YOUNG's modulus, cf. Eq. (4.34):

$$E(T) = f_E(T) = C_1 + C_2 T^3,$$

- the temperature response function for the inelastic strain rate, cf. Eq. (4.37):

$$f_T(T) = \exp\left(-\frac{Q}{RT}\right),$$

- the stress response function for the inelastic strain rates in the initial and the steady

4 One-Dimensional Phase Mixture Model

state, cf. Eq. (4.53):

$$f_{\sigma_i}(\sigma) = a_i \sinh\left(\frac{\sigma}{b_i}\right) \left[1 + \left(\frac{\sigma}{c_i}\right)^{m_i}\right] \quad \forall i \in \{\text{st}, \text{init}\}.$$

- the stress response function for the saturation backstress, cf. Eq. (4.65):

$$\beta_{\star}(\sigma) = \frac{2a_{\beta}}{1 + \exp(-b_{\beta} |\sigma|)} - a_{\beta},$$

- and the stress response function for the saturation softening variable, cf. Eq. (4.71):

$$\Gamma_{\star}(\sigma) = \frac{a_{\Gamma}}{1 + \exp[-b_{\Gamma} (|\sigma| - c_{\Gamma})]}.$$

Although the stress response function for the inelastic strain rates in the steady state $f_{\sigma_{\text{st}}}(\sigma)$ is not explicitly needed for the simulation, it is listed to provide a complete overview. All constants and material parameters, which are needed for the introduced phase mixture model, are compiled in Table 4.2. Here, their meaning and the value identified in the calibration process are listed. As a summary, all HT tensile tests are simulated with the phase mixture model by solving Eqs. (4.79)–(4.77) numerically with MATLAB's solver `ode45`, and the results of the approximation are compared to the experimental data. Figure 4.15 depicts the stress depending on the strain with respect to all strain rates and temperatures. Since the phase mixture model does not take necking into account, the simulation is stopped before the high decrease in stress takes place, which indicates necking. Figure 4.15 reveals that the phase mixture model is able to account for the hardening behavior, cf. the discussion in Sect. 4.2.4 and Fig. 4.13, as well as for the softening behavior, i.e. the slight and constant decrease in the stress value for strains exceeding the strain value corresponding to the maximum stress. In particular, the stress-strain curves with respect to higher temperatures $T \geq 823 \text{ K}$ exhibit this constant decrease in the stress level, while the phase mixture model predicts a constant saturation stress for the stress-strain curves corresponding to the lower temperatures $T \leq 773 \text{ K}$, since the stress-strain curves at the lower temperatures do not exhibit a significant softening effect, as discussed before.

Table 4.2: Constants and identified parameters in the binary phase mixture model.

variable	value	unit	meaning	equation
C_1	2.23×10^5	MPa	parameters in the temperature response function for the YOUNG's modulus	(4.34)
C_2	-1.64×10^{-4}	MPa K ⁻³		
Q	540.6×10^3	J mol ⁻¹	activation energy in the temperature response function for the inelastic strain rate	(4.37)
R	8.317	J (mol K) ⁻¹	universal gas constant in the temperature response function for the inelastic strain rate	(4.37)
a_{init}	1.54×10^{24}	s ⁻¹	parameters in the stress response function for the inelastic strain rates in the initial state	(4.53)
b_{init}	25.8	MPa		
c_{init}	483.6	MPa		
m_{init}	35.7	–		
a_{st}	1.30×10^{22}	s ⁻¹	parameters in the stress response function for the inelastic strain rates in the steady state	(4.53)
b_{st}	22.4	MPa		
c_{st}	593.1	MPa		
m_{st}	38.0	–		
η_{h0}	0.17	–	reference value for the volume fraction of the hard phase	(4.76)
a_β	80.0	MPa	maximum value for the saturation backstress	(4.65)
b_β	2.70×10^{-2}	MPa ⁻¹	parameter in the evolution function for the saturation backstress	(4.65)
C_Γ	5.0	–	parameter in the evolution equation for the softening variable	(4.77)
a_Γ	1.0	–	parameters in the stress response function for the saturation softening variable	(4.71)
b_Γ	1.30×10^{-2}	MPa ⁻¹		
c_Γ	520.0	MPa		

4 One-Dimensional Phase Mixture Model

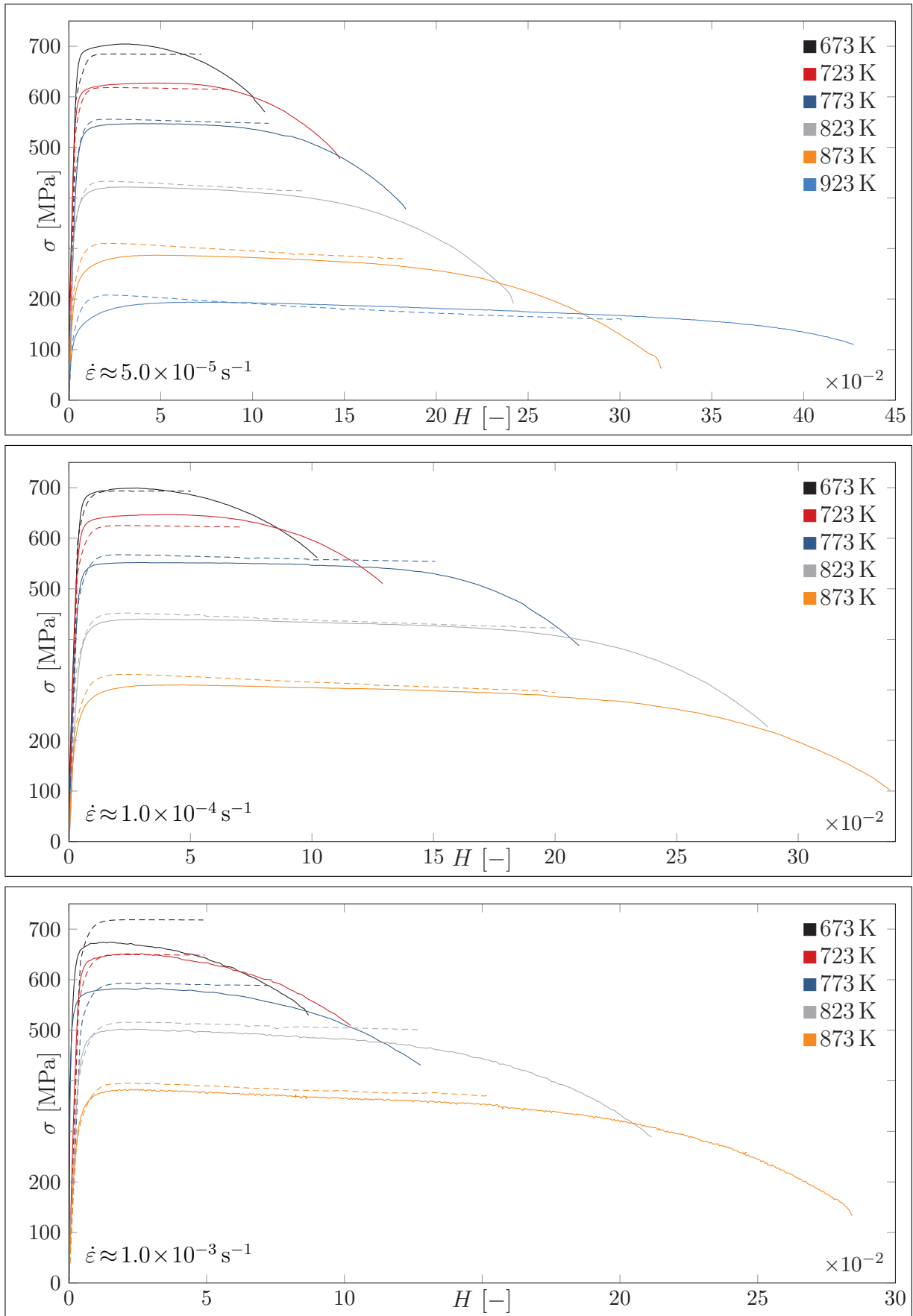


Figure 4.15: Stress σ vs strain H in the elastic, hardening, and softening regime. Experimental results (solid lines) compared to the phase mixture model (dashed lines).

4.3 Verification

In the previous section, the phase mixture model is calibrated based on HT tensile tests and creep tests. Since numerous tests at different temperatures $673 \text{ K} \leq T \leq 923 \text{ K}$ and under several strain rates $10^{-5} \text{ s}^{-1} \leq \dot{H} \leq 10^{-3} \text{ s}^{-1}$ are taken into account, the calibrated model covers a wide stress range, i.e. $100 \text{ MPa} \leq \sigma \leq 700 \text{ MPa}$. In order to verify the calibration and to examine the range of applicability of the model, additional creep tests, where pressure loads as well as tensile loads are applied, are simulated using the developed model.

Figure 4.16 presents the results of several creep tests under constant compressive CAUCHY stress. The experimental results are extracted from [13], and all creep tests are simulated by solving Eqs. (4.25), (4.76), and (4.77) with MATLAB's solver `ode45`. The diagram at the top left-hand side depicts the absolute inelastic strain rate $|\dot{H}^{\text{in}}|$ depending on the absolute inelastic strain $|H^{\text{in}}|$ at the temperature $T = 823 \text{ K}$ for three different stress levels, while the diagrams at the top right-hand side and the bottom left-hand side show the results with respect to higher temperatures $T = 873 \text{ K}$ and $T = 915 \text{ K}$. Moreover, additional results with respect to different temperatures at the stress level $\sigma = -230 \text{ MPa}$ are presented in the diagram at the bottom right-hand side.

Considering that these tests are not used for the calibration, the quality of approximation is judged to be good or at least sufficient, depending on the examined stress and temperature levels. The higher the absolute stress level and the higher the temperature, the more accurate the simulation. The deviations are higher for the tests at a low absolute stress level $|\sigma|$ and a relatively low temperature, e.g. $\sigma = -230 \text{ MPa}$ and $T = 823 \text{ K}$, or for tests at very low absolute stress levels, for example $\sigma = -140 \text{ MPa}$ and $T = 915 \text{ K}$. The majority of these tests exhibits small strain rates, i.e. $|\dot{H}^{\text{in}}| < 10^{-7} \text{ s}^{-1}$, and the deviations can be attributed to the selection of the tests used for the calibration, i.e. the model is calibrated mainly based on tests at higher strain rates, particularly for lower temperatures (673 K or 773 K), cf. the left diagram in Fig. 4.11.

Furthermore, Figure 4.17 presents the results of two cyclic creep tests. The upper diagram refers to the cyclic creep test presented in Sect. 3.2 and shows the inelastic strain rate \dot{H}^{in} depending on the inelastic strain H^{in} . During this test, the PIOLA-KIRCHHOFF stress is kept constant either at the minimum ($P_{\text{min}} \approx 100 \text{ MPa}$) or the maximum value ($P_{\text{max}} \approx 150 \text{ MPa}$), cf. the top left diagram in Fig. 3.9. In addition, the lower diagram depicts the absolute inelastic strain rate with respect to the absolute inelastic strain for a cyclic compressive creep test. The CAUCHY stress is kept constant either at the minimum ($\sigma_{\text{min}} = -196 \text{ MPa}$) or the maximum value ($\sigma_{\text{max}} = -150 \text{ MPa}$). In [13], the experimental results are provided. Since the stress is only given depending on the inelastic strain and the exact dependence with respect to the time is unknown in [13], Eqs. (4.76) and (4.77) must be modified for this simulation. The time derivative is transformed as follows:

$$\dot{\square} = \frac{\partial \square}{\partial H^{\text{in}}} \frac{\partial H^{\text{in}}}{\partial t} = \dot{H}^{\text{in}} \frac{\partial \square}{\partial H^{\text{in}}}.$$

Above transformation is applied to $\dot{\beta}$ and $\dot{\Gamma}$ in Eqs. (4.76) and (4.77). Both equations are divided by \dot{H}^{in} and a stationary temperature field is assumed such that one obtains:

$$\frac{\partial \beta}{\partial H^{\text{in}}} = E \frac{\eta_{\text{h}_0}}{1 - \eta_{\text{h}_0}} \left[1 - \frac{\beta}{\beta_{\star}} \text{sgn}(\dot{H}^{\text{in}}) \right], \quad (4.81)$$

$$\frac{\partial \Gamma}{\partial H^{\text{in}}} = C_{\Gamma} (\Gamma_{\star} - \Gamma) \text{sgn}(\dot{H}^{\text{in}}). \quad (4.82)$$

4 One-Dimensional Phase Mixture Model

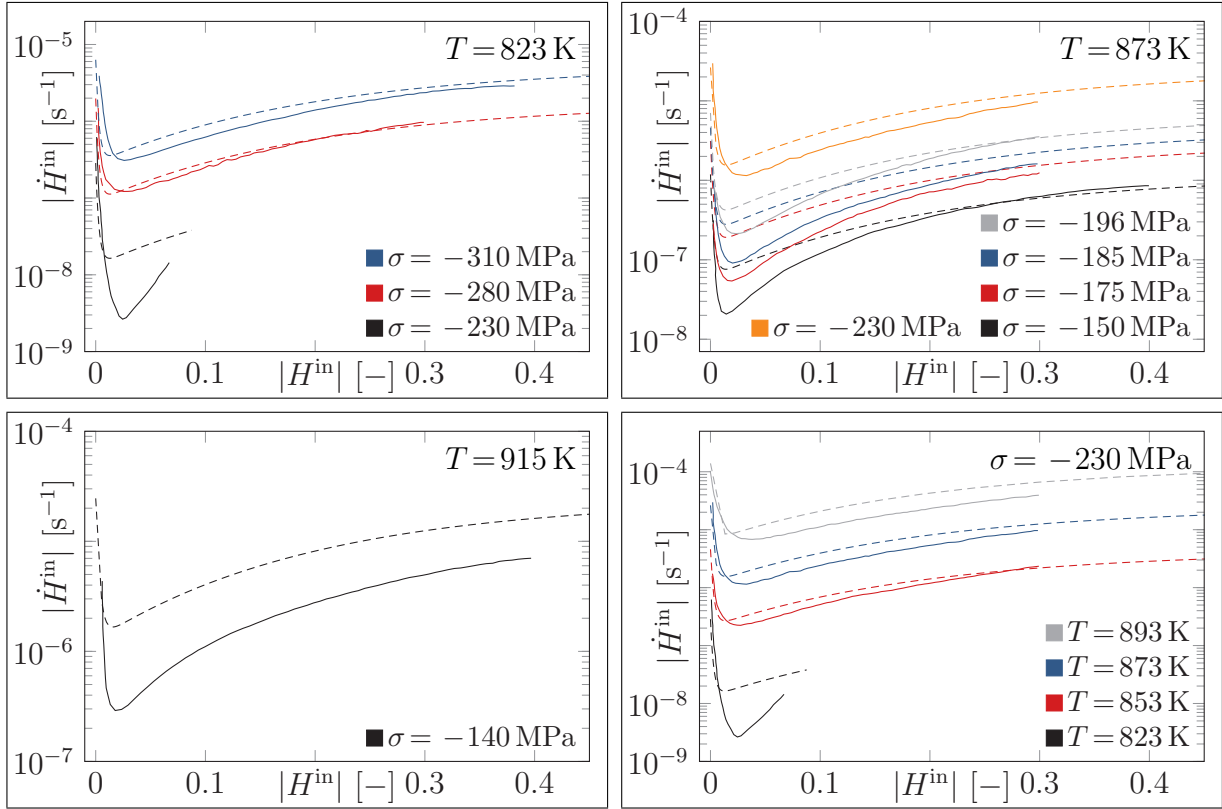


Figure 4.16: Inelastic strain rate \dot{H}^{in} vs inelastic strain H^{in} for creep tests under compressive loads. Experimental results after [13] (solid lines) compared to the phase mixture model (dashed lines).

The inelastic strain rate \dot{H}^{in} is calculated based on Eq. (4.25), while the inelastic strain and the stress serve as input for the numerical integration. This procedure allows to simulate the cyclic creep test without knowing the time-varying load explicitly.

Examining the top diagram in Fig. 4.17, it becomes obvious that the model underestimates the strains of the test results. Furthermore, the minimum strain rate is predicted with respect to a lower strain level compared to the experimental data. The high deviations are due to the very low strain rates $\dot{H}^{\text{in}} \leq 10^{-7} \text{ s}^{-1}$, as already discussed before. The simulation is more accurate for high strain rates $\dot{H}^{\text{in}} > 10^{-7} \text{ s}^{-1}$, as the lower diagram reveals. The phase mixture model is able to account for the slightly increasing strain rate, i.e. the softening effect during creep, and the jumps in the inelastic strain rate due to the cyclic load.

To sum up, the simulation of the additional creep tests demonstrates that the calibrated phase mixture model provides robust solutions with respect to uniaxial loads, which can be both monotonous and cyclic. It is applicable to strain rates $\dot{H}^{\text{in}} > 10^{-7} \text{ s}^{-1}$ and to large temperature and stress intervals, i.e. $673 \text{ K} \leq T \leq 923 \text{ K}$ and $100 \text{ MPa} \leq \sigma \leq 700 \text{ MPa}$, respectively. For the simulation, a total set of 14 parameters is required ($C_1, C_2, Q, a_{\text{init}}, b_{\text{init}}, c_{\text{init}}, m_{\text{init}}, \eta_{h_0}, a_\beta, b_\beta, C_\Gamma, a_\Gamma, b_\Gamma, c_\Gamma$, cf. Table 4.2). Note that these parameters are all temperature-independent. Several other models for tempered martensitic steels have been presented in Sect. 1.2. However, the majority of these models is based on at least 10 temperature-dependent material parameters. Here, one should bear in mind that additional parameters are required to define the dependence on the temperature. In the simplest scenario, all parameters are linearly dependent on the temperature such that the actual number of parameters is 20. If higher order polynomial functions are taken into account to approximate the temperature response functions, the number of parameters is likely to be even higher. This highlights one

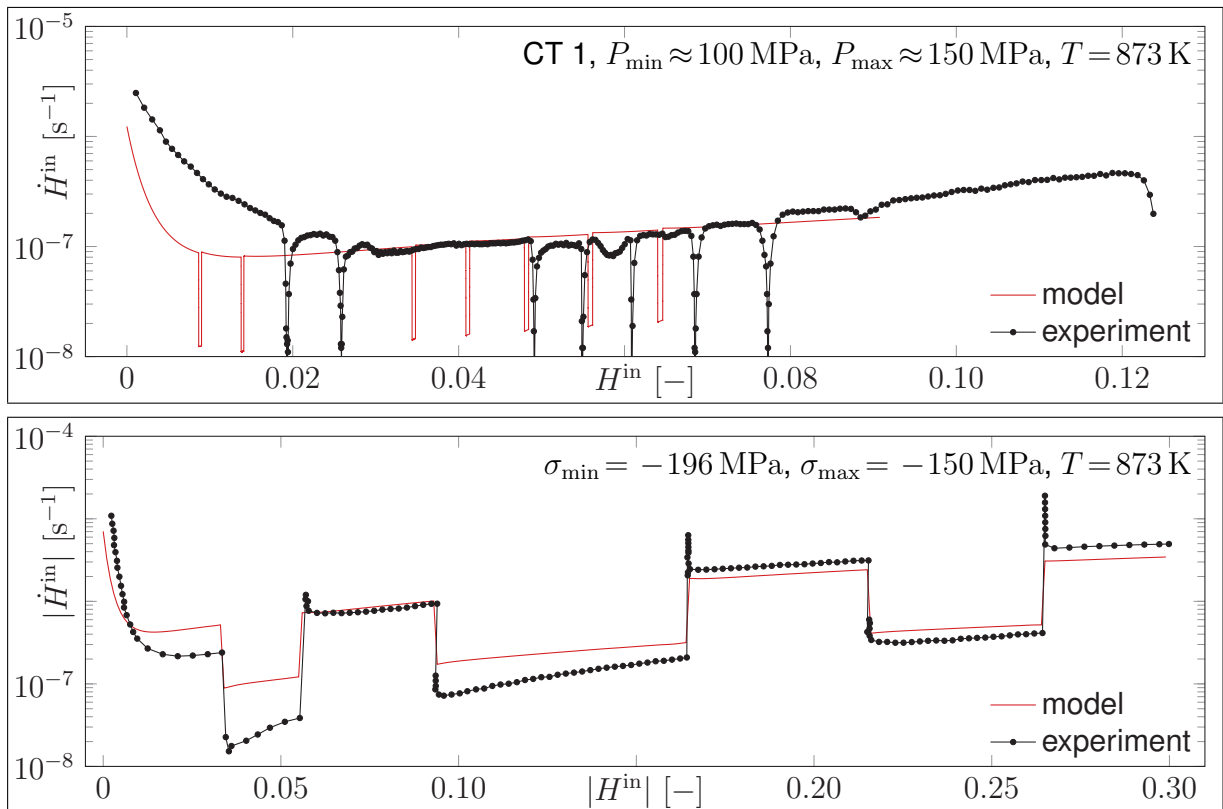


Figure 4.17: Inelastic strain rate \dot{H}^{in} vs inelastic strain H^{in} for two cyclic creep tests. Cyclic creep test from Sect. 3.2 (top) and cyclic creep test from [13] (bottom).

major advantage of the proposed phase mixture model: only 14 constant parameters are required to cover wide ranges with respect to the stress, temperature, and strain rate.

5 Three-Dimensional Phase Mixture Model

This chapter introduces the phase mixture model with respect to multiaxial stress and deformation states. To this end, it is divided into three sections. Section 5.1 summarizes the governing equations in an analogous manner to Sect. 4.1, where the one-dimensional model has been presented. In Sect. 5.2, it is checked whether the three-dimensional phase mixture model is thermodynamically consistent. The last section, Sect. 5.3, focuses on the implementation of the three-dimensional model into the FEM using an implicit time integration scheme. Regarding the verification of the implementation, the results of several finite element analyses are presented and discussed in detail.

5.1 Governing Equations

In this section, the one-dimensional governing equations presented in Sect. 4.1 are generalized to three-dimensional stress and deformation states. Note that the derivations in the remainder of this chapter are restricted to small strains, displacements, and rotations, similar to the majority of the proposed models for tempered martensitic steels, cf. the discussion in Sect. 1.2. These restrictions are due to two main reasons: Firstly, the solution of problems involving finite strains, displacements, and rotations demands significantly higher computational effort and time compared to problems which are restricted to small strains, displacements, and rotations, especially in cases where the mechanical behavior of complex components under transient loads is simulated [103, 109]. Secondly, power plant components in use must not deform to a high extent, i.e. large strains occurring in a component would result in the replacement of this component. Nevertheless, the reader should note that a number of viscoplasticity models for finite strains considering nonlinear hardening and softening is available in the literature [139–141].

The derivation of the governing equations in this section is based on several papers and monographs [16, 42, 71], where further information can be found. Because of the restriction to small strains, displacements, and rotations, we postulate the equality of the linear strain tensor $\boldsymbol{\epsilon}$ in the soft and the hard phase (iso-strain assumption) [42], cf. Eq. (4.1):

$$\boldsymbol{\epsilon} = \boldsymbol{\epsilon}_h = \boldsymbol{\epsilon}_s. \quad (5.1)$$

In three dimensions, the rule of mixture for the overall stress $\boldsymbol{\sigma}$ reads as follows [42], compare to Eq. (2.81):

$$\boldsymbol{\sigma} = \eta_s \boldsymbol{\sigma}_s + \eta_h \boldsymbol{\sigma}_h. \quad (5.2)$$

Furthermore, Eq. (4.3) is valid for the volume fractions η_k . For the sake of completeness, it is recalled at this point:

$$\eta_s + \eta_h = 1 \quad \forall \quad 0 < \eta_k < 1.$$

5 Three-Dimensional Phase Mixture Model

Based on Eq. (2.54), the additive split of the strains into the elastic and the inelastic part is deployed:

$$\boldsymbol{\varepsilon} = \boldsymbol{\varepsilon}_k^{\text{el}} + \boldsymbol{\varepsilon}_k^{\text{in}}. \quad (5.3)$$

The linear elastic behavior of the phases is described by the three-dimensional Hooke's law, cf. Eq. (2.45):

$$\boldsymbol{\sigma}_k = K\varepsilon_{V_k}\mathbf{I} + 2G\boldsymbol{\varepsilon}_k^{\text{el}} \quad \text{with } \varepsilon_{V_k} = \text{tr}(\boldsymbol{\varepsilon}_k), \quad (5.4)$$

or reformulated with respect to the strains, cf. Eq. (2.48):

$$\boldsymbol{\varepsilon}_k^{\text{el}} = \frac{\sigma_{m_k}}{3K}\mathbf{I} + \frac{\boldsymbol{\sigma}'_k}{2G} \quad \text{with } \sigma_{m_k} = \frac{1}{3}\text{tr}(\boldsymbol{\sigma}_k). \quad (5.5)$$

As before, we assume that both phases exhibit the same elastic behavior such that the material parameters E , G , K , and ν are identical for both phases. One should bear in mind that the temperature dependence of all elastic parameters is taken into account by the phase mixture model, cf. Eq. (4.6). Applying the trace operator to Eqs. (5.1), (5.3), and (5.5) yields:

$$\varepsilon_V = \varepsilon_{V_h} = \varepsilon_{V_s}, \quad (5.6)$$

$$\varepsilon_V = \varepsilon_{V_k}^{\text{el}} + \varepsilon_{V_k}^{\text{in}}, \quad (5.7)$$

$$\varepsilon_{V_k}^{\text{el}} = \frac{\sigma_{m_k}}{K}. \quad (5.8)$$

As already discussed in Sect. 2.1.4.2, we assume that the inelastic deformation does not produce a significant change in volume, i.e. $\varepsilon_{V_k}^{\text{in}} = 0$. If we take this assumption into account and insert Eqs. (5.7) and (5.8) into Eq. (5.6), we obtain:

$$\sigma_m = \sigma_{m_h} = \sigma_{m_s} = K\varepsilon_V. \quad (5.9)$$

Since the bulk modulus K is the same in both phases, above considerations result in an equal mean stress in the entire mixture. That is to say that Eqs. (5.1) and (5.2) can be written in terms of the deviatoric parts of the strain and stress tensors:

$$\boldsymbol{\varepsilon}' = \boldsymbol{\varepsilon}'_h = \boldsymbol{\varepsilon}'_s, \quad (5.10)$$

$$\boldsymbol{\sigma}' = \eta_s\boldsymbol{\sigma}'_s + \eta_h\boldsymbol{\sigma}'_h. \quad (5.11)$$

In order to derive a constitutive law for the mixture, the deviatoric stresses $\boldsymbol{\sigma}'_k$ for the phases are determined by rearranging Eq. (5.5). The resulting terms are inserted into Eq. (5.11), and after some transformations one obtains the constitutive law for the mixture, cf. Eq. (4.10):

$$\boldsymbol{\varepsilon} = \frac{\sigma_m}{3K}\mathbf{I} + \frac{\boldsymbol{\sigma}'}{2G} + \boldsymbol{\varepsilon}^{\text{in}}, \quad (5.12)$$

where $\boldsymbol{\varepsilon}^{\text{in}}$ describes the inelastic strain state in the mixture:

$$\boldsymbol{\varepsilon}^{\text{in}} = (1 - \eta_h)\boldsymbol{\varepsilon}_s^{\text{in}} + \eta_h\boldsymbol{\varepsilon}_h^{\text{in}}. \quad (5.13)$$

In a next step, the evolution equations for the inelastic strains $\boldsymbol{\varepsilon}_k^{\text{in}}$ are provided. The following

equations are suggested in [42, 71], compare to Eqs. (4.12) and (4.13):

$$\dot{\boldsymbol{\epsilon}}_s^{\text{in}} = \frac{3}{2} \dot{\epsilon}_{\text{vMs}}^{\text{in}} \frac{\boldsymbol{\sigma}'_s}{\sigma_{\text{vMs}}}, \quad (5.14)$$

$$\dot{\boldsymbol{\epsilon}}_h^{\text{in}} = \frac{3}{2} \dot{\epsilon}_{\text{vM}}^{\text{in}} \frac{\boldsymbol{\sigma}'_h - \boldsymbol{\sigma}'}{\sigma_{\text{vM}_*}}, \quad (5.15)$$

where $\dot{\epsilon}_{\text{vMs}}^{\text{in}}$ denotes the VON MISES inelastic strain rate in the soft phase, and $\dot{\epsilon}_{\text{vM}}^{\text{in}}$ stands for the VON MISES inelastic strain rate in the mixture. In addition, the VON MISES stress in the soft phase σ_{vMs} and the VON MISES saturation stress σ_{vM_*} are defined:

$$\dot{\epsilon}_{\text{vMs}}^{\text{in}} = \sqrt{\frac{2}{3} \dot{\boldsymbol{\epsilon}}_s^{\text{in}} : \dot{\boldsymbol{\epsilon}}_s^{\text{in}}}, \quad \dot{\epsilon}_{\text{vM}}^{\text{in}} = \sqrt{\frac{2}{3} \dot{\boldsymbol{\epsilon}}^{\text{in}} : \dot{\boldsymbol{\epsilon}}^{\text{in}}}, \quad (5.16)$$

$$\sigma_{\text{vMs}} = \sqrt{\frac{3}{2} \boldsymbol{\sigma}'_s : \boldsymbol{\sigma}'_s}, \quad \sigma_{\text{vM}_*} = \sqrt{\frac{3}{2} (\boldsymbol{\sigma}'_{h_*} - \boldsymbol{\sigma}') : (\boldsymbol{\sigma}'_{h_*} - \boldsymbol{\sigma}')}. \quad (5.17)$$

Note that the index \square_{vM} is used in the remainder of the thesis at hand to mark equivalent variables of VON MISES-type. Moreover, the variable $\boldsymbol{\sigma}'_{h_*}$ denotes the saturation stress deviator with respect to the hard phase. For the VON MISES inelastic strain in the soft phase, the following evolution equation is applied, cf. Eq. (4.12):

$$\dot{\epsilon}_{\text{vMs}}^{\text{in}} = f_{\sigma_{\text{init}}}(\sigma_{\text{vMs}}) f_T(T) \quad (5.18)$$

with the stress response function in the initial state $f_{\sigma_{\text{init}}}(\sigma_{\text{vMs}})$, cf. Eq. (4.53). Additionally, an evolution equation for the volume fraction of one phase must be formulated, cf. Eq. (4.8):

$$\dot{\eta}_h = f_\eta(\boldsymbol{\sigma}_h, \dot{\boldsymbol{\epsilon}}_h^{\text{in}}, T). \quad (5.19)$$

It is sufficient to find an evolution equation for the volume fraction of only *one* phase – e.g. with respect to the hard phase as in Eq. (5.19) – since the volume fractions cannot evolve independently. First, the volume fraction of the hard phase is computed on the basis of Eq. (5.19), and thereafter Eq. (4.3) is employed to compute the corresponding volume fraction for the soft phase. In an analogous procedure as discussed for the one-dimensional model, the backstress tensor $\boldsymbol{\beta}$ and the VON MISES backstress β_{vM} are introduced [42]:

$$\boldsymbol{\beta} = \frac{\eta_{h_0}}{1 - \eta_{h_0}} (\boldsymbol{\sigma}'_h - \boldsymbol{\sigma}') \quad \forall 0 < \eta_{h_0} < 1, \quad (5.20)$$

$$\beta_{\text{vM}} = \sqrt{\frac{3}{2} \boldsymbol{\beta} : \boldsymbol{\beta}} \quad \forall 0 \leq \beta_{\text{vM}} \leq \beta_{\text{vM}_*} \quad (5.21)$$

with their corresponding saturation values:

$$\boldsymbol{\beta}_* = \frac{\eta_{h_0}}{1 - \eta_{h_0}} (\boldsymbol{\sigma}'_{h_*} - \boldsymbol{\sigma}'), \quad (5.22)$$

$$\beta_{\text{vM}_*} = \sqrt{\frac{3}{2} \boldsymbol{\beta}_* : \boldsymbol{\beta}_*}. \quad (5.23)$$

The softening variable Γ and its saturation value Γ_* are identical in the one-dimensional and the three-dimensional model such that Eqs. (4.15) and (4.17) hold as well. For the sake of

5 Three-Dimensional Phase Mixture Model

clarity, we repeat both equations at this point:

$$\Gamma = \frac{\eta_h}{1 - \eta_h} \frac{1 - \eta_{h0}}{\eta_{h0}} \quad \forall \Gamma_* \leq \Gamma \leq 1,$$

$$\Gamma_* = \frac{\eta_{h*}}{1 - \eta_{h*}} \frac{1 - \eta_{h0}}{\eta_{h0}} \quad \forall 0 < \eta_{h*} < 1.$$

The computation of the stresses and inelastic strain rates for each phase depends on the introduced internal variables, i.e. the backstress tensor $\boldsymbol{\beta}$ and the softening variable Γ . Employing the definitions (5.20)–(5.23) and the Eqs. (4.15), (4.17), (5.11), (5.14), (5.15), and (5.18), we can derive expressions for the deviatoric stress tensors and the inelastic strain rates:

$$\boldsymbol{\sigma}'_h = \boldsymbol{\sigma}' + \frac{1 - \eta_{h0}}{\eta_{h0}} \boldsymbol{\beta}, \quad (5.24)$$

$$\boldsymbol{\sigma}'_s = \tilde{\boldsymbol{\sigma}}', \quad (5.25)$$

$$\dot{\boldsymbol{\epsilon}}_h^{\text{in}} = \frac{3}{2} \dot{\tilde{\epsilon}}_{\text{vM}}^{\text{in}} \frac{\boldsymbol{\beta}}{\beta_{\text{vM}*}}, \quad (5.26)$$

$$\dot{\boldsymbol{\epsilon}}_s^{\text{in}} = \frac{3}{2} f_{\sigma_{\text{init}}}(\tilde{\sigma}_{\text{vM}}) f_T(T) \frac{\tilde{\boldsymbol{\sigma}}'}{\tilde{\sigma}_{\text{vM}}}, \quad (5.27)$$

where we have introduced the effective stress tensor $\tilde{\boldsymbol{\sigma}}'$ and the corresponding VON MISES stress $\tilde{\sigma}_{\text{vM}}$:

$$\tilde{\boldsymbol{\sigma}}' = \boldsymbol{\sigma}' - \Gamma \boldsymbol{\beta}, \quad \tilde{\sigma}_{\text{vM}} = \sqrt{\frac{3}{2} \tilde{\boldsymbol{\sigma}}' : \tilde{\boldsymbol{\sigma}}'}. \quad (5.28)$$

Eqs. (5.24)–(5.27) are analogous to Eqs. (4.18)–(4.21), which have been derived for the one-dimensional model. In order to derive the evolution equations for the inelastic strain, the backstress, and the softening variable, an analogous procedure as the one presented in Sect. 4.1 is applied. Thus, Eq. (5.12) is differentiated once with respect to time and rearranged such that one obtains:

$$\dot{\boldsymbol{\epsilon}}^{\text{in}} = \dot{\boldsymbol{\epsilon}} - \frac{\partial}{\partial t} \left(\frac{\sigma_m}{3K} \mathbf{I} + \frac{\boldsymbol{\sigma}'}{2G} \right). \quad (5.29)$$

A similar equation is derived for the individual phases by substituting Eq. (5.5) into Eq. (5.3) and differentiating the result with respect to the time:

$$\dot{\boldsymbol{\epsilon}} = \frac{\partial}{\partial t} \left(\frac{\sigma_m}{3K} \mathbf{I} + \frac{\boldsymbol{\sigma}'_k}{2G} \right) + \dot{\boldsymbol{\epsilon}}_k^{\text{in}}. \quad (5.30)$$

Equation (5.30) is evaluated for the soft phase and inserted into Eq. (5.29). Furthermore, the stress deviator $\boldsymbol{\sigma}'_s$ and the inelastic strain rate tensor $\dot{\boldsymbol{\epsilon}}_s^{\text{in}}$ are replaced using Eqs. (5.25) and (5.27), respectively. After simple transformations, this results in the following differential equation with respect to the inelastic strain $\boldsymbol{\epsilon}^{\text{in}}$, compare to Eq. (4.24) for one-dimensional applications:

$$\dot{\boldsymbol{\epsilon}}^{\text{in}} = \frac{3}{2} f_{\sigma_{\text{init}}}(\tilde{\sigma}_{\text{vM}}) f_T(T) \frac{\tilde{\boldsymbol{\sigma}}'}{\tilde{\sigma}_{\text{vM}}} - \frac{\partial}{\partial t} \left(\frac{\Gamma \boldsymbol{\beta}}{2G} \right). \quad (5.31)$$

In analogy to Eq. (4.25), the last term in Eq. (5.31) is omitted because this term influences the inelastic strain rate only at the very beginning of the inelastic deformation [42]:

$$\dot{\boldsymbol{\epsilon}}^{\text{in}} = \frac{3}{2} f_{\sigma_{\text{init}}}(\tilde{\sigma}_{\text{vM}}) f_T(T) \frac{\tilde{\boldsymbol{\sigma}}'}{\tilde{\sigma}_{\text{vM}}}. \quad (5.32)$$

Afterwards, the procedure is repeated for the hard phase: Eq. (5.30) is evaluated with respect to the hard phase and inserted into Eq. (5.29). The stress deviator $\boldsymbol{\sigma}'_{\text{h}}$ and the inelastic strain rate tensor $\dot{\boldsymbol{\epsilon}}_{\text{h}}^{\text{in}}$ are replaced by Eqs. (5.24) and (5.26). Due to this methodology, one obtains an evolution equation for the backstress $\boldsymbol{\beta}$, cf. Eq. (4.26):

$$\dot{\boldsymbol{\beta}} = \frac{1}{G(T)} \frac{dG(T)}{dT} \dot{T} \boldsymbol{\beta} + 2G(T) \frac{\eta_{\text{h0}}}{1 - \eta_{\text{h0}}} \left[\dot{\boldsymbol{\epsilon}}^{\text{in}} - \frac{3}{2} \frac{\dot{\epsilon}_{\text{vM}}^{\text{in}}}{\beta_{\text{vM}^*}(\sigma_{\text{vM}})} \boldsymbol{\beta} \right]. \quad (5.33)$$

The evolution equation (4.27) for the softening variable Γ is adapted to three-dimensional stress and strain states by introducing the VON MISES stress and inelastic strain rate [42]:

$$\dot{\Gamma} = C_{\Gamma} [\Gamma_*(\sigma_{\text{vM}}) - \Gamma] \dot{\epsilon}_{\text{vM}}^{\text{in}}. \quad (5.34)$$

Finally, all evolution equations have been derived for the three-dimensional phase mixture model. For a prescribed stress state $\boldsymbol{\sigma}$, the system of the ODEs (5.32)–(5.34) must be solved in conjunction with the ICs. For simulating the response of a virgin material, the following ICs hold:

$$\boldsymbol{\epsilon}^{\text{in}}(t=0) = \mathbf{0}, \quad \boldsymbol{\beta}(t=0) = \mathbf{0}, \quad \Gamma(t=0) = 1. \quad (5.35)$$

If a process is controlled by the total strain rate $\dot{\boldsymbol{\epsilon}}$, the following differential equation with respect to the stress $\boldsymbol{\sigma}$ is solved in conjunction with Eqs. (5.33) and (5.34), while the inelastic strain rate is computed using Eq. (5.32):

$$\begin{aligned} \dot{\boldsymbol{\sigma}} = & K(T) \dot{\epsilon}_{\text{v}} \mathbf{I} + 2G(T) (\dot{\boldsymbol{\epsilon}} - \dot{\boldsymbol{\epsilon}}^{\text{in}}) + \left(\frac{dK(T)}{dT} + \frac{2}{3} \frac{dG(T)}{dT} \right) \dot{T} \frac{\sigma_{\text{m}}}{K(T)} \mathbf{I} \\ & + \frac{1}{G(T)} \frac{dG(T)}{dT} \dot{T} \boldsymbol{\sigma}'. \end{aligned} \quad (5.36)$$

Equation (5.36) is obtained by differentiating Eq. (5.12) once with respect to the time and rearranging the resulting expression with respect to the time derivative of the stress tensor. For processes controlled by the total strain rate, the following ICs can be applied for a virgin material:

$$\boldsymbol{\sigma}(t=0) = \mathbf{0}, \quad \boldsymbol{\beta}(t=0) = \mathbf{0}, \quad \Gamma(t=0) = 1. \quad (5.37)$$

Since the model has already been calibrated in its one-dimensional formulation in Sect. 4.2, the determined parameters and functions are also applied to the three-dimensional model. The material parameters are listed in Table 4.2. For the sake of completeness, let us recall the determined functions and – if necessary – reformulate with respect to three-dimensional stress states:

- the temperature response function for the YOUNG's modulus, cf. Eq. (4.34):

$$E(T) = f_E(T) = C_1 + C_2 T^3,$$

5 Three-Dimensional Phase Mixture Model

- the temperature response function for the inelastic strain rate, cf. Eq. (4.37):

$$f_T(T) = \exp\left(-\frac{Q}{RT}\right),$$

- the stress response function for the inelastic strain rates in the initial and the steady state, cf. Eq. (4.53):

$$f_{\sigma_i}(\tilde{\sigma}_{vM}) = a_i \sinh\left(\frac{\tilde{\sigma}_{vM}}{b_i}\right) \left[1 + \left(\frac{\tilde{\sigma}_{vM}}{c_i}\right)^{m_i}\right] \quad \forall i \in \{\text{st, init}\}. \quad (5.38)$$

- the stress response function for the saturation backstress, cf. Eq. (4.65):

$$\beta_{vM\star}(\sigma_{vM}) = \frac{2a_\beta}{1 + \exp(-b_\beta\sigma_{vM})} - a_\beta, \quad (5.39)$$

- and the stress response function for the saturation softening variable, cf. Eq. (4.71):

$$\Gamma_\star(\sigma_{vM}) = \frac{a_\Gamma}{1 + \exp[-b_\Gamma(\sigma_{vM} - c_\Gamma)]}. \quad (5.40)$$

Because three-dimensional stress and deformation states are the concern of the current chapter, two independent elastic parameters are required to determine the isotropic linear elastic behavior [68, 142]. Since the experimental set-up described in Chapt. 3 does not provide the data to determine additional elastic parameters (except for the YOUNG's modulus E), we make use of experimental data for the shear modulus G published in [13] with respect to the alloy X20CrMoV12-1. In [13], specific measured values of the shear modulus in the temperature range $298 \text{ K} \leq T \leq 973 \text{ K}$ are given. Based on these values, the temperature dependence of the shear modulus is approximated with a cubic polynomial, in analogy to the temperature response function of the YOUNG's modulus, cf. Eq. (4.34):

$$G(T) = C_3 + C_4 T^3, \quad (5.41)$$

where C_3 and C_4 are material parameters:

$$C_3 = 82.6 \times 10^3 \text{ MPa}, \quad C_4 = -2.87 \times 10^{-5} \text{ MPa K}^{-3}. \quad (5.42)$$

Figure 5.1 depicts the experimental values for the shear modulus depending on the temperature in conjunction with the temperature response function according to Eq. (5.41). Note that the bulk modulus K and the POISSON's ratio ν can be computed based on Eq. (2.46). Finally, all governing equations have been presented, and the required material parameters and functions have been provided. Considering the two additional material parameters in Eq. (5.42), a total of 16 temperature-independent material parameters is required by the three-dimensional phase mixture model, compare also to the discussion at the end of Sect. 4.3.

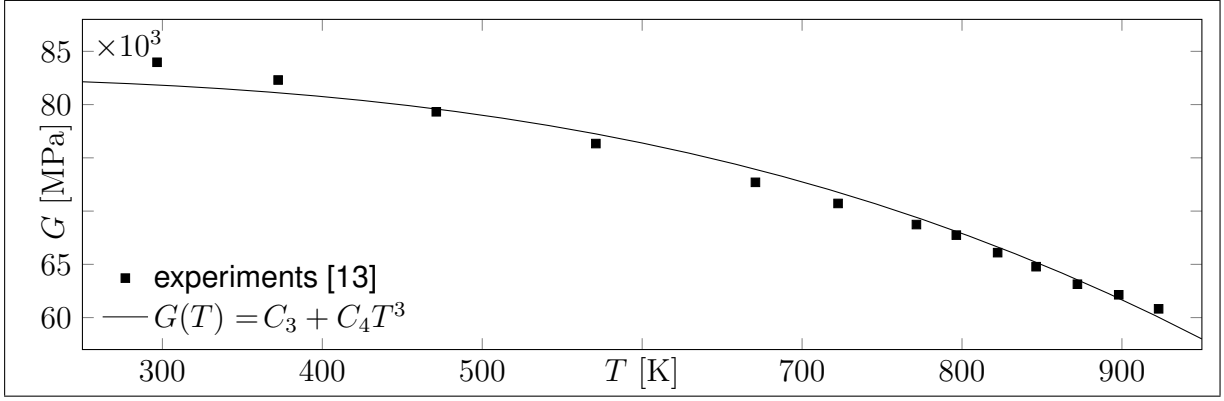


Figure 5.1: Calibration of the temperature response function for the shear modulus G .

5.2 Thermodynamic Consistency

In continuum mechanics, the second law of thermodynamics postulates a nonnegative entropy production [69, 74]. The local form of the second law of thermodynamics is the CLAUSIUS-DUHEM inequality, which must be fulfilled by a constitutive model. For isothermal processes, the CLAUSIUS-DUHEM inequality reduces to the CLAUSIUS-PLANCK inequality [69, 142]:

$$\boldsymbol{\sigma} : \dot{\boldsymbol{\epsilon}} \geq \dot{\mathcal{Y}}, \quad (5.43)$$

where \mathcal{Y} denotes the HELMHOLTZ free energy. In this section, it is checked whether the three-dimensional phase mixture model is in agreement with the CLAUSIUS-PLANCK inequality. Therefore, the free energy of the mixture is determined based on the free energies of each phase and their corresponding volume fractions [86, 87, 143]:

$$\mathcal{Y} = \eta_s \mathcal{Y}_s + \eta_h \mathcal{Y}_h. \quad (5.44)$$

Since the time derivative of the free energy is required in Eq. (5.43), Eq. (5.44) is differentiated with respect to time, while the volume fraction of the soft phase η_s is replaced using Eq. (4.3):

$$\dot{\mathcal{Y}} = \dot{\eta}_h (\mathcal{Y}_h - \mathcal{Y}_s) + (1 - \eta_h) \dot{\mathcal{Y}}_s + \eta_h \dot{\mathcal{Y}}_h. \quad (5.45)$$

The free energy of each phase and the corresponding derivatives with respect to time are determined based on the elastic parts [142]:

$$\mathcal{Y}_k = \frac{1}{2} \boldsymbol{\sigma}_k : \boldsymbol{\epsilon}_k^{\text{el}}, \quad (5.46)$$

$$\dot{\mathcal{Y}}_k = \boldsymbol{\sigma}_k : \dot{\boldsymbol{\epsilon}}_k^{\text{el}}. \quad (5.47)$$

Inserting Eqs. (5.46) and (5.47) into Eq. (5.45) results in:

$$\dot{\mathcal{Y}} = \frac{1}{2} \dot{\eta}_h (\boldsymbol{\sigma}_h : \boldsymbol{\epsilon}_h^{\text{el}} - \boldsymbol{\sigma}_s : \boldsymbol{\epsilon}_s^{\text{el}}) + (1 - \eta_h) \boldsymbol{\sigma}_s : \dot{\boldsymbol{\epsilon}}_s^{\text{el}} + \eta_h \boldsymbol{\sigma}_h : \dot{\boldsymbol{\epsilon}}_h^{\text{el}}. \quad (5.48)$$

In a next step, the left-hand side of Eq. (5.43) is evaluated taking Eqs. (5.1) and (5.2) into account:

$$\boldsymbol{\sigma} : \dot{\boldsymbol{\epsilon}} = (1 - \eta_h) \boldsymbol{\sigma}_s : \dot{\boldsymbol{\epsilon}}_s + \eta_h \boldsymbol{\sigma}_h : \dot{\boldsymbol{\epsilon}}_h. \quad (5.49)$$

5 Three-Dimensional Phase Mixture Model

Now, Eqs. (5.48) and (5.49) are inserted into Eq. (5.43), and the additive split of the strains, cf. Eq. (5.3), is employed:

$$(1 - \eta_h) \boldsymbol{\sigma}_s : \dot{\boldsymbol{\epsilon}}_s^{\text{in}} + \eta_h \boldsymbol{\sigma}_h : \dot{\boldsymbol{\epsilon}}_h^{\text{in}} \geq \frac{1}{2} \dot{\eta}_h (\boldsymbol{\sigma}_h : \boldsymbol{\epsilon}_h^{\text{el}} - \boldsymbol{\sigma}_s : \boldsymbol{\epsilon}_s^{\text{el}}). \quad (5.50)$$

The right-hand side of Eq. (5.50) is simplified based on the elastic law according to Eqs. (5.5) and (5.9). In addition, the deviatoric stresses are introduced on the left-hand side since $\text{tr}(\dot{\boldsymbol{\epsilon}}_k^{\text{in}}) = 0$ holds, as discussed in Sect. 5.1:

$$(1 - \eta_h) \boldsymbol{\sigma}'_s : \dot{\boldsymbol{\epsilon}}_s^{\text{in}} + \eta_h \boldsymbol{\sigma}'_h : \dot{\boldsymbol{\epsilon}}_h^{\text{in}} \geq \frac{1}{6G} \dot{\eta}_h (\sigma_{vM_h}^2 - \sigma_{vM_s}^2). \quad (5.51)$$

In the following, the left-hand side of Eq. (5.51) is examined in detail, and the deviatoric stresses are replaced by Eqs. (5.24) and (5.25). Introducing the effective stress tensor $\tilde{\boldsymbol{\sigma}}'$ according to Eq. (5.28) results in:

$$(1 - \eta_h) \boldsymbol{\sigma}'_s : \dot{\boldsymbol{\epsilon}}_s^{\text{in}} + \eta_h \boldsymbol{\sigma}'_h : \dot{\boldsymbol{\epsilon}}_h^{\text{in}} = \tilde{\boldsymbol{\sigma}}' : [(1 - \eta_h) \dot{\boldsymbol{\epsilon}}_s^{\text{in}} + \eta_h \dot{\boldsymbol{\epsilon}}_h^{\text{in}}] + \Gamma \boldsymbol{\beta} : \dot{\boldsymbol{\epsilon}}_h^{\text{in}}. \quad (5.52)$$

In order to simplify Eq. (5.52), the inelastic strain rate $\dot{\boldsymbol{\epsilon}}^{\text{in}}$ of the mixture is determined based on the time derivative of Eq. (5.13):

$$\dot{\boldsymbol{\epsilon}}^{\text{in}} = (1 - \eta_h) \dot{\boldsymbol{\epsilon}}_s^{\text{in}} + \eta_h \dot{\boldsymbol{\epsilon}}_h^{\text{in}} + \dot{\eta}_h (\boldsymbol{\epsilon}_h^{\text{in}} - \boldsymbol{\epsilon}_s^{\text{in}}). \quad (5.53)$$

The difference in the inelastic strains in the last term of Eq. (5.53) is replaced using Eqs. (5.1), (5.3), and (5.5):

$$\boldsymbol{\epsilon}_h^{\text{in}} - \boldsymbol{\epsilon}_s^{\text{in}} = \boldsymbol{\epsilon}_s^{\text{el}} - \boldsymbol{\epsilon}_h^{\text{el}} = \frac{1}{2G} (\boldsymbol{\sigma}'_s - \boldsymbol{\sigma}'_h). \quad (5.54)$$

Then, the deviatoric stresses in Eq. (5.54) are substituted again by Eqs. (5.24) and (5.25), and the definition of the softening variable is taken into account, cf. Eq. (4.15):

$$\boldsymbol{\epsilon}_h^{\text{in}} - \boldsymbol{\epsilon}_s^{\text{in}} = -\frac{1}{2G} \frac{1 - \eta_{h_0}}{\eta_{h_0}} \frac{1}{1 - \eta_h} \boldsymbol{\beta}. \quad (5.55)$$

Equation (5.55) is inserted into Eq. (5.53) to evaluate the inelastic strain rate of the mixture:

$$\dot{\boldsymbol{\epsilon}}^{\text{in}} = (1 - \eta_h) \dot{\boldsymbol{\epsilon}}_s^{\text{in}} + \eta_h \dot{\boldsymbol{\epsilon}}_h^{\text{in}} - \frac{1}{2G} \dot{\eta}_h \frac{1 - \eta_{h_0}}{\eta_{h_0}} \frac{1}{1 - \eta_h} \boldsymbol{\beta}. \quad (5.56)$$

Finally, Eq. (5.56) is used to substitute the expression in the square brackets in Eq. (5.52):

$$(1 - \eta_h) \boldsymbol{\sigma}'_s : \dot{\boldsymbol{\epsilon}}_s^{\text{in}} + \eta_h \boldsymbol{\sigma}'_h : \dot{\boldsymbol{\epsilon}}_h^{\text{in}} = \tilde{\boldsymbol{\sigma}}' : \dot{\boldsymbol{\epsilon}}^{\text{in}} + \frac{1}{2G} \dot{\eta}_h \frac{1 - \eta_{h_0}}{\eta_{h_0}} \frac{1}{1 - \eta_h} \tilde{\boldsymbol{\sigma}}' : \boldsymbol{\beta} + \Gamma \boldsymbol{\beta} : \dot{\boldsymbol{\epsilon}}_h^{\text{in}}. \quad (5.57)$$

In a next step, the right-hand side of Eq. (5.51) is recast. The difference in the VON MISES stresses of both phases is evaluated based on Eq. (5.17). Note that the VON MISES stress with respect to the hard phase is calculated in analogy to Eq. (5.17). Furthermore, the deviatoric stresses are replaced once more by Eqs. (5.24) and (5.25):

$$\sigma_{vM_h}^2 - \sigma_{vM_s}^2 = \frac{3}{2} \left(\frac{1 - \eta_{h_0}}{\eta_{h_0}} + \Gamma \right) \boldsymbol{\beta} : \left[2\boldsymbol{\sigma}' + \left(\frac{1 - \eta_{h_0}}{\eta_{h_0}} - \Gamma \right) \boldsymbol{\beta} \right]. \quad (5.58)$$

Equations (5.57) and (5.58) are inserted into Eq. (5.51), all terms containing $\dot{\eta}_h$ are summed, and Eq. (5.21) is taken into account to introduce the VON MISES backstress β_{vM} into the equations:

$$\tilde{\sigma}' : \dot{\epsilon}^{\text{in}} + \Gamma \beta : \dot{\epsilon}_h^{\text{in}} - \frac{3}{8G} \dot{\eta}_h \left(\frac{1 - \eta_{h0}}{\eta_{h0}} \frac{1}{1 - \eta_h} \right)^2 \beta_{vM}^2 \geq 0. \quad (5.59)$$

Based on the definition of the softening variable in Eq. (4.15), the expression $\dot{\eta}_h$ is replaced by the time derivative of the softening variable:

$$\dot{\eta}_h = (1 - \eta_h)^2 \frac{\eta_{h0}}{1 - \eta_{h0}} \dot{\Gamma}. \quad (5.60)$$

One inserts Eq. (5.60) into Eq. (5.59) to obtain the final inequality:

$$\tilde{\sigma}' : \dot{\epsilon}^{\text{in}} + \Gamma \beta : \dot{\epsilon}_h^{\text{in}} - \frac{3}{8G} \dot{\Gamma} \frac{1 - \eta_{h0}}{\eta_{h0}} \beta_{vM}^2 \geq 0. \quad (5.61)$$

To guarantee the consistency with the second law of thermodynamics, this inequality must be fulfilled by the constitutive model. To begin with, the term $\tilde{\sigma}' : \dot{\epsilon}^{\text{in}}$ is examined. The inelastic strain rate can be replaced by Eq. (5.32). Considering the structure of the functions $f_{\sigma_{\text{init}}}(\tilde{\sigma}_{vM})$ and $f_T(T)$, cf. Eqs. (4.34) and (5.38), as well as the positive parameters in Table 4.2, it becomes obvious that $f_{\sigma_{\text{init}}}(\tilde{\sigma}_{vM}) \geq 0$ and $f_T(T) \geq 0$ hold such that the entire term $\tilde{\sigma}' : \dot{\epsilon}^{\text{in}}$ is nonnegative:

$$\tilde{\sigma}' : \dot{\epsilon}^{\text{in}} \geq 0. \quad (5.62)$$

In a next step, we consider the second summand in Eq. (5.61), the inelastic strain rate of the hard phase is replaced by Eq. (5.26), and the VON MISES backstress β_{vM} is introduced according to Eq. (5.21):

$$\Gamma \beta : \dot{\epsilon}_h^{\text{in}} = \frac{9}{4} \dot{\epsilon}_{vM}^{\text{in}} \Gamma \frac{\beta_{vM}^2}{\beta_{vM*}(\sigma_{vM})}. \quad (5.63)$$

Due to its definition in Eq. (4.15), the softening variable Γ is always positive. In addition, $\beta_{vM*}(\sigma_{vM}) \geq 0$ holds, cf. Eq. (5.39). Note that the VON MISES stresses and strains are always nonnegative due to their definitions, cf. e.g. Eqs. (5.16) and (5.17). For these reasons, also the second summand in Eq. (5.61) is nonnegative:

$$\Gamma \beta : \dot{\epsilon}_h^{\text{in}} \geq 0. \quad (5.64)$$

Since it has already been shown that the first two summands in Eq. (5.61) are nonnegative, cf. Eqs. (5.62) and (5.64), only the change in the softening variable with time $\dot{\Gamma}$ must be examined in the following. Because Eq. (5.61) must be fulfilled, $\dot{\Gamma}$ has to be nonnegative:

$$\dot{\Gamma} \leq 0. \quad (5.65)$$

The change in the softening variable is determined by the postulated evolution equation, cf. Eq. (5.34). For the sake of clarity, we recall this equation:

$$\dot{\Gamma} = C_\Gamma [\Gamma_*(\sigma_{vM}) - \Gamma] \dot{\epsilon}_{vM}^{\text{in}}.$$

The parameter C_Γ is positive, cf. Table 4.2, and $\Gamma_*(\sigma_{vM}) \leq \Gamma$ holds due to the definitions of the softening variable and the corresponding saturation value in Eqs. (4.15) and (4.17) such that the condition (5.65) as well as Eq. (5.61) are fulfilled. To conclude, the CLAUSIUS-PLANCK inequality is valid, i.e. the phase mixture model is thermodynamically consistent with respect to the present calibration. Thereby, one should keep in mind that stationary temperatures are presumed. The phase mixture model is primarily a mechanical model, which accounts for changes in the material parameters due to instationary temperature fields. However, since the temperature changes relatively slowly during the start-ups or shut-downs of power plants, the simplification $\dot{T} \approx 0$ is justified. Considering applications with fast temperature changes, one should set up a thermo-mechanical model, which must fulfill the CLAUSIUS-DUHEM inequality [69].

5.3 Finite Element Analyses

This section presents the implementation of the three-dimensional phase mixture model into the finite element code ABAQUS employing a user material subroutine (UMAT) [144]. Note that the content of this section is based on [145], where selected results are shown. The theoretical background of the FEM has already been discussed in detail in Sect. 2.2. At the end of Sect. 2.2.1, it is shown that the stress as well as the internal variables must be updated and the tangent operator should be determined in order to implement a nonlinear material model into the FEM, which can be achieved by means of a UMAT.

The current section is divided into four parts. Section 5.3.1 presents the numerical integration of the evolution equations, discussed in Sect. 5.1, by means of the backward EULER method. In order to solve the resulting nonlinear system of equations, the NEWTON-RAPHSON method is applied, as already discussed in Sect. 2.2.1. Due to the application of the NEWTON-RAPHSON method, the derivatives of several residual quantities with respect to the stress and the internal variables must be determined, which is derived in Sect. 5.3.2. Based on these results, the final stress update algorithm and the computation of the tangent operator are described in Sect. 5.3.3. Finally, various finite element analyses are presented in Sect. 5.3.4 in order to verify the implementation of the phase mixture model.

5.3.1 Backward EULER Method

As shown in Sect. 5.1, the phase mixture model requires the solution of three evolution equations with respect to the stress σ , the backstress β , and the softening variable Γ , cf. Eqs. (5.32)–(5.34). These evolution equations must be integrated with respect to time. For this purpose, two classes of numerical methods are available: explicit and implicit methods. Explicit methods determine an unknown equilibrium state at the time step t_{n+1} only by using quantities with respect to the previous time step t_n [103]. Consequently, explicit methods are straightforward to implement. However, it is well known that explicit methods are only conditionally stable, and therefore their stability depends on the selected time step size [146], i.e. a critical time step size can be mathematically derived for each explicit time integration method based on the COURANT-FRIEDRICHS-LEWY condition [147]. As an alternative, implicit methods can be employed. Here, the computation of the quantities with respect to the new equilibrium state t_{n+1} is not only based on the previous time steps, but also includes the current and future time steps, such that a nonlinear system of equations must be solved at every time step [103]. The stability of implicit methods is independent from the increment size (unconditional stability), and consequently we make use of an implicit

method for the numerical integration, i.e. the backward EULER method. Due to its simplicity, this implicit method is commonly employed for the implementation of nonlinear material models, cf. e.g. [58, 105, 106, 111]. Suppose that we would like to find a solution for the ODE $\dot{\mathbf{Y}} = \mathcal{F}(\mathbf{Y}, t)$ with respect to the tensorial variable \mathbf{Y} . A time increment Δt is prescribed, and the variable \mathbf{Y}_n at the time step t_n is known. Then, the solution at the time step $t_{n+1} = t_n + \Delta t$ is approximated by the backward EULER method as follows [103]:

$$\mathbf{Y}_{n+1} = \mathbf{Y}_n + \Delta t \mathcal{F}(\mathbf{Y}_{n+1}, t_{n+1}). \quad (5.66)$$

In the following, we will apply the approximation according to Eq. (5.66) to the governing equations of the phase mixture model. With respect to an equilibrium state at the time step t_n , all quantities, i.e. the stress, the backstress, the softening variable, and the strains, are known. Based on the prescribed temperature, strain, and time increments ΔT_{n+1} , $\Delta \boldsymbol{\epsilon}_{n+1}$, and Δt_{n+1} , respectively, all other quantities with respect to the unknown equilibrium state at the time step t_{n+1} have to be determined. With the backward EULER method, the strains, the temperature, the stress, and the internal variables can be updated as follows [104]:

$$\boldsymbol{\epsilon}_{n+1} = \boldsymbol{\epsilon}_n + \Delta \boldsymbol{\epsilon}_{n+1}, \quad (5.67)$$

$$\boldsymbol{\epsilon}_{n+1}^{\text{in}} = \boldsymbol{\epsilon}_n^{\text{in}} + \Delta \boldsymbol{\epsilon}_{n+1}^{\text{in}}, \quad (5.68)$$

$$T_{n+1} = T_n + \Delta T_{n+1}, \quad (5.69)$$

$$\boldsymbol{\sigma}_{n+1} = \boldsymbol{\sigma}_n + \Delta \boldsymbol{\sigma}_{n+1}, \quad (5.70)$$

$$\boldsymbol{\beta}_{n+1} = \boldsymbol{\beta}_n + \Delta \boldsymbol{\beta}_{n+1}, \quad (5.71)$$

$$\Gamma_{n+1} = \Gamma_n + \Delta \Gamma_{n+1}. \quad (5.72)$$

For the sake of brevity, the index \square_{n+1} is omitted in the remainder of this chapter. Thus, if not stated otherwise, all quantities are evaluated with respect to the time step t_{n+1} . We apply the concept described in Eq. (5.66) to the evolution equations, cf. Eqs. (5.32)–(5.34):

$$\Delta \boldsymbol{\epsilon}^{\text{in}} = \frac{3}{2} \Delta t f_{\sigma_{\text{init}}}(\tilde{\sigma}_{\text{vM}}) f_T(T) \frac{\tilde{\boldsymbol{\sigma}}'}{\tilde{\sigma}_{\text{vM}}}, \quad (5.73)$$

$$\Delta \boldsymbol{\beta} = \frac{1}{G} \frac{dG}{dT} \Delta T \boldsymbol{\beta} + 2G \frac{\eta_{h_0}}{1 - \eta_{h_0}} \left[\Delta \boldsymbol{\epsilon}^{\text{in}} - \frac{3}{2} \frac{\Delta \epsilon_{\text{vM}}^{\text{in}}}{\beta_{\text{vM},*}(\sigma_{\text{vM}})} \boldsymbol{\beta} \right], \quad (5.74)$$

$$\Delta \Gamma = C_\Gamma [\Gamma_*(\sigma_{\text{vM}}) - \Gamma] \Delta \epsilon_{\text{vM}}^{\text{in}}. \quad (5.75)$$

In addition, the additive split of the strain tensor into the elastic and the inelastic part holds, cf. Eq. (2.54). Inserting Eqs. (5.67) and (5.68) into Eq. (2.54) results in:

$$\boldsymbol{\epsilon}^{\text{el}} = \boldsymbol{\epsilon}_n + \Delta \boldsymbol{\epsilon} - (\boldsymbol{\epsilon}_n^{\text{in}} + \Delta \boldsymbol{\epsilon}^{\text{in}}). \quad (5.76)$$

Afterwards, Eq. (5.76) is inserted into HOOKE's law, cf. Eq. (2.45), taking the relation $\text{tr}(\boldsymbol{\epsilon}_n^{\text{in}}) = \text{tr}(\Delta \boldsymbol{\epsilon}^{\text{in}}) = 0$ (cf. the discussion in Sect. 2.1.4.2) into account:

$$\boldsymbol{\sigma} = K \text{tr}(\boldsymbol{\epsilon}_n + \Delta \boldsymbol{\epsilon}) \mathbf{I} + 2G (\boldsymbol{\epsilon}_n + \Delta \boldsymbol{\epsilon} - \boldsymbol{\epsilon}_n^{\text{in}} - \Delta \boldsymbol{\epsilon}^{\text{in}}). \quad (5.77)$$

In a next step, Eq. (5.77) is reformulated by introducing the elastic stiffness tensor \mathcal{C} of fourth rank [104, 142]:

$$\boldsymbol{\sigma} = \mathcal{C} : (\boldsymbol{\epsilon}_n + \Delta \boldsymbol{\epsilon} - \boldsymbol{\epsilon}_n^{\text{in}} - \Delta \boldsymbol{\epsilon}^{\text{in}}). \quad (5.78)$$

For linear elastic and isotropic materials, the elastic stiffness tensor is defined as:

$$\mathbf{C} = \frac{1}{3} (3K - 2G) \mathbf{I} \otimes \mathbf{I} + 2G\mathcal{I}, \quad \mathcal{I} = \mathbf{e}_i \otimes \mathbf{e}_j \otimes \mathbf{e}_j \otimes \mathbf{e}_i, \quad (5.79)$$

where \mathcal{I} denotes the unit tensor of fourth rank. Equations (5.71)–(5.75) and (5.78) constitute a nonlinear system of algebraic equations. This system must be solved for prescribed deformation states with respect to the three unknowns, i.e. the stress $\boldsymbol{\sigma}$, the backstress $\boldsymbol{\beta}$, and the softening variable Γ . Therefore, the NEWTON-RAPHSON method is used [103], and Eqs. (5.71), (5.72), and (5.78) are reformulated:

$$\mathbf{R}_\sigma^i = \mathbf{0}, \quad (5.80)$$

$$\mathbf{R}_\beta^i = \mathbf{0}, \quad (5.81)$$

$$r_\Gamma^i = 0, \quad (5.82)$$

where the residual quantities \mathbf{R}_σ^i , \mathbf{R}_β^i , and r_Γ^i are defined as:

$$\mathbf{R}_\sigma^i = -\boldsymbol{\epsilon} + \boldsymbol{\epsilon}_n^{\text{in}} + \mathbf{C}^{-1} : \boldsymbol{\sigma}^i + \Delta\boldsymbol{\epsilon}^{\text{in}^i}, \quad (5.83)$$

$$\mathbf{R}_\beta^i = -\boldsymbol{\beta}_n + \boldsymbol{\beta}^i - \Delta\boldsymbol{\beta}^i, \quad (5.84)$$

$$r_\Gamma^i = -\Gamma_n + \Gamma^i - \Delta\Gamma^i. \quad (5.85)$$

As used in Sect. 2.2, the index \square^i represents the iteration step. Note that Eqs. (5.73)–(5.75) still hold to compute the increments with respect to the inelastic strain, the backstress, and the softening variable.

5.3.2 Derivatives for the Linearization

The nonlinear system of equations (5.80)–(5.82) is solved by means of the NEWTON-RAPHSON method. For this purpose, the equations must be linearized, and consequently the derivatives of the residual quantities \mathbf{R}_σ^i , \mathbf{R}_β^i , and r_Γ^i with respect to the stress $\boldsymbol{\sigma}$, the backstress $\boldsymbol{\beta}$, and the softening variable Γ have to be determined, which is the main goal of the current section.

5.3.2.1 Derivatives of the Stress Response Functions

To begin with, the required derivatives of the stress response functions for the inelastic strain $f_{\sigma_{\text{init}}}(\tilde{\sigma}_{\text{vM}})$, the saturation backstress $\beta_{\text{vM}\star}(\sigma_{\text{vM}})$, and the saturation softening variable $\Gamma_\star(\sigma_{\text{vM}})$ with respect to their arguments can be given as closed-form expressions based on the definitions of the functions in Eqs. (5.38)–(5.40):

$$\begin{aligned} \frac{\partial f_{\sigma_{\text{init}}}(\tilde{\sigma}_{\text{vM}})}{\partial \tilde{\sigma}_{\text{vM}}} &= \frac{a_{\text{init}}}{b_{\text{init}}} \cosh\left(\frac{\tilde{\sigma}_{\text{vM}}}{b_{\text{init}}}\right) \left[1 + \left(\frac{\tilde{\sigma}_{\text{vM}}}{c_{\text{init}}}\right)^{m_{\text{init}}} \right] \\ &\quad + \frac{a_{\text{init}} m_{\text{init}}}{\tilde{\sigma}_{\text{vM}}} \sinh\left(\frac{\tilde{\sigma}_{\text{vM}}}{b_{\text{init}}}\right) \left(\frac{\tilde{\sigma}_{\text{vM}}}{c_{\text{init}}}\right)^{m_{\text{init}}}, \end{aligned} \quad (5.86)$$

$$\frac{\partial \beta_{\text{vM}\star}(\sigma_{\text{vM}})}{\partial \sigma_{\text{vM}}} = \frac{2a_\beta b_\beta \exp(-b_\beta \sigma_{\text{vM}})}{[1 + \exp(-b_\beta \sigma_{\text{vM}})]^2}, \quad (5.87)$$

$$\frac{\partial \Gamma_\star(\sigma_{\text{vM}})}{\partial \sigma_{\text{vM}}} = \frac{a_\Gamma b_\Gamma \exp[-b_\Gamma (\sigma_{\text{vM}} - c_\Gamma)]}{\{1 + \exp[-b_\Gamma (\sigma_{\text{vM}} - c_\Gamma)]\}^2}. \quad (5.88)$$

5.3.2.2 Derivatives of the VON MISES Variables

Furthermore, the derivative of the VON MISES stress σ_{vM} with respect to the stress tensor $\boldsymbol{\sigma}$ is determined based on the standard rules of tensor calculus, cf. [69, 148]:

$$\begin{aligned} \frac{\partial \sigma_{vM}}{\partial \boldsymbol{\sigma}} &= \frac{\partial \sqrt{\frac{3}{2} \boldsymbol{\sigma}' : \boldsymbol{\sigma}'}}{\partial \boldsymbol{\sigma}'} : \frac{\partial \boldsymbol{\sigma}'}{\partial \boldsymbol{\sigma}} = \frac{3}{4} \frac{1}{\sigma_{vM}} \left(\frac{\partial \boldsymbol{\sigma}'}{\partial \boldsymbol{\sigma}'} : \boldsymbol{\sigma}' + \boldsymbol{\sigma}' : \frac{\partial \boldsymbol{\sigma}'}{\partial \boldsymbol{\sigma}'} \right) : \left(\boldsymbol{\mathcal{I}} - \frac{1}{3} \boldsymbol{I} \otimes \boldsymbol{I} \right) \\ &= \frac{3}{2} \frac{1}{\sigma_{vM}} \boldsymbol{\sigma}'. \end{aligned} \quad (5.89)$$

In analogy, the derivatives of other VON MISES quantities are determined here, since they are required to compute the derivatives of the residual variables in the following sections:

$$\frac{\partial \sigma_{vM}}{\partial \boldsymbol{\sigma}'} = \frac{3}{2} \frac{1}{\sigma_{vM}} \boldsymbol{\sigma}', \quad (5.90)$$

$$\frac{\partial \tilde{\sigma}_{vM}}{\partial \boldsymbol{\sigma}} = \frac{\partial \tilde{\sigma}_{vM}}{\partial \tilde{\boldsymbol{\sigma}}} = \frac{\partial \tilde{\sigma}_{vM}}{\partial \tilde{\boldsymbol{\sigma}'}} = \frac{3}{2} \frac{1}{\tilde{\sigma}_{vM}} \tilde{\boldsymbol{\sigma}'}, \quad (5.91)$$

$$\frac{\partial \boldsymbol{\varepsilon}_{vM}^{in}}{\partial \boldsymbol{\varepsilon}^{in}} = \frac{2}{3} \frac{1}{\boldsymbol{\varepsilon}_{vM}^{in}} \boldsymbol{\varepsilon}^{in} \quad \text{with } \boldsymbol{\varepsilon}_{vM}^{in} = \sqrt{\frac{2}{3} \boldsymbol{\varepsilon}^{in} : \boldsymbol{\varepsilon}^{in}}. \quad (5.92)$$

Note that the VON MISES stress σ_{vM} and the effective VON MISES stress $\tilde{\sigma}_{vM}$ are introduced in Eqs. (5.28) and (2.64), respectively. The inelastic VON MISES strain $\boldsymbol{\varepsilon}_{vM}^{in}$ is defined in analogy to Eq. (5.16).

5.3.2.3 Derivatives of the Strain Increments

This section focuses on the derivatives of the inelastic strain increment $\Delta \boldsymbol{\varepsilon}^{in}$ and the corresponding VON MISES quantity $\Delta \boldsymbol{\varepsilon}_{vM}^{in}$ with respect to the stress $\boldsymbol{\sigma}$, the backstress $\boldsymbol{\beta}$, and the softening variable T , which are required to calculate the derivatives of the residual quantities. Based on Eq. (5.73), the derivative of the inelastic strain increment with respect to the stress is computed:

$$\frac{\partial \Delta \boldsymbol{\varepsilon}^{in}}{\partial \boldsymbol{\sigma}} = \frac{3}{2} \frac{\Delta t f_T(T)}{\tilde{\sigma}_{vM}} \left[\frac{\partial f_{\sigma_{init}}(\tilde{\sigma}_{vM})}{\partial \boldsymbol{\sigma}} \otimes \tilde{\boldsymbol{\sigma}'} + \frac{f_{\sigma_{init}}(\tilde{\sigma}_{vM})}{\tilde{\sigma}_{vM}} \left(\tilde{\sigma}_{vM} \frac{\partial \tilde{\boldsymbol{\sigma}'}}{\partial \boldsymbol{\sigma}} - \frac{\partial \tilde{\sigma}_{vM}}{\partial \boldsymbol{\sigma}} \otimes \tilde{\boldsymbol{\sigma}'} \right) \right]. \quad (5.93)$$

Considering Eq. (5.91) and the relations

$$\frac{\partial f_{\sigma_{init}}(\tilde{\sigma}_{vM})}{\partial \boldsymbol{\sigma}} = \frac{\partial f_{\sigma_{init}}(\tilde{\sigma}_{vM})}{\partial \tilde{\sigma}_{vM}} \frac{\partial \tilde{\sigma}_{vM}}{\partial \boldsymbol{\sigma}} = \frac{3}{2} \frac{1}{\tilde{\sigma}_{vM}} \frac{\partial f_{\sigma_{init}}(\tilde{\sigma}_{vM})}{\partial \tilde{\sigma}_{vM}} \tilde{\boldsymbol{\sigma}'}, \quad (5.94)$$

$$\frac{\partial \tilde{\boldsymbol{\sigma}'}}{\partial \boldsymbol{\sigma}} = \boldsymbol{\mathcal{I}} - \frac{1}{3} \boldsymbol{I} \otimes \boldsymbol{I}, \quad (5.95)$$

Eq. (5.93) is simplified as follows:

$$\begin{aligned} \frac{\partial \Delta \boldsymbol{\varepsilon}^{in}}{\partial \boldsymbol{\sigma}} &= \frac{3}{2} \frac{\Delta t f_T(T)}{\tilde{\sigma}_{vM}} \left[\frac{3}{2} \left(\frac{1}{\tilde{\sigma}_{vM}} \frac{\partial f_{\sigma_{init}}(\tilde{\sigma}_{vM})}{\partial \tilde{\sigma}_{vM}} - \frac{f_{\sigma_{init}}(\tilde{\sigma}_{vM})}{\tilde{\sigma}_{vM}^2} \right) \tilde{\boldsymbol{\sigma}'} \otimes \tilde{\boldsymbol{\sigma}'} \right. \\ &\quad \left. + f_{\sigma_{init}}(\tilde{\sigma}_{vM}) \left(\boldsymbol{\mathcal{I}} - \frac{1}{3} \boldsymbol{I} \otimes \boldsymbol{I} \right) \right]. \end{aligned} \quad (5.96)$$

5 Three-Dimensional Phase Mixture Model

In the next step, the derivative of the incremental inelastic VON MISES strain $\Delta\varepsilon_{vM}^{in}$ is evaluated using Eqs. (5.92) and (5.96):

$$\frac{\partial\Delta\varepsilon_{vM}^{in}}{\partial\boldsymbol{\sigma}} = \frac{\partial\Delta\varepsilon_{vM}^{in}}{\partial\Delta\boldsymbol{\varepsilon}^{in}} : \frac{\partial\Delta\boldsymbol{\varepsilon}^{in}}{\partial\boldsymbol{\sigma}} = \frac{3}{2} \frac{(\Delta t)^2 f_T^2(T) f_{\sigma_{init}}(\tilde{\sigma}_{vM})}{\tilde{\sigma}_{vM} \Delta\varepsilon_{vM}^{in}} \frac{\partial f_{\sigma_{init}}(\tilde{\sigma}_{vM})}{\partial\tilde{\sigma}_{vM}} \tilde{\boldsymbol{\sigma}}'. \quad (5.97)$$

In order to find a compact expression for the incremental inelastic VON MISES strain $\Delta\varepsilon_{vM}^{in}$, we insert Eq. (5.73) into the definition of the incremental inelastic VON MISES strain, cf. Eq. (5.16), and take Eq. (5.28) into account:

$$\Delta\varepsilon_{vM}^{in} = \sqrt{\frac{2}{3} \Delta\boldsymbol{\varepsilon}^{in} : \Delta\boldsymbol{\varepsilon}^{in}} = \sqrt{\frac{2}{3} \frac{(\Delta t)^2 f_T^2(T) f_{\sigma_{init}}^2(\tilde{\sigma}_{vM})}{\tilde{\sigma}_{vM}^2} \tilde{\boldsymbol{\sigma}}' : \tilde{\boldsymbol{\sigma}}'} = \Delta t f_T(T) f_{\sigma_{init}}(\tilde{\sigma}_{vM}). \quad (5.98)$$

Afterwards, Eq. (5.98) is inserted into Eq. (5.97) such that one obtains a final expression for the derivative of the incremental inelastic VON MISES strain with respect to the stress tensor:

$$\frac{\partial\Delta\varepsilon_{vM}^{in}}{\partial\boldsymbol{\sigma}} = \frac{3}{2} \frac{\Delta t f_T(T)}{\tilde{\sigma}_{vM}} \frac{\partial f_{\sigma_{init}}(\tilde{\sigma}_{vM})}{\partial\tilde{\sigma}_{vM}} \tilde{\boldsymbol{\sigma}}'. \quad (5.99)$$

Since the derivatives of the incremental inelastic strains with respect to the stress tensor have been determined in Eqs. (5.96) and (5.99), the corresponding derivatives with respect to the backstress are evaluated in the following. First, the derivative of the incremental inelastic strain tensor $\Delta\boldsymbol{\varepsilon}^{in}$ is calculated based on Eq. (5.73):

$$\frac{\partial\Delta\boldsymbol{\varepsilon}^{in}}{\partial\boldsymbol{\beta}} = \frac{3}{2} \frac{\Delta t f_T(T)}{\tilde{\sigma}_{vM}} \left[\frac{\partial f_{\sigma_{init}}(\tilde{\sigma}_{vM})}{\partial\boldsymbol{\beta}} \otimes \tilde{\boldsymbol{\sigma}}' + \frac{f_{\sigma_{init}}(\tilde{\sigma}_{vM})}{\tilde{\sigma}_{vM}} \left(\tilde{\sigma}_{vM} \frac{\partial\tilde{\boldsymbol{\sigma}}'}{\partial\boldsymbol{\beta}} - \frac{\partial\tilde{\sigma}_{vM}}{\partial\boldsymbol{\beta}} \otimes \tilde{\boldsymbol{\sigma}}' \right) \right]. \quad (5.100)$$

In the next step, Eq. (5.91) as well as the relations

$$\frac{\partial\tilde{\sigma}_{vM}}{\partial\boldsymbol{\beta}} = \frac{\partial\tilde{\sigma}_{vM}}{\partial\tilde{\boldsymbol{\sigma}}} : \frac{\partial\tilde{\boldsymbol{\sigma}}}{\partial\boldsymbol{\beta}} = -\frac{3}{2} \frac{\Gamma}{\tilde{\sigma}_{vM}} \tilde{\boldsymbol{\sigma}}', \quad (5.101)$$

$$\frac{\partial f_{\sigma_{init}}(\tilde{\sigma}_{vM})}{\partial\boldsymbol{\beta}} = \frac{\partial f_{\sigma_{init}}(\tilde{\sigma}_{vM})}{\partial\tilde{\sigma}_{vM}} \frac{\partial\tilde{\sigma}_{vM}}{\partial\boldsymbol{\beta}} = -\frac{3}{2} \frac{\Gamma}{\tilde{\sigma}_{vM}} \frac{\partial f_{\sigma_{init}}(\tilde{\sigma}_{vM})}{\partial\tilde{\sigma}_{vM}} \tilde{\boldsymbol{\sigma}}' \quad (5.102)$$

are taken into account to transform Eq. (5.100):

$$\begin{aligned} \frac{\partial\Delta\boldsymbol{\varepsilon}^{in}}{\partial\boldsymbol{\beta}} = & -\frac{3}{2} \frac{\Delta t f_T(T)}{\tilde{\sigma}_{vM}} \Gamma \left[\frac{3}{2} \frac{1}{\tilde{\sigma}_{vM}} \left(\frac{\partial f_{\sigma_{init}}(\tilde{\sigma}_{vM})}{\partial\tilde{\sigma}_{vM}} - \frac{f_{\sigma_{init}}(\tilde{\sigma}_{vM})}{\tilde{\sigma}_{vM}} \right) \tilde{\boldsymbol{\sigma}}' \otimes \tilde{\boldsymbol{\sigma}}' \right. \\ & \left. + f_{\sigma_{init}}(\tilde{\sigma}_{vM}) \boldsymbol{\mathcal{I}} \right]. \end{aligned} \quad (5.103)$$

Additionally, the derivative of the incremental inelastic VON MISES strain with respect to the backstress is determined analogously to Eq. (5.97). Here, Eqs. (5.92), (5.98), and (5.103) are taken into consideration:

$$\frac{\partial\Delta\varepsilon_{vM}^{in}}{\partial\boldsymbol{\beta}} = \frac{\partial\Delta\varepsilon_{vM}^{in}}{\partial\Delta\boldsymbol{\varepsilon}^{in}} : \frac{\partial\Delta\boldsymbol{\varepsilon}^{in}}{\partial\boldsymbol{\beta}} = -\frac{3}{2} \frac{\Delta t f_T(T)}{\tilde{\sigma}_{vM}} \frac{\partial f_{\sigma_{init}}(\tilde{\sigma}_{vM})}{\partial\tilde{\sigma}_{vM}} \Gamma \tilde{\boldsymbol{\sigma}}'. \quad (5.104)$$

So far, the derivatives of the incremental inelastic strains with respect to the backstress have been computed, cf. Eqs. (5.103) and (5.104). Thus, we proceed to evaluate the derivative of

the inelastic strain increment with respect to the softening variable considering Eq. (5.73):

$$\frac{\partial \Delta \boldsymbol{\epsilon}^{\text{in}}}{\partial \Gamma} = \frac{3}{2} \frac{\Delta t f_T(T)}{\tilde{\sigma}_{\text{vM}}} \left[\frac{\partial f_{\sigma_{\text{init}}}(\tilde{\sigma}_{\text{vM}})}{\partial \Gamma} \tilde{\boldsymbol{\sigma}}' + \frac{f_{\sigma_{\text{init}}}(\tilde{\sigma}_{\text{vM}})}{\tilde{\sigma}_{\text{vM}}} \left(\tilde{\sigma}_{\text{vM}} \frac{\partial \tilde{\boldsymbol{\sigma}}'}{\partial \Gamma} - \frac{\partial \tilde{\sigma}_{\text{vM}}}{\partial \Gamma} \tilde{\boldsymbol{\sigma}}' \right) \right]. \quad (5.105)$$

We take Eq. (5.91) into account and consider the relations

$$\frac{\partial \tilde{\sigma}_{\text{vM}}}{\partial \Gamma} = \frac{\partial \tilde{\sigma}_{\text{vM}}}{\partial \tilde{\boldsymbol{\sigma}}} : \frac{\partial \tilde{\boldsymbol{\sigma}}}{\partial \Gamma} = -\frac{3}{2} \frac{1}{\tilde{\sigma}_{\text{vM}}} \tilde{\boldsymbol{\sigma}}' : \boldsymbol{\beta}, \quad (5.106)$$

$$\frac{\partial f_{\sigma_{\text{init}}}(\tilde{\sigma}_{\text{vM}})}{\partial \Gamma} = \frac{\partial f_{\sigma_{\text{init}}}(\tilde{\sigma}_{\text{vM}})}{\partial \tilde{\sigma}_{\text{vM}}} \frac{\partial \tilde{\sigma}_{\text{vM}}}{\partial \Gamma} = -\frac{3}{2} \frac{1}{\tilde{\sigma}_{\text{vM}}} \frac{\partial f_{\sigma_{\text{init}}}(\tilde{\sigma}_{\text{vM}})}{\partial \tilde{\sigma}_{\text{vM}}} \tilde{\boldsymbol{\sigma}}' : \boldsymbol{\beta} \quad (5.107)$$

to transform Eq. (5.105) as follows:

$$\begin{aligned} \frac{\partial \Delta \boldsymbol{\epsilon}^{\text{in}}}{\partial \Gamma} = & -\frac{3}{2} \frac{\Delta t f_T(T)}{\tilde{\sigma}_{\text{vM}}} \left[\frac{3}{2} \left(\frac{1}{\tilde{\sigma}_{\text{vM}}} \frac{\partial f_{\sigma_{\text{init}}}(\tilde{\sigma}_{\text{vM}})}{\partial \tilde{\sigma}_{\text{vM}}} - \frac{f_{\sigma_{\text{init}}}(\tilde{\sigma}_{\text{vM}})}{\tilde{\sigma}_{\text{vM}}^2} \right) (\tilde{\boldsymbol{\sigma}}' : \boldsymbol{\beta}) \tilde{\boldsymbol{\sigma}}' \right. \\ & \left. + f_{\sigma_{\text{init}}}(\tilde{\sigma}_{\text{vM}}) \boldsymbol{\beta} \right]. \end{aligned} \quad (5.108)$$

In addition, the derivative of the incremental inelastic VON MISES strain with respect to the softening variable is determined in analogy to Eq. (5.97) and under consideration of Eqs. (5.92), (5.98), and (5.108):

$$\frac{\partial \Delta \varepsilon_{\text{vM}}^{\text{in}}}{\partial \Gamma} = \frac{\partial \Delta \varepsilon_{\text{vM}}^{\text{in}}}{\partial \Delta \boldsymbol{\epsilon}^{\text{in}}} : \frac{\partial \Delta \boldsymbol{\epsilon}^{\text{in}}}{\partial \Gamma} = -\frac{3}{2} \frac{\Delta t f_T(T)}{\tilde{\sigma}_{\text{vM}}} \frac{\partial f_{\sigma_{\text{init}}}(\tilde{\sigma}_{\text{vM}})}{\partial \tilde{\sigma}_{\text{vM}}} \tilde{\boldsymbol{\sigma}}' : \boldsymbol{\beta}. \quad (5.109)$$

5.3.2.4 Derivatives of the Residual Variables

Based on the results presented in Sects. 5.3.2.1–5.3.2.3, the derivatives of the residual quantities \mathbf{R}_{σ}^i , \mathbf{R}_{β}^i , and r_{Γ}^i with respect to the stress $\boldsymbol{\sigma}$, the backstress $\boldsymbol{\beta}$, and the softening variable Γ are evaluated in this section. The derivative of the residual stress tensor \mathbf{R}_{σ}^i with respect to the stress tensor $\boldsymbol{\sigma}$ is computed based on Eqs. (5.83) and (5.96):

$$\begin{aligned} \frac{\partial \mathbf{R}_{\sigma}^i}{\partial \boldsymbol{\sigma}} = & \mathbf{C}^{-1} + \frac{\partial \Delta \boldsymbol{\epsilon}^{\text{in}}}{\partial \boldsymbol{\sigma}} \\ = & \mathbf{C}^{-1} + \frac{3}{2} \frac{\Delta t f_T(T)}{\tilde{\sigma}_{\text{vM}}} \left[\frac{3}{2} \frac{1}{\tilde{\sigma}_{\text{vM}}} \left(\frac{\partial f_{\sigma_{\text{init}}}(\tilde{\sigma}_{\text{vM}})}{\partial \tilde{\sigma}_{\text{vM}}} - \frac{f_{\sigma_{\text{init}}}(\tilde{\sigma}_{\text{vM}})}{\tilde{\sigma}_{\text{vM}}} \right) \tilde{\boldsymbol{\sigma}}' \otimes \tilde{\boldsymbol{\sigma}}' \right. \\ & \left. + f_{\sigma_{\text{init}}}(\tilde{\sigma}_{\text{vM}}) \left(\boldsymbol{\mathcal{I}} - \frac{1}{3} \mathbf{I} \otimes \mathbf{I} \right) \right]. \end{aligned} \quad (5.110)$$

In the next step, we determine the derivative of the residual stress tensor with respect to the backstress based on Eqs. (5.83) and (5.103):

$$\begin{aligned} \frac{\partial \mathbf{R}_{\sigma}^i}{\partial \boldsymbol{\beta}} = & \frac{\partial \Delta \boldsymbol{\epsilon}^{\text{in}}}{\partial \boldsymbol{\beta}} \\ = & -\frac{3}{2} \frac{\Delta t f_T(T)}{\tilde{\sigma}_{\text{vM}}} \Gamma \left[\frac{3}{2} \frac{1}{\tilde{\sigma}_{\text{vM}}} \left(\frac{\partial f_{\sigma_{\text{init}}}(\tilde{\sigma}_{\text{vM}})}{\partial \tilde{\sigma}_{\text{vM}}} - \frac{f_{\sigma_{\text{init}}}(\tilde{\sigma}_{\text{vM}})}{\tilde{\sigma}_{\text{vM}}} \right) \tilde{\boldsymbol{\sigma}}' \otimes \tilde{\boldsymbol{\sigma}}' \right. \\ & \left. + f_{\sigma_{\text{init}}}(\tilde{\sigma}_{\text{vM}}) \boldsymbol{\mathcal{I}} \right]. \end{aligned} \quad (5.111)$$

5 Three-Dimensional Phase Mixture Model

Furthermore, the derivative of the residual stress tensor with respect to the softening variable is computed based on Eqs. (5.83) and (5.108):

$$\begin{aligned} \frac{\partial \mathbf{R}_\sigma^i}{\partial \Gamma} &= \frac{\partial \Delta \boldsymbol{\varepsilon}^{\text{in}}}{\partial \Gamma} \\ &= -\frac{3}{2} \frac{\Delta t f_T(T)}{\tilde{\sigma}_{\text{vM}}} \left[\frac{1}{2 \tilde{\sigma}_{\text{vM}}} \left(\frac{\partial f_{\sigma_{\text{init}}}(\tilde{\sigma}_{\text{vM}})}{\partial \tilde{\sigma}_{\text{vM}}} - \frac{f_{\sigma_{\text{init}}}(\tilde{\sigma}_{\text{vM}})}{\tilde{\sigma}_{\text{vM}}} \right) (\tilde{\boldsymbol{\sigma}}' : \boldsymbol{\beta}) \tilde{\boldsymbol{\sigma}}' \right. \\ &\quad \left. + f_{\sigma_{\text{init}}}(\tilde{\sigma}_{\text{vM}}) \boldsymbol{\beta} \right]. \end{aligned} \quad (5.112)$$

Since the derivatives of the residual stress tensor with respect to the stress, the backstress, and the softening variable have been determined in Eqs. (5.110)–(5.112), we proceed with the derivatives of the residual backstress tensor \mathbf{R}_β^i . With Eqs. (5.74) and (5.84), one obtains the derivative of this tensor with respect to the stress:

$$\begin{aligned} \frac{\partial \mathbf{R}_\beta^i}{\partial \boldsymbol{\sigma}} &= -\frac{\partial \Delta \boldsymbol{\beta}^{\text{in}}}{\partial \boldsymbol{\sigma}} \\ &= G \frac{\eta_{\text{h0}}}{1 - \eta_{\text{h0}}} \left\{ -2 \frac{\partial \Delta \boldsymbol{\varepsilon}^{\text{in}}}{\partial \boldsymbol{\sigma}} + \frac{3}{\beta_{\text{vM}\star}^2(\sigma_{\text{vM}})} \left[\beta_{\text{vM}\star}(\sigma_{\text{vM}}) \frac{\partial \Delta \varepsilon_{\text{vM}}^{\text{in}}}{\partial \boldsymbol{\sigma}} \right. \right. \\ &\quad \left. \left. - \Delta \varepsilon_{\text{vM}}^{\text{in}} \frac{\partial \beta_{\text{vM}\star}(\sigma_{\text{vM}})}{\partial \boldsymbol{\sigma}} \right] \otimes \boldsymbol{\beta} \right\}. \end{aligned} \quad (5.113)$$

Afterwards, the derivatives of the incremental inelastic strains with respect to the stress in Eq. (5.113) are replaced by Eqs. (5.96) and (5.99):

$$\begin{aligned} \frac{\partial \mathbf{R}_\beta^i}{\partial \boldsymbol{\sigma}_{n+1}} &= -\frac{9}{2} \frac{\eta_{\text{h0}}}{1 - \eta_{\text{h0}}} G \frac{\Delta t f_T(T)}{\tilde{\sigma}_{\text{vM}}} \left[\frac{1}{\tilde{\sigma}_{\text{vM}}} \left(\frac{\partial f_{\sigma_{\text{init}}}(\tilde{\sigma}_{\text{vM}})}{\partial \tilde{\sigma}_{\text{vM}}} - \frac{f_{\sigma_{\text{init}}}(\tilde{\sigma}_{\text{vM}})}{\tilde{\sigma}_{\text{vM}}} \right) \tilde{\boldsymbol{\sigma}}' \otimes \tilde{\boldsymbol{\sigma}}' \right. \\ &\quad + \frac{2}{3} f_{\sigma_{\text{init}}}(\tilde{\sigma}_{\text{vM}}) \left(\boldsymbol{\mathcal{I}} - \frac{1}{3} \boldsymbol{\mathcal{I}} \otimes \boldsymbol{\mathcal{I}} \right) - \frac{1}{\beta_{\text{vM}\star}(\sigma_{\text{vM}})} \frac{\partial f_{\sigma_{\text{init}}}(\tilde{\sigma}_{\text{vM}})}{\partial \tilde{\sigma}_{\text{vM}}} \tilde{\boldsymbol{\sigma}}' \otimes \boldsymbol{\beta} \\ &\quad \left. + \frac{\tilde{\sigma}_{\text{vM}}}{\sigma_{\text{vM}}} \frac{f_{\sigma_{\text{init}}}(\tilde{\sigma}_{\text{vM}})}{\beta_{\text{vM}\star}^2(\sigma_{\text{vM}})} \frac{\partial \beta_{\text{vM}\star}(\sigma_{\text{vM}})}{\partial \sigma_{\text{vM}}} \boldsymbol{\sigma}' \otimes \boldsymbol{\beta} \right]. \end{aligned} \quad (5.114)$$

In the following, the derivative of the residual backstress tensor with respect to the backstress is calculated based on Eqs. (5.74) and (5.84):

$$\begin{aligned} \frac{\partial \mathbf{R}_\beta^i}{\partial \boldsymbol{\beta}} &= \boldsymbol{\mathcal{I}} - \frac{\partial \Delta \boldsymbol{\beta}}{\partial \boldsymbol{\beta}} \\ &= \left(1 - \frac{1}{G} \frac{dG}{dT} \Delta T \right) \boldsymbol{\mathcal{I}} - 2G \frac{\eta_{\text{h0}}}{1 - \eta_{\text{h0}}} \left[\frac{\partial \Delta \boldsymbol{\varepsilon}^{\text{in}}}{\partial \boldsymbol{\beta}} \right. \\ &\quad \left. - \frac{3}{2} \frac{1}{\beta_{\text{vM}\star}(\sigma_{\text{vM}})} \frac{\partial \Delta \varepsilon_{\text{vM}}^{\text{in}}}{\partial \boldsymbol{\beta}} \otimes \boldsymbol{\beta} - \frac{3}{2} \frac{\Delta \varepsilon_{\text{vM}}^{\text{in}}}{\beta_{\text{vM}\star}(\sigma_{\text{vM}})} \boldsymbol{\mathcal{I}} \right]. \end{aligned} \quad (5.115)$$

Now, one replaces the derivatives with respect to the backstress in Eq. (5.115) by Eqs. (5.103) and (5.104) to obtain a final expression for the derivative of the residual backstress tensor

with respect to the backstress:

$$\begin{aligned} \frac{\partial \mathbf{R}_\beta^i}{\partial \boldsymbol{\beta}} = & \left[1 - \frac{1}{G} \frac{dG}{dT} \Delta T + 3G \frac{\eta_{h_0}}{1 - \eta_{h_0}} \Delta t f_T(T) \frac{f_{\sigma_{\text{init}}}(\tilde{\sigma}_{\text{vM}})}{\beta_{\text{vM}^*}(\sigma_{\text{vM}})} \right] \mathbf{I} \\ & + 3G \frac{\eta_{h_0}}{1 - \eta_{h_0}} \frac{\Delta t f_T(T)}{\tilde{\sigma}_{\text{vM}}} \Gamma \left[\frac{3}{2} \frac{1}{\tilde{\sigma}_{\text{vM}}} \left(\frac{\partial f_{\sigma_{\text{init}}}(\tilde{\sigma}_{\text{vM}})}{\partial \tilde{\sigma}_{\text{vM}}} - \frac{f_{\sigma_{\text{init}}}(\tilde{\sigma}_{\text{vM}})}{\tilde{\sigma}_{\text{vM}}} \right) \tilde{\boldsymbol{\sigma}}' \otimes \tilde{\boldsymbol{\sigma}}' \right. \\ & \left. + f_{\sigma_{\text{init}}}(\tilde{\sigma}_{\text{vM}}) \mathbf{I} - \frac{3}{2} \frac{1}{\beta_{\text{vM}^*}(\sigma_{\text{vM}})} \frac{\partial f_{\sigma_{\text{init}}}(\tilde{\sigma}_{\text{vM}})}{\partial \tilde{\sigma}_{\text{vM}}} \tilde{\boldsymbol{\sigma}}' \otimes \boldsymbol{\beta} \right]. \end{aligned} \quad (5.116)$$

Finally, the derivative of the residual backstress tensor with respect to the softening variable is computed using Eqs. (5.74) and (5.84):

$$\frac{\partial \mathbf{R}_\beta^i}{\partial \Gamma} = -\frac{\partial \Delta \boldsymbol{\beta}}{\partial \Gamma} = -2G \frac{\eta_{h_0}}{1 - \eta_{h_0}} \left[\frac{\partial \Delta \boldsymbol{\varepsilon}^{\text{in}}}{\partial \Gamma} - \frac{3}{2} \frac{1}{\beta_{\text{vM}^*}(\sigma_{\text{vM}})} \frac{\partial \Delta \varepsilon_{\text{vM}}^{\text{in}}}{\partial \Gamma} \boldsymbol{\beta} \right]. \quad (5.117)$$

The derivatives with respect to the softening variable in Eq. (5.117) are replaced by Eqs. (5.108) and (5.109):

$$\begin{aligned} \frac{\partial \mathbf{R}_\beta^i}{\partial \Gamma} = & 3G \frac{\eta_{h_0}}{1 - \eta_{h_0}} \frac{\Delta t f_T(T)}{\tilde{\sigma}_{\text{vM}}} \left\{ \frac{3}{2} \frac{1}{\tilde{\sigma}_{\text{vM}}} \left[\frac{\partial f_{\sigma_{\text{init}}}(\tilde{\sigma}_{\text{vM}})}{\partial \tilde{\sigma}_{\text{vM}}} - \frac{f_{\sigma_{\text{init}}}(\tilde{\sigma}_{\text{vM}})}{\tilde{\sigma}_{\text{vM}}} \right] (\tilde{\boldsymbol{\sigma}}' : \boldsymbol{\beta}) \tilde{\boldsymbol{\sigma}}' \right. \\ & \left. + \left[f_{\sigma_{\text{init}}}(\tilde{\sigma}_{\text{vM}}) - \frac{3}{2} \frac{\tilde{\boldsymbol{\sigma}}' : \boldsymbol{\beta}}{\beta_{\text{vM}^*}(\sigma_{\text{vM}})} \frac{\partial f_{\sigma_{\text{init}}}(\tilde{\sigma}_{\text{vM}})}{\partial \tilde{\sigma}_{\text{vM}}} \right] \boldsymbol{\beta} \right\}. \end{aligned} \quad (5.118)$$

So far, the derivatives of the residual backstress tensor with respect to the stress, the backstress, and the softening variable have been determined, cf. Eqs. (5.114), (5.116), and (5.118). For this reason, we proceed to compute the derivative of the residual softening variable with respect to the stress by means of Eqs. (5.75) and (5.85):

$$\frac{\partial r_\Gamma^i}{\partial \boldsymbol{\sigma}} = -\frac{\partial \Delta \Gamma}{\partial \boldsymbol{\sigma}} = -C_\Gamma \Delta \varepsilon_{\text{vM}}^{\text{in}} \frac{\partial \Gamma_*(\sigma_{\text{vM}})}{\partial \boldsymbol{\sigma}} + C_\Gamma [\Gamma - \Gamma_*(\sigma_{\text{vM}})] \frac{\partial \Delta \varepsilon_{\text{vM}}^{\text{in}}}{\partial \boldsymbol{\sigma}}. \quad (5.119)$$

Equations (5.89) and (5.99) are taken into account to transform Eq. (5.119):

$$\frac{\partial r_\Gamma^i}{\partial \boldsymbol{\sigma}} = -\frac{3}{2} C_\Gamma \frac{\Delta t f_T(T)}{\tilde{\sigma}_{\text{vM}}} \left\{ f_{\sigma_{\text{init}}}(\tilde{\sigma}_{\text{vM}}) \frac{\partial \Gamma_*(\sigma_{\text{vM}})}{\partial \sigma_{\text{vM}}} \boldsymbol{\sigma}' + [\Gamma - \Gamma_*(\sigma_{\text{vM}})] \frac{\partial f_{\sigma_{\text{init}}}(\tilde{\sigma}_{\text{vM}})}{\partial \tilde{\sigma}_{\text{vM}}} \tilde{\boldsymbol{\sigma}}' \right\}. \quad (5.120)$$

In the next step, the derivative of the residual softening variable with respect to the backstress is calculated under consideration of Eqs. (5.75) and (5.85):

$$\frac{\partial r_\Gamma^i}{\partial \boldsymbol{\beta}} = -\frac{\partial \Delta \Gamma}{\partial \boldsymbol{\beta}} = C_\Gamma [\Gamma - \Gamma_*(\sigma_{\text{vM}})] \frac{\partial \Delta \varepsilon_{\text{vM}}^{\text{in}}}{\partial \boldsymbol{\beta}}. \quad (5.121)$$

The derivative in Eq. (5.121) is replaced by Eq. (5.104). Further manipulations result in the final expression for the derivative of the residual softening variable with respect to the backstress:

$$\frac{\partial r_\Gamma^i}{\partial \boldsymbol{\beta}} = \frac{3}{2} \frac{\Delta t f_T(T)}{\tilde{\sigma}_{\text{vM}}} C_\Gamma [\Gamma_*(\sigma_{\text{vM}}) - \Gamma] \Gamma \frac{\partial f_{\sigma_{\text{init}}}(\tilde{\sigma}_{\text{vM}})}{\partial \tilde{\sigma}_{\text{vM}}} \tilde{\boldsymbol{\sigma}}'. \quad (5.122)$$

5 Three-Dimensional Phase Mixture Model

To conclude this section, the derivative of the residual softening variable with respect to the softening variable itself is calculated using Eqs. (5.75) and (5.85):

$$\frac{\partial r_\Gamma^i}{\partial \Gamma} = 1 - \frac{\partial \Delta \Gamma}{\partial \Gamma} = 1 + C_\Gamma [\Gamma - \Gamma_\star(\sigma_{vM})] \frac{\partial \Delta \varepsilon_{vM}^{\text{in}}}{\partial \Gamma}. \quad (5.123)$$

We replace the derivative in Eq. (5.123) by Eq. (5.109) and manipulate the resulting expression to obtain:

$$\frac{\partial r_\Gamma^i}{\partial \Gamma} = 1 + C_\Gamma \Delta t f_T(T) \left[f_{\sigma_{\text{init}}}(\tilde{\sigma}_{vM}) + \frac{3}{2} \frac{\Gamma_\star(\sigma_{vM}) - \Gamma}{\tilde{\sigma}_{vM}} \frac{\partial f_{\sigma_{\text{init}}}(\tilde{\sigma}_{vM})}{\partial \tilde{\sigma}_{vM}} \tilde{\boldsymbol{\sigma}}' : \boldsymbol{\beta} \right]. \quad (5.124)$$

5.3.3 Numerical Implementation

5.3.3.1 Stress Update Algorithm

This section presents the implemented algorithm to determine the stresses and the internal variables with respect to the unknown equilibrium state at the time step t_{n+1} . Although the internal variables are updated as well, this algorithm is commonly referred to as “stress update algorithm” [104], which is why we will also employ this term. For the implementation of the phase mixture model into the FEM, we switch to matrix notation, while making use of the VOIGT notation, as already introduced in Sect. 2.2. In addition to the strain and stress vectors $\boldsymbol{\varepsilon}$ and $\boldsymbol{\sigma}$, introduced in Eqs. (2.116) and (2.121), respectively, the vector of the effective stresses $\tilde{\boldsymbol{\sigma}}$ and the backstress vector $\boldsymbol{\beta}$ are defined based on the corresponding symmetric tensors of second rank $\tilde{\boldsymbol{\sigma}} = \tilde{\sigma}_{ij} \mathbf{e}_i \otimes \mathbf{e}_j$ and $\boldsymbol{\beta} = \beta_{ij} \mathbf{e}_i \otimes \mathbf{e}_j$:

$$\tilde{\boldsymbol{\sigma}} = [\tilde{\sigma}_{11} \quad \tilde{\sigma}_{22} \quad \tilde{\sigma}_{33} \quad \tilde{\sigma}_{12} \quad \tilde{\sigma}_{13} \quad \tilde{\sigma}_{23}]^T, \quad (5.125)$$

$$\boldsymbol{\beta} = [\beta_{11} \quad \beta_{22} \quad \beta_{33} \quad \beta_{12} \quad \beta_{13} \quad \beta_{23}]^T. \quad (5.126)$$

Note that the vectors of the deviatoric stresses, the inelastic or elastic strain, and the incremental entities are formulated analogously. Furthermore, the residual vectors \mathbf{r}_σ^i and \mathbf{r}_β^i are defined similar to Eqs. (5.83) and (5.84):

$$\mathbf{r}_\sigma^i = -\boldsymbol{\varepsilon} + \boldsymbol{\varepsilon}_n^{\text{in}} + \mathbf{C}^{-1} \boldsymbol{\sigma} + \Delta \boldsymbol{\varepsilon}^{\text{in}}, \quad (5.127)$$

$$\mathbf{r}_\beta^i = -\boldsymbol{\beta}_n + \boldsymbol{\beta} - \Delta \boldsymbol{\beta}, \quad (5.128)$$

where the elastic stiffness matrix \mathbf{C} has been introduced:

$$\mathbf{C} = \frac{1}{3} \begin{bmatrix} 3K + 4G & 3K - 2G & 3K - 2G & 0 & 0 & 0 \\ 3K - 2G & 3K + 4G & 3K - 2G & 0 & 0 & 0 \\ 3K - 2G & 3K - 2G & 3K + 4G & 0 & 0 & 0 \\ 0 & 0 & 0 & 3G & 0 & 0 \\ 0 & 0 & 0 & 0 & 3G & 0 \\ 0 & 0 & 0 & 0 & 0 & 3G \end{bmatrix}. \quad (5.129)$$

The corresponding inverse matrix is computed as follows:

$$\mathbf{C}^{-1} = \frac{1}{18KG} \begin{bmatrix} 6K + 2G & 2G - 3K & 2G - 3K & 0 & 0 & 0 \\ 2G - 3K & 6K + 2G & 2G - 3K & 0 & 0 & 0 \\ 2G - 3K & 2G - 3K & 6K + 2G & 0 & 0 & 0 \\ 0 & 0 & 0 & 18K & 0 & 0 \\ 0 & 0 & 0 & 0 & 18K & 0 \\ 0 & 0 & 0 & 0 & 0 & 18K \end{bmatrix}. \quad (5.130)$$

In analogy to Eqs. (5.80)–(5.82), the following system of equations holds:

$$\mathbf{r}_\sigma^i = \mathbf{0}, \quad (5.131)$$

$$\mathbf{r}_\beta^i = \mathbf{0}, \quad (5.132)$$

$$r_\Gamma^i = 0. \quad (5.133)$$

To solve this nonlinear system of equations, the NEWTON-RAPHSON method is applied, such that Eqs. (5.131)–(5.133) are linearized by introducing the JACOBIAN matrix \mathbf{A}^i :

$$\mathbf{A}^i \Delta \mathbf{p}^{i+1} = -\mathbf{r}^i, \quad (5.134)$$

where \mathbf{p}^{i+1} denotes the vector of unknowns and \mathbf{r}^i is the overall residual vector:

$$\mathbf{p}^{i+1} = [\sigma^{i+1} \quad \beta^{i+1} \quad \Gamma^{i+1}]^T, \quad (5.135)$$

$$\mathbf{r}^i = [\mathbf{r}_\sigma^i \quad \mathbf{r}_\beta^i \quad r_\Gamma^i]^T. \quad (5.136)$$

Here, one should bear in mind that the indices \square^i and \square^{i+1} denote steps in the NEWTON-RAPHSON iteration to find the new equilibrium state at the time step t_{n+1} , cf. Sect. 2.2.1. The solution of Eq. (5.134) provides the increments of the unknowns $\Delta \mathbf{p}^{i+1}$, which are used to update the stress, the backstress, and the softening variable, cf. Eq. (5.135):

$$\mathbf{p}^{i+1} = \mathbf{p}^i + \Delta \mathbf{p}^{i+1}. \quad (5.137)$$

For the linearization of the system of equations, the JACOBIAN matrix \mathbf{A}^i is defined based on the derivatives of the residuals:

$$\mathbf{A}^i = \begin{bmatrix} \frac{\partial \mathbf{r}_\sigma^i}{\partial \sigma} & \frac{\partial \mathbf{r}_\sigma^i}{\partial \beta} & \frac{\partial \mathbf{r}_\sigma^i}{\partial \Gamma} \\ \frac{\partial \mathbf{r}_\beta^i}{\partial \sigma} & \frac{\partial \mathbf{r}_\beta^i}{\partial \beta} & \frac{\partial \mathbf{r}_\beta^i}{\partial \Gamma} \\ \frac{\partial r_\Gamma^i}{\partial \sigma} & \frac{\partial r_\Gamma^i}{\partial \beta} & \frac{\partial r_\Gamma^i}{\partial \Gamma} \end{bmatrix}. \quad (5.138)$$

The derivatives of the residuals are formulated using tensor notation in Sect. 5.3.2.4. In order to simplify the expressions used to compute the derivatives, the auxiliary variables $c_l \forall l \in \{1, 2, \dots, 5\}$ and matrices \mathbf{A}_1 and \mathbf{A}_2 are introduced:

$$c_1 = \frac{3}{2} \frac{\Delta t f_T(T)}{\tilde{\sigma}_{vM}}, \quad c_2 = \frac{f_{\sigma_{init}}(\tilde{\sigma}_{vM})}{\tilde{\sigma}_{vM}^2}, \quad c_3 = \frac{1}{\tilde{\sigma}_{vM}} \frac{\partial f_{\sigma_{init}}(\tilde{\sigma}_{vM})}{\partial \tilde{\sigma}_{vM}},$$

5 Three-Dimensional Phase Mixture Model

$$c_4 = \tilde{\sigma}' : \boldsymbol{\beta} = \tilde{\sigma}'_{ij} \beta_{ji}, \quad c_5 = \frac{\eta_{h_0}}{1 - \eta_{h_0}},$$

$$\mathbf{A}_1 = \begin{bmatrix} 1 & 0 & 0 & 0 & 0 & 0 \\ 0 & 1 & 0 & 0 & 0 & 0 \\ 0 & 0 & 1 & 0 & 0 & 0 \\ 0 & 0 & 0 & 1 & 0 & 0 \\ 0 & 0 & 0 & 0 & 1 & 0 \\ 0 & 0 & 0 & 0 & 0 & 1 \end{bmatrix}, \quad \mathbf{A}_2 = \begin{bmatrix} 1 & 1 & 1 & 0 & 0 & 0 \\ 1 & 1 & 1 & 0 & 0 & 0 \\ 1 & 1 & 1 & 0 & 0 & 0 \\ 0 & 0 & 0 & 0 & 0 & 0 \\ 0 & 0 & 0 & 0 & 0 & 0 \\ 0 & 0 & 0 & 0 & 0 & 0 \end{bmatrix}.$$

Considering the variables introduced above, the derivatives of the residuals \mathbf{r}_σ , \mathbf{r}_β , and r_Γ are expressed in matrix notation, cf. Eqs. (5.110)–(5.112), (5.114), (5.116), (5.118), (5.120), (5.122), and (5.124):

$$\frac{\partial \mathbf{r}_\sigma^i}{\partial \boldsymbol{\sigma}} = \mathbf{C}^{-1} + c_1 \left[-\frac{3}{2} (c_2 - c_3) \tilde{\boldsymbol{\sigma}}' \tilde{\boldsymbol{\sigma}}'^T + c_2 \tilde{\sigma}_{\text{vM}}^2 \left(\mathbf{A}_1 - \frac{1}{3} \mathbf{A}_2 \right) \right], \quad (5.139)$$

$$\frac{\partial \mathbf{r}_\sigma^i}{\partial \boldsymbol{\beta}} = c_1 \Gamma \left[\frac{3}{2} (c_2 - c_3) \tilde{\boldsymbol{\sigma}}' \tilde{\boldsymbol{\sigma}}'^T - c_2 \tilde{\sigma}_{\text{vM}}^2 \mathbf{A}_1 \right], \quad (5.140)$$

$$\frac{\partial \mathbf{r}_\sigma^i}{\partial \Gamma} = c_1 \left[\frac{3}{2} (c_2 - c_3) c_4 \tilde{\boldsymbol{\sigma}}' - c_2 \tilde{\sigma}_{\text{vM}}^2 \boldsymbol{\beta} \right], \quad (5.141)$$

$$\begin{aligned} \frac{\partial \mathbf{r}_\beta^i}{\partial \boldsymbol{\sigma}} &= 3Gc_1c_5 \left[(c_2 - c_3) \tilde{\boldsymbol{\sigma}}' \tilde{\boldsymbol{\sigma}}'^T - \frac{2}{3} c_2 \tilde{\sigma}_{\text{vM}}^2 \left(\mathbf{A}_1 - \frac{1}{3} \mathbf{A}_2 \right) + \frac{c_3 \tilde{\sigma}_{\text{vM}}}{\beta_{\text{vM}\star}(\sigma_{\text{vM}})} \tilde{\boldsymbol{\sigma}}' \boldsymbol{\beta}^T \right. \\ &\quad \left. - \frac{\tilde{\sigma}_{\text{vM}}^3}{\sigma_{\text{vM}} \beta_{\text{vM}\star}^2(\sigma_{\text{vM}})} \frac{\partial \beta_{\text{vM}\star}(\sigma_{\text{vM}})}{\partial \sigma_{\text{vM}}} \boldsymbol{\sigma}' \boldsymbol{\beta}^T \right], \end{aligned} \quad (5.142)$$

$$\begin{aligned} \frac{\partial \mathbf{r}_\beta^i}{\partial \boldsymbol{\beta}} &= \left[1 - \frac{1}{G} \frac{dG}{dT} \Delta T + 2Gc_1c_2c_5 \frac{\tilde{\sigma}_{\text{vM}}^3}{\beta_{\text{vM}\star}(\sigma_{\text{vM}})} \right] \mathbf{A}_1 \\ &\quad - 2Gc_1c_5 \Gamma \left[\frac{3}{2} (c_2 - c_3) \tilde{\boldsymbol{\sigma}}' (\tilde{\boldsymbol{\sigma}}')^T - c_2 \tilde{\sigma}_{\text{vM}}^2 \mathbf{A}_1 + \frac{3}{2} \frac{c_3 \tilde{\sigma}_{\text{vM}}}{\beta_{\text{vM}\star}(\sigma_{\text{vM}})} \tilde{\boldsymbol{\sigma}}' \boldsymbol{\beta}^T \right], \end{aligned} \quad (5.143)$$

$$\frac{\partial \mathbf{r}_\beta^i}{\partial \Gamma} = -3Gc_1c_5 \left\{ (c_2 - c_3) c_4 \tilde{\boldsymbol{\sigma}}' + \left[\frac{c_3 c_4}{\beta_{\text{vM}\star}(\sigma_{\text{vM}})} - \frac{2}{3} c_2 \tilde{\sigma}_{\text{vM}} \right] \tilde{\sigma}_{\text{vM}} \boldsymbol{\beta} \right\}, \quad (5.144)$$

$$\frac{\partial r_\Gamma^i}{\partial \boldsymbol{\sigma}} = c_1 C_\Gamma \tilde{\sigma}_{\text{vM}} \left\{ c_3 [\Gamma - \Gamma_\star(\sigma_{\text{vM}})] (\tilde{\boldsymbol{\sigma}}')^T - c_2 \tilde{\sigma}_{\text{vM}} \frac{\partial \Gamma_\star(\sigma_{\text{vM}})}{\partial \sigma_{\text{vM}}} (\boldsymbol{\sigma}')^T \right\}, \quad (5.145)$$

$$\frac{\partial r_\Gamma^i}{\partial \boldsymbol{\beta}} = c_1 c_3 C_\Gamma [\Gamma_\star(\sigma_{\text{vM}}) - \Gamma] \Gamma (\tilde{\boldsymbol{\sigma}}')^T, \quad (5.146)$$

$$\frac{\partial r_\Gamma^i}{\partial \Gamma} = 1 + c_1 C_\Gamma \tilde{\sigma}_{\text{vM}} \left\{ \frac{2}{3} c_2 \tilde{\sigma}_{\text{vM}} + c_3 c_4 [\Gamma_\star(\sigma_{\text{vM}}) - \Gamma] \right\}. \quad (5.147)$$

With Eqs. (5.139)–(5.147), the JACOBIAN matrix \mathbf{A}^i in Eq. (5.138) is completely defined. The system of equations (5.131)–(5.133) is solved by means of the NEWTON-RAPHSON method, cf. [103], using the following iteration loop:

1. set initial values ($i = 0$):

$$\boldsymbol{\sigma}_{n+1}^0 = \boldsymbol{\sigma}_n, \quad \boldsymbol{\beta}_{n+1}^0 = \boldsymbol{\beta}_n, \quad \Gamma_{n+1}^0 = \Gamma_n \quad (5.148)$$

2. iterate $i \in \{0, 1, \dots, i_{\max}\}$

- a) compute the residual vector \mathbf{r}_{n+1}^i using Eqs. (5.136), (5.127), (5.128), and (5.85)

- b) calculate the JACOBIAN matrix \mathbf{A}_{n+1}^i and its inverse $(\mathbf{A}_{n+1}^i)^{-1}$ by means of Eq. (5.138)
- c) determine the incremental change in the residual vector based on Eq. (5.134):

$$\Delta \mathbf{p}_{n+1}^{i+1} = - (\mathbf{A}_{n+1}^i)^{-1} \mathbf{r}_{n+1}^i \quad (5.149)$$

- d) update all variables, cf. Eq. (5.137):

$$\square_{n+1}^{i+1} = \square_{n+1}^i + \Delta \square_{n+1}^{i+1} \quad \forall \square \in \{\mathbf{p}, \boldsymbol{\sigma}, \boldsymbol{\beta}, \Gamma\}$$

3. check for convergence: $|\mathbf{r}_{n+1}^i| \stackrel{?}{<} 10^{-6}$

- criterion fulfilled \blacksquare exit loop
- criterion not fulfilled \blacksquare $i \mapsto i + 1$, go to Step 2

Note that the time step \square_{n+1} has been written explicitly for the sake of clarity. A tolerance of 10^{-6} is chosen for Step 3 based on [149], where a range of $10^{-2} \dots 10^{-6}$ is recommended. After exiting the iteration loop, the stress $\boldsymbol{\sigma}_{n+1}$, the backstress $\boldsymbol{\beta}_{n+1}$, and the softening variable Γ_{n+1} with respect to the time step t_{n+1} are known.

5.3.3.2 Inversion of the JACOBIAN Matrix

Step 2b of the iteration loop requires the calculation of the inverse JACOBIAN matrix $(\mathbf{A}^i)^{-1}$. This matrix is determined analytically based on the inversion rules for partitioned matrices [150]. Let us introduce the general quadratic matrix \mathbf{H} , which is partitioned as follows:

$$\mathbf{H} = \begin{bmatrix} \mathbf{T}^{(m \times m)} & \mathbf{U}^{(m \times n)} \\ \mathbf{V}^{(n \times m)} & \mathbf{W}^{(n \times n)} \end{bmatrix}^{(m+n) \times (m+n)} \quad (5.150)$$

The superscripts $\square^{(m \times n)}$ denote the numbers of rows and columns, respectively. According to [150], the inverse matrix is computed in the following way:

$$\mathbf{H}^{-1} = \begin{bmatrix} \mathbf{T}^{-1} + \mathbf{T}^{-1} \mathbf{U} \mathbf{Q}^{-1} \mathbf{V} \mathbf{T}^{-1} & -\mathbf{T}^{-1} \mathbf{U} \mathbf{Q}^{-1} \\ -\mathbf{Q}^{-1} \mathbf{V} \mathbf{T}^{-1} & \mathbf{Q}^{-1} \end{bmatrix}, \quad (5.151)$$

where the auxiliary matrix \mathbf{Q} has been introduced. Furthermore, the matrices \mathbf{T} and \mathbf{Q} must be invertible such that the corresponding determinants must not equal zero:

$$\mathbf{Q} = \mathbf{W} - \mathbf{V} \mathbf{T}^{-1} \mathbf{U}, \quad \det(\mathbf{T}) \neq 0, \quad \det(\mathbf{Q}) \neq 0. \quad (5.152)$$

Considering Eqs. (5.139)–(5.147), we observe that the matrix \mathbf{A}^i has 13 rows and columns, and it is partitioned based on Eq. (5.150) with $m \equiv 6$ and $n \equiv 7$. The matrices \mathbf{T} , \mathbf{U} , \mathbf{V} , and \mathbf{W} are defined as follows:

$$\mathbf{T} = \begin{bmatrix} \frac{\partial \mathbf{r}_\sigma^i}{\partial \boldsymbol{\sigma}} \end{bmatrix}, \quad \mathbf{U} = \begin{bmatrix} \frac{\partial \mathbf{r}_\sigma^i}{\partial \boldsymbol{\beta}} & \frac{\partial \mathbf{r}_\sigma^i}{\partial \Gamma} \end{bmatrix}, \quad \mathbf{V} = \begin{bmatrix} \frac{\partial \mathbf{r}_\beta^i}{\partial \boldsymbol{\sigma}} \\ \frac{\partial \mathbf{r}_\Gamma^i}{\partial \boldsymbol{\sigma}} \end{bmatrix}, \quad \mathbf{W} = \begin{bmatrix} \frac{\partial \mathbf{r}_\beta^i}{\partial \boldsymbol{\beta}} & \frac{\partial \mathbf{r}_\beta^i}{\partial \Gamma} \\ \frac{\partial \mathbf{r}_\Gamma^i}{\partial \boldsymbol{\beta}} & \frac{\partial \mathbf{r}_\Gamma^i}{\partial \Gamma} \end{bmatrix}. \quad (5.153)$$

For computing the inverse matrix $(\mathbf{A}^i)^{-1}$ by means of Eq. (5.151), the inverse matrices \mathbf{T}^{-1} and \mathbf{Q}^{-1} need to be determined. For this purpose, separate subroutines are included in the UMAT in order to compute the inverse of quadratic matrices with 6 rows and columns as well as 7 rows and columns. In these subroutines, the matrix is partitioned once more according to Eq. (5.150), and Eq. (5.151) is applied to compute the inverse. To this end, the inverse of quadratic matrices with 3 rows and columns as well as 4 rows and columns are computed analytically by two separate subroutines based on the standard rules of matrix algebra [150].

5.3.3.3 Consistent Tangent Operator

The notion of the “consistent tangent operator” (CTO) has been introduced by SIMO and TAYLOR [151]. They state that the CTO should be used in order to guarantee the convergence properties of the NEWTON-RAPHSON method, which is demonstrated by numerical examples for rate-independent plasticity. Later, BRAUDEL *et al.* have investigated the CTO in a more general way [152]. Meanwhile, the CTO is commonly applied to implement nonlinear material models into the FEM, cf. [105, 111, 153, 154] for example. The CTO is based on the consistent linearization of the PVW, as introduced in Sect. 2.2.1, while accounting for the employed stress update algorithm [106]. Finally, the CTO is determined as the GÂTEAUX derivative of the stress with respect to the strains, cf. Eq. (2.100). For the implementation into ABAQUS, we introduce the matrix of the CTO $\tilde{\mathbf{C}}$, which is calculated based on Eq. (2.100):

$$\tilde{\mathbf{C}} = \frac{\partial \boldsymbol{\sigma}}{\partial \boldsymbol{\varepsilon}}. \quad (5.154)$$

In the thesis at hand, the CTO is determined based on the inverse matrix $(\mathbf{A}^i)^{-1}$ in the converged state of the NEWTON-RAPHSON iteration [103]. For the phase mixture model, this matrix can be represented by means of the submatrices $\mathbf{A}_{ij}^{(m \times n)}$:

$$(\mathbf{A}^i)^{-1} = \begin{bmatrix} \mathbf{A}_{11}^{(6 \times 6)} & \mathbf{A}_{12}^{(6 \times 6)} & \mathbf{A}_{13}^{(6 \times 1)} \\ \mathbf{A}_{21}^{(6 \times 6)} & \mathbf{A}_{22}^{(6 \times 6)} & \mathbf{A}_{23}^{(6 \times 1)} \\ \mathbf{A}_{31}^{(1 \times 6)} & \mathbf{A}_{32}^{(1 \times 6)} & \mathbf{A}_{33}^{(1 \times 1)} \end{bmatrix}. \quad (5.155)$$

According to [103], the CTO is obtained by extraction of the first six rows and columns in the converged state:

$$\tilde{\mathbf{C}} = \mathbf{A}_{11}. \quad (5.156)$$

5.3.4 Verification of the UMAT

The stress update algorithm as well as the consistent tangent operator, introduced in Sects. 5.3.3.1 and 5.3.3.3, respectively, are implemented into the commercial finite element code ABAQUS using a UMAT. The current section presents the results of several benchmark problems, which are solved in order to verify the implementation of the phase mixture model. In a first step, the model is applied to uniaxial stress states, and the HT tensile tests presented in Sect. 3.1 are simulated. Figure 5.2 summarizes the obtained stress-strain curves under constant prescribed strain rates considering different temperatures. The dashed lines refer to the one-dimensional phase mixture model, i.e. the system of equations (4.76),

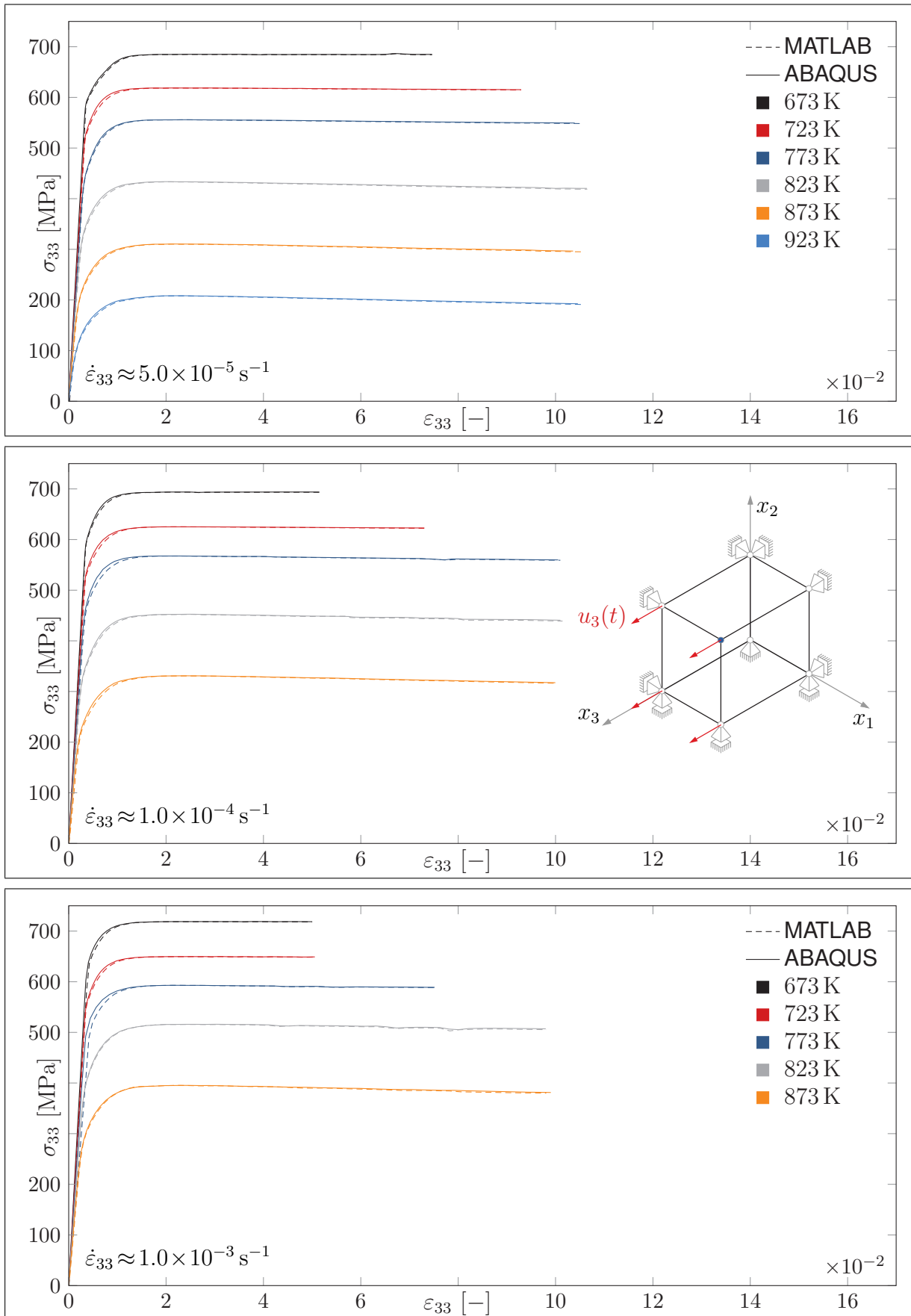


Figure 5.2: Simulation of HT tensile tests with 1D MATLAB model and 3D ABAQUS model.

5 Three-Dimensional Phase Mixture Model

(4.77), and (4.79) is solved using MATLAB's solver ode45. For the ABAQUS simulation based on the three-dimensional phase mixture model (the corresponding results are indicated by the solid lines), an 8-node hexahedral continuum element with linear shape functions (C3D8) is taken into account, as depicted in the sketch in Fig. 5.2. The model is comprised of only one element since this is sufficient to represent the homogeneous stress and strain states caused by uniaxial tension. The applied BCs for the FEM are also visualized in Fig. 5.2. In order to simulate the tests controlled by the total strain rate, the measured displacement $u_3(t_n)$ in x_3 direction serves as input with respect to each time step. In addition, the displacements in the normal direction of the three faces defined by $x_1 = 0$, $x_2 = 0$, and $x_3 = 0$ are fixed. Note that the results are extracted at the upper node, depicted in dark blue. As can be seen from the figure, the results of the one-dimensional phase mixture model and the implementation of the three-dimensional phase mixture model are in very good agreement with respect to all strain rates and the entire temperature range $673 \text{ K} \leq T \leq 923 \text{ K}$. This indicates a correct implementation of the three-dimensional model into ABAQUS.

Since the simulation of the HT tensile tests has been successful, we proceed with a creep test. In Sect. 4.1, the simulation of creep tests deploying the one-dimensional phase mixture model has been discussed, cf. also Fig. 4.3. This solution serves as benchmark for the subsequent simulation of an exemplary creep test at a constant temperature of $T = 873 \text{ K}$. Because standard creep tests result in uniaxial homogeneous stress and strain states, the finite element model from the simulation of the HT tensile tests is adopted with different BCs, compare Figs. 5.2 (middle) and 5.3 (top left). As depicted in the top left diagram of Fig. 5.3, a distributed load of 200 MPa in x_3 direction is prescribed. The load is held constant over 80 h, cf. the top left diagram, such that very large inelastic strains ($\varepsilon_{33}^{\text{in}} \approx 70\%$) occur, which is shown in the top right diagram of Fig. 5.3. Here, one should keep in mind that the three-dimensional phase mixture model is restricted to small strains, as discussed at the beginning of Sect. 5.1. However, the simulation of the creep test serves only as a case study, and the loads are applied over a long time in order to observe a strong softening effect, cf. the bottom right diagram of Fig. 5.3. Due to the ICs, cf. Eq. (5.35), the softening variable Γ starts at $\Gamma(\varepsilon_{33}^{\text{in}} = 0) = 1$ and decreases towards a saturation value, as also predicted in Fig. 4.3 on the right-hand side. In contrast, the backstress β_{33} increases towards its saturation value, cf. the bottom left diagram of Fig. 5.3 as well as the diagram on the left-hand side of Fig. 4.3. To conclude, the implemented model yields plausible results with respect to a creep test, which is in agreement with the discussion of Fig. 4.3 in Sect. 4.1.

In a next step, a simple shear test at a constant temperature of $T = 873 \text{ K}$ is discussed. Figure 5.4 is comprised of a sketch of the finite element model and the diagrams with the corresponding results. As can be seen in the top left diagram in Fig. 5.4, the same finite element model as for the previous benchmarks is employed with different DIRICHLET BCs. Here, the displacement is prescribed as linear function of the time, resulting in a constant displacement rate $\dot{u}_2 = 6.94 \times 10^{-6} \text{ mm s}^{-1}$, such that an overall shear strain of $\varepsilon_{23} = 2.5\%$ is reached after a test duration of $t = 1 \text{ h}$, cf. the top right diagram in Fig. 5.4, where the total, the elastic, and the inelastic shear strains are depicted depending on the time. Since results for shear tests with respect to the alloy X20CrMoV12-1 could not be found in literature, the results of the finite element analysis are checked for plausibility. As expected, the finite element model yields uniform results for the stresses, the strains, the backstress, and the softening variable within the entire element. In the top left diagram in Fig. 5.4, the shear stress σ_{23} is depicted with respect to the time. One can observe a behavior similar to the HT tensile tests, cf. Fig. 5.2, i.e. the linear increase of the stress in the elastic range, the leveling of the stress due to hardening and a decrease with constant slope for $t \geq 0.3 \text{ h}$, which is attributed to the softening processes. The top right diagram presents the strains

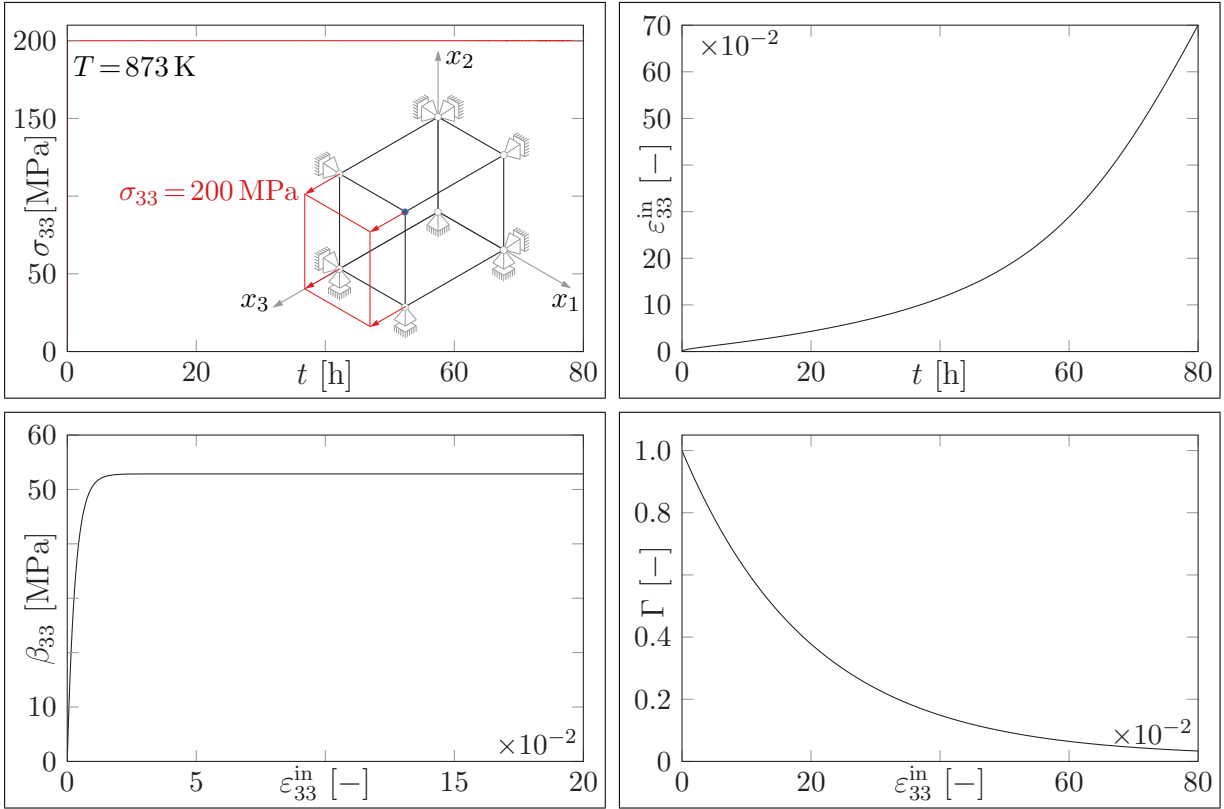


Figure 5.3: Simulation of a creep test under constant tensile load $\sigma_{33} = 200$ MPa at 873 K.

depending on time. Due to the input, the overall strain ε_{23} increases with *constant* slope. As one would expect, the elastic strain $\varepsilon_{23}^{\text{el}}$ shows the same qualitative behavior as the stress, whereas the curve of the inelastic strain $\varepsilon_{23}^{\text{in}}$ increases in parallel with the total strain. The backstress β_{23} , which is depicted in the bottom left diagram with respect to the time, starts from zero and increases until the saturation value $\beta_{23} \approx 46$ MPa is reached. In addition, the softening variable Γ is depicted with respect to the time in the bottom right diagram. Similar to Fig. 5.3, the softening variable Γ decreases such that the occurrence of softening is evident. Nevertheless due to the shorter test duration compared to the creep test, the softening effect is not as strong as in the bottom right diagram of Fig. 5.3. Considering these observations, the simulation results for the simple shear tests are deemed plausible.

In addition, the performance of the phase mixture model under cyclic loads is examined. For this purpose, the same finite element model as shown in Fig. 5.2 is utilized, while we prescribe a time-dependent displacement $u_3(t)$, in order to obtain the following strain path with respect to one cycle:

$$\varepsilon_{33}(t) = \begin{cases} |\dot{\varepsilon}| t & \text{if } 0 \leq t < 0.25t_{\text{end}} \\ 2\hat{\varepsilon} - |\dot{\varepsilon}| t & \text{if } 0.25t_{\text{end}} \leq t < 0.75t_{\text{end}} \\ -4\hat{\varepsilon} + |\dot{\varepsilon}| t & \text{if } 0.75t_{\text{end}} \leq t \leq t_{\text{end}} \end{cases}. \quad (5.157)$$

The time t_{end} denotes the duration of one cycle. The triangular strain path described by Eq. (5.157) results in the following function for the strain rate $\dot{\varepsilon}_{33}(t)$:

$$\dot{\varepsilon}_{33}(t) = \begin{cases} |\dot{\varepsilon}| & \text{if } 0 \leq t < 0.25t_{\text{end}} \\ -|\dot{\varepsilon}| & \text{if } 0.25t_{\text{end}} \leq t < 0.75t_{\text{end}} \\ |\dot{\varepsilon}| & \text{if } 0.75t_{\text{end}} \leq t \leq t_{\text{end}} \end{cases}. \quad (5.158)$$

5 Three-Dimensional Phase Mixture Model

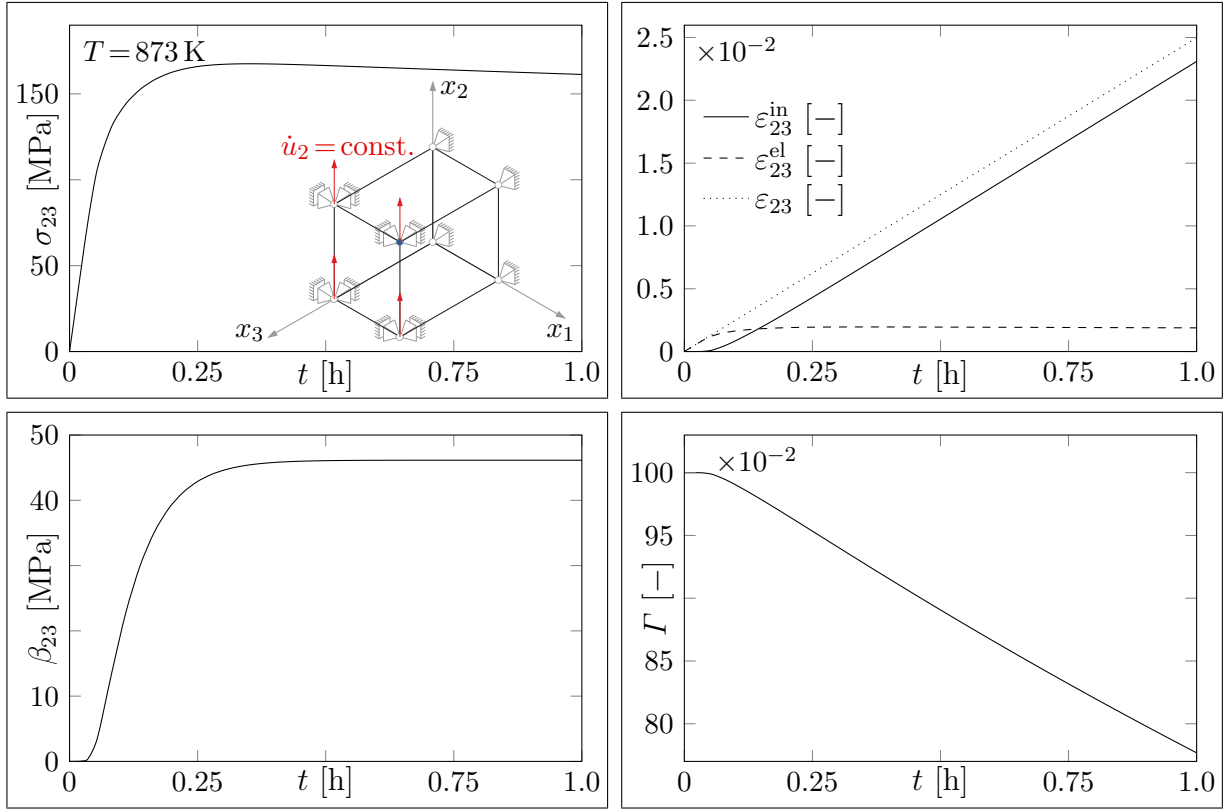


Figure 5.4: Simulation of a simple shear test with prescribed displacement rate $\dot{u}_2 = 6.94 \times 10^{-6} \text{ mm s}^{-1}$ at 873 K.

In order to study the influence of the strain and the temperature, two different strain rates $|\dot{\varepsilon}| = \{5.0 \times 10^{-5} \text{ s}^{-1}, 1.0 \times 10^{-3} \text{ s}^{-1}\}$, two strain amplitudes $\hat{\varepsilon} = \frac{1}{4} \dot{\varepsilon} t_{\text{end}} = \{1.0 \times 10^{-2}, 5.0 \times 10^{-2}\}$, and two temperatures $T = \{673 \text{ K}, 923 \text{ K}\}$ are taken into account. Note that the strain rates and the temperatures mark the minimum and the maximum values under consideration for the HT tensile tests discussed in Sect. 3.1, which is the reason to make use of these representative values for this parameter study. Figures 5.5 and 5.6 present the results of the simulation of two cycles with respect to the higher strain rate $|\dot{\varepsilon}| = 1.0 \times 10^{-3} \text{ s}^{-1}$ and the lower strain rate $|\dot{\varepsilon}| = 5.0 \times 10^{-5} \text{ s}^{-1}$, respectively. One can observe hysteresis effects, which are typical for rate-dependent materials, cf. [74]. The diagrams on the left-hand side of Fig. 5.5 depict the results for the small strain amplitude of $\hat{\varepsilon} = 1\%$, while the diagrams on the right-hand side illustrate the behavior for the higher strain amplitude of $\hat{\varepsilon} = 5\%$. Whereas the left diagrams are dominated by hardening processes such that the stress starts to level, an almost constant stress value is observed in the right diagrams for large strains $|\varepsilon_{33}| > 2\%$. It is remarkable that the maximum stress level does not change throughout both cycles with respect to the temperature 673 K, cf. the top diagrams in Fig. 5.5, while the maximum stress level in the second cycle is slightly lower than the maximum stress level in the first cycle for the temperature 923 K in the bottom left diagram. Note that this phenomenon is even more pronounced at the top right diagram due to the large strain amplitude of $\hat{\varepsilon} = 5\%$. This decrease in the stress amplitude for strain controlled cyclic tests has often been observed for tempered martensitic steels, cf. Sect. 1.1.1, and it is attributed to softening [10].

Comparing Fig. 5.5 to Fig. 5.6, the influence of the strain rate is demonstrated. As already discussed in Sect. 3.1, a decrease in the strain rate results in a decrease of the maximum stress level, which is more distinctive at higher temperatures. Furthermore, the maximum

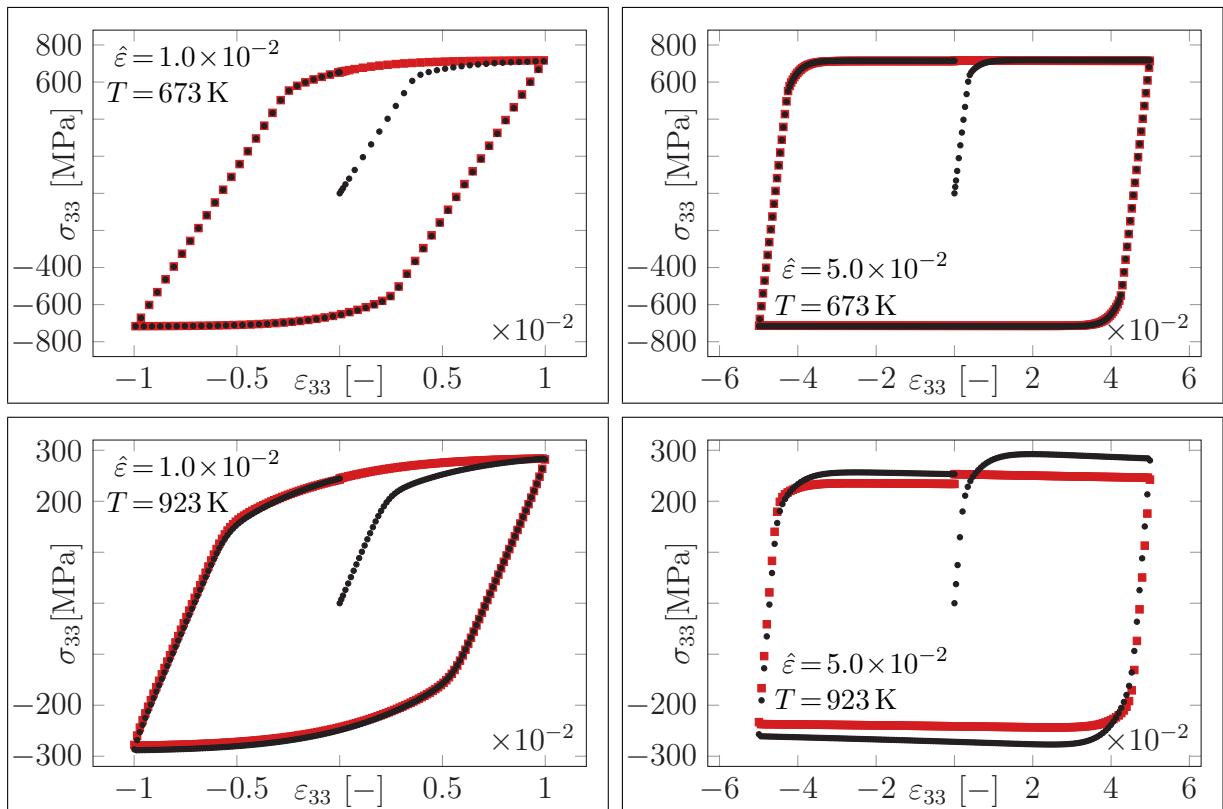


Figure 5.5: Simulation of two strain cycles with one finite element at absolute strain rate $|\dot{\epsilon}| = 1.0 \times 10^{-3} \text{ s}^{-1}$. Hystereses for first (black) and second (red) cycle.

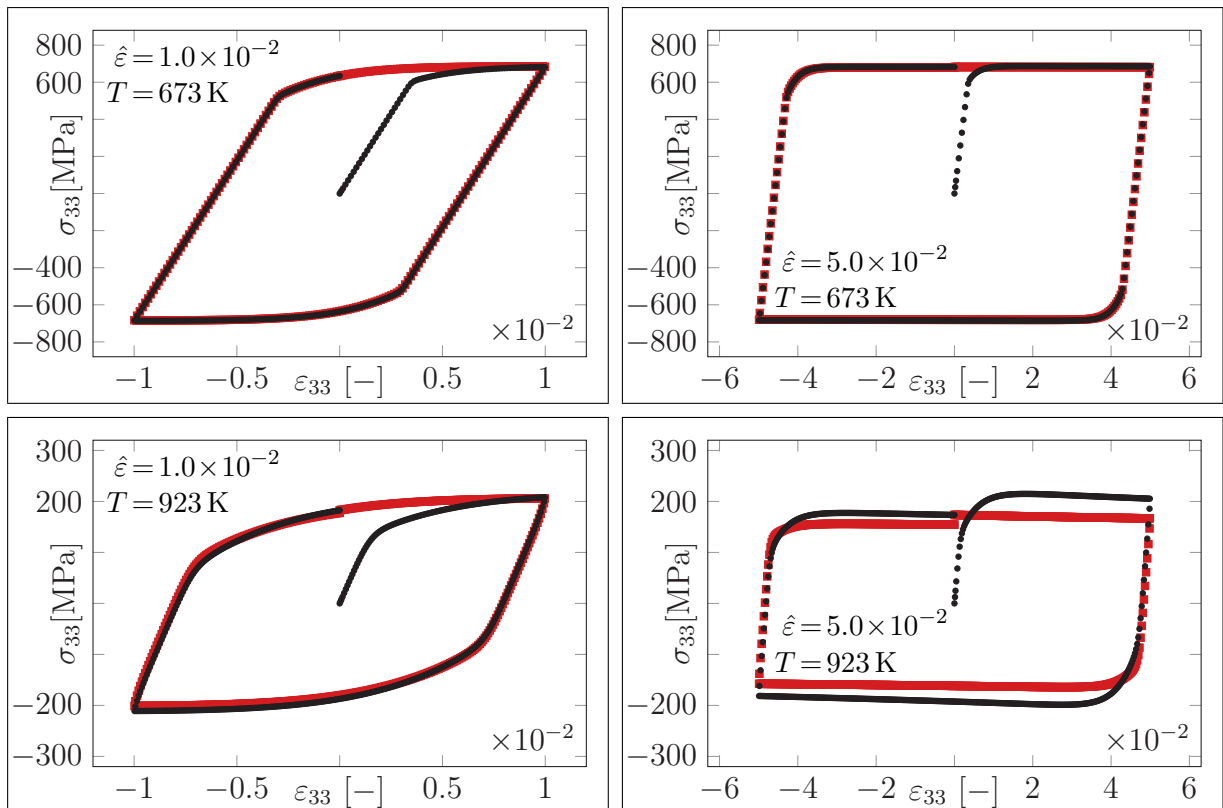


Figure 5.6: Simulation of two strain cycles with one finite element at absolute strain rate $|\dot{\epsilon}| = 5.0 \times 10^{-5} \text{ s}^{-1}$. Hystereses for first (black) and second (red) cycle.

5 Three-Dimensional Phase Mixture Model

stress decreases during both cycles to a higher extent at a temperature of 923 K compared to a temperature of 673 K, cf. the bottom diagrams in Figs. 5.5 and 5.6. Finally, one can conclude that the phase mixture model is able to account for the cyclic softening effect. The influence of softening on the overall material behavior gets stronger with increasing temperature and decreasing strain rate, what is also confirmed by the experimental findings in Sect. 3.1.

Since the previous benchmarks have been passed successfully, we move on to more complex stress and deformation states. Figures 5.7 and 5.8 summarize the simulation results for a stationary creep test of a thick hollow cylinder under the constant internal pressure $p = 80$ MPa. Stationary creep is modeled with the phase mixture model by neglecting hardening ($\beta = 0$) and softening ($\Gamma = 1$). The bottom right picture of Fig. 5.7 illustrates the applied BCs. Note that the displacements u_z are set to zero at the horizontal edges, such that the conditions of a plane strain state are fulfilled, i.e. $\dot{\epsilon}_{zz} = 0$. If one takes the simplifications $\beta = 0$ and $\Gamma = 1$ into account, the following restriction for the deviatoric stress σ'_{zz} is obtained by means of Eq. (5.32):

$$\sigma'_{zz} = 0 \quad \Rightarrow \quad r_{\sigma_{zz}} = \sigma_{zz} - \frac{1}{2}(\sigma_{rr} + \sigma_{\varphi\varphi}) = 0 \quad (5.159)$$

The fulfillment of Eq. (5.159) is a benchmark for the multiaxial implementation of the phase mixture model. For this reason, Fig. 5.7 presents the contour plots for the residuum $r_{\sigma_{zz}}$ taking different meshes into account. An axisymmetric 8-node quadrilateral element with quadratic shape functions (CAX8) is used, and the results of three different regular meshes with 1, 5, and 20 elements are compared. The results are evaluated after 50 h with respect to the constant temperature $T = 873$ K. The top left plot in Fig. 5.7 clearly shows that Eq. (5.159) is not fulfilled for the coarsest mesh consisting of only one element. However, during the h -refinement process, the residuum approaches zero and the quality of the approximation is significantly improved, cf. the top right and the bottom left pictures in Fig. 5.7. For the finest mesh with 20 elements, the maximum residuum accounts for $\approx 4 \times 10^{-2}$ MPa. These negligible deviations are observed near the edges of the elements, what is to be expected due to boundary effects.

In addition, Fig. 5.8 provides the simulation results for different components of the stress tensor with respect to the finest mesh containing 20 elements. Contour plots of the VON MISES stress (top left), the radial stress (top right), the hoop stress (bottom left), and the longitudinal stress (bottom right) are shown. The results agree qualitatively with [81]. As one would expect, the VON MISES stress σ_{vM} (top left) attains its maximum at the inner radius and reduces with increasing radius. For the radial stress, $\sigma_{rr}(r=r_i) = -p = -80$ MPa and $\sigma_{rr}(r=r_a) \approx 0$ MPa hold due to the BCs, cf. the top right diagram. The hoop stress $\sigma_{\varphi\varphi}$ (bottom left) and the axial stress σ_{zz} (bottom right) are minimum at the inner radius and increase with the radial coordinate.

So far, all benchmarks have been passed successfully such that the model is applied to simulate a service-type TMF test. This procedure is often applied in literature, cf. [34, 155–158]. The simulation is based on strain and temperature profiles, which represent typical sequences of warm and hot starts of power plants [34]. These profiles are depicted in the top left diagram of Fig. 5.9 for several cycles with respect to the time. Since homogeneous stress and strain states are simulated, we apply the same finite element model as used for the HT tensile tests, cf. the sketch in the bottom right diagram of Fig. 5.9, while a spatially homogeneous temperature field is prescribed over the entire elemental domain. The top right diagram of Fig. 5.9 presents the stress and the backstress response of the phase mixture

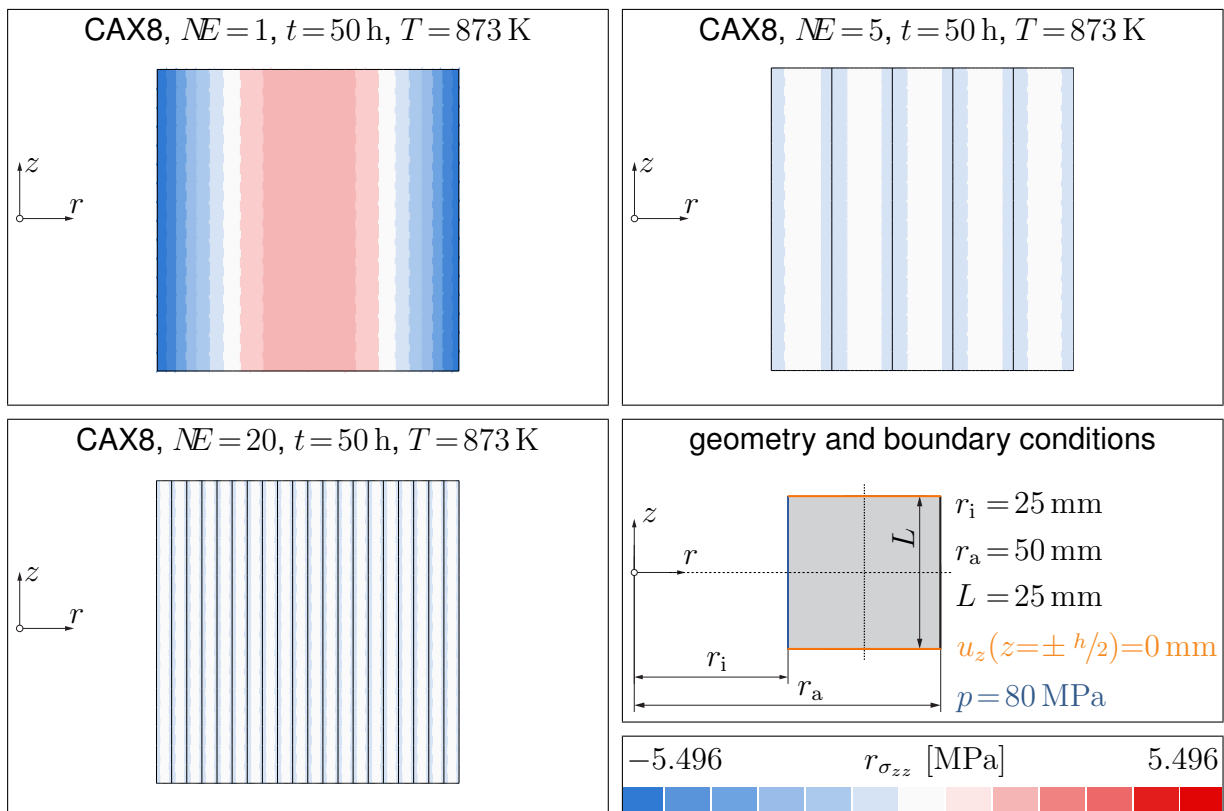


Figure 5.7: Simulation of a stationary creep test of a thick hollow cylinder with an axisymmetric model. Results for the residuum $r_{\sigma_{zz}}$ considering different meshes.

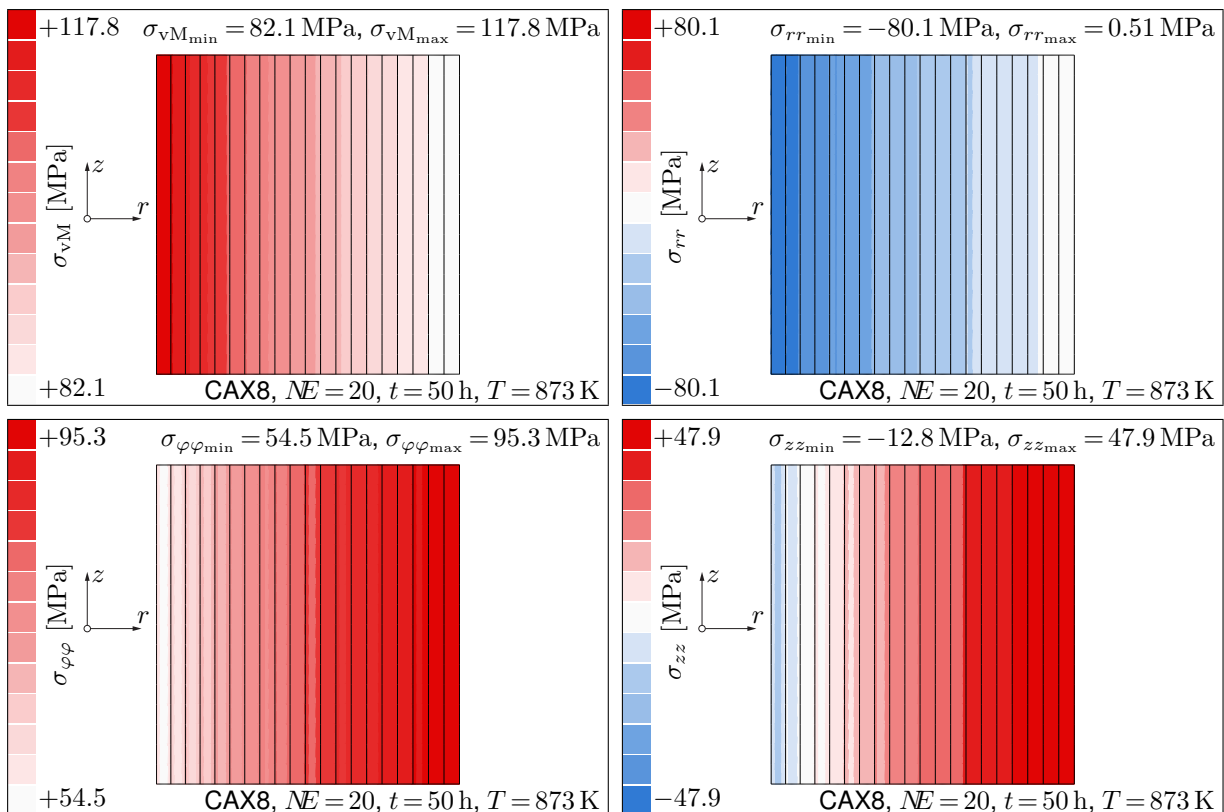


Figure 5.8: Simulation of stationary creep in a pressurized cylinder with an axisymmetric model. Results for the stresses σ_{vM} , σ_{rr} , $\sigma_{\varphi\varphi}$, and σ_{zz} for the finest mesh.

5 Three-Dimensional Phase Mixture Model

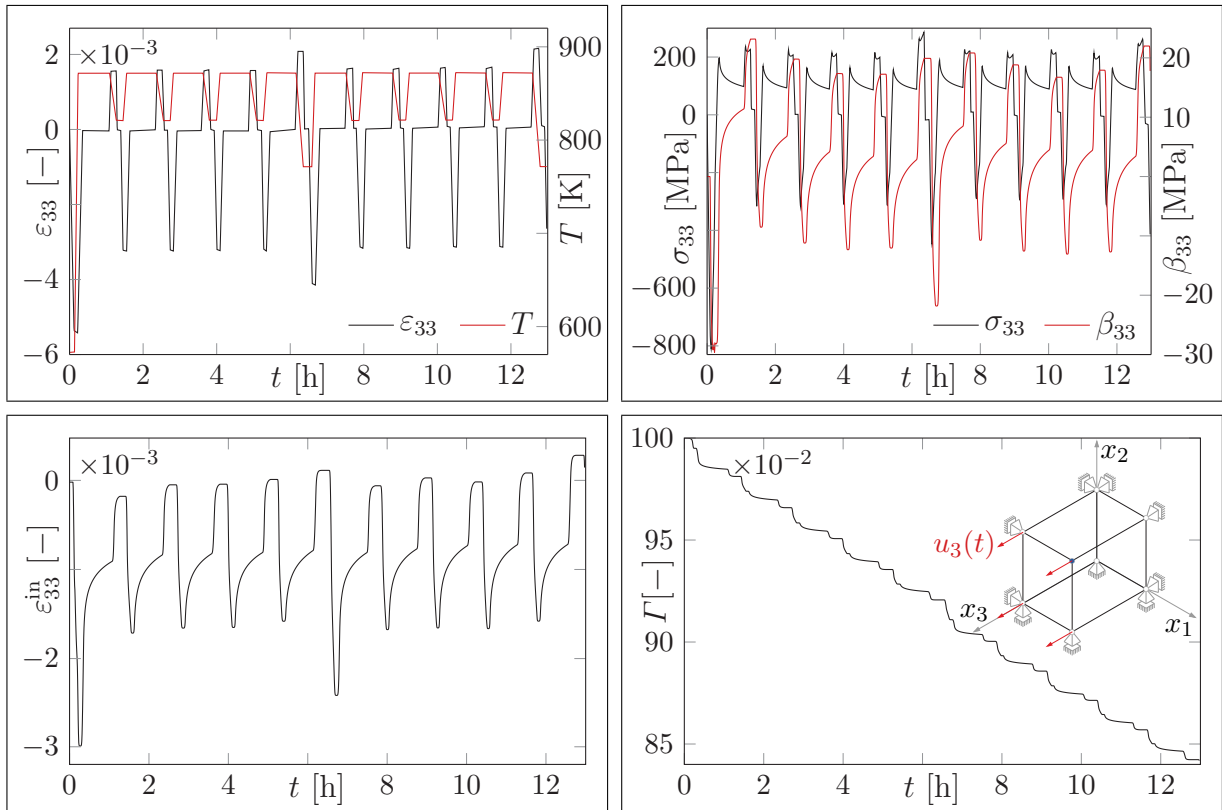


Figure 5.9: Simulation of typical start-ups and shut-downs of power plants as uniaxial thermo-mechanical fatigue (TMF) test with one finite element. Strain and temperature input according to [34].

model, whereas the results for the inelastic strain and the softening variable are shown in the bottom diagrams on the left- and right-hand side, respectively. In [34], normalized stress responses for the simulation and the TMF tests are reported, and it is found that the results in Fig. 5.9 and the findings reported in [34] agree qualitatively. Furthermore, the bottom right diagram of Fig. 5.9 clearly shows a decrease in the softening variable Γ during the cycles, i.e. the material exhibits softening.

In the current section, the results of numerous finite element analyses have been discussed in detail. Thereby, we have accounted for both uniaxial and multiaxial stress states. The results of all benchmark problems under consideration indicate a correct implementation of the three-dimensional phase mixture model into the FEM, such that the simulation of a service-type TMF test concludes the current chapter. Nevertheless, the results of a TMF test are hardly comparable to simulations of the mechanical behavior of power plant components under realistic loading conditions, as described in Sect. 1.1.1, since the geometry of real components is not accounted for and the loads are idealized. For these reasons, the next chapter is dedicated to the simulation of the behavior of industrially relevant power plant components under service-type loading conditions.

6 Analysis of a Steam Turbine Rotor

As a last step, the proposed constitutive model is used to simulate the mechanical behavior of a steam turbine rotor. Similar analyses have been presented in [58, 159]. In [58], a unified model for viscoplasticity is used to simulate the cyclic thermo-mechanical behavior of an industrial gas turbine rotor by means of an axisymmetric finite element model. The thermo-mechanical analysis of the rotor is conducted in two steps. First, a heat transfer analysis is used to determine the temperature distribution in the rotor. Therefore, the gas temperatures are applied as thermal BCs, and the temperature distribution is obtained based on the corresponding heat transfer coefficients. Afterwards, a structural analysis is conducted with the temperature distribution as input. In [159], the results of a similar decoupled thermo-mechanical analysis are given, using a three-dimensional finite element model.

However, both publications provide insufficient or normalized information with respect to the precise geometry of the rotors or the cyclic loading. For this reason, we set up a different model and analyze an idealized steam turbine rotor with an inlet groove. The model is also used in [16], where a sequence comprising a hot start, a holding stage, as well as a cool-down is simulated. However, it is of crucial importance to take cold starts into account as well because the loads caused by the temperature gradients are expected to be significantly higher than the thermal loads during a hot start. In the thesis at hand, the calibration of the phase mixture model has been extended to lower temperatures, which offers the possibility to additionally consider cold starts. Therefore, a cold start and a subsequent hot start are simulated. As in [58, 159], a decoupled thermo-mechanical analysis is conducted since the required computational effort is significantly reduced compared to a fully coupled thermo-mechanical analysis. Thus, the preceding thermal analysis (described in Sect. 6.1) yields the temperature distribution, which serves as an input for the subsequent structural analysis, cf. Sect. 6.2. Note that mutual interactions between the mechanical variables and the temperature field are not accounted for due to the decoupling of the analyses.

6.1 Heat Transfer Analysis

This section discusses the BCs and the results of the heat transfer analysis using ABAQUS. The geometry of the rotor and the finite element mesh are shown in Fig. 6.1 in the upper pictures. We deploy the heat transfer element DCAX8, which is an axisymmetric quadrilateral finite element with 8 nodes and quadratic shape functions. Note that the notch induces stress and strain gradients, which should be accounted for while generating the mesh. Therefore, the mesh is refined near the notch root, and several partitions have been used in order to obtain a structured regular mesh. The steam temperature is prescribed depending on the longitudinal coordinate z , as illustrated in the bottom left diagram in Fig. 6.1. As can be seen, the steam temperature varies linearly with respect to the longitudinal coordinate and is constant near the notch, i.e. $T(L_1 \leq z \leq L_2) = T_2$. The temperatures at the left and the right edge of the rotor are equal, i.e. $T(z=0) = T(z=L_3) = T_1$. Furthermore, changes in

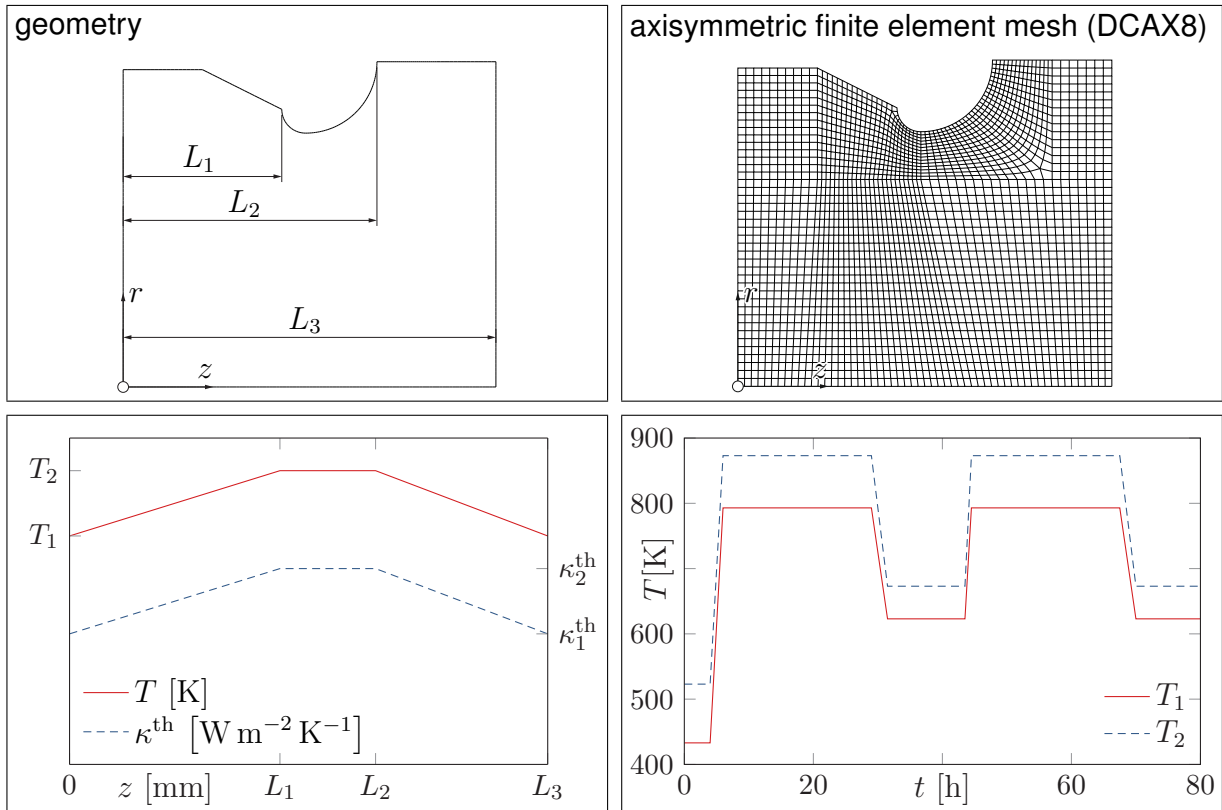


Figure 6.1: Geometry, mesh, and loads for the heat transfer analysis of a steam turbine rotor with an inlet groove based on [16].

the steam parameters are taken into account by different heat transfer coefficients κ_1^{th} and κ_2^{th} , which are dependent on the steam temperatures.

The changes in the steam temperatures T_1 and T_2 with respect to time are shown in the bottom right diagram of Fig. 6.1. Due to the complex thermo-mechanical loads in power plants, specific information in literature on the temperature fields during the start-ups and the shut-downs is rare and varies strongly. According to [25], start-ups are commonly subdivided into three categories named cold, warm, and hot starts. For a cold start, the time period after the previous shut-down exceeds approximately three days or the maximum pre-start temperature of the components does not exceed 393 K–433 K. In [26], similar values are given with respect to the steam temperatures. Before a hot start, the outage should not take longer than 8 h–10 h, and all intermediate start-ups are referred to as warm start-ups [25]. Therefore, pre-start steam temperatures $T_1(t=0 \text{ h}) = 433 \text{ K}$ and $T_2(t=0 \text{ h}) = 523 \text{ K}$ are chosen. After heating up to a maximum temperature of 873 K, the steam temperature is held constant over 23 h. Afterwards, it is decreased to 623 K–673 K, and the rotor is restarted after a holding time of 12 h. Once more, the temperature is held constant over 23 h before the final cool-down.

Figure 6.2 presents the results of the transient thermal analysis. The temperatures are evaluated at two specific points: point A is located at the notch root, while point B is positioned on the axis of rotation. Both temperatures are depicted with respect to the time, whereas the results of the cold start are depicted at the left-hand side. The corresponding results of the hot start are shown at the right-hand side. In addition, the points with maximum absolute temperature differences $|T_A - T_B|$ during the warm-up and the cool-down are indicated by vertical lines, and the corresponding temperature distributions are visualized by means of contour plots. The largest temperature gradients are observed during the start-ups,

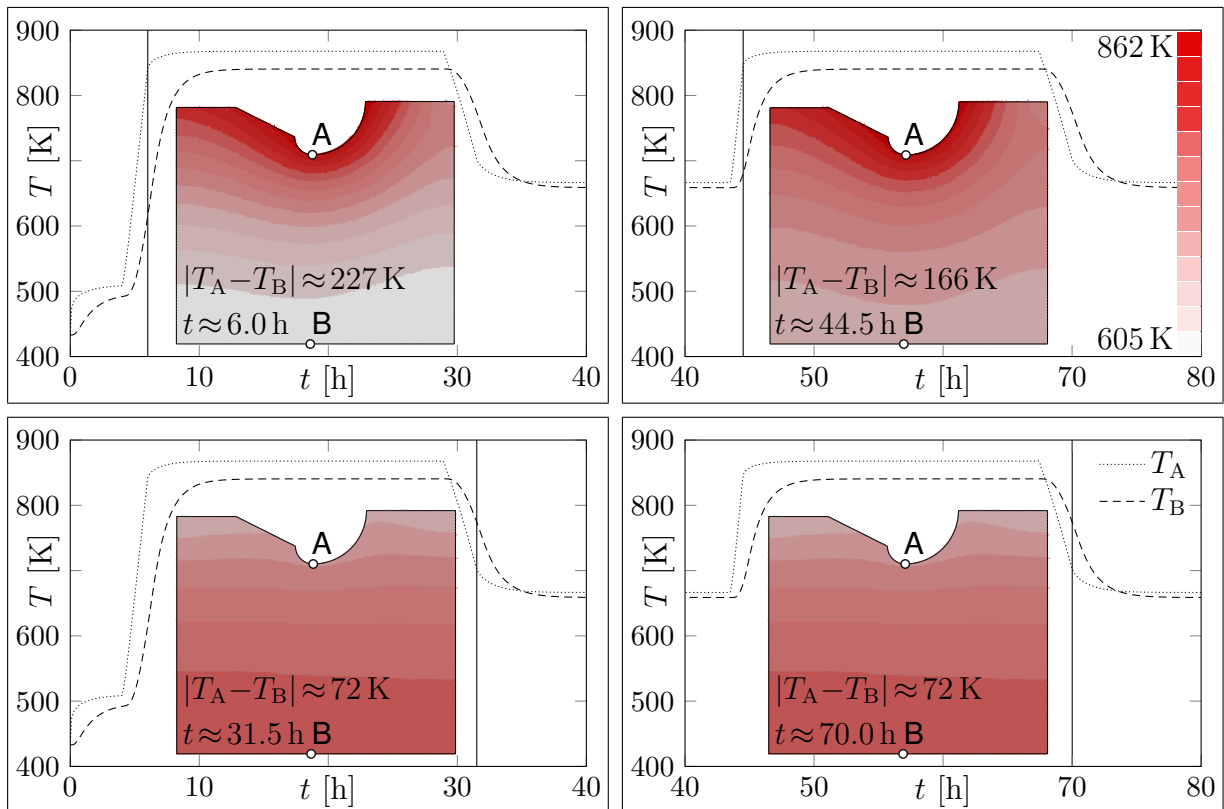


Figure 6.2: Temperature distributions within the rotor and the temperatures T_A and T_B in points A and B vs time. Cold start (left) and hot start (right).

which is in agreement to the findings in [58]. Here, the cold start induces a significantly higher temperature difference (≈ 227 K) than the hot start (≈ 166 K), which was to be expected. Since the rotor is heated by the steam, the temperature in point A at the surface is higher than the temperature in point B during the heating-up. However, during the cool-down, the temperature in point A decreases faster than the temperature in point B such that the internal temperatures are higher than the temperatures at the surface. During the cool-down, the maximum absolute temperature difference is relatively low (≈ 72 K). Considering the holding stages, the temperature difference is even lower (≈ 27 K).

6.2 Structural Analysis

In a next step, the obtained temperature fields serve as an input for the subsequent structural analysis, whereby we employ the continuum element CAX8, which is also an axisymmetric quadrilateral finite element with 8 nodes and quadratic shape functions. The upper pictures in Fig. 6.3 illustrate once more the geometry of the rotor and the finite element mesh. Note that we can reuse the mesh from the heat transfer analysis, cf. Fig. 6.1, since the employed elements DCAX8 and CAX8 are 8-node quadrilateral finite elements with quadratic shape functions, i.e. the description of the geometry and the field of unknowns is identical in both cases. Furthermore, the mechanical boundary conditions are illustrated in the bottom left diagram in Fig. 6.3. Due to the rotational symmetry and in order to avoid rigid body motions, the displacements normal to the edges $r=0$ and $z=0$ are set to zero. On the upper edge (marked in red), the steam pressure $p(t)$ is applied. In addition, the rotation along the z axis is prescribed based on the frequency $f(t)$. The steam pressure as well as the frequency are

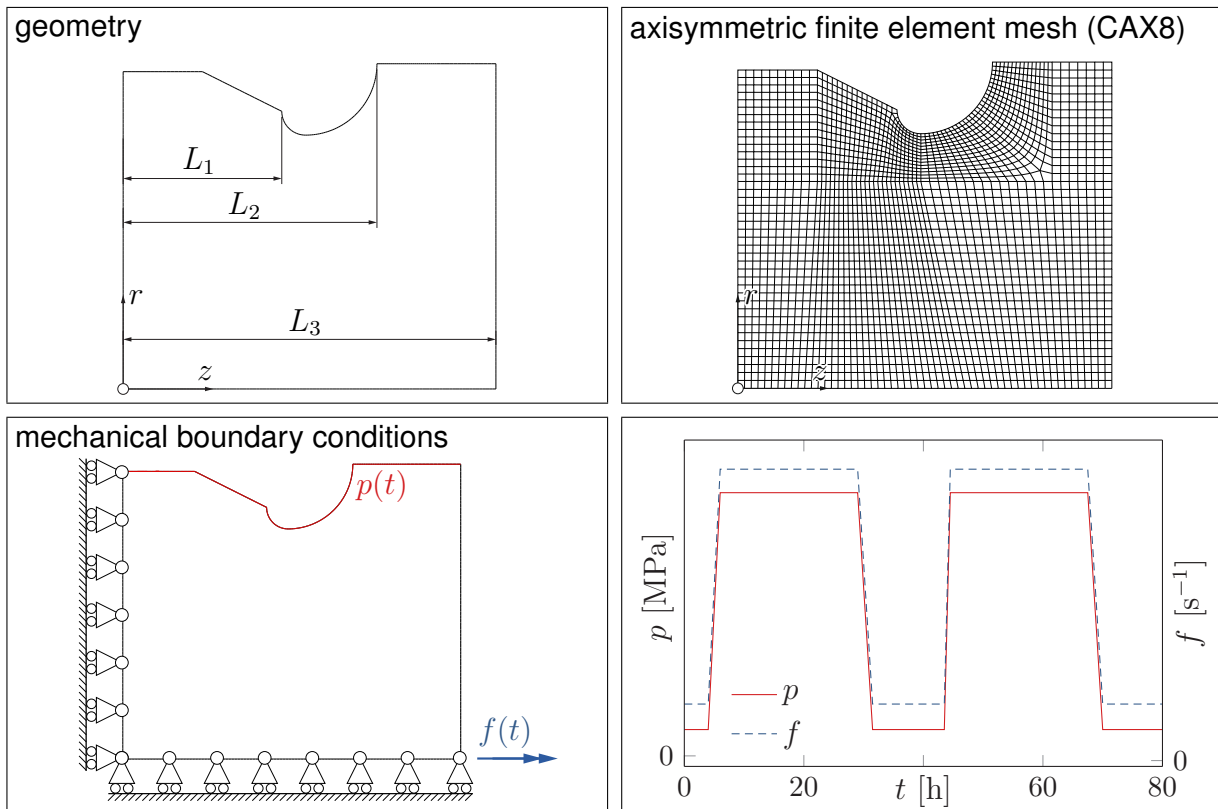


Figure 6.3: Geometry, mesh, and loads for the structural analysis of a steam turbine rotor with an inlet groove based on [16].

time-dependent, which is depicted in the bottom right diagram in Fig. 6.3

Figure 6.4 summarizes the results for the mechanical strains and stresses in point A with respect to the unit orthogonal vectors \mathbf{n} , \mathbf{e}_t , and \mathbf{e}_φ , which are depicted in the bottom right diagram in Fig. 6.4 and represent the principal directions of both the mechanical strain tensor and the stress tensor [16]. The strains are normalized with respect to the absolute minimum tangential strain $|\varepsilon_{tt_{\min}}|$ and the corresponding results are shown at the top of Fig. 6.4. At the bottom of the same figure, the stresses (normalized with respect to the absolute minimum tangential stress $|\sigma_{tt_{\min}}|$) are depicted with respect to time. In analogy to the previous figure, the results of the cold and the hot start are located at the left-hand and the right-hand side, respectively.

One should note that the normal stress can be evaluated based on the steam pressure, i.e. $\sigma_{nn} = -p$. During the warm-up, i.e. with respect to the points $t \approx 6$ h and $t \approx 44.5$ h, the rotor is compressed, and the tangential and circumferential stresses and strains reach the corresponding minima. It is apparent that the highest absolute tangential and circumferential stresses and strains occur during the cold start. Furthermore, we can observe a steady increase in the tangential strain, which is attributed to creep during the holding stages. Simultaneously, the tangential and circumferential stresses decrease steadily, thus revealing stress relaxation. During the cool-down, tangential and circumferential stresses and strains are positive, such that the rotor is subjected to tension. Generally speaking, the stresses and the strains during the holding stages and the cool-down are only slightly affected by the different start-up procedures.

Since the tangential stress and the corresponding strain exhibit the highest absolute values throughout both cycles, cf. Fig. 6.4, these components are analyzed in detail. Figure 6.5 illustrates the normalized tangential strain and the corresponding stress in point A depending

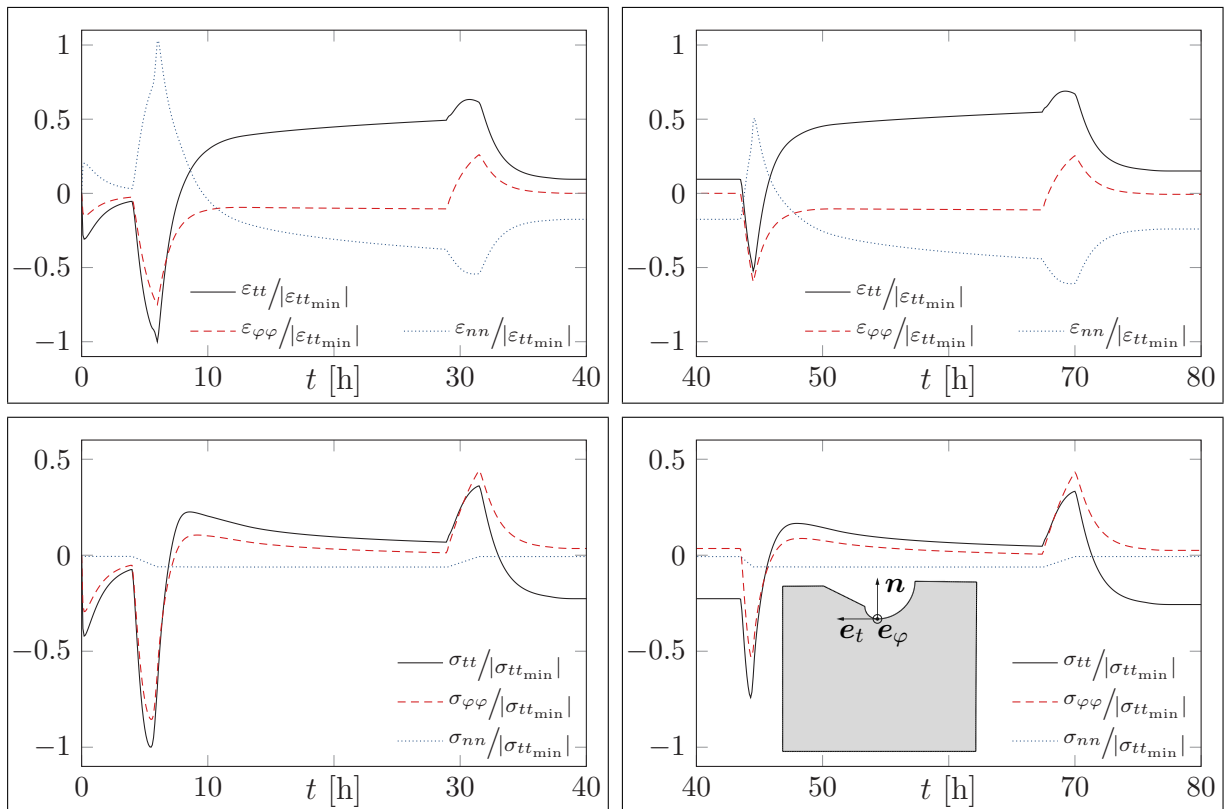


Figure 6.4: Normalized mechanical strains (top) and stresses (bottom) in point A vs time. Cold start (left) and hot start (right).

on the time in the upper diagrams, whereas the two diagrams at the bottom show the results for the normalized tangential stress depending on the normalized tangential strain. Specific points are marked in red and numbered in order to illustrate the different stages during the temperature cycle, cf. Fig. 6.2. The path from point 1 to point 2 during the cold start (and 6–7 during the hot start) corresponds to the warm-up with increasing temperature difference $T_A - T_B$. Here, the tangential strain and stress decrease such that the rotor is compressed. The following line segment (2–3 or 7–8, respectively) describes the warm-up with a decreasing temperature difference. Thus, the absolute strain and stress values are reduced due to the lower temperature differences. Thereafter, the holding stage, where the creep and relaxation processes are triggered, follows, i.e. the strain increases steadily, while the stress decreases simultaneously between the points 3–4 or 8–9, respectively. Finally, the points 4–5 and 9–10 mark the first stage of the cool-down. The temperature difference decreases up to $T_A - T_B \approx -72$ K and tensile stresses and strains occur. The last range (5–6 and 10–11) refers to the cool-down and the holding stage with low absolute temperature differences $|T_A - T_B|$.

In the following, we focus on the normal and circumferential stresses and strains. The upper diagrams of Fig. 6.6 provide information on the dependence of the normalized circumferential and normal strains on the normalized tangential strain in point A. It becomes obvious that the ratios of the principal strains are not constant during the cycles such that the loading in point A is clearly nonproportional [160]. However, one should note that the principal directions n , e_t , and e_φ are fixed. The diagrams at the bottom of Fig. 6.6 present the hysteresis loops for the tangential and the circumferential components. This reveals that the circumferential components have a significant influence compared to the tangential components and cannot be neglected when evaluating the mechanical work dissipated during the cycles [16].

6 Analysis of a Steam Turbine Rotor

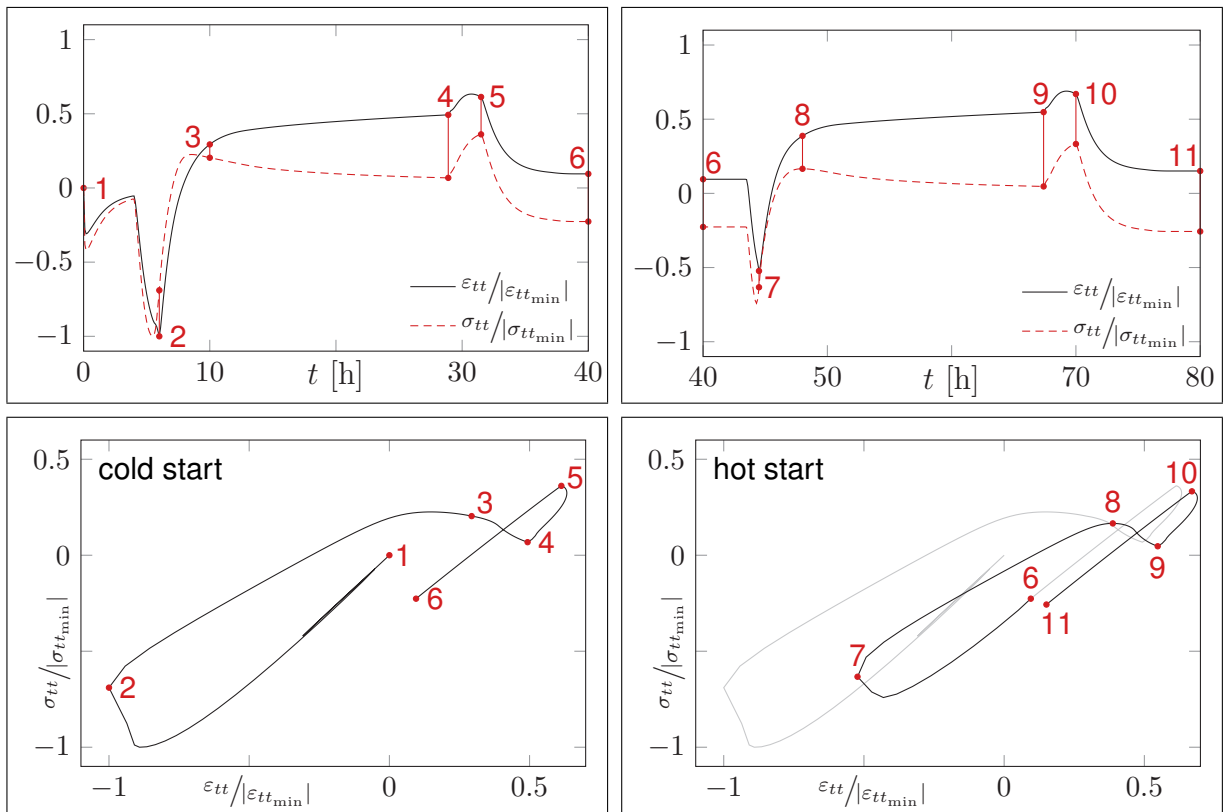


Figure 6.5: Normalized tangential strain and stress in point A vs time (top). Normalized tangential stress vs normalized tangential strain in point A (bottom).

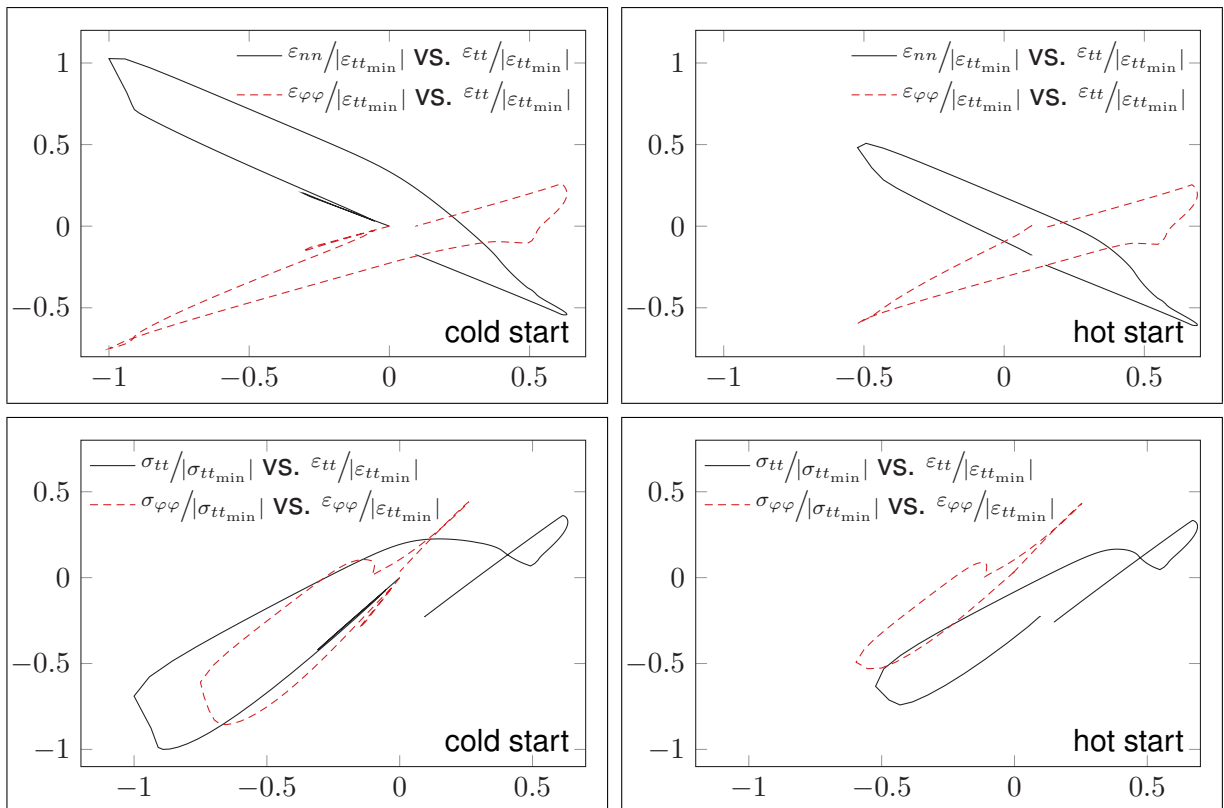


Figure 6.6: Normalized circumferential and normal strains vs tangential strain (top). Normalized tangential and circumferential stresses vs corresponding strains (bottom).

The findings in this section are in good agreement with the results for a hot start published in [16]. In order to extend the applicability of the phase mixture model, also data from tests at lower temperatures such as 673 K has been considered during the calibration in Sect. 4.2, thus allowing for the simulation of cold starts as well. The presented results highlight the differences between the two starting procedures and the influence of the temperature gradients on the stresses and strains. Furthermore, the computed stress and strain tensors could be used in a subsequent analysis to evaluate the creep and fatigue damage and to predict the lifetime of power plant components [16]. In the current thesis, a rotor with relatively simple geometry subjected to idealized thermo-mechanical loads is investigated, due to the lack of precise data with respect to the geometry and the loads of real parts in the available literature. Therefore, future studies should focus on the application of the phase mixture model for the analysis of power plant components under service-type loads, which requires the publication of further experimental data concerning the thermo-mechanical loads on the components, such as the resulting temperature distribution on the surface of the steam turbine rotors.

7 Summary and Outlook

The thesis at hand presents a framework for modeling the mechanical behavior of tempered martensitic steels at elevated temperatures. In order to demonstrate the applicability of the proposed methods, we focused on the alloy X20CrMoV12-1 as a typical representative of tempered martensitic steels. Due to their exceptional mechanical and thermal properties, these steels are well-established for applications in power plants at elevated temperatures up to $T \approx 903$ K. In addition to the thermal loads, the components are subjected to creep-fatigue loads because of frequent start and stop operations of power plants. Furthermore, tempered martensitic steels suffer from softening effects under constant and cyclic loads, which should be accounted for by a constitutive model.

To model the mechanical behavior of tempered martensitic steels, several models have been proposed during the last years, cf. the discussion in Sect. 1.2. Micromechanical models are based on parameters which can be directly and explicitly related to microstructural quantities. These models demand for expensive and time-consuming observations with microscopes in order to generate the data required for the calibration. To avoid the conduction of these observations, one can employ macromechanical models, which describe the material behavior with respect to the macroscale and are calibrated based on macroscopic material tests. Nevertheless, most macromechanical models introduce a large number of parameters, which complicates the calibration procedure. Furthermore, it is often difficult to provide physical interpretations for all variables. As an alternative to the proposed models, the current thesis focuses on a phase mixture model to simulate the mechanical behavior of tempered martensitic steels.

Originally, the phase mixture model is closely related to the microscale, and thus the rate-dependent inelastic behavior of an alloy, including the softening and the hardening processes, is described using an iso-strain approach with a soft and a hard phase. The hard phase represents the subgrain boundaries and areas of high dislocation density, while the soft phase accounts for the interior of the subgrains and regions with a low dislocation density. It is assumed that the total strains in both phases are equal. Additionally, the model postulates that the individual constituents exhibit an identical elastic behavior, while their inelastic behavior differs significantly. To allow for the calibration based on macroscopic material tests and to simplify the identification of the parameters, a backstress of ARMSTRONG-FREDERICK-type and a softening variable are introduced as internal variables. Note that the backstress represents the hardening behavior, while the softening variable is related to the volume fraction of the hard constituent, which is assumed to decrease during deformation. After all, one obtains a macromechanical phase mixture model with a microscopic foundation.

The current thesis describes the phase mixture model, the calibration procedure, and the implementation into the FEM in seven chapters. In the first chapter, the operating conditions in power plants, the mechanical properties and the microstructure of tempered martensitic steels were introduced. Furthermore, several models for tempered martensitic steels were discussed, and an outline of the thesis was given.

Chapter 2 focused on the theoretical foundations for the conducted research. In the first section, the governing equations of continuum mechanics, i.e. kinematics, kinetics, the balance laws, and the constitutive equations, were presented, while emphasis was placed

on the description of the inelastic material behavior. Section 2.2 introduced the finite element method, starting with the principle of virtual work. Afterwards, the spatial discretization into finite elements and the resulting system of DAEs were described.

The next chapter, cf. Chapt. 3, discussed different experimental investigations conducted on a multitude of specimens made of the alloy X20CrMoV12-1. In the current literature, only the results of some creep and cyclic tests with respect to the steel X20CrMoV12-1 are available, cf. [10, 13]. In order to extend this database for the calibration of the phase mixture model, numerous HT tensile and creep tests were conducted, which allows for a systematic analysis of the mechanical behavior of the alloy under consideration. The HT tensile tests were controlled by the strain rate under constant temperature levels, whereas temperatures and strain rates in the ranges $673 \text{ K} \leq T \leq 923 \text{ K}$ and $5.0 \times 10^{-5} \text{ s}^{-1} \leq \dot{\varepsilon} \leq 1.0 \times 10^{-3} \text{ s}^{-1}$, respectively, were taken into account. The test results highlighted the strong influence of the strain rate on the overall mechanical behavior. Furthermore, the stress-strain curves exhibited a slight, but constant decrease in the stress for the temperatures $823 \text{ K} \leq T \leq 923 \text{ K}$, which was attributed to the softening of the material. Since the phase mixture model aims to account for the softening processes, but does not consider macroscopic necking, it is essential to clearly distinguish the softening phenomenon from necking. For this purpose, a second series of HT tensile tests was conducted, i.e. a tensile test was performed several times at a temperature of 923 K under a strain rate of $5.0 \times 10^{-5} \text{ s}^{-1}$, while the test was terminated at different strain levels in order to examine the onset of necking. Using different methods of investigation (visual examination of the specimens' shape, the hypothesis of volume conservation during inelastic deformation, tactile measurement of the specimens' shape with a profilometer), one could conclude that necking started at a strain level of $\varepsilon > 15\%$. Thus, it was found that softening processes determine the material behavior over a wide strain range of $2\% < \varepsilon < 15\%$ even *before* the onset of necking. In addition to the HT tensile tests, three creep tests at a constant temperature of $T = 873 \text{ K}$ with respect to the engineering stress levels $P = \{100 \text{ MPa}, 150 \text{ MPa}\}$ were conducted. The creep curves exhibited an extended primary and tertiary creep stage, while a secondary creep stage with a constant strain rate was not observed, which is typical for tempered martensitic steels.

Afterwards, the one-dimensional phase mixture model was presented in Chapt. 4. The governing equations were derived starting with the micromechanical formulation of the model. In a next step, the backstress and the softening variable were introduced into the governing equations, and a coupled system of three evolution equations with respect to the inelastic strain, the backstress, and the softening variable was obtained. Thereafter, a new complex calibration procedure for the model was presented in Sect. 4.2, which was based on the experimental results discussed in Chapt. 3 and additional results of creep tests from literature. First, the elastic material parameters were determined using the stress-strain curves of the HT tensile tests. The subsequent calibration of the inelastic material behavior, the softening and the hardening range was based on the definition of an initial and a steady state with respect to the HT tensile tests and the creep tests. Using MATLAB, the material parameters were determined partly manually and partly automatically by means of mathematical optimization. To verify the calibrated model, the HT tensile tests as well as additional creep tests were simulated, which demonstrated that the phase mixture model was able to account for the elastic material behavior as well as the hardening regime and the softening range. The model provided accurate approximations of the experimental data for wide ranges of the temperature and the stress, i.e. $673 \text{ K} \leq T \leq 923 \text{ K}$ and $100 \text{ MPa} \leq \sigma \leq 700 \text{ MPa}$, respectively. Thus, the range of applicability of the phase mixture model was significantly extended compared to [42], where the model is calibrated based on creep tests for relatively narrow ranges of stress and temperature ($150 \text{ MPa} \leq \sigma \leq 200 \text{ MPa}$, $773 \text{ K} \leq T \leq 873 \text{ K}$). Furthermore, the

verification of the calibrated model revealed that the model should only be applied to strain rates $\dot{H} > 10^{-7} \text{ s}^{-1}$, which was due to the fact that the calibration was mainly based on material tests with respect to higher strain rates. After all, the one-dimensional phase mixture model in the current calibration requires only 14 material parameters for simulations with respect to the wide ranges of stress and temperature, as indicated above. This highlights an important advantage of the presented phase mixture model, i.e. the low number of parameters used for simulations with respect to wide ranges of stress and temperature. Note that the majority of the proposed models for tempered martensitic steels includes 20 parameters and more, as already discussed in Sect. 4.3.

In Chapt. 5, the phase mixture model was extended to multiaxial stress and deformation states. The derivation of the governing equations in Sect. 5.1 was executed analogously to the one-dimensional model, cf. Chapt. 4, while introducing the corresponding stress and strain tensors as well as equivalent VON MISES quantities and the backstress tensor. Similar to the one-dimensional model, the derivations resulted in a coupled system of three evolution equations with respect to the inelastic strain tensor, the backstress tensor, and the scalar softening variable. Since the thermodynamic consistency of the three-dimensional model is only stated in [42] without giving a proof, the current thesis demonstrates the thermodynamic consistency of the three-dimensional phase mixture model based on the CLAUSIUS-PLANCK inequality, cf. Sect. 5.2. The derivation was restricted to stationary temperatures, which was deemed adequate due to the relatively slow temperature changes during the start-ups and shut-downs of power plants. In a next step, the three-dimensional phase mixture model was implemented into the finite element code ABAQUS using a UMAT subroutine, cf. Sect. 5.3. So far, the implementation of the phase mixture model into the FEM has not been discussed in literature. Therefore, the thesis at hand describes the implementation of the model in detail, using the backward EULER method for the implicit time integration of the evolution equations. The application of the backward EULER method resulted in a nonlinear system of equations, which was solved by means of the NEWTON-RAPHSON method. Furthermore, the consistent tangent operator was computed based on the inverse JACOBIAN matrix of the NEWTON-RAPHSON method with respect to the converged state. In order to verify the implementation of the phase mixture model into the FEM, the results of various finite element analyses were presented. Since the HT tensile tests, a creep test, a simple shear test, cyclic tests, and a creep test of a thick hollow cylinder were simulated, both uniaxial and multiaxial stress and deformation states were taken into account. All benchmarks were passed successfully, which is why the phase mixture model was applied to simulate a service-type TMF test. The simulation was based on strain and temperature profiles, which represent typical sequences of warm and hot starts of power plants. It was found that the simulation results agreed qualitatively with the corresponding normalized results from literature.

As a final step of the proposed framework, the application of the phase mixture model for the simulation of an idealized steam turbine rotor was discussed in Chapt. 6. Although finite element analyses have already been presented in literature, cf. [16, 58, 159], the influence of the different start-up procedures has not been taken into account yet. For this reason, a cold start as well as a subsequent hot start were simulated by means of a thermo-mechanical analysis. Within the preceding heat transfer analysis, the instationary steam temperature and the heat transfer coefficients were prescribed, and the resulting temperature distribution in the rotor was computed. It was found that the largest temperature differences occurred during the cold start. In a next step, the obtained temperature fields served as input for the subsequent structural analysis. As expected, the results showed that the highest absolute stresses and strains occurred during the cold start. Furthermore, creep and stress relaxation were observed during the holding stages of the two cycles. After all,

7 Summary and Outlook

the results highlighted the differences in the temperature, stress, and strain fields depending on the start-up procedure under consideration, i.e. a cold or a hot start. It became obvious that it is crucial to take cold starts into account simulating the mechanical behavior of power plant components. The computed stress and strain tensors could be used in a subsequent analysis to evaluate the creep and fatigue damage and to predict the lifetime of power plant components.

There are many ways to refine the proposed framework for tempered martensitic steels. In its current formulation, the phase mixture model accounts for temperature changes with respect to the time and for the influence of the temperature on the material parameters. However, spatial temperature gradients are not taken into account, which is one aspect that could be included in future applications. In addition, the proof of the thermodynamic consistency of the model is restricted to stationary temperatures. Thus, one should develop a fully coupled thermo-mechanical model, which is thermodynamically consistent, i.e. the CLAUSIUS-PLANCK inequality should be fulfilled unconditionally. Further research might also investigate the modeling of the softening processes in detail. Note that the evolution equation for the softening variable, cf. Eq. (4.27), is postulated and restricted to proportional loading. One should deduce an evolution equation closely connected to the microstructural softening processes, similar to the approach presented in [127], which is based on the dislocation density and is also applicable to nonproportional loads. In its current form, the phase mixture model accounts for softening processes due to the coarsening of subgrains by including only two phases – the soft phase, which represents the interior of the subgrains, and the hard phase with respect to the subgrain boundaries. Nevertheless, it has been shown in [13] that the macroscopic softening under creep conditions is also caused by the coarsening of carbides on the microstructural level. In order to account for this phenomenon, the phase mixture model can be refined by extending the model to three or more constituents.

Additionally, one could replace the employed iso-strain concept, cf. Eq. (5.1), by more sophisticated approaches. For example, the interaction of the phases in the mixture could be modeled using the continuum theory of mixtures, cf. [85]. Moreover, models have been presented, which are neither based on the iso-strain (VOIGT) model nor on the iso-stress (REUSS) concept. Instead, these models provide results that lie between the VOIGT-REUSS bounds, e.g. the multiphase creep model presented in [125].

Although cyclic tests have been taken into account in the current work, we mainly focused on tests under monotonic loads, e.g. the HT tensile tests or the creep tests. But power plant components are also subjected to cyclic loads, as discussed in Sect. 1.1.1, and therefore a thorough examination of the simulation of fatigue tests is recommended. In cases where the presented phase mixture model does not provide accurate predictions of the fatigue behavior, one should consider a refinement of the model itself or a new calibration of the existing model based on monotonic as well as cyclic tests. Furthermore, additional creep tests and HT tensile tests with respect to lower strain rates should be conducted in order to extend the range of applicability of the phase mixture model, which is – up to now – restricted to higher strain rates $\dot{H} > 10^{-7} \text{ s}^{-1}$. Finally, it is suggested to automatize the calibration procedure. In its current form, the calibration is conducted partly manually, such that the recalibration of the model including additional (fatigue) tests would be a cumbersome process. One should try to set up a general optimization function, which allows for the automatic determination of the material parameters.

The calibrated one-dimensional model is extended to multiaxial stress and deformation states in a straightforward way, i.e. by replacing scalar variables such as the stress, the strain, the strain rate, or the backstress by tensors and the introduction of equivalent VON MISES quantities with respect to the corresponding tensors. Based on this procedure, the

three-dimensional phase mixture model makes use of the material parameters determined by means of the one-dimensional model. In order to verify this calibrated three-dimensional model, additional experimental results are required, i.e. different material tests considering multiaxial and nonproportional loads should be conducted.

Furthermore, the phase mixture model should be used to analyze the mechanical behavior of complex power plant components under service-type loads. Since also cyclic loads should be taken into account, a fine resolution of the temporal scale is required, which results in high computational effort, considering also complicated geometries and BCs. For this reason, one should examine the numerical performance and efficiency of the current numerical implementation. If the computational costs are too high, the (currently applied) full NEWTON-RAPHSON method could be replaced by less expensive approaches, e.g. the discretized or modified NEWTON-RAPHSON methods, cf. [103]. However, it is well known that the rate of convergence often deteriorates, which should be checked carefully when applying other iterative methods.

Only in cases where other iteration approaches do not yield satisfying results in combination with implicit integration methods, one could consider the use of explicit integration methods instead of a backward EULER method. As already discussed in Sect. 5.3.1, the discrete constitutive equations are considerably easier to derive for explicit integration methods compared to implicit methods, and the solution of a nonlinear system of equations is not necessary. However, it is well known that explicit methods are only conditionally stable. Nevertheless, automatic time stepping could be implemented considering a critical time step size, which is determined based on the COURANT-FRIEDRICHS-LEWY condition [147]. As one example, an explicit integration method is combined with automatic time stepping and error control in [161]. Future research could examine whether computational costs can be reduced by implementing the phase mixture model using explicit integration methods with automatic time stepping.

The possible improvements of the implementation of the phase mixture model mentioned above are proposed having the overall goal of this thesis in mind, i.e. enabling the in-service assessment of power plant components, such that one can deduce measures to improve the design and extend the lifetime of the components. In order to simulate the mechanical behavior of power plant components under service-type loads, one should try to obtain additional data concerning the exact geometry of the components as well as the thermal and mechanical loads during the operational cycles. Using an axisymmetric finite element model, cf. Chapt. 6 and [58], is an acceptable simplification, but it would be beneficial to employ a three-dimensional model to account for the influence of the rotor blades, as depicted in Fig. 1.1. The refined phase mixture model could be used to determine the stress and strain fields during the different cycles in an efficient way. Based on these results, one could evaluate the creep and fatigue damage, thus laying the foundations for a precise assessment of the lifetime of the individual components.

Bibliography

- [1] Guo, K. W. "Current Issues of Fossil Fuels and Their Future Prospects". In: *Fossil Fuels: Sources, Environmental Concerns and Waste Management Practices*. Ed. by Kumar, R. Nova Science Publishers, Inc., 2013.
- [2] Pedraza, J. M. *Nuclear Power: Current and Future Role in the World Electricity Generation*. Nova Science Publishers, Inc., 2012.
- [3] Breeze, P. A. *Power Generation Technologies*. Newnes, 2014.
- [4] Dincer, I. and Zamfirescu, C. *Advanced Power Generation Systems*. Elsevier, 2014.
- [5] Masuyama, F. "Advances in Physical Metallurgy and Processing of Steels. History of Power Plants and Progress in Heat Resistant Steels". In: *The Iron and Steel Institute of Japan International* 41(6), 2001, pp. 612–625. DOI: 10.2355/isijinternational.41.612.
- [6] Fournier, B., Sauzay, M., Mottot, M., Brillet, H., Monnet, I., and Pineau, A. "Experimentally Based Modelling of Cyclically Induced Softening in a Martensitic Steel at High Temperature". In: *ECCC Creep Conference*. Ed. by Shibli, I., Holdsworth, S., and Merckling, G. DES tech publications, 2005, pp. 649–661.
- [7] Fournier, B., Sauzay, M., Renault, A., Barcelo, F., and Pineau, A. "Microstructural evolutions and cyclic softening of 9%Cr martensitic steels". In: *Journal of Nuclear Materials* 386-388, 2009, pp. 71–74. DOI: 10.1016/j.jnucmat.2008.12.061.
- [8] Fournier, B., Dalle, F., Sauzay, M., Longour, J., Salvi, M., Caës, C., Tournié, I., Giroux, P.-F., and Kim, S.-H. "Comparison of various 9–12%Cr steels under fatigue and creep-fatigue loadings at high temperature". In: *Materials Science and Engineering: A* 528(22–23), 2011, pp. 6934–6945. DOI: 10.1016/j.msea.2011.05.046.
- [9] Fournier, B., Salvi, M., Dalle, F., Carlan, Y. de, Caës, C., Sauzay, M., and Pineau, A. "Lifetime prediction of 9–12% Cr martensitic steels subjected to creep–fatigue at high temperature". In: *International Journal of Fatigue* 32(6), 2010, pp. 971–978. DOI: 10.1016/j.ijfatigue.2009.10.017.
- [10] Röttger, D. R. "Untersuchungen zum Wechselverformungs- und Zeitstandverhalten der Stähle X20CrMoV121 und X10CrMoVNb91". PhD thesis. Essen: Universität GH Essen, 1997.
- [11] [siemens.com/gasturbines. Siemens SGT-8000H series](http://www.energy.siemens.com/hq/pool/hq/power-generation/gas-turbines/SGT6-8000H/downloads/SGT6-8000H-Poster-final-141016.pdf). 2016. URL: <http://www.energy.siemens.com/hq/pool/hq/power-generation/gas-turbines/SGT6-8000H/downloads/SGT6-8000H-Poster-final-141016.pdf> (visited on 07/20/2016).
- [12] [stern.de. Turbine - Technik VIEW Fotocommunity](http://view.stern.de/de/picture/2914112/schwarz-weiss-kraftwerk-krieg-technikmuseum-turbine-peenemuende-turbine-1920.jpg). 2016. URL: <http://view.stern.de/de/picture/2914112/schwarz-weiss-kraftwerk-krieg-technikmuseum-turbine-peenemuende-turbine-1920.jpg> (visited on 07/20/2016).
- [13] Straub, S. "Verformungsverhalten und Mikrostruktur warmfester martensitischer 12%-Chromstähle". PhD thesis. Erlangen-Nürnberg: Friedrich-Alexander-Universität, 1995.
- [14] Fournier, B., Sauzay, M., and Pineau, A. "Micromechanical model of the high temperature cyclic behavior of 9–12%Cr martensitic steels". In: *International Journal of Plasticity* 27(11), 2011, pp. 1803–1816. DOI: 10.1016/j.ijplas.2011.05.007.

Bibliography

- [15] Pétry, C. and Lindet, G. “Modelling creep behaviour and failure of 9Cr–0.5Mo–1.8W–VNb steel”. In: *International Journal of Pressure Vessels and Piping* 86(8), 2009, pp. 486–494. DOI: 10.1016/j.ijpvp.2009.03.006.
- [16] Naumenko, K., Kutschke, A., Kostenko, Y., and Rudolf, T. “Multi-axial thermo-mechanical analysis of power plant components from 9–12%Cr steels at high temperature”. In: *Engineering Fracture Mechanics* 78(8), 2011, pp. 1657–1668. DOI: 10.1016/j.engfracmech.2010.12.002.
- [17] Götz, G. “Langzeitentwicklung der Mikrostruktur neuer 9-12% Chromstähle für den Einsatz in Kraftwerken”. PhD thesis. Erlangen-Nürnberg: Friedrich-Alexander-Universität, 2004. URN: urn:nbn:de:bvb:29-opus-678.
- [18] DIN EN 10027-2:2015. *Designation systems for steels. Part 2: Numerical system*. July 2015.
- [19] Polcik, P. “Modellierung des Verformungsverhaltens der warmfesten 9-12% Chromstähle im Temperaturbereich von 550-650°C”. PhD thesis. Erlangen-Nürnberg: Friedrich-Alexander-Universität, 1998.
- [20] Hosseini, E., Kalyanasundaram, V., Li, X., and Holdsworth, S. R. “Effect of prior deformation on the subsequent creep and anelastic recovery behaviour of an advanced martensitic steel”. In: *Materials Science and Engineering: A* 717, 2018, pp. 68–77. DOI: 10.1016/j.msea.2018.01.049.
- [21] Pickard, A. and Meinecke, G. *The Future Role of Fossil Power Generation*. Siemens AG Energy, 2011. URL: <http://www.energy.siemens.com/ru/pool/hq/energy-topics/technical-papers/The%20Future%20Role%20of%20Fossil%20Power%20Generation.pdf> (visited on 03/05/2018).
- [22] Miettinen, J. and Howe, A. A. “Estimation of liquidus temperatures for steels using thermodynamic approach”. In: *Ironmaking & Steelmaking* 27(3), 2000, pp. 212–227. DOI: 10.1179/030192300677516.
- [23] Stahlschlüssel. *Verlag Stahlschlüssel Wegst GmbH*. Marbach, 2004.
- [24] Frost, H. J. and Ashby, M. F. *Deformation-Mechanism Maps: The Plasticity and Creep of Metals and Ceramics*. Pergamon Press, 1982.
- [25] Leizerovich, A. S. *Steam Turbines for Modern Fossil Fuel Power Plants*. Fairmont Press, 2008.
- [26] Strauß, K. *Kraftwerkstechnik zur Nutzung fossiler, nuklearer und regenerativer Energiequellen*. Springer Berlin Heidelberg, 2009. DOI: 10.1007/978-3-642-01431-4.
- [27] Czichos, H., Skrotzki, B., and Simon, F.-G. *Das Ingenieurwissen: Werkstoffe*. Springer Berlin Heidelberg, 2014. DOI: 10.1007/978-3-642-41126-7.
- [28] Weißbach, W., Dahms, M., and Jaroschek, C. *Werkstoffkunde*. Springer Fachmedien Wiesbaden, 2015. DOI: 10.1007/978-3-658-03919-6.
- [29] Priester, L. *Grain Boundaries. From Theory to Engineering*. Springer Science+Business Media Dordrecht, 2013. DOI: 10.1007/978-94-007-4969-6.
- [30] Berns, H. and Theisen, W. *Eisenwerkstoffe - Stahl und Gusseisen*. Springer Berlin Heidelberg, 2008. DOI: 10.1007/978-3-540-79957-3.
- [31] Giroux, P. F., Dalle, F., Sauzay, M., Malaplate, J., Fournier, B., and Gourgues-Lorenzon, A. F. “Mechanical and microstructural stability of P92 steel under uniaxial tension at high temperature”. In: *Materials Science and Engineering: A* 527(16-17), 2010, pp. 3984–3993. DOI: 10.1016/j.msea.2010.03.001.

- [32] Wang, L., Li, M., and Almer, J. "In situ characterization of Grade 92 steel during tensile deformation using concurrent high energy X-ray diffraction and small angle X-ray scattering". In: *Journal of Nuclear Materials* 440(1-3), 2013, pp. 81–90. DOI: 10.1016/j.jnucmat.2013.04.063.
- [33] Alsagabi, S., Shrestha, T., and Charit, I. "High temperature tensile deformation behavior of Grade 92 steel". In: *Journal of Nuclear Materials* 453(1-3), 2014, pp. 151–157. DOI: 10.1016/j.jnucmat.2014.06.033.
- [34] Kostenko, Y., Almstedt, H., Naumenko, K., Linn, S., and Scholz, A. "Robust methods for creep fatigue analysis of power plant components under cyclic transient thermal loading". In: *ASME Turbo Expo 2013: Turbine Technical Conference and Exposition*. American Society of Mechanical Engineers. 2013, V05BT25A040. DOI: 10.1115/GT2013-95680.
- [35] Chilukuru, H., Durst, K., Wadekar, S., Schwienheer, M., Scholz, A., Berger, C., Mayer, K. H., and Blum, W. "Coarsening of precipitates and degradation of creep resistance in tempered martensite steels". In: *Materials Science and Engineering: A* 510-511, 2009, pp. 81–87. DOI: 10.1016/j.msea.2008.04.088.
- [36] Agamennone, R., Blum, W., Gupta, C., and Chakravarty, J. K. "Evolution of microstructure and deformation resistance in creep of tempered martensitic 9–12%Cr–2%W–5%Co steels". In: *Acta Materialia* 54(11), 2006, pp. 3003–3014. DOI: 10.1016/j.actamat.2006.02.038.
- [37] Orlová, A., Buršík, J., Kuchřoavá, K., and Sklenička, V. "Microstructural development during high temperature creep of 9% Cr steel". In: *Materials Science and Engineering: A* 245, 1998, pp. 39–48. DOI: 10.1016/S0921-5093(97)00708-9.
- [38] Fournier, B., Sauzay, M., Barcelo, F., Rauch, E., Renault, A., Cozzika, T., Dupuy, L., and Pineau, A. "Creep-Fatigue Interactions in a 9 Pct Cr-1 Pct Mo Martensitic Steel: Part II. Microstructural Evolutions". In: *Metallurgical and Materials Transactions A* 40(2), 2009, pp. 330–341. DOI: 10.1007/s11661-008-9687-y.
- [39] Blum, W. "Mechanisms of creep deformation in steel". In: *Creep-Resistant Steels*. Ed. by Abe, F., Kern, T.-U., and Viswanathan, R. Woodhead Publishing Limited, 2008, pp. 365–402.
- [40] Nabarro, F. R. N. and Villiers, H. L. de. *The Physics of Creep: Creep and Creep-Resistant Alloys*. Taylor & Francis, 1995.
- [41] F. Abe, T.-U. Kern, R. Viswanathan, ed. *Creep-Resistant Steels*. Woodhead Publishing Limited, 2004.
- [42] Naumenko, K., Altenbach, H., and Kutschke, A. "A Combined Model for Hardening, Softening, and Damage Processes in Advanced Heat Resistant Steels at Elevated Temperature". In: *International Journal of Damage Mechanics* 20(4), 2011, pp. 578–597. DOI: 10.1177/1056789510386851.
- [43] Verma, P., Srinivasa, N. S. C., and Singha, V. "Low cycle fatigue behavior of modified 9Cr-1Mo steel at 300 °C". In: *Materials Science and Engineering: A* 715, 2018, pp. 17–24. DOI: 10.1016/j.msea.2017.12.105.
- [44] Giroux, P.-F. "Experimental study and simulation of cyclic softening of tempered martensite ferritic steels". PhD thesis. École Nationale Supérieure des Mines de Paris, 2011.
- [45] Chaboche, J.-L. and Rousselier, G. "On the Plastic and Viscoplastic Constitutive Equations: Part II: Application of Internal Variable Concepts to the 316 Stainless Steel". In: *Journal of Pressure Vessel Technology* 105(2), 1983, p. 159. DOI: 10.1115/1.3264258.
- [46] Wang, J., Steinmann, P., Rudolph, J., and Willuweit, A. "Simulation of creep and cyclic viscoplastic strains in high-Cr steel components based on a modified Becker–Hackenberg model". In: *International Journal of Pressure Vessels and Piping* 128, 2015, pp. 36–47. DOI: 10.1016/j.ijpvp.2015.02.003.

Bibliography

- [47] Velay, V., Bernhart, G., and Penazzi, L. "Cyclic behavior modeling of a tempered martensitic hot work tool steel". In: *International Journal of Plasticity* 22(3), 2006, pp. 459–496. DOI: 10.1016/j.ijplas.2005.03.007.
- [48] Chaboche, J.-L. "Constitutive equations for cyclic plasticity and cyclic viscoplasticity". In: *International Journal of Plasticity* 5(3), 1989, pp. 247–302. DOI: 10.1016/0749-6419(89)90015-6.
- [49] Armstrong, P. J. and Frederick, C. O. *A Mathematical Representation of the Multiaxial Bauschinger Effect*. Tech. rep. Berkeley Nuclear Laboratories, 1966.
- [50] Farragher, T. P., Scully, S., O'Dowd, N. P., and Leen, S. B. "Thermomechanical Analysis of a Pressurized Pipe Under Plant Conditions". In: *Journal of Pressure Vessel Technology* 135, 2013, pp. 011204–1–011204–9. DOI: 10.1115/1.4007287.
- [51] Farragher, T. P., Scully, S., O'Dowd, N. P., Hyde, C. J., and Leen, S. B. "High Temperature, Low Cycle Fatigue Characterization of P91 Weld and Heat Affected Zone Material". In: *Journal of Pressure Vessel Technology* 136(2), 2014, pp. 021403–1–021403–10. DOI: 10.1115/1.4025943.
- [52] Koo, G.-H. and Kwon, J.-H. "Identification of inelastic material parameters for modified 9Cr-1Mo steel applicable to the plastic and viscoplastic constitutive equations". In: *International Journal of Pressure Vessels and Piping* 88, 2011, pp. 26–33. DOI: 10.1016/j.ijpvp.2010.11.004.
- [53] Wang, P., Cui, L., Lyschik, M., Scholz, A., Berger, C., and Oechsner, M. "A local extrapolation based calculation reduction method for the application of constitutive material models for creep fatigue assessment". In: *International Journal of Fatigue* 44, 2012, pp. 253–259. DOI: 10.1016/j.ijfatigue.2012.04.018.
- [54] Saad, A. A., Sun, W., Hyde, T. H., and Tanner, D. "Cyclic softening behaviour of a P91 steel under low cycle fatigue at high temperature". In: *Procedia Engineering* 10, 2011, pp. 1103–1108. DOI: 10.1016/j.proeng.2011.04.182.
- [55] Saad, A. A. "Cyclic plasticity and creep of power plant materials". PhD thesis. Nottingham: University of Nottingham, 2012. URL: <http://eprints.nottingham.ac.uk/id/eprint/12538>.
- [56] Barrett, R. A., O'Donoghue, P. E., and Leen, S. B. "An improved unified viscoplastic constitutive model for strain-rate sensitivity in high temperature fatigue". In: *International Journal of Fatigue* 48, 2013, pp. 192–204. DOI: 10.1016/j.ijfatigue.2012.11.001.
- [57] Zhang, S.-L. and Xuan, F.-Z. "Interaction of cyclic softening and stress relaxation of 9–12% Cr steel under strain-controlled fatigue-creep condition: Experimental and modeling". In: *International Journal of Plasticity*, 2017, pp. 1–20. DOI: 10.1016/j.ijplas.2017.06.007.
- [58] Benaarbia, A., Rae, Y., and Sun, W. "Unified viscoplasticity modelling and its application to fatigue-creep behaviour of gas turbine rotor". In: *International Journal of Mechanical Sciences* 136, 2018, pp. 36–49. DOI: 10.1016/j.ijmecsci.2017.12.008.
- [59] Saad, A. A., Hyde, C. J., Sun, W., and Hyde, T. H. "Thermal-mechanical fatigue simulation of a P91 steel in a temperature range of 400–600 °C". In: *Materials at High Temperatures* 28(3), 2011, pp. 212–218. DOI: 10.3184/096034011X13072954674044.
- [60] Estrin, Y., Braasch, H., and Brechet, Y. "A Dislocation Density Based Constitutive Model for Cyclic Deformation". In: *Journal of Engineering Materials and Technology* 118(4), 1996, pp. 441–447. DOI: 10.1115/1.2805940.
- [61] Sauzay, M., Brilliet, H., Monneta, I., Mottot, M., Barcelo, F., Fournier, B., and Pineau, A. "Cyclically induced softening due to low-angle boundary annihilation in a martensitic steel". In: *Materials Science and Engineering: A* 400–401, 2005, pp. 241–244. DOI: 10.1016/j.msea.2005.02.092.

- [62] Sauzay, M., Fournier, B., Mottot, M., Pineau, A., and Monnet, I. "Cyclic softening of martensitic steels at high temperature: Experiments and physically based modelling". In: *Materials Science and Engineering: A* 483–484, 2008, pp. 410–414. DOI: 10.1016/j.msea.2006.12.183.
- [63] Barrett, R. A., O'Donoghue, P. E., and Leen, S. B. "A dislocation-based model for high temperature cyclic viscoplasticity of 9-12Cr steels". In: *Computational Materials Science* 92, 2014, pp. 286–297. DOI: 10.1016/j.commatsci.2014.05.034.
- [64] Barrett, R. A., O'Donoghue, P. E., and Leen, S. B. "A physically-based constitutive model for high temperature microstructural degradation under cyclic deformation". In: *International Journal of Fatigue* 100, 2017, pp. 388–406. DOI: 10.1016/j.ijfatigue.2017.03.018.
- [65] Barkar, T. and Ågren, J. "Creep simulation of 9–12% Cr steels using the composite model with thermodynamically calculated input". In: *Materials Science and Engineering: A* 395(1–2), 2005, pp. 110–115. DOI: 10.1016/j.msea.2004.12.004.
- [66] Blum, W. "Mechanisms of creep deformation in steel". In: *Creep-Resistant Steels*. Ed. by Abe, F., Kern, T.-U., and Viswanathan, R. Woodhead Publishing Limited, 2008, pp. 365–402.
- [67] Naumenko, K. and Gariboldi, E. "A phase mixture model for anisotropic creep of forged Al–Cu–Mg–Si alloy". In: *Materials Science and Engineering: A* 618, 2014, pp. 368–376. DOI: 10.1016/j.msea.2014.09.012.
- [68] Altenbach, H. *Kontinuumsmechanik. Einführung in die materialunabhängigen und materialabhängigen Gleichungen*. 3rd ed. Springer Vieweg, 2015. DOI: 10.1007/978-3-662-47070-1.
- [69] Bertram, A. *Elasticity and Plasticity of Large Deformations*. 3rd ed. Springer Berlin Heidelberg, 2008. DOI: 10.1007/978-3-540-69400-7.
- [70] Stein, E. and Barthold, F.-J. "Elastizitätstheorie". In: *Der Ingenieurbau, Grundwissen: Werkstoffe, Elastizitätstheorie*. Ed. by Mehlhorn, G. Ernst & Sohn, 1996, pp. 165–428.
- [71] Naumenko, K. and Altenbach, H. *Modeling High Temperature Materials Behavior for Structural Analysis. Part I: Continuum Mechanics Foundations and Constitutive Models*. Vol. 28. Advanced Structured Materials. Springer International Publishing, 2016. DOI: 10.1007/978-3-319-31629-1.
- [72] Bowen, R. M. *Introduction to Continuum Mechanics for Engineers*. Plenum Press, 2007.
- [73] Lai, W. M., Rubin, D., and Krempl, E. *Introduction to Continuum Mechanics*. Butterworth-Heinemann, 2010.
- [74] Haupt, P. *Continuum Mechanics and Theory of Materials*. Springer Berlin Heidelberg, 2002. DOI: 10.1007/978-3-662-04775-0.
- [75] Kaliszky, S. *Plastizitätslehre: Theorie und technische Anwendungen*. Düsseldorf: VDI Verlag GmbH, 1984.
- [76] Bodner, S. R. and Partom, Y. "Constitutive Equations for Elastic-Viscoplastic Strain-Hardening Materials". In: *Journal of Applied Mechanics* 42(2), 1975, pp. 385–389. DOI: 10.1115/1.3423586.
- [77] Miller, A. "An Inelastic Constitutive Model for Monotonic, Cyclic, and Creep Deformation: Part I - Equations Development and Analytical Procedures". In: *Journal of Engineering Materials and Technology* 98(2), 1976, pp. 97–105. DOI: 10.1115/1.3443367.
- [78] Miller, A. "An Inelastic Constitutive Model for Monotonic, Cyclic, and Creep Deformation: Part II - Application to Type 304 Stainless Steel". In: *Journal of Engineering Materials and Technology* 98(2), 1976, pp. 106–113. DOI: 10.1115/1.3443346.
- [79] Coleman, B. D. and Gurtin, M. E. "Thermodynamics with Internal State Variables". In: *The Journal of Chemical Physics* 47(2), 1967, pp. 597–613. DOI: 10.1063/1.1711937.

Bibliography

- [80] Odqvist, F. K. G. *Mathematical Theory of Creep and Creep Rupture*. Oxford University Press, 1974.
- [81] Odqvist, F. K. G. and Hult, J. *Kriechfestigkeit metallischer Werkstoffe*. Springer, 1962.
- [82] Chaboche, J.-L. "A review of some plasticity and viscoplasticity constitutive theories". In: *International Journal of Plasticity* 24(10), 2008, pp. 1642–1693. DOI: 10.1016/j.ijplas.2008.03.009.
- [83] Penny, R. K. and Marriott, D. L. *Design for Creep*. Chapman & Hall, 1995.
- [84] Ilschner, B. *Hochtemperatur-Plastizität: Warmfestigkeit und Warmverformbarkeit metallischer und nichtmetallischer Werkstoffe*. Vol. 23. Reine und angewandte Metallkunde in Einzeldarstellungen. Springer Berlin Heidelberg New York, 1973.
- [85] Atkin, R. J. and Craine, R. E. "Continuum theories of mixtures: basic theory and historical development". In: *The Quarterly Journal of Mechanics and Applied Mathematics* 29(2), 1976, pp. 209–244. DOI: 10.1093/qjmam/29.2.209.
- [86] Atkin, R. J. and Craine, R. E. "Continuum Theories of Mixtures: Applications". In: *IMA Journal of Applied Mathematics* 17(2), 1976, pp. 153–207. DOI: 10.1093/imamat/17.2.153.
- [87] Rajagopal, K. R. and Tao, L. *Mechanics of Mixtures*. Vol. 35. Series on Advances in Mathematics for Applied Sciences. World Scientific, 1995.
- [88] Altenbach, H., Naumenko, K., and Zhilin, P. A. "A micro-polar theory for binary media with application to phase-transitional flow of fiber suspensions". In: *Continuum Mechanics and Thermodynamics* 15(6), 2003, pp. 539–570. DOI: 10.1007/s00161-003-0133-5.
- [89] Massoudi, M. "A note on the meaning of mixture viscosity using the classical continuum theories of mixtures". In: *International Journal of Engineering Science* 46(7), 2008, pp. 677–689. DOI: 10.1016/j.ijengsci.2008.01.008.
- [90] Passarella, F., Tibullo, V., and Zampoli, V. "On microstretch thermoviscoelastic composite materials". In: *European Journal of Mechanics - A/Solids* 37, 2013, pp. 294–303. DOI: 10.1016/j.euromechsol.2012.07.002.
- [91] Surana, K. S., Powell, M., and Reddy, J. N. "A simple mixture theory for ν Newtonian and generalized Newtonian constituents". In: *Continuum Mechanics and Thermodynamics* 26(1), 2014, pp. 33–65. DOI: 10.1007/s00161-012-0274-5.
- [92] Voigt, W. "Ueber die Beziehung zwischen den beiden Elasticitätsconstanten isotroper Körper". In: *Annalen der Physik* 274(12), 1889, pp. 573–587. DOI: 10.1002/andp.18892741206.
- [93] Reuss, A. "Berechnung der Fließgrenze von Mischkristallen auf Grund der Plastizitätsbedingung für Einkristalle". In: *Zeitschrift für Angewandte Mathematik und Mechanik* 9(1), 1929, pp. 49–58. DOI: 10.1002/zamm.19290090104.
- [94] Zohdi, T. I. and Wriggers, P. *An Introduction to Computational Micromechanics*. Springer Berlin Heidelberg, 2005. DOI: 10.1007/978-3-540-32360-0.
- [95] Hill, R. "The Elastic Behaviour of a Crystalline Aggregate". In: *Proceedings of the Physical Society. Section A* 65(5), 1952, pp. 349–354. DOI: 10.1088/0370-1298/65/5/307.
- [96] Durand, L. "Models of tensile behaviour of two-phase alloys from their components". In: *Materials Science and Technology* 3(2), 2013, pp. 105–109. DOI: 10.1179/mst.1987.3.2.105.
- [97] Poeh, M. H. and Fischmeister, H. F. "Deformation of two-phase materials: A model based on strain compatibility". In: *Acta Metallurgica et Materialia* 40(3), 1992, pp. 487–494. DOI: 10.1016/0956-7151(92)90397-W.
- [98] Koo, J. Y., Young, M. J., and Thomas, G. "On the law of mixtures in dual-phase steels". In: *Metallurgical Transactions A* 11(5), 1980, pp. 852–854. DOI: 10.1007/BF02661217.

- [99] Cho, K. and Gurland, J. "The law of mixtures applied to the plastic deformation of two-phase alloys of coarse microstructures". In: *Metallurgical Transactions A* 19(8), 1988, pp. 2027–2040. DOI: 10.1007/BF02645206.
- [100] Bao, G., Hutchinson, J. W., and McMeeking, R. M. "The flow stress of dual-phase, non-hardening solids". In: *Mechanics of Materials* 12(2), 1991, pp. 85–94. DOI: 10.1016/0167-6636(91)90056-6.
- [101] Li, Z., Schmauder, S., and Dong, M. "A simple mechanical model to predict fracture and yield strengths of particulate two-phase materials". In: *Computational Materials Science* 15(1), 1999, pp. 11–21. DOI: 10.1016/S0927-0256(99)00014-2.
- [102] Altenbach, H., Altenbach, J., and Kissing, W. *Mechanics of Composite Structural Elements*. Springer Berlin Heidelberg, 2004. DOI: 10.1007/978-3-662-08589-9.
- [103] Wriggers, P. *Nonlinear Finite Element Methods*. Springer Berlin Heidelberg, 2008. DOI: 10.1007/978-3-540-71001-1.
- [104] Belytschko, T., Liu, W., and Moran, B. *Nonlinear Finite Elements for Continua and Structures*. John Wiley & Sons, 2000.
- [105] Hartmann, S. and Haupt, P. "Stress computation and consistent tangent operator using non-linear kinematic hardening models". In: *International Journal for Numerical Methods in Engineering* 36(22), 1993, pp. 3801–3814. DOI: 10.1002/nme.1620362204.
- [106] Hartmann, S., Lühns, G., and Haupt, P. "An efficient stress algorithm with applications in viscoplasticity and plasticity". In: *International Journal for Numerical Methods in Engineering* 40(6), 1997, pp. 991–1013. DOI: 10.1002/(SICI)1097-0207(19970330)40:6<991::AID-NME98>3.0.CO;2-H.
- [107] Oñate, E. *Structural Analysis with the Finite Element Method: Linear Statics. Volume 1. Basis and Solids*. Springer Netherlands, 2009. DOI: 10.1007/978-1-4020-8733-2.
- [108] Zienkiewicz, O. C. and Taylor, R. L. *The Finite Element Method for Solid and Structural Mechanics*. Elsevier Butterworth-Heinemann, 2005.
- [109] Bathe, K.-J. *Finite Element Procedures*. K.-J. Bathe, 2014.
- [110] Ellsiepen, P. and Hartmann, S. "Remarks on the interpretation of current non-linear finite element analyses as differential–algebraic equations". In: *International Journal for Numerical Methods in Engineering* 51(6), 2001, pp. 679–707. DOI: 10.1002/nme.179.
- [111] Kobayashi, M., Mukai, M., Takahashi, H., Ohno, N., Kawakami, T., and Ishikawa, T. "Implicit integration and consistent tangent modulus of a time-dependent non-unified constitutive model". In: *International Journal for Numerical Methods in Engineering* 58(10), 2003, pp. 1523–1543. DOI: 10.1002/nme.825.
- [112] Rothe, S., Erbts, P., Düster, A., and Hartmann, S. "Monolithic and partitioned coupling schemes for thermo-viscoplasticity". In: *Computer Methods in Applied Mechanics and Engineering* 293, 2015, pp. 375–410. ISSN: 00457825. DOI: 10.1016/j.cma.2015.05.002.
- [113] Hartmann, S. "A remark on the application of the Newton-Raphson method in non-linear finite element analysis". In: *Computational Mechanics* 36(2), 2005, pp. 100–116. DOI: 10.1007/s00466-004-0630-9.
- [114] Burkard, R. E. and Zimmermann, U. T. *Einführung in die Mathematische Optimierung*. Springer Berlin Heidelberg, 2012. DOI: 10.1007/978-3-642-28673-5.
- [115] Nocedal, J. and Wright, S. J. *Numerical Optimization*. Springer Series in Operations Research and Financial Engineering. Springer New York, 2006. DOI: 10.1007/978-0-387-40065-5.
- [116] *MATLAB R2015a Documentation*. The MathWorks, Inc. 2015.

Bibliography

- [117] Byrd, R. H., Hribar, M. E., and Nocedal, J. “An Interior Point Algorithm for Large-Scale Nonlinear Programming”. In: *SIAM Journal on Optimization* 9(4), 1999, pp. 877–900. DOI: 10.1137/S1052623497325107.
- [118] Eisenträger, J., Naumenko, K., Altenbach, H., and Gariboldi, E. “Analysis of Temperature and Strain Rate Dependencies of Softening Regime for Tempered Martensitic Steel”. In: *The Journal of Strain Analysis for Engineering Design* 52, 2017, pp. 226–238. DOI: 10.1177/0309324717699746.
- [119] DIN 17175:1979-05. *Seamless steel tubes for elevated temperatures*. May 1979.
- [120] DIN EN ISO 6892-2:2011-05. *Metallic materials – Tensile testing – Part 2: Method of test at elevated temperature*. May 2011.
- [121] Considère, A. G. “Mémoire sur l’emploi du fer et de l’acier dans les constructions”. In: *Annales des Ponts et Chaussées* 9, 1885, pp. 574–775.
- [122] Havner, K. S. “On the onset of necking in the tensile test”. In: *International Journal of Plasticity* 20(4-5), 2004, pp. 965–978. DOI: 10.1016/j.ijplas.2003.05.004.
- [123] Needleman, A. “A numerical study of necking in circular cylindrical bar”. In: *Journal of the Mechanics and Physics of Solids* 20(2), 1972, pp. 111–127. DOI: 10.1016/0022-5096(72)90035-X.
- [124] Needleman, A. “Plastic Strain Localization in Metals”. In: *The Integration of Material, Process and Product Design*, 1999, pp. 59–70.
- [125] Raj, S. V., Iskovitz, I. S., and Freed, A. D. “Modeling the Role of Dislocation Substructure during Class M and Exponential Creep”. In: *Unified Constitutive Laws of Plastic Deformation*. Ed. by Krausz, A. S. and Krausz, K. Academic Press, Inc., 1996, pp. 343–439.
- [126] Vogler, S. and Blum, W. “Micromechanical modelling of creep in terms of the composite model”. In: *Creep and Fracture of Engineering Materials and Structures*. Ed. by Wilshire, B. and Evans, R. London: Institute of Metals, 1990, pp. 65–79.
- [127] Silbermann, C. B., Shutov, A. V., and Ihlemann, J. “Modeling the evolution of dislocation populations under non-proportional loading”. In: *International Journal of Plasticity* 55, 2014, pp. 58–79. DOI: 10.1016/j.ijplas.2013.09.007.
- [128] Eisenträger, J., Naumenko, K., and Altenbach, H. “Calibration of a phase mixture model for hardening and softening regimes in tempered martensitic steel over wide stress and temperature ranges”. In: *The Journal of Strain Analysis for Engineering Design*, 2018. DOI: 10.1177/0309324718755956.
- [129] Ievdokymov, M. “Identification Technique of Mechanism-Based Constitutive Model for Cast Iron under Thermo-Mechanical Loads”. PhD thesis. Magdeburg: Otto-von-Guericke-Universität, 2015. URN: urn:nbn:de:gbv:ma9:1-6160.
- [130] Melody van Rooyen and Thorsten Hermann Becker. “High-temperature tensile property measurements using digital image correlation over a non-uniform temperature field”. In: *The Journal of Strain Analysis for Engineering Design*, 2018, pp. 1–13. DOI: 10.1177/0309324717752029.
- [131] Längler, F., Naumenko, K., Altenbach, H., and Ievdokymov, M. “A constitutive model for inelastic behavior of casting materials under thermo-mechanical loading”. In: *The Journal of Strain Analysis for Engineering Design* 49(6), 2014, pp. 421–428. DOI: 10.1177/0309324714522034.
- [132] Xiao, Y.-H. and Guo, C. “Constitutive modelling for high temperature behavior of 1Cr12Ni3Mo-2VNbN martensitic steel”. In: *Materials Science and Engineering: A* 528(15), 2011, pp. 5081–5087. DOI: 10.1016/j.msea.2011.03.050.

- [133] Kestin, J. *A Course In Thermodynamics*. Taylor & Francis, 1979.
- [134] Garofalo, F. "An Empirical Relation Defining the Stress Dependence of Minimum Creep Rate in Metals". In: *Transactions of the Metallurgical Society of AIME* 227, 1963, pp. 351–356.
- [135] Blum, W. and Reppich, B. "On the stress dependence of the stationary deformation rate". In: *Acta Metallurgica* 17(8), 1969, pp. 959–966. DOI: 10.1016/0001-6160(69)90040-6.
- [136] Kassner, M. and Perez-Prado, M.-T. *Fundamentals of Creep in Metals and Alloys*. Elsevier, 2007. DOI: 10.1016/B978-008043637-1/50013-2.
- [137] Dorn, J. "Some fundamental experiments on high temperature creep". In: *Journal of the Mechanics and Physics of Solids* 3(2), 1955, pp. 85–116. DOI: 10.1016/0022-5096(55)90054-5.
- [138] Reed, L. J. and Berkson, J. "The application of the logistic function to experimental data". In: *The Journal of Physical Chemistry* 33(5), 1929, pp. 760–779.
- [139] Shutov, A. V. and KreiBig, R. "Finite strain viscoplasticity with nonlinear kinematic hardening: Phenomenological modeling and time integration". In: *Computer Methods in Applied Mechanics and Engineering* 197(21-24), 2008, pp. 2015–2029. DOI: 10.1016/j.cma.2007.12.017.
- [140] Zhu, Y., Kang, G., Kan, Q., and Bruhns, O. T. "Logarithmic stress rate based constitutive model for cyclic loading in finite plasticity". In: *International Journal of Plasticity* 54, 2014, pp. 34–55. DOI: 10.1016/j.ijplas.2013.08.004.
- [141] Zhu, Y. "Thermo-mechanically coupled cyclic elasto-viscoplastic constitutive model of metals: Theory and application". In: *International Journal of Plasticity* 79, 2016, pp. 111–152. DOI: 10.1016/j.ijplas.2015.12.005.
- [142] Bertram, A. and Glüge, R. *Solid Mechanics*. Springer International Publishing, 2015. DOI: 10.1007/978-3-319-19566-7.
- [143] Pekař, M. and Samohýl, I. *The Thermodynamics of Linear Fluids and Fluid Mixtures*. Springer International Publishing, 2014. DOI: 10.1007/978-3-319-02514-8.
- [144] *Abaqus 2017 Documentation*. Dassault Systèmes. 2017.
- [145] Eisenträger, J., Naumenko, K., and Altenbach, H. "Numerical Implementation of a Phase Mixture Model for Rate-Dependent Inelasticity of Tempered Martensitic Steels". In: *Acta Mechanica (accepted)*, 2018.
- [146] Luccioni, L. X., Pestana, J. M., and Taylor, R. L. "Finite element implementation of non-linear elastoplastic constitutive laws using local and global explicit algorithms with automatic error control". In: *International Journal for Numerical Methods in Engineering* 50(5), 2001, pp. 1191–1212. DOI: 10.1002/1097-0207(20010220)50:5<1191::AID-NME73>3.0.CO;2-T.
- [147] Courant, R., Friedrichs, K., and Lewy, H. "Über die partiellen Differenzgleichungen der mathematischen Physik". In: *Mathematische Annalen* 100, 1928, pp. 32–74. DOI: 10.1007/978-1-4612-5385-3_7.
- [148] Lurie, A. I. *Theory of Elasticity*. Springer Berlin Heidelberg, 2005. DOI: 10.1007/978-3-540-26455-2.
- [149] Bergan, P. G., Horrigmoe, G., Bråkeland, B., and Soreide, T. H. "Solution techniques for non-linear finite element problems". In: *International Journal for Numerical Methods in Engineering* 12(11), 1978, pp. 1677–1696. DOI: 10.1002/nme.1620121106.
- [150] Harville, D. A. *Matrix Algebra From a Statistician's Perspective*. Springer New York, 1997. DOI: 10.1007/b98818.
- [151] Simo, J. C. and Taylor, R. L. "Consistent tangent operators for rate-independent elastoplasticity". In: *Computer Methods in Applied Mechanics and Engineering* 48(1), 1985, pp. 101–118. DOI: 10.1016/0045-7825(85)90070-2.

Bibliography

- [152] Braudel, H. J., Abouaf, M., and Chenot, J. L. "An implicit and incremental formulation for the solution of elastoplastic problems by the finite element method". In: *Computers & Structures* 22(5), 1986, pp. 801–814. DOI: 10.1016/0045-7949(86)90269-5.
- [153] Duxbury, P., Crook, T., and Lyons, P. "A consistent formulation for the integration of combined plasticity and creep". In: *International Journal for Numerical Methods in Engineering* 37(8), 1994, pp. 1277–1295. DOI: 10.1002/nme.1620370803.
- [154] Chaboche, J. L. and Cailletaud, G. "Integration methods for complex plastic constitutive equations". In: *Computer Methods in Applied Mechanics and Engineering* 133(1–2), 1996, pp. 125–155. DOI: 10.1016/0045-7825(95)00957-4.
- [155] Samir, A., Simon, A., Scholz, A., and Berger, C. "Service-type creep-fatigue experiments with cruciform specimens and modelling of deformation". In: *International Journal of Fatigue* 28(5–6), 2006, pp. 643–651. DOI: 10.1016/j.ijfatigue.2005.08.010.
- [156] Holdsworth, S. R., Mazza, E., Binda, L., and Ripamonti, L. "Development of thermal fatigue damage in 1CrMoV rotor steel". In: *Nuclear Engineering and Design* 237(24), 2007, pp. 2292–2301. DOI: 10.1016/j.nucengdes.2007.05.002.
- [157] Colombo, F., Mazza, E., Holdsworth, S., and Skelton, R. "Thermo-mechanical fatigue tests on uniaxial and component-like 1CrMoV rotor steel specimens". In: *International Journal of Fatigue* 30(2), 2008, pp. 241–248. DOI: 10.1016/j.ijfatigue.2007.01.036.
- [158] Cui, L., Scholz, A., Hartrott, P. von, and Schlesinger, M. *Entwicklung von Modellen zur Lebensdauervorhersage von Kraftwerksbauteilen unter thermisch-mechanischer Kriechermü-dungsbeanspruchung*. Final report. AVIF Project 895, FVV, Issue 888, 2009.
- [159] Zhu, X., Chen, H., Xuan, F., and Chen, X. "Cyclic plasticity behaviors of steam turbine rotor subjected to cyclic thermal and mechanical loads". In: *European Journal of Mechanics - A/Solids* 66, 2017, pp. 243–255. DOI: 10.1016/j.euromechsol.2017.07.012.
- [160] Suresh, S. *Fatigue of Materials*. Cambridge University Press, 2006.
- [161] Sloan, S. W. "Substepping schemes for the numerical integration of elastoplastic stress-strain relations". In: *International Journal for Numerical Methods in Engineering* 24(5), 1987, pp. 893–911. DOI: 10.1002/nme.1620240505.

Appendix

A1 Results of Profilometry

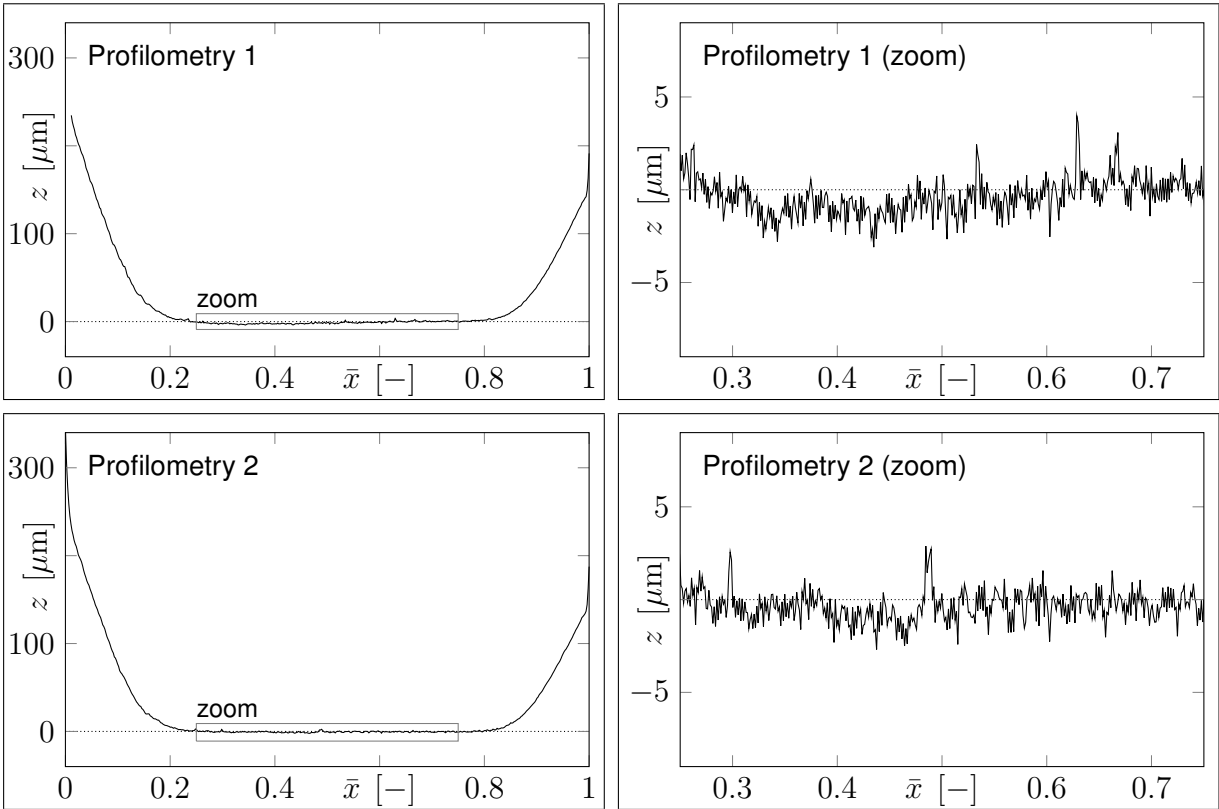


Figure A1.1: Profilometry of Specimen 2.

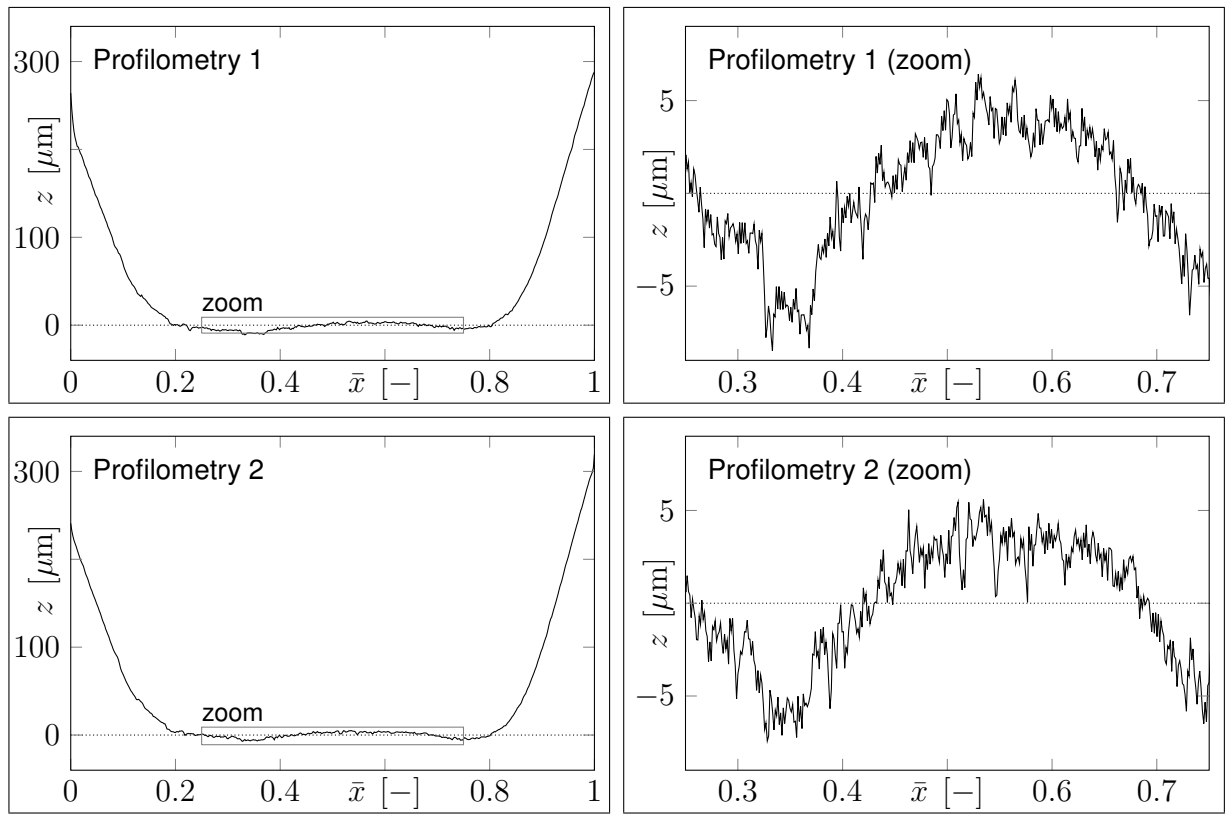


Figure A1.2: Profilometry of Specimen 3.

A2 Stress Response Functions for Inelastic Strain Rates

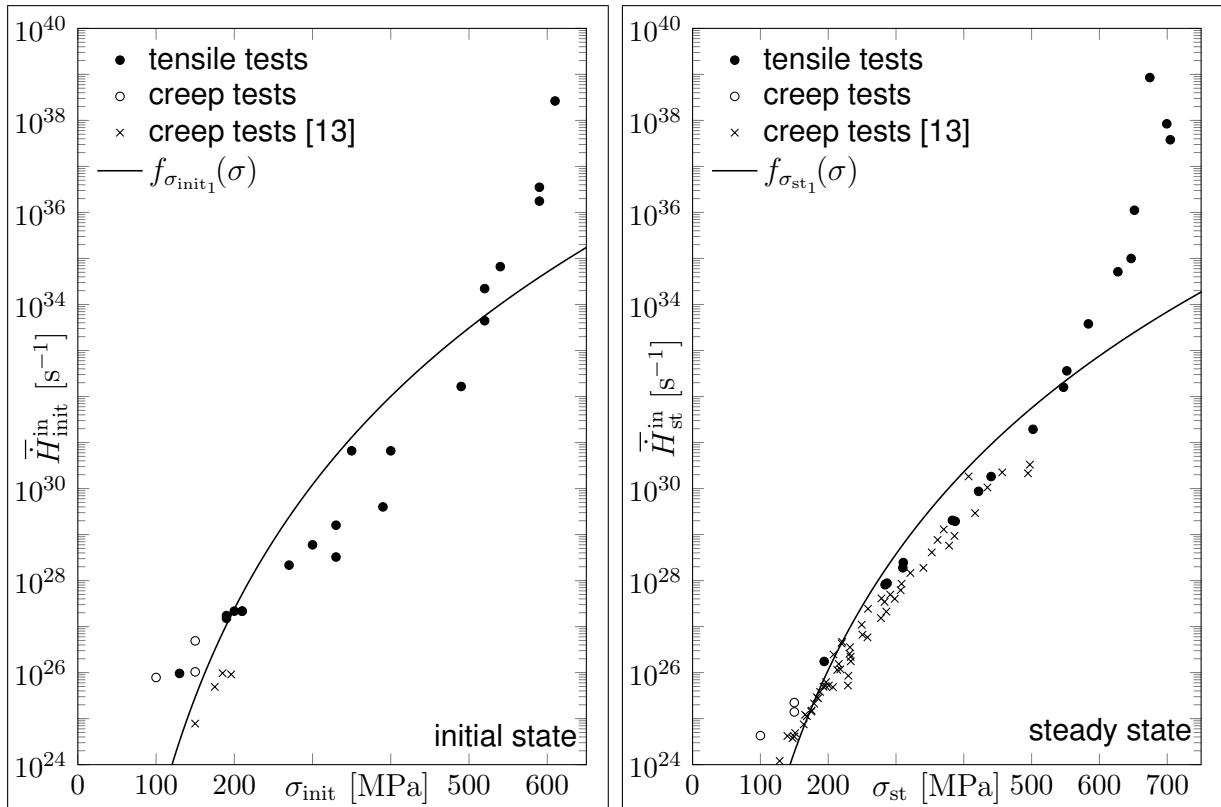


Figure A2.1: Approximation of the normalized inelastic strain rates with the response functions $f_{\sigma_{i_1}}(\sigma)$.

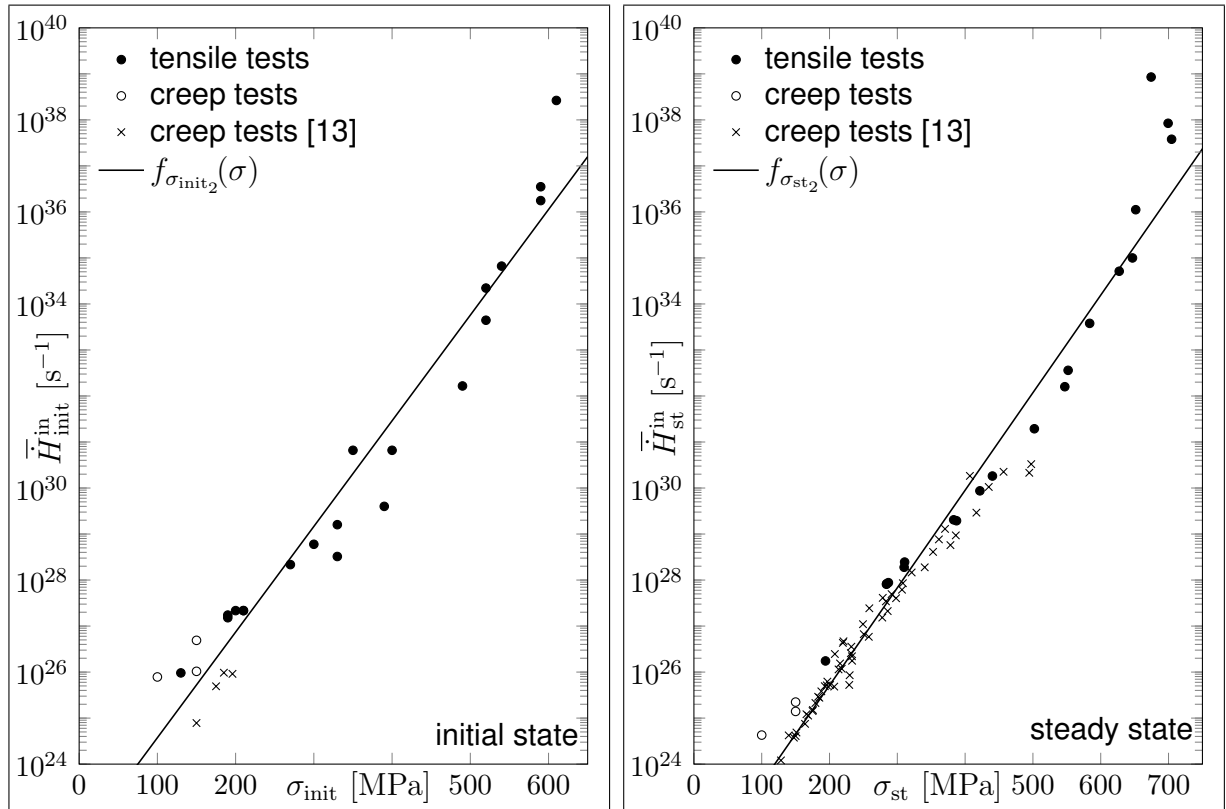


Figure A2.2: Approximation of the normalized inelastic strain rates with the response functions $f_{\sigma_{i_2}}(\sigma)$.

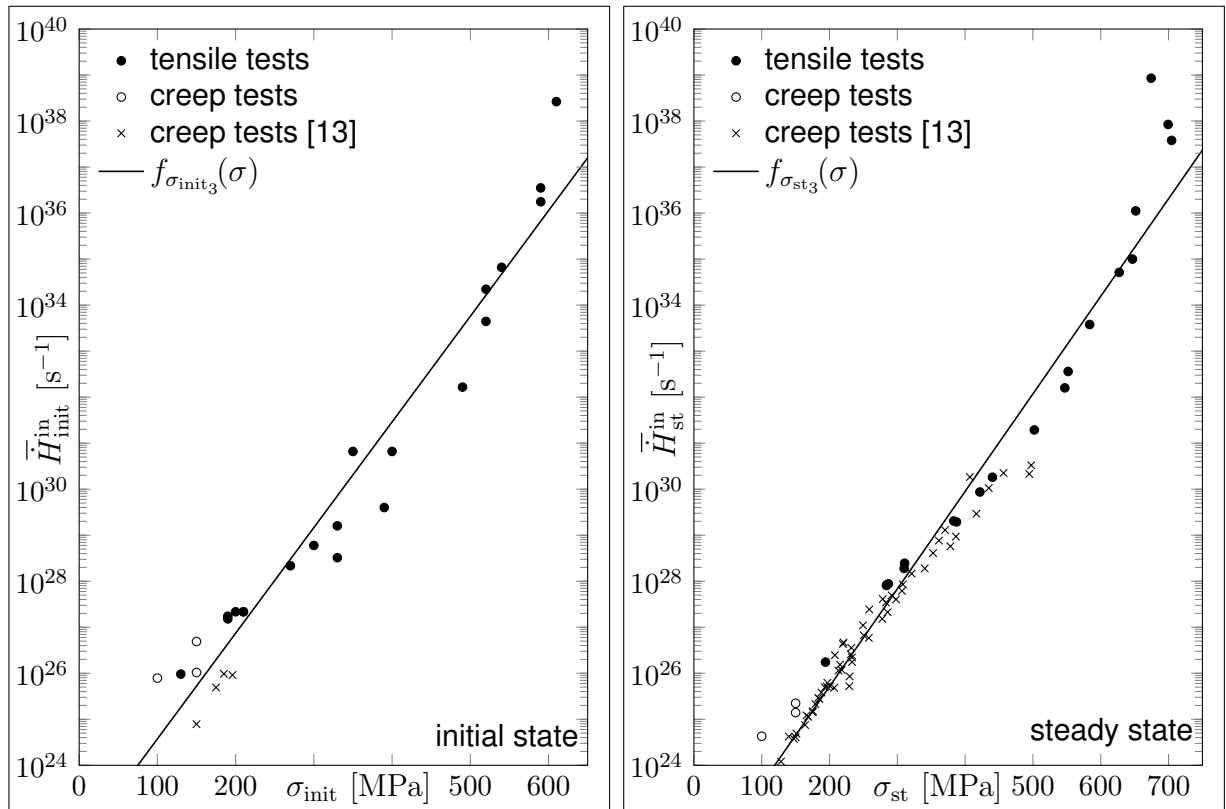


Figure A2.3: Approximation of the normalized inelastic strain rates with the response functions $f_{\sigma_{i_3}}(\sigma)$.

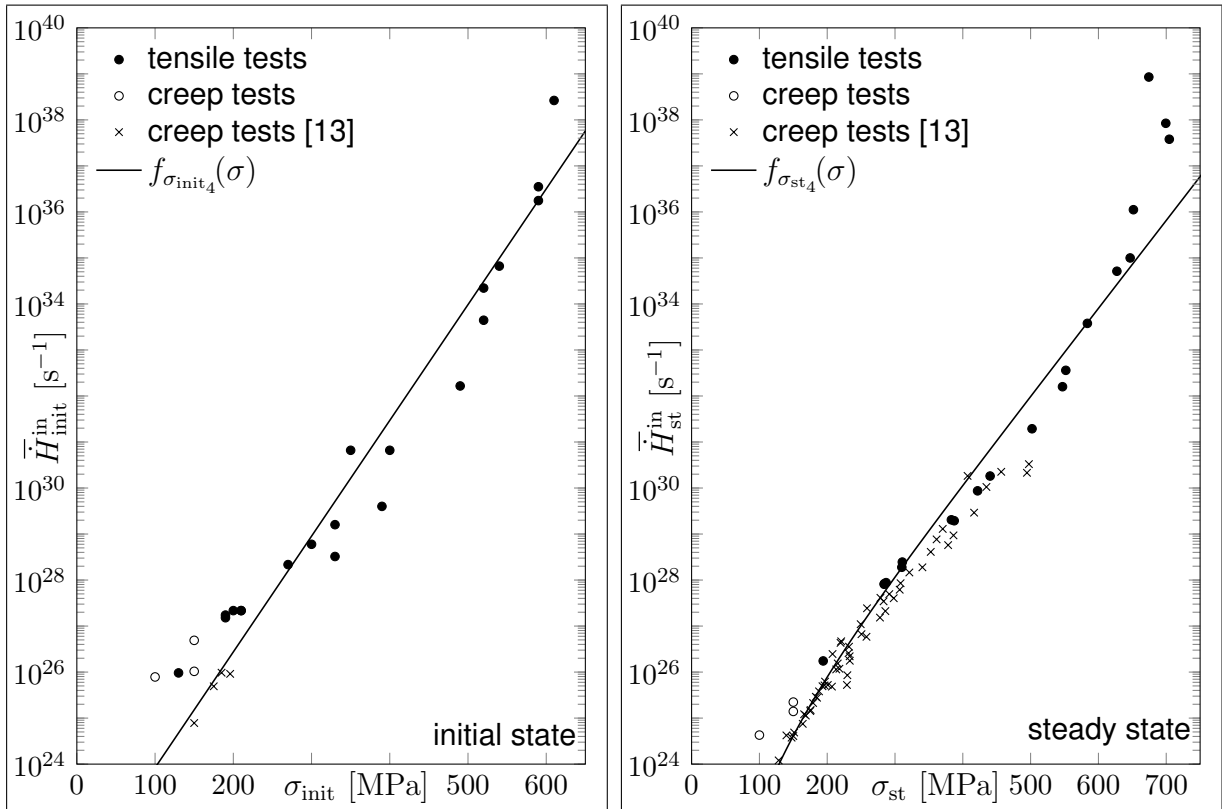


Figure A2.4: Approximation of the normalized inelastic strain rates with the response functions $f_{\sigma_{i4}}(\sigma)$.

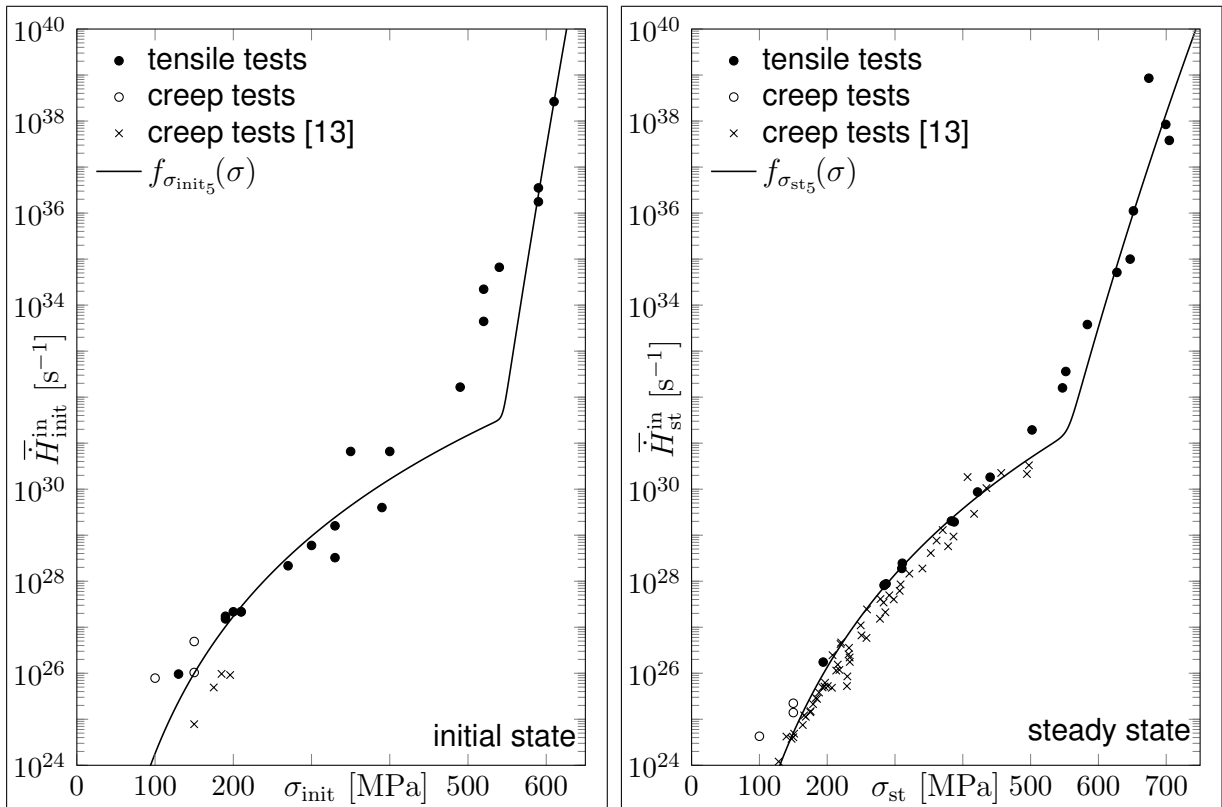


Figure A2.5: Approximation of the normalized inelastic strain rates with the response functions $f_{\sigma_{i5}}(\sigma)$.

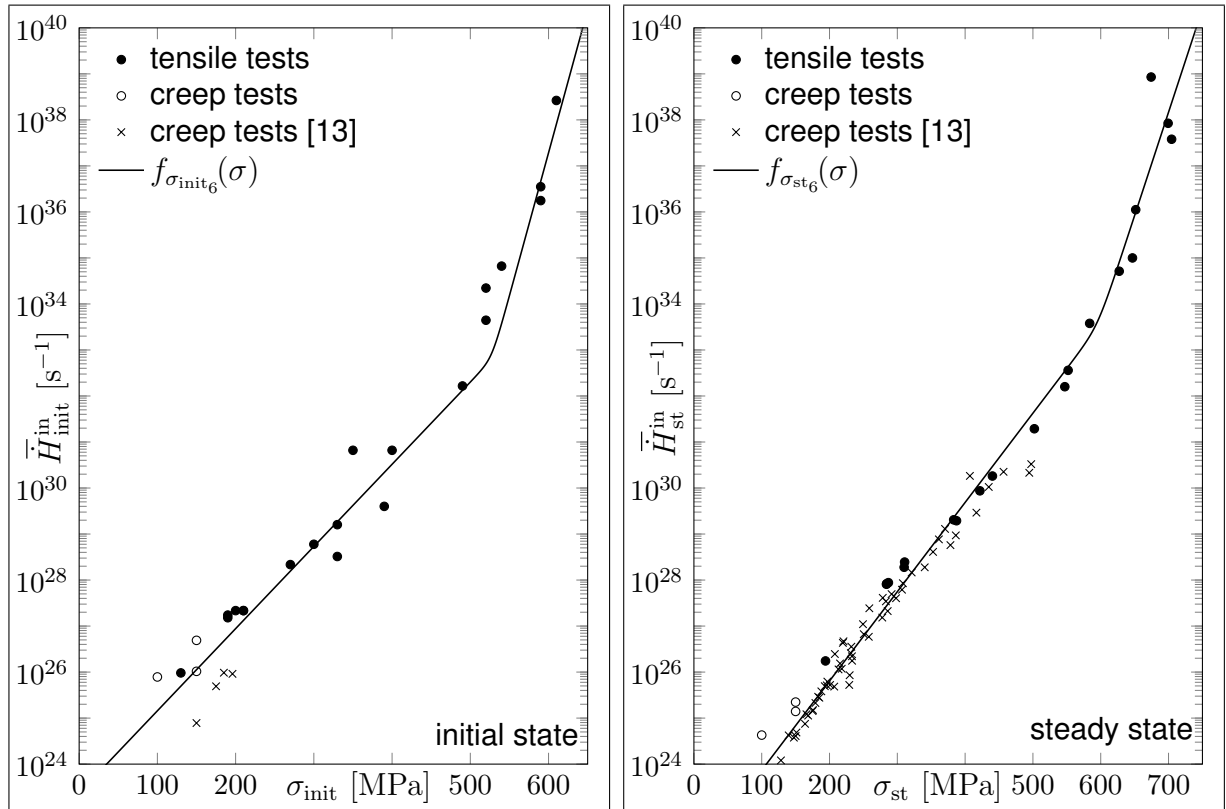


Figure A2.6: Approximation of the normalized inelastic strain rates with the response functions $f_{\sigma_{i6}}(\sigma)$.

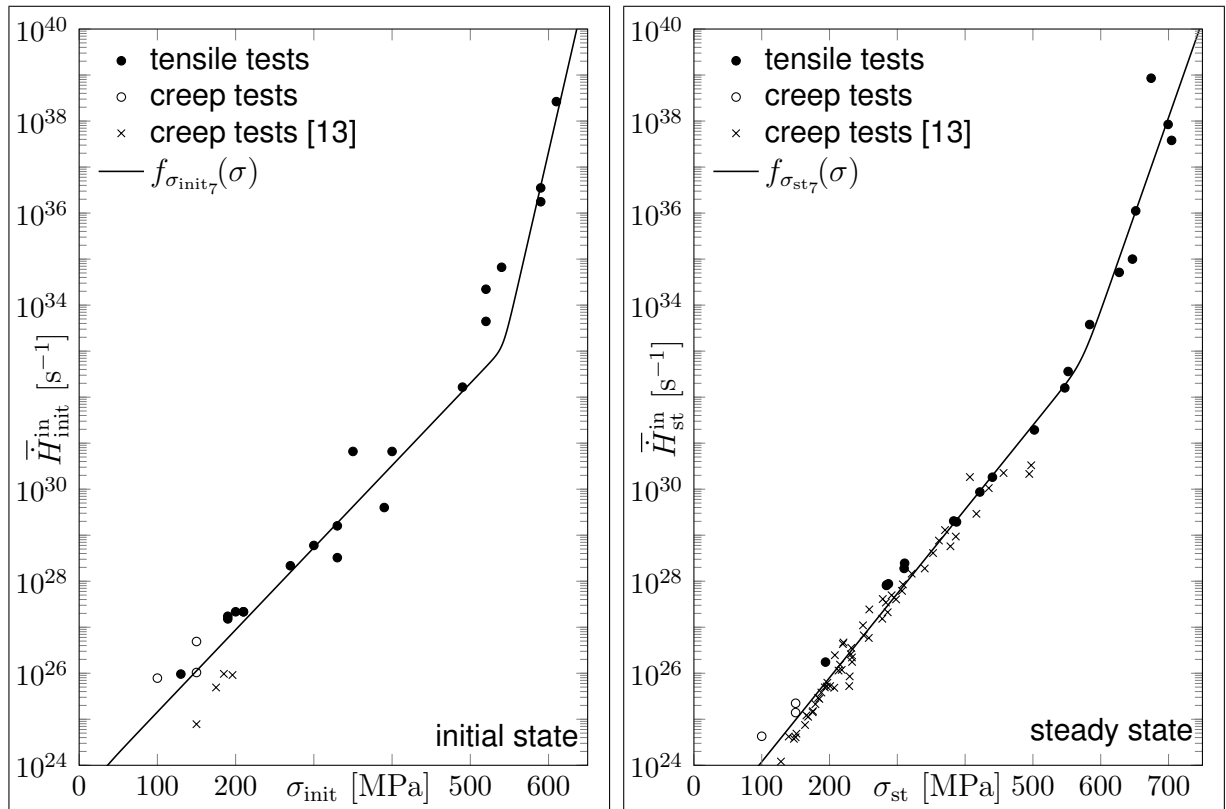


Figure A2.7: Approximation of the normalized inelastic strain rates with the response functions $f_{\sigma_{i7}}(\sigma)$.

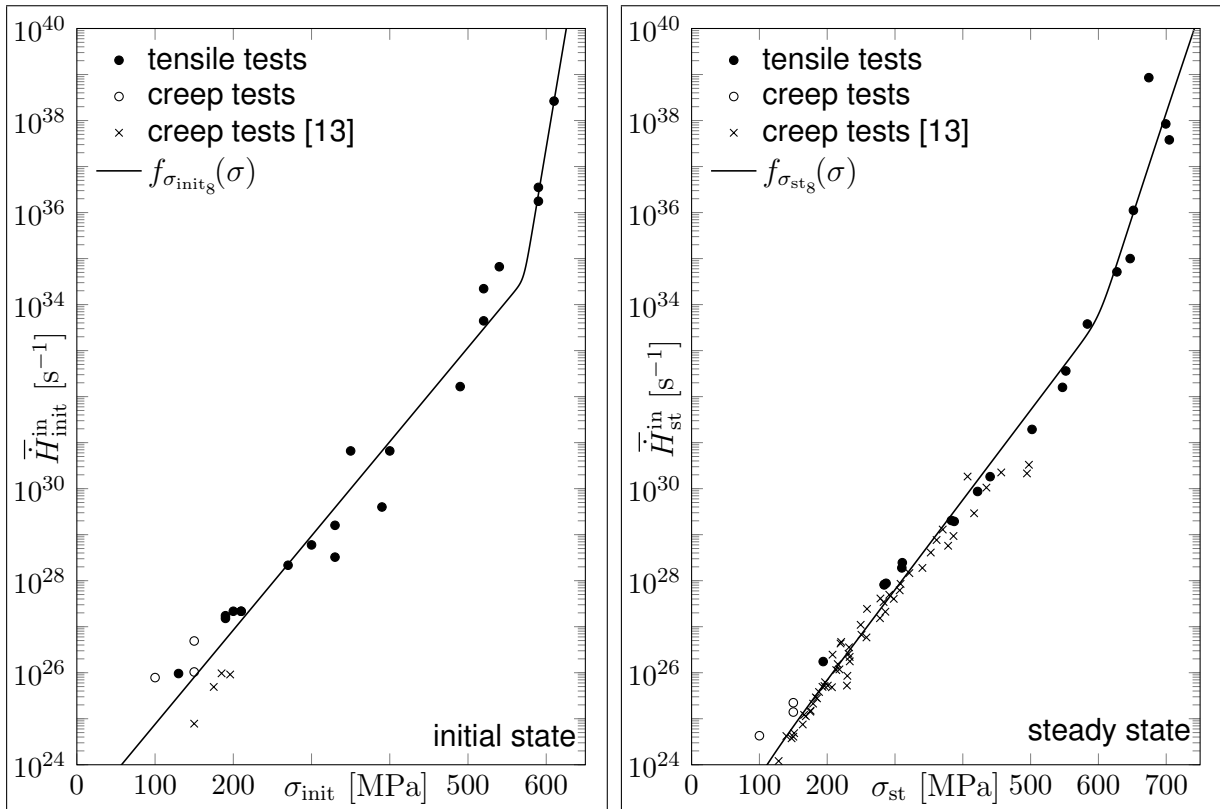


Figure A2.8: Approximation of the normalized inelastic strain rates with the response functions $f_{\sigma_{i_8}}(\sigma)$.

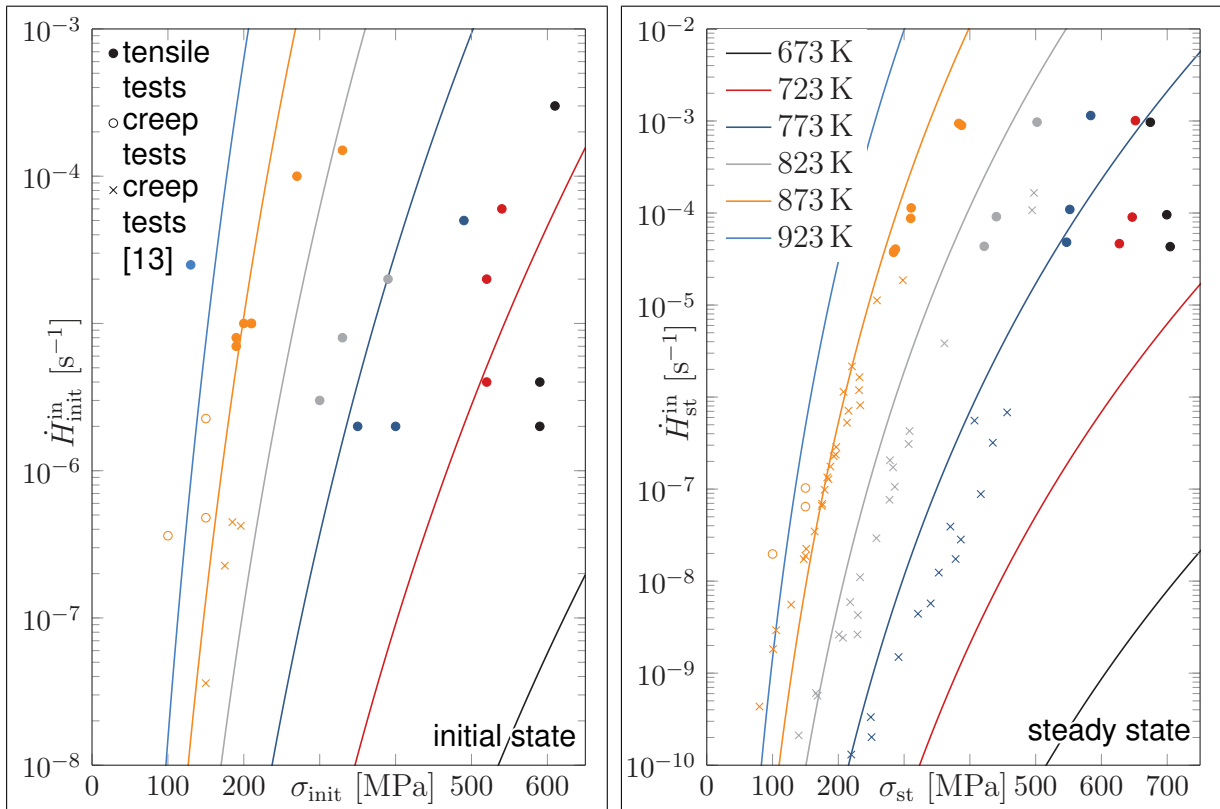


Figure A2.9: Approximation of the inelastic strain rates with the response functions $f_{\sigma_{i_1}}(\sigma)$.

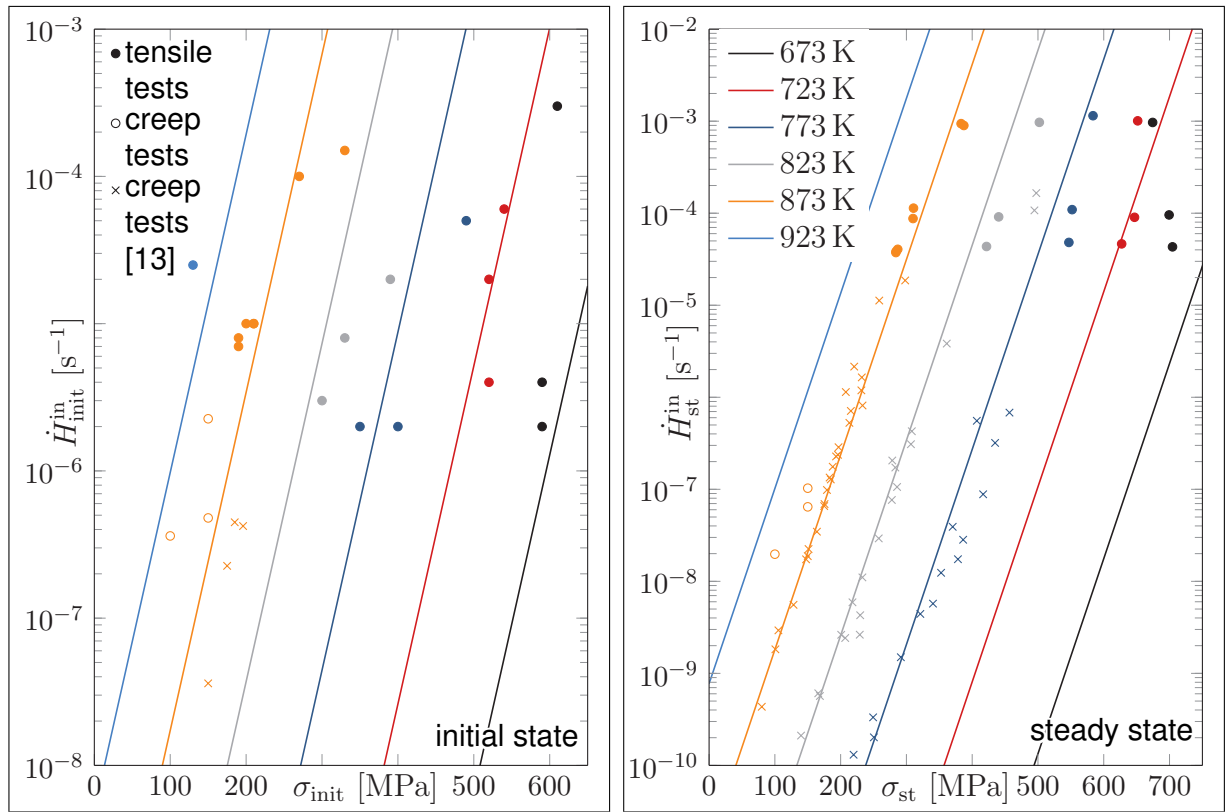


Figure A2.10: Approximation of the inelastic strain rates with the response functions $f_{\sigma_{i_2}}(\sigma)$.

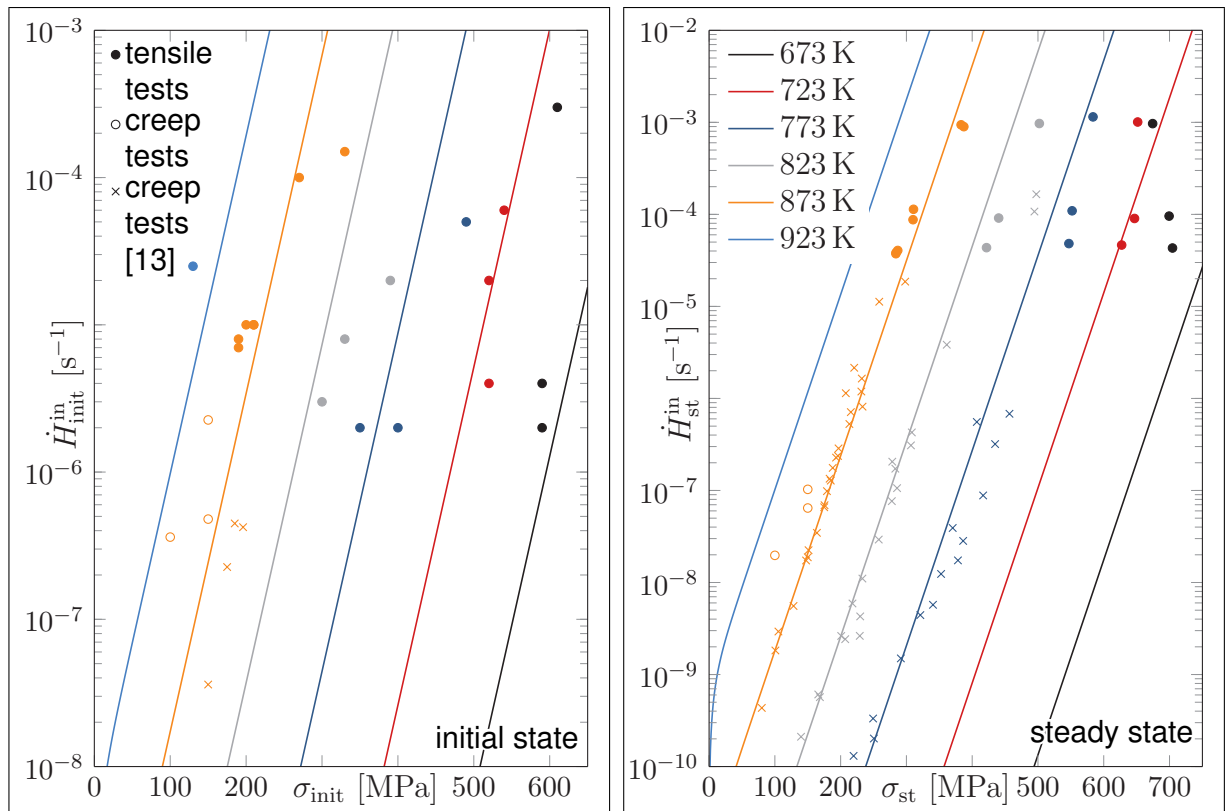


Figure A2.11: Approximation of the inelastic strain rates with the response functions $f_{\sigma_{i_3}}(\sigma)$.

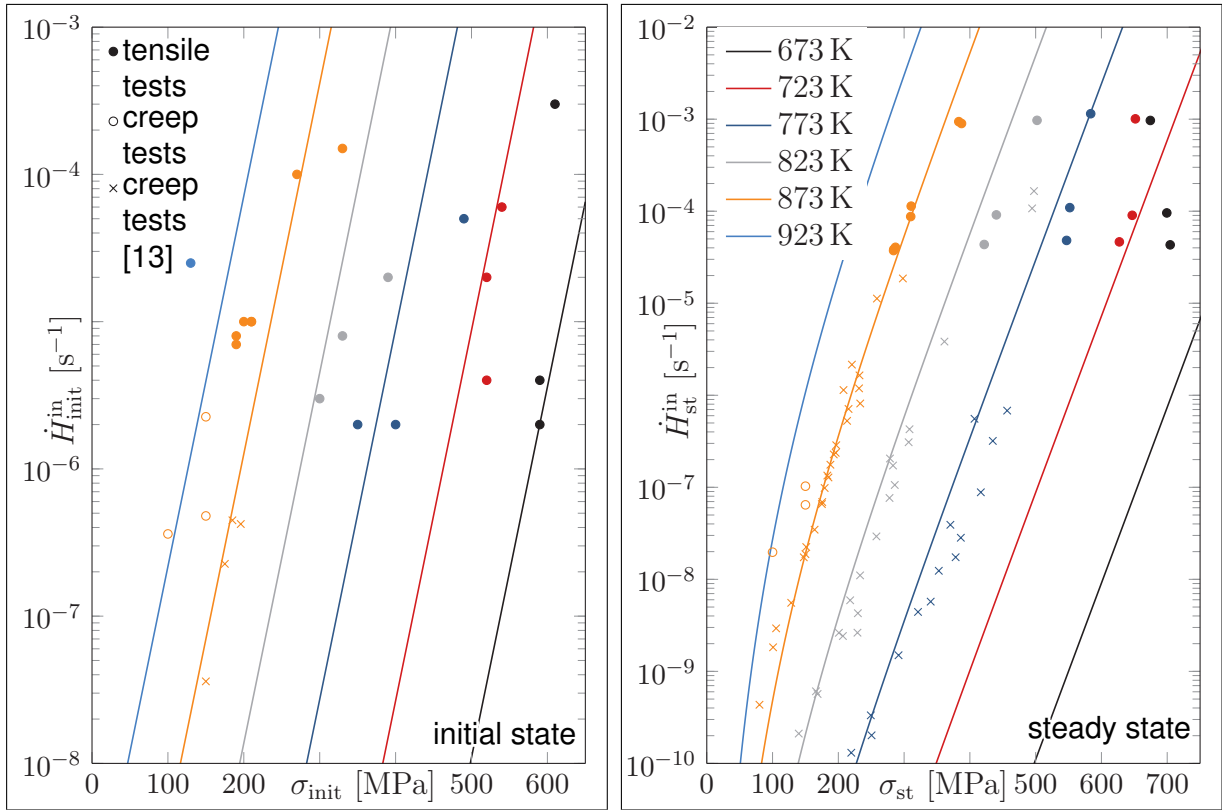


Figure A2.12: Approximation of the inelastic strain rates with the response functions $f_{\sigma_{i4}}(\sigma)$.

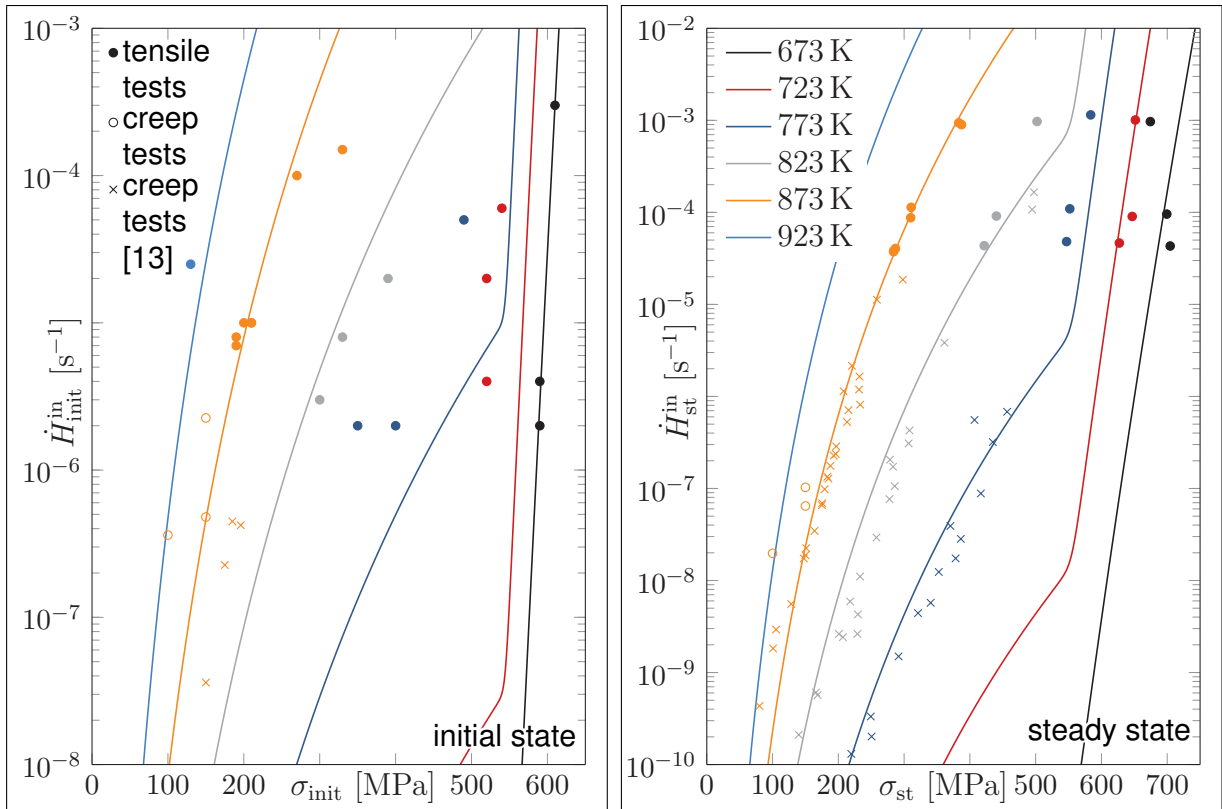


Figure A2.13: Approximation of the inelastic strain rates with the response functions $f_{\sigma_{i5}}(\sigma)$.

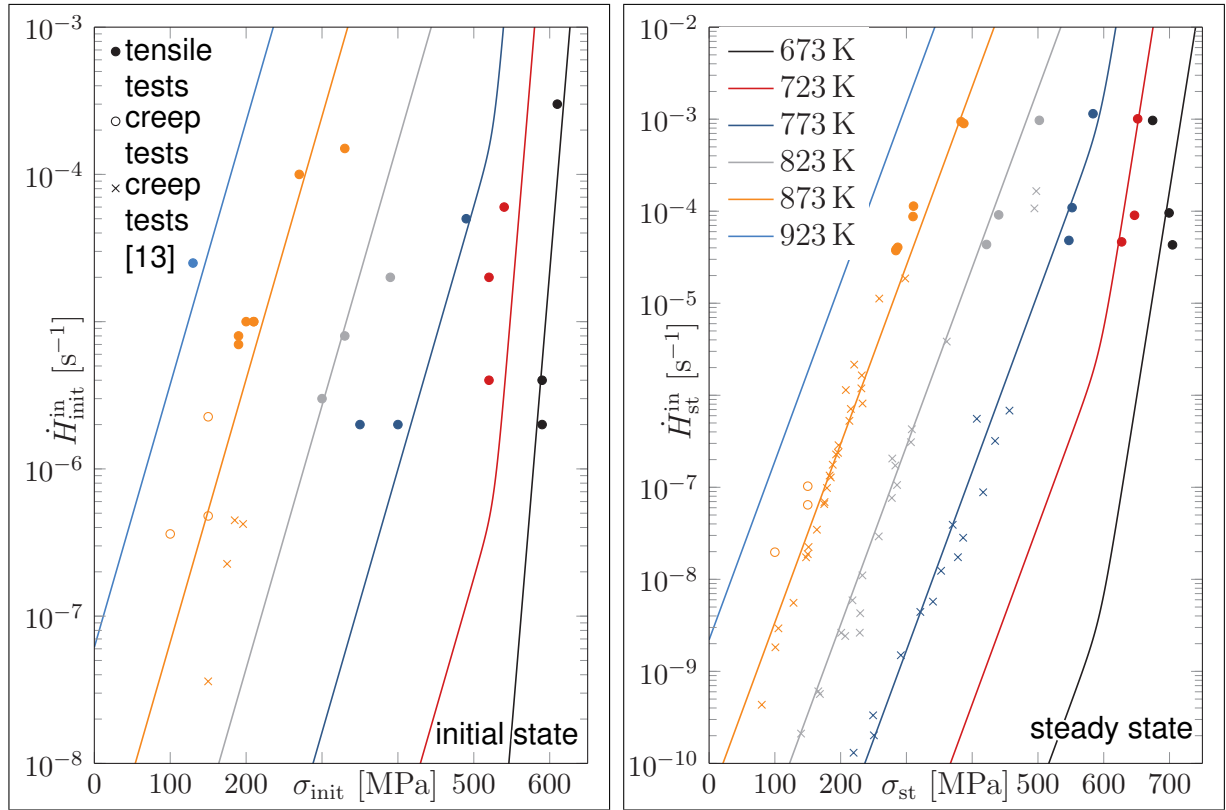


Figure A2.14: Approximation of the inelastic strain rates with the response functions $f_{\sigma_{i6}}(\sigma)$.

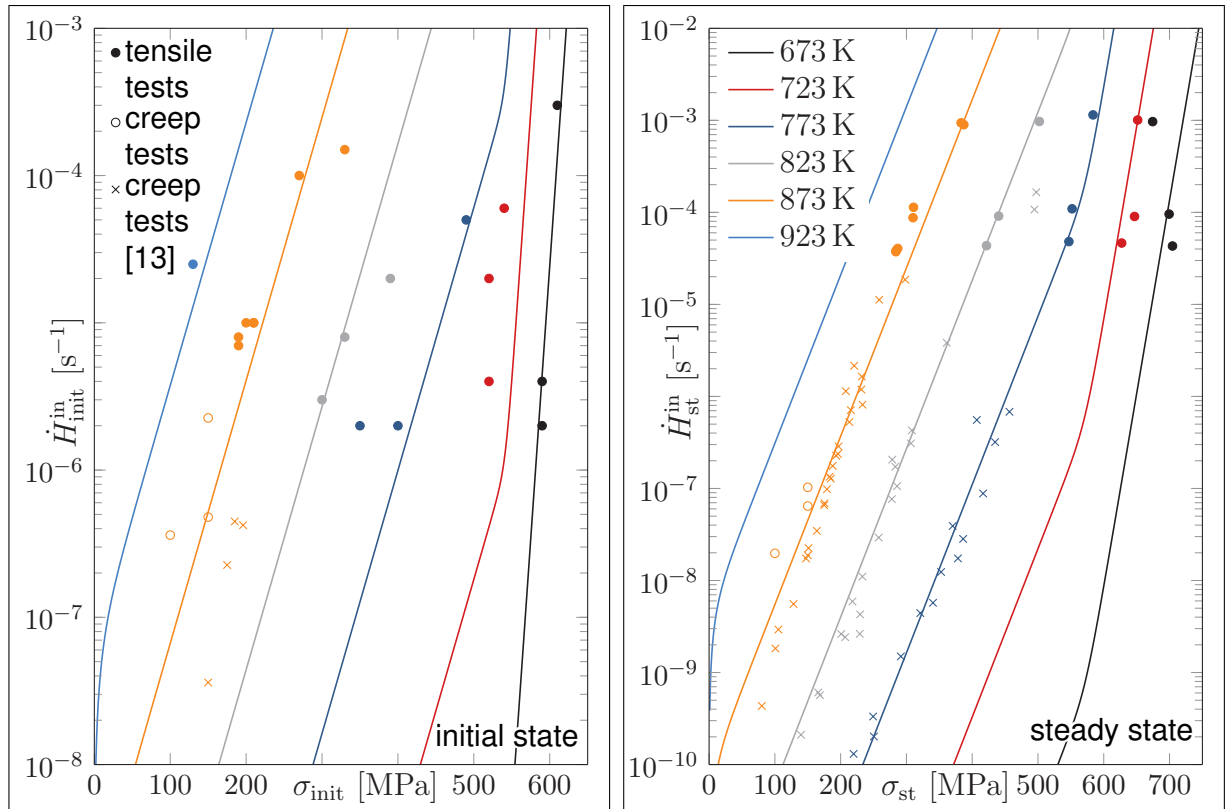


Figure A2.15: Approximation of the inelastic strain rates with the response functions $f_{\sigma_{i7}}(\sigma)$.

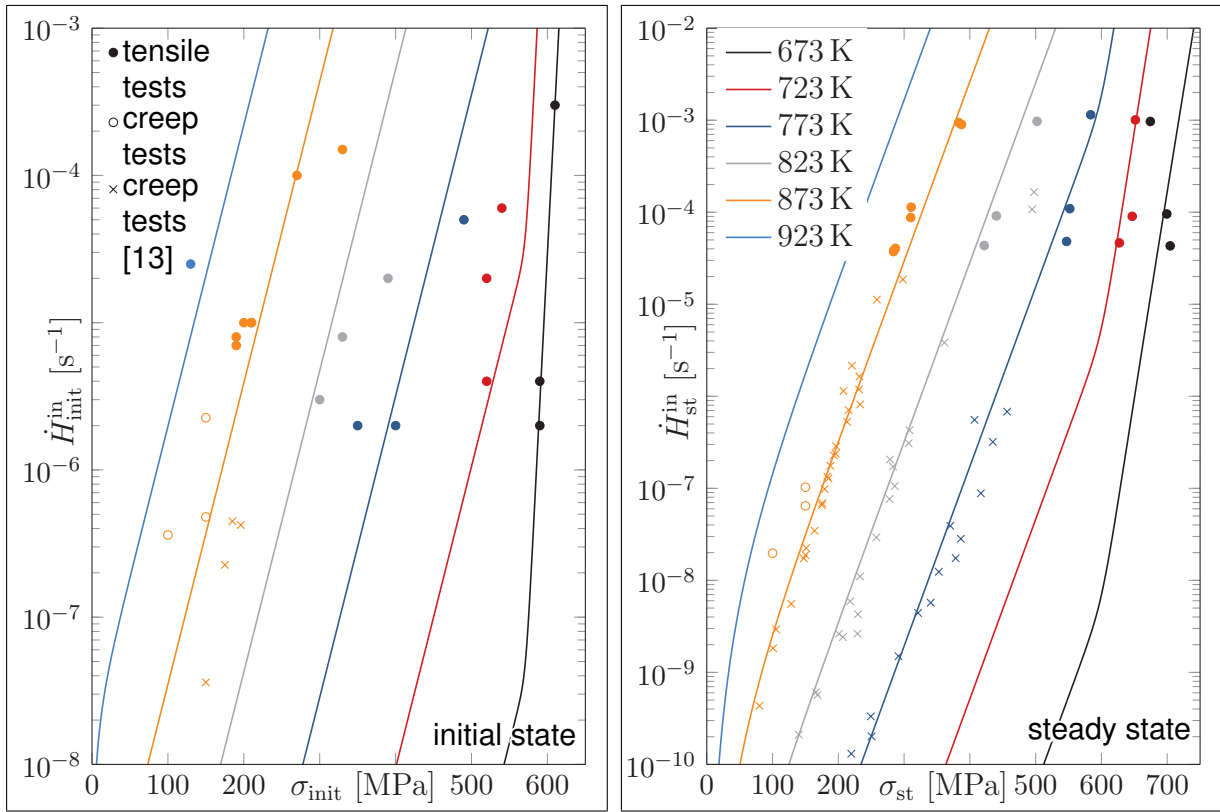


Figure A2.16: Approximation of the inelastic strain rates with the response functions $f_{\sigma_{i8}}(\sigma)$.

Publikationen

Referierte Artikel

1. Eisenträger, J., Naumenko, K. und Altenbach, H.: „Numerical Implementation of a Phase Mixture Model for Rate-Dependent Inelasticity of Tempered Martensitic Steels“. Angenommen von: *Acta Mechanica*, 2018
2. Eisenträger, J., Naumenko, K. und Altenbach, H.: „Calibration of a phase mixture model for hardening and softening regimes in tempered martensitic steel over wide stress and temperature ranges“. *The Journal of Strain Analysis for Engineering Design*, 2018. DOI: 10.1177/0309324718755956
3. Eisenträger, J., Naumenko, K., Altenbach, H. und Gariboldi, E.: „Analysis of Temperature and Strain Rate Dependencies of Softening Regime for Tempered Martensitic Steel“. In: *The Journal of Strain Analysis for Engineering Design* 52, 2017, S. 226–238. DOI: 10.1177/0309324717699746
4. Aßmus, M., Eisenträger, J. und Altenbach, H.: „Projector representation of isotropic linear elastic material laws for directed surfaces“. In: *Zeitschrift für angewandte Mathematik und Mechanik* 97 (12), 2017, S. 1625–1634. DOI: 10.1002/zamm.201700122
5. Eisenträger, J., Naumenko, K., Altenbach, H. und Meenen, J.: „A user-defined finite element for laminated glass panels and photovoltaic modules based on a layer-wise theory“. In: *Composite Structures* 133, 2015, S. 265–277. DOI: 10.1016/j.compstruct.2015.07.049
6. Eisenträger, J., Naumenko, K., Altenbach, H. und Köppe, H.: „Application of the first-order shear deformation theory to the analysis of laminated glasses and photovoltaic panels“. In: *International Journal of Mechanical Sciences* 96–97, 2015, S. 163–171. DOI: 10.1016/j.ijmecsci.2015.03.012
7. Eisenträger, J., Naumenko, K., Altenbach, H. und Lenz, W.: „Näherungsverfahren zur Berechnung von Kerbspannungen und -dehnungen bei Plastizität und Kriechen“. In: *Forschung im Ingenieurwesen* 77, 2013, S. 71-80. DOI: 10.1007/s10010-013-0166-2

Konferenzbeiträge

1. Aßmus, M., Eisenträger, J. und Altenbach, H.: „On isotropic linear elastic material laws for directed planes“. In: Pietraszkiewicz, W., Witkowski, W.: *Shell Structures: Theory and Applications Volume 4. Proceedings of the 11th International Conference*, 2017, S. 57-60
2. Eisenträger, J., Naumenko, K. und Altenbach, H.: „A layer-wise user element for the analysis of photovoltaic modules“. In: Kleiber, M. et al.: *3rd Polish Congress of Mechanics and 21st International Conference on Computer Methods in Mechanics. Short Papers Vol. 2*, 2015, S. 883–884

3. Altenbach, H., Eisenträger, J. und Naumenko, K.: „Approximate Rules for Calculation of Notch Stresses Considering Plasticity and Creep“. In: Khan, A. S.: *Plastic Behavior of Conventional and Advanced Materials: Theory, Experiment, and Modeling - Proceedings of PLASTICITY '15: The Twenty First International Symposium on Plasticity and its Current Applications*, NEAT PRESS, 2015, S. 124–126
4. Eisenträger, J., Naumenko, K. und Altenbach, H.: „Robust approaches for the assessment of stress concentration in the creep range“. In: *Proceedings of 3rd International ECCO Creep & Fracture Conference*, 2014
5. Eisenträger, J., Naumenko, K., Altenbach, H. und Lenz, W.: „Näherungsweise Ermittlung der Spannungskonzentration an Kerben bei inelastischen Verformungen im Hochtemperaturbereich“. In: U. Gabbert et al.: *Effizienz, Präzision, Qualität. 11. Magdeburger Maschinenbau-Tage*, 2013

Buchbeiträge

1. Aßmus, M., Bergmann, S., Eisenträger, J., Naumenko, K. und Altenbach, H.: „Consideration of Non-Uniform and Non-Orthogonal Mechanical Loads for Structural Analysis of Photovoltaic Composite Structures“. In: Altenbach, H., Goldstein, R. V. und Murashkin, E.: *Mechanics for Materials and Technologies*, Springer, 2017, S. 73-122, DOI: 10.1007/978-3-319-56050-2_4